UNIVERSITÀ
DEGLI STUDI
DI PADOVA

UNIVERSITÀ DEGLI STUDI DI PADOVA
DIPARTIMENTO DI INGEGNERIA INDUSTRIALE

SCUOLA DI DOTTORATO DI RICERCA IN INGEGNERIA INDUSTRIALE
INDIRIZZO INGEGNERIA CHIMICA, DEI MATERIALI E DELLA PRODUZIONE
CICLO XXVI

DEVELOPMENT OF HUMAN TISSUES ON A CHIP FROM PLURIPOTENT STEM CELLS

Direttore della Scuola: Ch.mo Prof. Paolo Colombo
Coordinatore d'indirizzo: Ch.mo Prof. Enrico Savio
Supervisore: Dr. Nicola Elvassore

Dottoranda: Federica Michielin

Foreword

The PhD program was performed at “Dipartimento di Ingegneria Industriale sede M Via Marzolo” of “Università degli Studi di Padova” and at “Venetian Institute of Molecular Medicine” of “Fondazione per la ricerca biomedica avanzata onlus” in Padova.

Part of the work concerning the study of microRNAs involvment in human pluripotent stem cells differentiation was carried out at the Scripps Research Institute in La Jolla, CA (USA) under the supervision of Prof. J.F. Loring.

I would like to thank my supervisor and BioERA Lab group for their support to this work, and Prof. Loring and her group for gave me the opportunity to perform part of the work in their laboratory in La Jolla.

All the material reported in this dissertation is original unless explicit references to studies carried out by other people are indicated.

During this PhD program, the following publications have been published:

1. S. Martewicz*, F. Michielin*, E. Serena, A. Zambon, M. Mongillo, N. Elvassore (2012). Reversible alteration of calcium dynamics in cardiomyocytes during acute hypoxia transient in a microfluidic platform. INTEGRATIVE BIOLOGY, vol. 4(2), p. 153-164, ISSN: 1757-9694, doi: 10.1039/c1ib00087j (*equal contribution)
2. C. Luni*, F. Michielin*, L. Barzon, V. Calabrò, N. Elvassore (2013). Stochastic Model-Assisted Development of Efficient Low-Dose Viral Transduction in Microfluidics. BIOPHYSICAL JOURNAL, vol. 104, p. 934-942, ISSN: 0006-3495, doi: 10.1016/j.bpj.2012.12.049 (*equal contribution)
3. M. Aragona, T. Panciera, A. Manfrin, S. Giulitti, F. Michielin, N. Elvassore, S. Dupont, S. Piccolo (2013). A Mechanical Checkpoint Controls Multicellular Growth through YAP/TAZ Regulation by Actin-Processing Factors. CELL, ISSN: 0092-8674, doi: 10.1016/j.cell.2013.07.042

The following work has been submitted and is currently under revision:

1. G.G. Giobbe*, F. Michielin*, S. Martewicz, S. Giulitti, C. Luni, A. Floreani, N.

Elvassore. Integrated multi-stage tissue on a chip generation from human pluripotent stem cells. NATURE METHODS. (*equal contribution)

The following work has to be submitted:

1. F. Michielin, E. Serena, P. Pavan, N. Elvassore. Cyclic mechanical microscale-stimulation affects cellular membrane integrity in a human muscle dystrophy *in vitro* model.

Poster presentations:

1. Giobbe GG, Tonon F, Zambon A, Michielin F, Elvassore N, Floreani A. Oxygen gradient on a chip for optimizing the differentiation of human pluripotent stem cells into hepatic cells. 64th Annual Meeting of the American Association for the Study of Liver Diseases, November 1 - 5, 2013, Washington DC, USA.
2. Michielin F, Serena E, Pavan P, Elvassore N. Cyclic mechanical microscale-stimulation affects cellular membrane integrity in a human muscle dystrophy in vitro model. Alternative Muscle Club Meeting, June 28, 2013, San Diego, CA, USA.
3. Michielin F, Giobbe GG, Martewicz S, Giulitti S, Floreani, Elvassore N. Integrated multi-stage tissue on a chip generation from human pluripotent stem cells. ISSCR's 11° Annual Meeting, June 12-15, 2013, Boston, MA, USA.
4. Michielin F, Giobbe GG, Giulitti S, Elvassore N. Development of an automated microfluidic platform for colturing and differentiating human stem cells. Convegno Nazionale Gricu 2012, September 16 – 19, Montesilvano (PE).
5. Michielin F, Serena E, Giulitti S, Pavan P, Elvassore N. Cyclic mechanical stretch affects membrane integrity during myogenesis. GNB 2012 - 3rd National Congress of Italian Group of Bioengineering, June 27 - 29, 2012, Rome, Italy.
6. Michielin F, Luni C, Giulitti S, Elvassore N. Efficient adenoviral transduction in stem cells through cyclic microfluidic-assisted infections at low MOI. SBE's 3rd International Conference on Stem Cell Engineering, April 29 – May 2, 2012, Seattle, WA, USA.
7. Michielin F, Serena E, Giulitti S, Pavan P, Elvassore N. Cyclic mechanical stretch affects membrane integrity during myogenesis. SBE's 3rd International Conference on Stem Cell Engineering, April 29 – May 2, 2012, Seattle, WA, USA.

8. Martewicz S, Michielin F, Serena E, Zambon A, Elvassore N. Alteration of calcium dynamics in murine cardiomyocytes during acute hypoxia. Keystone Symposia on Molecular and Cellular Biology. Mechanisms of Cardiac Growth, Death and Regeneration, February 22 – 27, 2011, Keystone, Colorado, USA.

Sommario

Lo sviluppo di nuove tecnologie di microscala volte a generare tessuti e organi umani on a chip si sta rivelando una nuova strategia per compiere esperimenti multi-parametrici a basso costo per sviluppo di modelli di malattia e screening di specifiche strategie terapeutiche, come ampiamente riconosciuto dalla comunità scientifica, dalle maggiori compagnie farmaceutiche e da agenzie governative.

La generazione di organi umani on a chip, in cui le tecnologie di microscale, come la tecnologia microfluidica, sono combinate colture cellulari umane allo scopo di mimare l'intero ambiente di un organo vivente, offre un'opportunità unica per studiare la fisiologia e la fisiopatologia umane, in modo rappresentativo delle condizioni in vivo. Questa prospettiva tecnologica potrebbe fornire una soluzione efficace alle attuali limitazioni dei modelli animali, che si dimostrano altamente costosi e non predittivi della fisiologia umana, e dei modelli convenzionali di colture cellulari che non sono in grado di rappresentare i complessi processi che caratterizzano una patologia a livello di organo.

La possibilità di rappresentare l'organogenesi direttammente on a chip partendo da cellule staminali umane pluripotenti, che hanno il potenziale per generare tutti I tipi cellular presenti nel corpo umano, consentirebbe di superare i limiti legati alla disponibilità di cellule primarie umane, come epatociti o cardiomiociti umani. Per di più, la generazione di cellule staminali umane pluripotenti indotte da cellule somatiche adulte ottenuta di recente tramite l'espressione ectopica di fattori di trascrizione definiti, fornisce un nuovo mezzo per ottenere cellule staminali paziente-specifiche con diversità genetica specifica.

Questo studio è volto allo sviluppo di tessuti funzionali umani on a chip partendo da cellule staminali pluripotenti, da usare nello sviluppo di nuovi modelli di patologie in vitro o per screening di farmaci e test di tossicità, con più capacità predittiva degli attuali modelli animali, superando i problemi legati al reclutamento di fonti cellulari primari.

A questo proposito, è stato sviluppato un sistema su microscale integrato, basato sulla tecnologia microfluidica, al fine di derivare tessuti cardiaco ed epatico funzionali on a

chip da cellule staminali umani pluripotenti, tramite la somministrazione accurata di composti chimici e fattori di crescita, all'interno del microambiente cellulare, e un'appropriata regolazione dei fattori esogeni ed endogeni, che hanno un effetto riconosciuto nello sviluppo embrionale in vivo.

Queste cellule funzionalmente differenziate on a chip possono essere usate direttamente screening multi-parametrici e su larga scala di farmaci o per sviluppare modelli micro-ingegnerizzati di organo umano. Quest'ultimo aspetto richiede inoltre di progettare nuove tecnologie che assistano gli esperimenti in vitro e sviluppare nuove strategie terapeutiche o per scrinare potenziali cure cliniche. In particolare, la sono stati progettati test funzionali appropriati per valutare la risposta a farmaci o stimoli esterni, come lo stress meccanico o l'ipossia, in un contesto fisiologico o patologico.

Grazie allo sviluppo di uno scambiatore di gas microfluidico per rimuovere velocemnete il contenuto di ossigeno nel medium di coltura, è stato analizzto il ruolo di un'ipossia acuta sulle dinamiche dei flussi del calcio, mimando gli effetti iniziali di un'ischemia nel microambiente cardiaco.

Inoltre, è stato analizzato il ruolo dello stress meccanico ciclico, che svolge un ruolo cruciale nello studio di nuove risposte fisiologiche e patologiche al microambiente cellulare, in un modello in vitro di Distrofia Muscolare di Duchenne (DMD), tramite un dispositivo di stretching cellulare basato sulla tecnologia microfluidica con cui è possibile riprodurre in modo accurato deformazioni meccaniche cicliche nel tempo.

Combinando lo sviluppo di tessuti on a chip e microtecnologie che assistano test funzionali on a chip si aprono nuove e sostanziali prospettive nella generazione di un modello umano in vitro che riassuma le caratteristiche fisio-patologiche dei tessuti e organi all'interno del corpo umano.

Summary

The development of new microscale technologies aimed at generating human tissues and organs on a chip is emerging as a novel effective strategy to perform cost effective and multi-parametric assays for disease modeling investigations and screening specific therapeutic strategies, as broadly recognized from the scientific community, the major pharmaceutical companies and the governmental agencies.

The generation of human organs on a chip, in which microscale technologies, such as microfluidics, are combined with cultured human cells in order to mimic whole living organ environment, offers a unique opportunity to study human physiology and pathophysiology, resembling in vivo conditions. This technological perspective could provide an effective solution to the current limitations of animal models, which result highly expensive and non predictive of human physiology, and conventional cell culture models that fail to recapitulate complex, organ-level disease processes.

The possibility of developing direct organogenesis on a chip from human pluripotent stem cells, which have the potential to generate all cellular types of the human body, could overcome the limited availability of human primary cells, such as human hepatocytes or cardiomyocytes. Moreover, the recent generation of human induced pluripotent stem cells (hiPSCs) from adult somatic cells through the ectopic expression of defined transcription factors, provides a new effective tool to obtain populations of patient-specific stem cells with distinctive genetic diversity.

This work is aimed at the development of functional human tissues on a chip from pluripotent stem cells, to be used in developing new in vitro disease models or drug screening and toxicity assays, more predictive than current animal models, overcoming issues related to primary cell sources recruitment.

To this purpose, an integrated microscale system, based on the microfluidic technology, was developed, in order to derive functional cardiac and hepatic tissues on a chip, from human pluripotent stem cells, through the accurate delivery of chemical compounds and growth factors, within cellular microenvironment, and proper regulation of exogenous and endogenous factors, which are known to affect embryonic development in vivo.

These functionally differentiated cells on a chip can be directly used for multi-parametric and large-scale drug screening or for developing micro-engineered human organ models. This last aspect also requires to design new technology for assisting in vitro assays and developing new therapeutic strategies or for screening among potential clinical cures. In particular, design of proper functional assays to test cellular responses to drugs or external stimuli, such as mechanical stress or hypoxia, in a physiologic or pathologic context has been addressed.

Thanks to the development of a microfluidic gas exchanger for generating rapid depletion of oxygen content in culture medium, the role of acute hypoxia in calcium handling machinery of a cardiomyocytes population was investigated, mimicking early effects of ischemia on cardiac microenvironment. Moreover, the role of cyclic mechanical stress, which plays a crucial role in the investigation of new physiological and pathological responses to cell culture microenvironment, was analyzed in a human Duchenne Muscular Dystrophy (DMD) in vitro model, through a microfluidic-based cell stretching device accurately reproducing cyclic mechanical deformations along time.

The combination of tissues development on a chip and micro-technology assisting for functional assay on a chip opens new and substantial perespective in generating a human in vitro model that properly resemble the physiological and pathophysiological behaviro of a tissues or organs within humna body.

Contents

Chapter 1

Introduction and aim

1.1 Tissues on a chip development

Emerging micro-fabrication technologies, developed in recent years, opened new perspectives in deriving cost-effective in vitro models of relevant human diseases for high-throughput patho-physiologic investigations and drug screening assays. These new capabilities, arisen from the convergence of micro-engineering with cell biology, have led to development of "Tissues on a chip" and, later, "Organs on a chip", that reconstitute the structural tissue arrangements and functional complexity of living organs, using cells cultured in engineered devices with relevant micro-architecture and micro-environmental signals[1,2,3].

1.1.1 Potentialities of tissues and organs on a chip

These micro-scale tissues and organs on a chip permit study of biological processes in ways that are not possible using conventional cell culture systems, or animal models, which result poor predictive of human physiology[4]. Engineering microenvironments that simulate *in vivo* organ systems provide critical insight into the cellular basis for pathologies, development and homeostasis, while curtailing the high experimental costs and complexities associated with *in vivo* studies[5]. Indeed, *in vivo* models can be expensive, highly variable, difficult to manipulate, and experimental results could be confounded or challenging to interpret. As a result, in the pharmaceutical industry, *in vivo* studies require exorbitant resources, but often fail to translate promising *in vitro* results for drug compounds to clinically viable solutions[5].

For this reason, chemical and pharmaceutical industries are now demonstrating an increasing interest in developing costly effective human tissues on a chip. They recognize the ability of micro-fabrication techniques, and in particular of microfluidic technology, to recapitulate key structures and functions of human tissues and organs in vitro, thanks to the possibility to accurately control flow dynamics and, consequently, pharmacodynamics and pharmacokinetics, and other cellular features such as morphology and substrate stiffness.

A growing number of in vitro models based on lab on a chip technology are being developed for disease and toxicity studies. These range from cell-free assays to cell-based systems (including single-cell arrays and three-dimensional cell culture system), in addition to small multicellular "organism on a chip". These on chip devices have shown the capability to immobilize, manipulate and transport particles, biological parts or cells. They have generated stable static or dynamic gradients of chemical and biochemical compounds, provided a constant or intermittent supply of nutrients and removal of metabolites and allowed multiplexed analyses including parallel read-outs of cell-culture parameters by on chip integrated sensors. Integrating these tools with cell culture facilities and cell-based assays will lead to more and advanced culture techniques, highly sophisticated, and integrated devices as well as higher-throughput and multiplexed assays[6]. As a result, these microsystems offer the unique opportunity to study cells functions in an organ-specific context, thanks to the possibility to accurate reproduce spatial and temporal gradients to which they are exposed *in vivo*, and topological and mechanical cues that cells experience in the human body, as well.

Indeed, in their normal environment, cells are subjected to multiple cues that vary in time and space, including variations of soluble molecules, biochemical and mechanical interactions with the extracellular matrix and cell-cell contacts[7]. Physiologic stresses or pathologic conditions may arise from genetic diseases or external cues and in both cases cells are exposed to different stimuli such as mechanical stress or decreased nutrients supply to the tissues, which may lead to altered cellular homeostasis.

Micro-fabricated systems allow cells to experience these cues in vitro in a controllable and reproducible fashion that cannot easily be achieved by standard tissue culture systems. Moreover, they can be used to link cell culture with integrated analytical devices that can probe the biochemical processes governing cell behavior in both physiologic and pathologic conditions.

1.1.2 Microfluidic technology

Micro-fabrication techniques allow creating devices with structures of dimensions that are relevant for biological systems, such as cell sizes (on the order of 10 μm) and the sizes of human blood vessels with spacing between capillaries on the

order of 100 or 200 μm. At this size scale, it is possible to create more physiological growth environments with relevant shear stress, liquid-to-cell ratios, and physiological fluid resistance times in tissue compartments. Only small quantities of reagents and cells are needed, and parallel processing is possible. Laminar flow allows producing highly controlled microenvironments with defined composition of nutrient and factors into the media, generation of temporal and spatial concentration gradients and regulation of shear stress induced on cells.
The small physical dimensions of microfluidic culture systems inherently contain small numbers of cells, leading to mass-limited quantities of molecules to be analyzed and placing further constraints on the required sensitivity of analytical methodologies. The optical transparency of many common device materials such as polydimethylsiloxane, poly(methyl-methacrylate), and glass readily accommodates optical measurements, and the sizes of both microfluidic device features and eukaryotic cells are commensurate with the size scales accessible via optical microscopy[8].
The control of cellular microenvironment through microfluidic systems represents a valuable tool to investigate pathways controlling cell phenotype and behaviors by monitoring cellular responses to controlled perturbations in the extracellular microenvironment.

1.1.3 Organs on a chip: state of the art

Recently several studies reported about generation of organs on a chip in order to recapitulate key structures of living organs *in vivo*.
Few years ago, Ingber and colleagues developed a biomimetic microsystem reconstituting the critical functional alveolar-capillary interface of the human lung and able to reproduce complex integrated organ-level responses to bacteria and inflammatory cytokines introduced in the alveolar space[9] (Fig. 1.1). The device was used to reproduce drug-toxicity induced pulmonary edema observed in human cancer patients treated with interleukin-2 drug[10].

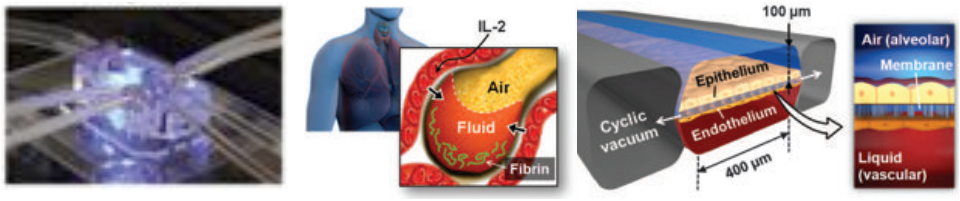

Figure 1.1 Artificial lung on a chip. The system, developed by microfluidic technology, reproduces integrated organ-level responses to bacteria and inflammatory cytokines present in the alveolar space.

This in vitro artificial lung well represents the main goal of tissue and organ on a chip development, which is not to make replacement tissues or organ for transplants, but replicate organs' functions in vitro. This makes the chips useful in testing substances for therapeutic and toxic effects or to investigate the onset and the evolution of specific diseases mimicking *in vivo* physiologic and pathologic stimuli (i.e. shear stress, mechanical stress, hypoxia, etc.).

Many other works focused on recapitulation of human organ functions on a chip include heart, liver and gut[11,12,13,14,15,16]. Liver and cardiac toxicity is among the most common biological reasons for drug candidates to be pulled from clinical development, so it is important to be able to predict it. In this perspective, Toh et al., 2009, developed a microfluidic 3D hepatocyte chip for in vitro drug toxicity testing, based on multiplexed microfluidic channels in which hepatocytes maintain *in vivo* synthetic and metabolic functions[17].

Micro-fabrication techniques were also employed to develop an array of anisotropic cardiac micro-tissues recapitulating laminar architecture of the heart ventricle through mini-cantilevers of soft elastomers. Deflection of these cantilevers, during muscle contraction allows calculation of diastolic and systolic stresses generated by the engineered tissues[16].

1.1.4 Cell sources for in vitro models development: current limitations and perspectives

As mentioned before, animal models have a low potential to represent human physiology and pathophysiology, basically due to intrinsic differences among species. Drug-toxicity tests carried out using animal models often fail to be predictive of toxicity in humans, due to significant differences in interspecies metabolic capacities, physiologies, and ignored disease adaptation mechanisms. Indeed, functional differences in drug handling by kidneys and drug absorption in

the digestive tract, drug-protein interactions and metabolic mechanisms are recognized[18]. Therefore multiple species testing in combination with human cell line assays might better predict eventual toxicity profiles.

In vivo animal models also result in highly expensive and low-throughput experimental tools, to which human in vitro models are good alternatives, with the advantage of a better representation of human physiology. Ex-vivo tissue slices have been widely used for biomedical studies and they are suitable for assays that may require visual analysis like immunocytochemistry. The main restrictions of using organ culture are careful and laborious preparation, lack of standardized protocols and short-term survival.

Primary cells, directly derived from tissues harvests represent the main tool for in vitro culture as they can be easily expanded in standard petri dish, with lower costs compared to animal models. Compared to immortalized cell lines, they can maintain wild-type un-altered nature, which translates to in vitro cultures with cells preserving better structural and biochemical complexity found *in vivo*. However, limitations due to contaminations by minority cells of distinct origins, dedifferentiation in culture and sensitivity to passaging result in altered phenotypes, slow proliferation rate and early senescence after few expansion passages. Moreover, intrinsic limits in human cells recruitment exist for cardiomyocytes and hepatocytes, due to the impossibility of ex-vivo extractions.

On the other hand, immortalized cell lines, derived from primary cells and genetically modified in order to obtain more proliferative cells, stable and resistant to dedifferentiation, have been demonstrated to possess altered genomic content, abnormal expression of intracellular proteins and functional alterations such as loss of contact inhibition[18], thus failing to be representative of human physiology.

In this perspective, human pluripotent stem cells (hPSCs), with their ability to potentially give rise to any cell type of the human body, offer a great advantage for deriving functional tissue-specific cells which can be used both in the development of relevant diseases in vitro model and for testing toxicity of new drugs. Though the perspective for human embryonic stem cells in clinical medicine has been centered on their potential for cell replacement and tissue repair, for many diseases and injures is still clearly a distant goal. Instead, the ability to generate pluripotent stem cells (PSCs) from adult somatic cells and

improved methods for directing differentiation, has shifted the focus to using PSCs for disease modeling and drug development[19].

1.2 Human pluripotent stem cells

Human pluripotent stem cells (hPSCs) comprise human embryonic stem cells (hESCs), derived from the inner cell mass of the blastocyst of a human embryo, and induced pluripotent stem cells (hiPSCs), derived from adult somatic cells through a process of reprogramming with the use of specific factors. They have distinctive features of pluripotency and self-renewal and the potential to generate all cellular types of the human body, allowing generation of tissue-specific functional cells to be used in disease modeling and drug screening applications (Fig. 1.2).

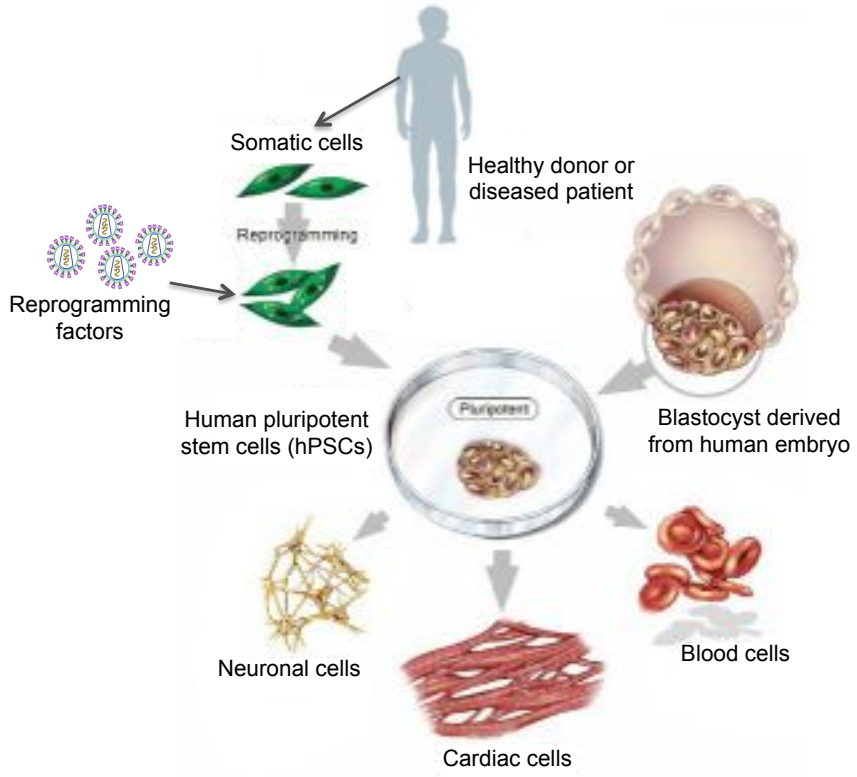

Figure 1.2 Human pluripotent stem cells (hPSCs) can be derived from inner cell mass of embryonic blastocyst or from adult somatic cells of healthy donors or diseased patients through overexpression of reprogramming factors. HPSCs cultured in vitro have the potential to generate all cell types of the human body, included neuronal, cardiac and blood cells.

Human induced pluripotent stem cells were derived for the first time in 2006 from Yamanaka and coworkers starting from adult somatic cells through the retrovirus-mediated transduction of four specific genes (Oct4, Sox2, Klf4 and c-Myc). These

cells are identical to embryonic stem cells with the advantage they can be generated from specific diseased patients.

Thus, induced pluripotent stem cells technology provides a unique opportunity to generate 'disease phenotypes in a dish' for use as in vitro model systems and substrates for small molecules screens. While it is unlikely that an in vitro system can adequately represent all aspects of a multi-faceted disease, the ability to generate any human tissue cells from any genotype or disease provides unparalleled access for these studies.

1.2.1 Pluripotency and self-renewal

HPSCs have unique features of pluripotency and self-renewal, meaning that they can proliferate indefinitely in culture while maintaining their characteristic phenotype and the potentiality to differentiate into all embryonic germ layers, i.e. endoderm, mesoderm and ectoderm. HPSCs can be cultured in standard Petri dish in both feeder-layer, consisting in mouse or human embryonic fibroblasts, and feeder-free conditions[20,21]. They possess typical round-shape morphology and grow in homogeneous colonies with defined smooth edges. Beside these features, expression of core transcriptional factors Nanog, Oct4 and Sox2 is essential to maintain their characteristic phenotype, as well as expression of several other markers involved in pluripotency and self-renewal maintenance.

Although there is still incomplete elucidation about all the signaling pathways sustaining undifferentiated proliferation of hPSCs, several signals have been found to play a central role. Among them fibroblasts growth factor (FGF) and transforming growth factor β (TGFβ)/Activin family members are recognized to play a central role in promoting hPSCs self-renewal[22,23,24,25].

FGF-pathway plays also an important role in maintaining pluripotency and self-renewal, as elevated concentrations of exogenous b-FGF permit hPSCs culture even in the absence of feeder layer or feeder-conditioned medium[26].

The effect of TGFβ signaling is mediated by binding to cell-surface type I and type II receptors with threonine/serine kinase activity. Upon ligand binding, the type II receptor phosphorylates the type I receptor, which in turn phosphorylates intracellular receptor-Smads (R-Smads). Upon phosphorylation, the R-Smads associate with Smad4 and localize to the nucleus, activating transcription. Maintenance of hESCs is associated with active Smad2/3, whereas Smads 1/5/8

activation, induced by bone morphogenic protein BMP signaling, promote differentiation[27].

IGF/PI3K signaling is also associated with maintenance of pluripotency in vitro. PI3K maintains human pluripotent cells by suppressing the ability of specification factors, such as ActivinA, to promote differentiation. This finding indicates that PI3K/Akt cooperates with ActivinA to promote the pluripotent state and suggests that ActivinA has context-dependent functions in promoting and antagonizing self-renewal pathways[22].

Despite the addition of exogenous factors that manipulate the activation of pluripotency-associated signaling pathways, the local cellular microenvironment and hence the signaling inputs vary significantly in hESC maintenance cultures. In fact, it is likely that hESCs are exposed to a wide range of signaling environments by virtue of the properties of hESC colonies (size, distribution and culture condition-specific associated differentiated cells), and individual hESC position in a particular colony, consistently with properties of the *in vivo* stem cell niche. Localized effects in ESCs niches are likely mediated by interactions between exogenously controlled parameters and autocrine and paracrine secretion of endogenously produced factors[27]. Indeed, continuous wash-out of cell culture medium in a continuously perfused microfluidic cell culture system has been shown to lead to pluripotency markers expression down-regulation and premature differentiation into neuro-ectoderm[28], suggesting that extrinsic and endogenous signaling cooperate to maintain stem cells pluripotency and self-renewal.

Fig. 1.3 shows a schematic representation of the recognized role of both exogenous and endogenous cell-secreted factors comprising members of FGF2, TGFβ and IGF pathways in promoting pluripotency and self-renewal of hPSCs.

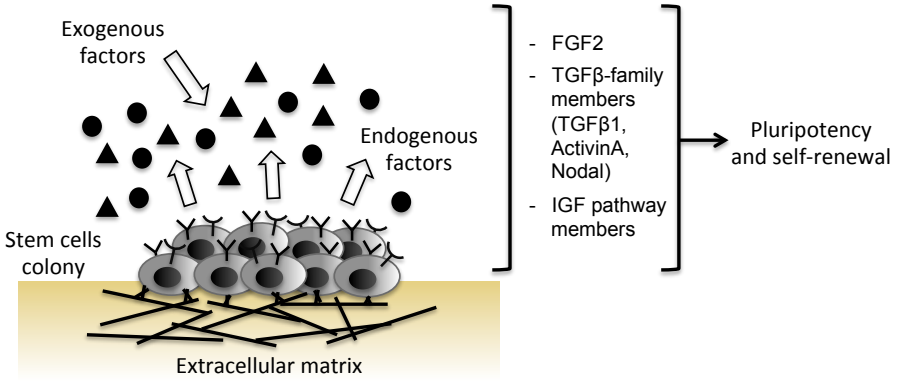

Figure 1.3 Cultured pluripotent stem cells require proper exogenous and endogenous factors supply. Among them, members of FGF2, TGFβ and IGF pathways play central role in maintaining pluripotency and self-renewal.

1.2.2 Germ-layers specification

Embryology has offered important insights into key pathways regulating ESC differentiation, resulting in advances in modeling gastrulation in culture and in the efficient induction of embryonic germ layers and many of their downstream derivatives[29]. One of the most important events during embryogenesis is the generation of the three primary germ layers: ectoderm, mesoderm, and endoderm during the process of gastrulation (Fig. 1.4a). Whereas embryonic gastrulation in mouse has been widely investigated *in vivo*, human embryonic development still remains an open question. Moreover, mouse and human ESCs represent different stages of development and clearly display different requirements for growth and maintenance in the undifferentiated state[30]. However, the signaling pathways that regulate hESC differentiation are similar to those that regulate these processes in mouse ESC cultures.

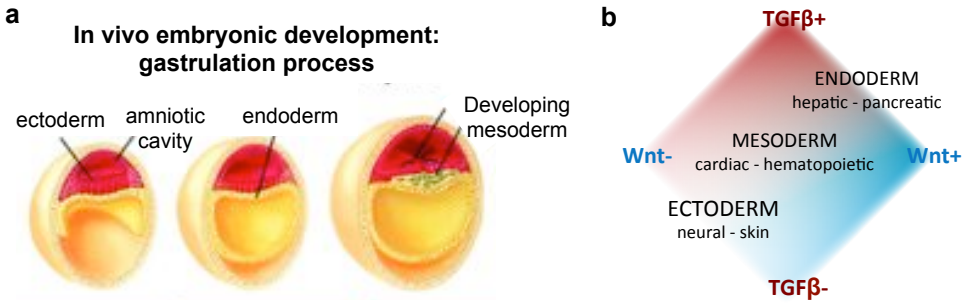

Figure 1.4 (**a**) *In vivo* gastrulation in embryonic development. Ectoderm, endoderm and mesoderm germ layers formation occurs at different time stages. (**b**) Specific derivation of the three germ layers in vitro is achieved through manipulation of key pathways (i.e. TGFβ and Wnt pathways) regulating embryonic development *in vivo*.

Gene-targeting studies have shown that members of the TGFβ family including BMP4 and Nodal as well as members of the Wnt family are essential for these developmental steps. Thus, manipulation of these pathways in hESC cultures in vitro allows the regulation of germ layers development, as summarized in Fig. 1.4b.

High levels of Activin/Nodal, in combination with WNT3A stimulation, induce endoderm formation in vitro, whereas lower doses specify mesoderm identity. Alternatively, canonical mesoderm markers, such as GATA2, can be induced using ActivinA, BMP4, VEGF, and FGF2 treatment. After transient up-regulation of early mesendodermal markers, activation of mesodermal markers such as GATA2, HAND2, SOX9, and TAL1 is detected specifically in the mesoderm conditions, whereas definitive endoderm is characterized by expression of

markers EOMES, FOXA2 GATA6, SOX17, and HHEX. These hESCs can also be differentiated into a neuroectoderm-like progenitor population, positive for SOX2 and PAX6, by inhibition of TGFβ, Wingless/integrase1 (WNT), and bone morphogenetic protein (BMP) signaling.

1.3 HPSCs-based in vitro models for disease and drug screening assays

In vitro models representative of human tissues have become indispensable tools for representing human physiology and studying diseases pathogenesis and possible therapies[31]. Functional cardiac and hepatic cells, expressing a mature phenotype, were efficiently derived from hPSCs as new tools for drug screening and toxicity assays and in vitro disease modeling.

1.3.1 HPSCs-derived cardiomyocytes

With cardiac diseases being the primary cause of morbidity and mortality in Western countries, and with paucity in therapeutic interventions, the identification of novel and experimental cardiac drug targets has recently received renewed interest.

One reason for slow cardiac drug target discovery is the limited predictive value and high costs of animal-based model systems. From the human heart itself, harvesting mature cardiomyocytes is confounded by limitations in cell numbers, proliferative capacity, variability in preparation, disease state and viability, especially from cadavers[32]. Recent repots have provided promising preliminary data that hiPSC-CMs from disease models display expected responses to anti-arrhythmic compounds and can also be used to validate the efficacy of experimental therapeutic interventions.

Because hPSCs can generate the major cardiomyocytes subtypes (atrial, ventricular and pacemaker cells) and many cardiac diseases are autonomous to the cardiomyocyte, hPSCs represent potential in vitro paradigms for understanding disease pathophysiology and for identifying pathways to target in ameliorating the conditions.

Essential for modeling cardiac disease are robust, reproducible differentiation protocols to obtain functional cardiomyocytes in vitro, able to mimic developmental cues occurring in early embryonic development *in vivo*[33]. These

includes regulation of bone morphogenetic proteins (BMPs), Nodal/ActivinA and fibroblast growth factors signaling pathways to induce mesoderm formation and specification, which precedes cardio genesis. Signaling through the canonical Wnt pathway also plays discrete time-specific roles, with expression of Wnts promoting the formation of cardiogenic mesoderm, but repressing the subsequent specification to cardiomyocytes[19].

During hPSCs differentiation into beating cardiomyocytes, pluripotency markers, such as Oct4 and Nanog are down-regulated concurrently with the up-regulation of cardiac transcription factors (NKX2.5, TBX5, MEF2C) and subsequently genes encoding structural proteins (MYH6, MYH7, cTnT). Immunofluorescence can show presence of structural proteins, like α-actinin, even with relatively organized striations[32].

HPSCs-derived cardiomyocytes usually display gene expression and microRNA expression profiles, ion channel functionality, ultra-structures, and pharmacological responses sharing similarities with an embryonic/fetal cardiac phenotype. However, further maturation of the cells has also been reported after long- term culture in vitro[34]. Increasing number and organization of myofibrils and progressive withdrawal from the cell cycle in beating hPSCs-derived cardiomyocytes are first evidences of cellular maturation towards an adult phenotype.

1.3.2 HPSCs-derived hepatocytes

The liver is a major location for the detoxification of drugs or other xenobiotics as well as endogenous substrates; therefore, metabolic function is a critical role of hepatocytes in vitro and *in vivo*[35]. Many studies focused in the last years in the derivation of functional hepatocytes from both hESCs and hiPSCs able to respond to drugs and potentially utilizable for in vitro hepatotoxicity assays.

Mature hepatocytes can be recognized first of all through morphological analysis, presence of bi-nucleated cells and markers expression. Albumin (ALB), alpha1-antitrypsin (α1-AT), tyrosine aminotransferase (TAT), hepatic nuclear factor 4α (HNF4α) and glucose 6 phosphatase (G-6-P) are all indicators of mature hepatocytes.

Metabolic activity is the most important function of hepatocytes in vitro and *in vivo*; this function is performed by the complex bio-transforming system, which

consists of phase I and II metabolizing enzymes and phase III transporters. Metabolizing enzymes such as cytochrome P450 and glutathione S-transferase and transporting proteins such as multidrug-resistant protein 1 (MRP1), organic anion transporting polypeptide 2 (OATP2), and glucose transporter 2 (Glut2) are important for drug screening and hepatotoxicity investigations. Functionality of hPSCs-derived hepatocytes can also be assessed through cellular uptake and excretion of indocianine green, ICG, which is a unique characteristic of primary hepatocytes, as well as the capacity of accumulate glycogen, revealed by PAS staining, and the secretion of functioning proteins, such as albumin.

Toxicity phenotypes using live cells include characterization of cell shape, cell adhesion and spreading, nuclear condensation, accumulation of lipids, cytoskeleton integrity, in addition to short-term and long-term changes of MP[36], but cell loss, cell cycle arrest, DNA degradation/apoptosis, nuclear size, oxidative stress, stress kinase activation, DNA damage, mitochondrial membrane potential, mitochondrial mass, mitotic arrest are also indicators of hepatotoxicity.

Usually all these parameters are evaluated in a dose-dependent manner and different exposure time, i.e. 30 min (acute effect), 24h and 72h (chronic effect). Certainly the possibility to accurate control drug delivery with different temporal pattern of exposure, maybe by using microfluidic-based systems could greatly improve the sphere of possible read-outs.

1.4 Motivations and aim of the thesis

The development of new microscale technologies, which allow performing cost effective and multi-parametric assays for disease modeling investigations or for screening specific therapeutic strategies, has been recognized of paramount importance from the scientific community, the major pharmaceutical companies and the governmental agencies.

Indeed, the generation of human organs on a chip, in which the microscale engineering technologies are combined with cultured human cells in order to recapitulate whole living organ environment, offers a unique opportunity to study human physiology and pathophysiology, closely mimicking *in vivo* conditions. This technological perspective could provide an effective solution to the limitations of both animal models, which result highly expensive and non predictive of human physiology, and conventional cell culture models that fail to

recapitulate complex, organ-level disease processes in humans.

Recently, successful examples of organ on a chip development have been provided[37,38,39,40], however, they were obtained from primary animal cells and, in few cases, from primary human cells. The possibility of developing direct organogenesis on a chip from human pluripotent stem cells, which have the potential to generate all cellular types of the human body, could overcome the limited availability of human primary cells, such as human hepatocytes or cardiomyocytes. Human embryonic stem cells and induced pluripotent stem cells grown in culture also showed intrinsic and unexpected levels of emergent self-organization for generating highly ordered structures and tissues[41,42,43], thus opening a wide perspective for multi-organ generation on a chip.

Moreover, the recent generation of human induced pluripotent stem cells (hiPSCs) from adult somatic cells through the ectopic expression of four defined transcription factors, provided a new effective tool to get patient-specific stem cells, skipping ethical issues related to embryos manipulation.

In this new perspective, patient-specific reprogrammed cells or human embryonic stem cells can be integrated within microscale devices, differentiated into functional tissue-specific cells on a chip and used for *in vitro* assays, aimed at developing new disease models and drug testing. Design of proper functional assays to test cellular responses to drugs or external stimuli, such as mechanical stress or hypoxia, in a physiologic or pathologic context allow investigations of new therapies and effective drugs.

Hypothetically, a screen of genetic diversity panels of cardiomyocytes or hepatocytes to identify rare responders, analyze drug toxicity, or perform 'clinical trials on a chip' using hiPSC-derived diseased cells allows a safe and efficient study of potential therapies of genetic defects before initiating Phase I studies in patients.

In this context, the general aim of this work is to design and develop an integrated microscale system, based on the microfluidic technology, to derive functional cardiac and hepatic tissues on a chip, from human pluripotent stem cells, through the accurate delivery of chemical compounds and growth factors, within cellular microenvironment, and proper regulation of exogenous and endogenous factors, which are known to affect embryonic development *in vivo*.

Evaluation of the functionality of these cells in a physiologic or pathologic context require to develop new tools for supporting *in vitro* models development of human diseases (disease on a chip). Specifically, the role of early hypoxia-induced effects on cardiac tissue will be investigated and the role of the mechanical stress in a skeletal muscle human model of Duchenne Muscular Dystrophy.

To address this aim, specific microscale-based devices will be developed in order to achieve long-term culture of mammalian cells, and in particular stem cells, within microfluidic platforms, controlled delivery of factors and nutrients to drive germ layer commitment and functional differentiation. Moreover, *ad hoc* devices for the temporal regulation of oxygen partial pressure in the culture medium and the control of mechanical stress on the cells, will be designed and developed.

1.5 References

1. Ghaemmaghami, A. M., Hancock, M. J., Harrington, H., Kaji, H. & Khademhosseini, A. Biomimetic tissues on a chip for drug discovery. *Drug Discov. Today* **17,** 173–181 (2012).

2. Huh, D., Hamilton, G. A. & Ingber, D. E. From 3D cell culture to organs-on-chips. *Trends Cell Biol.* **21,** 745–754 (2011).

3. Huh, D., Torisawa, Y., Hamilton, G. A., Kim, H. J. & Ingber, D. E. Microengineered physiological biomimicry: Organs-on-Chips. *Lab. Chip* **12,** 2156–2164 (2012).

4. Beebe, D. J., Ingber, D. E. & den Toonder, J. Organs on Chips 2013. *Lab. Chip* **13,** 3447–3448 (2013).

5. Moraes, C., Mehta, G., Lesher-Perez, S. C. & Takayama, S. Organs-on-a-chip: a focus on compartmentalized microdevices. *Ann. Biomed. Eng.* **40,** 1211–1227 (2012).

6. Neuži, P., Giselbrecht, S., Länge, K., Huang, T. J. & Manz, A. Revisiting lab-on-a-chip technology for drug discovery. *Nat. Rev. Drug Discov.* **11,** 620–632 (2012).

7. El-Ali, J., Sorger, P. K. & Jensen, K. F. Cells on chips. *Nature* **442,** 403–411 (2006).

8. Esch, M. B., King, T. L. & Shuler, M. L. The role of body-on-a-chip devices in drug and toxicity studies. *Annu. Rev. Biomed. Eng.* **13,** 55–72 (2011).

9. Huh, D. *et al.* Reconstituting Organ-Level Lung Functions on a Chip. *Science* **328,** 1662–1668 (2010).

10. Huh, D. *et al.* A human disease model of drug toxicity-induced pulmonary edema in a lung-on-a-chip microdevice. *Sci. Transl. Med.* **4,** 159ra147 (2012).

11. Kim, H. J., Huh, D., Hamilton, G. & Ingber, D. E. Human gut-on-a-chip inhabited by microbial flora that experiences intestinal peristalsis-like motions and flow. *Lab. Chip* **12,** 2165–2174 (2012).

12. Lee, S.-A. *et al.* Spheroid-based three-dimensional liver-on-a-chip to investigate hepatocyte-hepatic stellate cell interactions and flow effects. *Lab. Chip* **13,** 3529–3537 (2013).

13. Kim, H. J. & Ingber, D. E. Gut-on-a-Chip microenvironment induces human intestinal cells to undergo villus differentiation. *Integr. Biol.* **5,** 1130–1140 (2013).

14. Lee, J., Kim, S. H., Kim, Y.-C., Choi, I. & Sung, J. H. Fabrication and characterization of microfluidic liver-on-a-chip using microsomal enzymes. *Enzyme Microb. Technol.* **53,** 159–164 (2013).

15. Prot, J.-M. *et al.* Predictive toxicology using systemic biology and liver microfluidic 'on chip' approaches: Application to acetaminophen injury. *Toxicol. Appl. Pharmacol.* **259,** 270–280 (2012).

16. Agarwal, A., Goss, J. A., Cho, A., McCain, M. L. & Parker, K. K. Microfluidic heart on a chip for higher throughput pharmacological studies. *Lab. Chip* **13,** 3599–3608 (2013).

17. Toh, Y.-C. *et al.* A microfluidic 3D hepatocyte chip for drug toxicity testing. *Lab. Chip* **9,** 2026–2035 (2009).

18. Astashkina, A., Mann, B. & Grainger, D. W. A critical evaluation of in vitro cell culture models for high-throughput drug screening and toxicity. *Pharmacol. Ther.* **134,** 82–106 (2012).

19. Davis, R. P., van den Berg, C. W., Casini, S., Braam, S. R. & Mummery, C. L. Pluripotent stem cell models of cardiac disease and their implication for drug discovery and development. *Trends Mol. Med.* **17,** 475–484 (2011).

20. Xu, C. *et al.* Feeder-free growth of undifferentiated human embryonic stem cells. *Nat. Biotechnol.* **19,** 971–974 (2001).

21. Chen, G. *et al.* Chemically defined conditions for human iPS cell derivation and culture. *Nat. Methods* **8,** 424–429 (2011).

22. Singh, A. M. *et al.* Signaling Network Crosstalk in Human Pluripotent Cells: A Smad2/3-Regulated Switch that Controls the Balance between Self-Renewal and Differentiation. *Cell Stem Cell* **10,** 312–326 (2012).

23. James, D., Levine, A. J., Besser, D. & Hemmati-Brivanlou, A. TGFβ/activin/nodal signaling is necessary for the maintenance of pluripotency in human embryonic stem cells. *Development* **132,** 1273–1282 (2005).

24. Xu, R.-H. *et al.* NANOG is a direct target of TGFbeta/activin-mediated SMAD signaling in human ESCs. *Cell Stem Cell* **3,** 196–206 (2008).

25. Vallier, L. *et al.* Signaling pathways controlling pluripotency and early cell fate decisions of human induced pluripotent stem cells. *Stem Cells Dayt. Ohio* **27,** 2655–2666 (2009).

26. Levenstein, M. E. *et al.* Basic fibroblast growth factor support of human embryonic stem cell self-renewal. *Stem Cells Dayt. Ohio* **24,** 568–574 (2006).

27. Peerani, R. *et al.* Niche-mediated control of human embryonic stem cell self-renewal and differentiation. *EMBO J.* **26,** 4744–4755 (2007).

28. Blagovic, K., Kim, L. Y. & Voldman, J. Microfluidic Perfusion for Regulating Diffusible Signaling in Stem Cells. *PLoS ONE* **6,** (2011).

29. Murry, C. E. & Keller, G. Differentiation of embryonic stem cells to clinically relevant populations: lessons from embryonic development. *Cell* **132,** 661–680 (2008).

30. Thomson, J. A. *et al.* Embryonic Stem Cell Lines Derived from Human Blastocysts. *Science* **282,** 1145–1147 (1998).

31. Van der Meer, A. D. & van den Berg, A. Organs-on-chips: breaking the in vitro impasse. *Integr. Biol. Quant. Biosci. Nano Macro* **4,** 461–470 (2012).

32. Dick, E., Rajamohan, D., Ronksley, J. & Denning, C. Evaluating the utility of cardiomyocytes from human pluripotent stem cells for drug screening. *Biochem. Soc. Trans.* **38,** 1037 (2010).

33. Burridge, P. W., Keller, G., Gold, J. D. & Wu, J. C. Production of de novo cardiomyocytes: human pluripotent stem cell differentiation and direct reprogramming. *Cell Stem Cell* **10,** 16–28 (2012).

34. Sartipy, P. & Björquist, P. Concise review: Human pluripotent stem cell-based models for cardiac and hepatic toxicity assessment. *Stem Cells Dayt. Ohio* **29,** 744–748 (2011).

35. Ma, X. *et al.* Highly Efficient Differentiation of Functional Hepatocytes

From Human Induced Pluripotent Stem Cells. *Stem Cells Transl. Med.* **2,** 409–419 (2013).

36. Sirenko, O., Hesley, J., Rusyn, I. & Cromwell, E. F. High-Content Assays for Hepatotoxicity Using Induced Pluripotent Stem Cell-Derived Cells. *Assay Drug Dev. Technol.* (2013). doi:10.1089/adt.2013.520

37. Huh, D. *et al.* Reconstituting organ-level lung functions on a chip. *Science* **328,** 1662–1668 (2010).

38. Lee, S.-A. *et al.* Spheroid-based three-dimensional liver-on-a-chip to investigate hepatocyte–hepatic stellate cell interactions and flow effects. *Lab. Chip* (2013). doi:10.1039/C3LC50197C

39. Jang, K.-J. *et al.* Human kidney proximal tubule-on-a-chip for drug transport and nephrotoxicity assessment. *Integr. Biol. Quant. Biosci. Nano Macro* (2013). doi:10.1039/c3ib40049b

40. Grosberg, A., Alford, P. W., McCain, M. L. & Parker, K. K. Ensembles of engineered cardiac tissues for physiological and pharmacological study: Heart on a chip. *Lab. Chip* **11,** 4165–4173 (2011).

41. Sasai, Y. Cytosystems dynamics in self-organization of tissue architecture. *Nature* **493,** 318–326 (2013).

42. Eiraku, M. *et al.* Self-organizing optic-cup morphogenesis in three-dimensional culture. *Nature* **472,** 51–56 (2011).

43. Eiraku, M. *et al.* Self-Organized Formation of Polarized Cortical Tissues from ESCs and Its Active Manipulation by Extrinsic Signals. *Cell Stem Cell* **3,** 519–532 (2008).

Chapter 2

Microscale technologies development and validation

The development of functional human tissues on a chip require to proper design and develop technologies based on the microscale (i.e. microfluidic platforms) to efficiently control stem cells culture integration, delivery of nutrients and growth factors or vectors.

Control of oxygen content with possibility of generating accurate spatial and temporal gradients will be achieved through the development of a microfluidic oxygen exchanger. Similarly, an *ad hoc* cell-stretching device will be designed in order to induce specific mechanical stresses to the cells.

2.1 Microfluidic platforms fabrication: soft-lithography technique

Microfluidic devices are usually fabricated by standard soft-lytography technique[1,2], which is suitable to construct features measured on the micrometer to the nanometer scale. An elastomeric stamp made in polidymethylsiloxane (PDMS) is prepared by replica molding by casting a liquid prepolymer and curing agent solution (Sylgard 184 from Dow Corning) onto a premade master with patterned relief structure in its surface.

Photolithography is the most common method to fabricate micro-patterned molds. Depending on the characteristic length of the structure, which has to be patterned, chrome masks or cheaper masks in polymer sheets can be designed. Generally, when masters' features size is greater than or equal to 20μm, patterns can be drawn in AUTOCAD and printed onto polymer sheets, through commercially available printers. Photomasks are used to selectively polymerize UV-sensible photoresists, previously spun onto a silicon wafer with defined film-thickness. Parameters such as viscosity of the photoresist, UV-light intensity and baking time should be taken into account in order to achieve selective polymerization of the desired structure.

Elastomeric stamps obtained through soft-lithography technique offer several properties proper to coupling with biological systems. PDMS is chemically inert which makes microfluidic platform biocompatible, but appropriate surface functionalization is required when using adherent cells. It is homogeneous, isotropic, and optically transparent down to about 300nm, which makes possible coupling with detection analysis instruments like fluorescence microscopy. It is highly permeable to several gases, included oxygen and carbon dioxide, allowing fast equilibration time in standard cell culture incubators. It is a durable elastomer, allowing long-term experiments to be performed and its surface properties can be rapidly modified by plasma treatment. Air or oxygen-base treatments lead to the formation of OH- groups, which permit covalent bonding between the stamp and glass slides or other PDMS substrates.

Soft-lithography technique has been used in this work in order to develop microfluidic platforms to carry out stem cells culture expansion and differentiation, experiments of viral infections and functional differentiation. Each microfluidic device contains 10 channels (18mm long, 1.5mm wide and 0.2mm high), working in parallel. Photomask shown in Fig. 2.1a, was designed in AUTOCAD, printed onto a transparent polymer sheet and photolitographically patterned onto a silicon wafer with SU8-2100 negative photoresist, to obtain a final thickness of 200μm, according to manufacturer instructions. The master was then treated with hexamethyldisilazane (HDMS) at room temperature for 1h under vacuum, in order to facilitate extraction of PDMS mold from silicon wafer. A 10:1 solution of PDMS pre-polymer and curing agent was cast and cured for 2h at 70°C in an oven. PDMS mold was cut and peeled off, punched to obtain liquid inlets and outlets and sealed to a previously cleaned glass slide by plasma bonding (Fig. 2.1b).

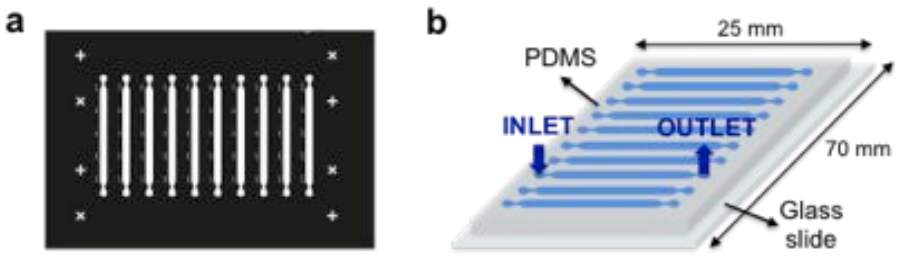

Figure 2.1 Microfluidic device for cell cultures integration. (**a**) Photomask with microfluidic channels. (**b**) Microfluidic chip with 10 independent channels.

Before cell culture integration, microfluidic platforms were rinsed with isopropanol and sterilized in autoclave, to prevent bacterial contaminations. Glass surface has to be opportunely functionalized, with proper adhesion protein solutions, in order to promote cellular adhesion, survival and growth.

2.2 Cell cultures integration into microfluidic devices

Efficient cell cultures integration into microfluidic devices can be achieved through proper supply of nutrients and growth factors along time. Human pluripotent stem cells are highly sensitive to microenvironment compositions in terms of both exogenous factors, provided with external medium, and endogenous cell-secreted factors. Different strategies of medium delivery can also affect homogeneity of the cell population inside microfluidic channels.

2.2.1 System for automatic control of medium delivery

Microfluidic cell culture systems allow accurate control of medium perfusion, delivery of exogenous factors or drug compounds, generation of concentration gradient and temporal defined soluble microenvironment composition.

Syringe pumps are the most common delivery system employed in microfluidic applications, as they ensure an accurate control of shear stress induced on cells. Here, CAVRO pumps, obtained from Tecan, have been employed. CAVRO pumps XLP6000 are fully programmable syringe pumps, that can be used as a stand alone module or, when controlled by an external computer or microprocessor, can automate pipetting, diluting and dispensing operations in the 5 μL to 25 mL range. A multiport head has been integrated within the pump in order to obtain 10 different operating channels, and 1 single discharge channel, with the advantage to independently control each of them. Labview software has been used to create a user-friendly interfacial window to automatically set up experimental parameters, such as medium flowrate, frequency of medium delivery (number of medium changes per day) and number of cycles. Fig. 2.2 shows the experimental set-up adopted for performing biological experiments within microfluidic platforms.

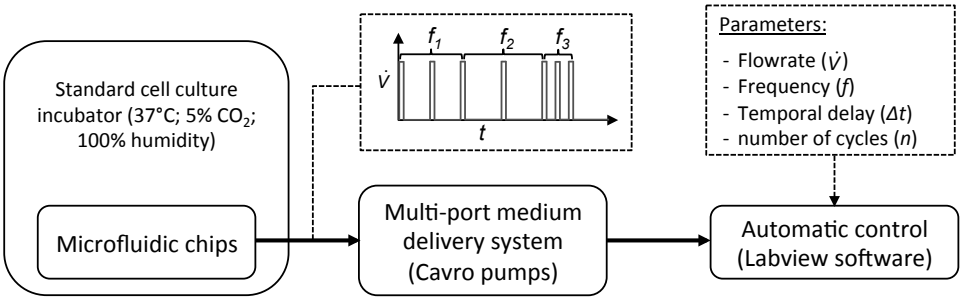

Figure 2.2 Experimental set-up. Medium delivery in microfluidic chips, placed in standard cell culture incubators, is controlled by a multi-port delivery system. Flowrate, frequency of medium delivery, temporal delay and total number of cycle are set independently in every microfluidic channel and automatically controlled through labview software.

A standard cell culture incubator at 37°C, with 5%CO_2 and 100% humidity atmosphere was used to arrange microfluidic devices with integrated cell cultures. High PDMS permeability allows fast equilibration of temperature and gas content in the culture medium.

Each independent channel of microfluidic chips was provided with a built-in medium reservoir of ~70 μL, obtained by sealing an additional PDMS block to the top of the device by plasma bonding, and connected to Cavro pumps (one per chip), through Tygon micro-tubings (500μm diameter). Automatic delivery was used to control the medium flow rate from the reservoirs into the microfluidic channels. Medium flowrate, frequency of medium delivery (*f*), temporal delay between two different cycles and total number of cycles were set independently in every single microfluidic channel. If continuous perfusion is adopted, *f* is equal to 0 and temporal delay does not need to be set. Periodic refill of medium reservoirs has been made with manual intervention.

2.2.2 Continuous versus intermittent flow perfusion

Once cells are injected and seeded into microfluidic channels, a continuous or an intermittent flowrate with specific frequency of medium delivery can be chosen. Importantly, shear stress imposed on cells should be accurately calculated in order to not infer detrimental effects. For microfluidic perfusion culture in 2D Poiseuille flow systems, the resulting parabolic flow profile yields a simple estimate of shear stress at the wall:

$$\tau = \frac{6\mu Q}{h^2 w},$$

where μ is the viscosity of the medium (kg m^{-1} s^{-1}), Q is the flow rate (m^3 s^{-1}), h is the channel height (m), and w the channel width $(m)^3$. Beside this, the content of

the soluble microenvironment, the effects on nutrient delivery and secreted factors must also be considered.

In order to evaluate proper conditions to culture pluripotent stem cells within a microfluidic platform, human embryonic stem cells were injected in microfluidic channels and cultured up to 5 days with a continuous medium perfusion or with an intermittent delivery with f=2d^{-1}. Flowrate and frequency parameters were chosen in order to deliver the same volume of medium during all 5 days in both conditions. Cells were compared with standard hESCs culture on Petri dish, showing similar colony morphology. However, significant differences in cell growth from inlet to the outlet of the channel was observed in the first condition, whereas homogeneous growth was observed by using an intermittent perfusion, as reported in Fig. 2.3a.

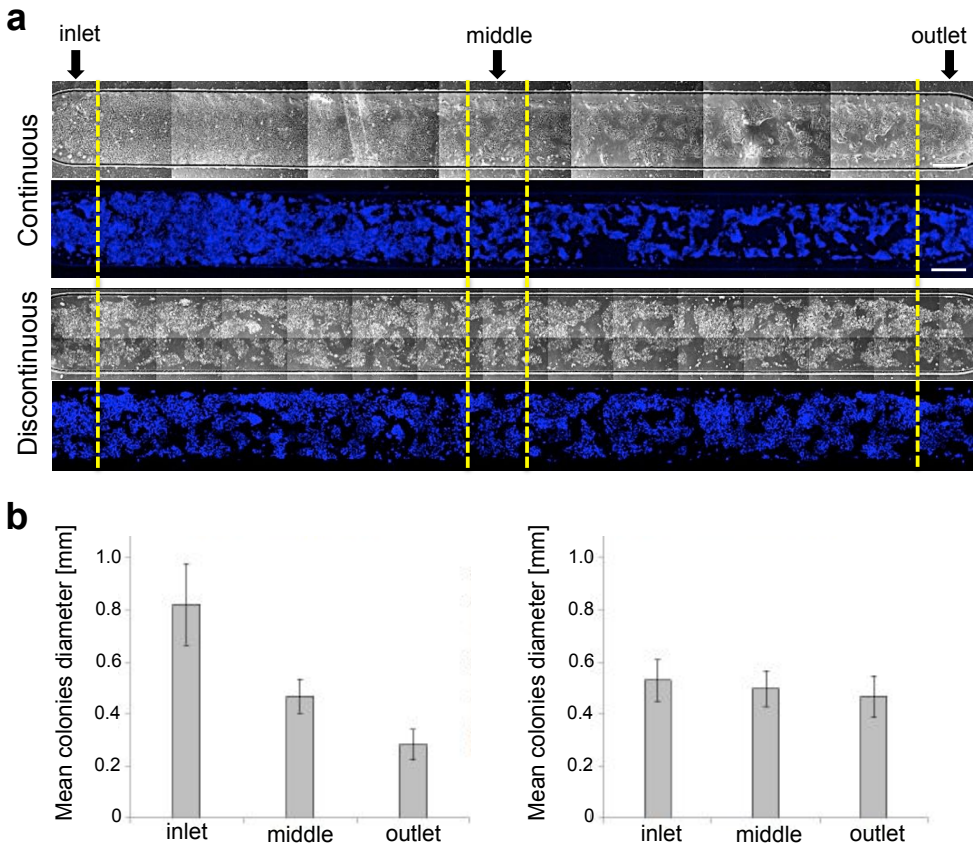

Figure 2.3 HESCs cultured in microfluidic channels in both continuous and discontinuous medium delivery conditions. (**a**) Bright field and nuclei staining pictures show significant differences in colonies growth in continuous perfusion from inlet to outlet of the channel, whereas no inlet/outlet effects are observed in discontinuous delivery conditions. (**b**) Quantification of mean colonies diameters in three distinct regions of the channel (inlet, middle and outlet) for continuous (left) and discontinuous (right) conditions confirms previous result.

Quantification of colonies diameter in three distinct regions of the channel (i.e. inlet, middle and outlet) confirmed previous result, as shown in Fig.2.3b for continuous (left) and discontinuous (right).

This result proves discontinuous medium delivery is an efficient method to maintain homogenous culture condition inside the channel without inlet/outlet effects, as a continuous perfusion was found to induce dramatic reduction of colony growth from the inlet to the outlet of the channel.

In this culture condition both embryonic and induced pluripotent stem cells display similar morphology to cells cultured in standard Petri dish (Fig. 2.4a).

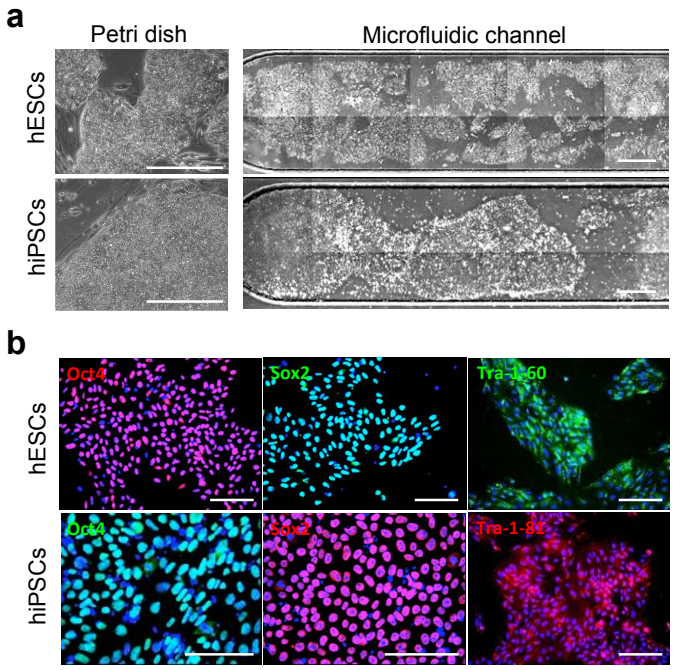

Figure 2.4 HPSCs culture in microfluidics. (**a**) HESCs and hiPSCs cultured in microfluidic channels up to 5 days display standard morphology as in standard Petri dish. Scale bars are 200μm. (**b**) HESCs and hiPSCs cultured in microfluidic channels homogenously express pluripotency markers (Oct4, Sox2, Tra1-60 and Tra1-80) as revealed by immunofluorescence analysis. Scale bars are 50μm.

Moreover, they homogeneously express pluripotency markers such as Oct4, Sox2, Tra1-60 and Tra1-81, as revealed through immunofluorescence analysis (Fig. 2.4b).

2.2.3 Adenoviral vectors-mediated gene delivery

Beside the delivery of growth factors and nutrients, the efficient introduction of genetic material inside the cells is another aspect to take into account for biological investigations, such as optimization of gene therapies, RNA

interference experiments, induced pluripotent stem cell production or for promoting stem cell differentiation. Viral particles are widely used as genetic material carriers, as they ensure stable and efficient insertion of genomic material in host cells. In particular, adenoviruses have the advantage to introduce transgenes into the cells without uncontrollable random integrations in host DNA[4], minimizing perturbations of cells homeostasis.

As proof of concept, non-replicating adenoviral vectors (AdVs), carrying enhanced green fluorescent protein (EGFP) were used as reporter for infection of a human fibroblast cell line in the microfluidic system. Optimal conditions for high efficiency of infection and minimal toxic effects on the cells were investigated. High efficiency of infection can be obtained by tuning the following parameters:

- viral concentration, defined by the MOI (number of viral particles, PFU, for cell);
- frequency of virus-containing medium delivery;
- medium flowrate.

In order to predict the percentage of infected cells and the associated infecting-virus distribution in the cell population, a stochastic mathematical model, which accounts for the discrete nature of cells and viruses, was developed and experimentally validated, as reported in Appendix B. The developed model was adopted in order to predict not only the efficiency of infection but also the distribution of the viral population (i.e. number of viruses per cell).

Two different medium delivery strategies were analyzed by using the same global MOI equal to 20. A continuous convection-driven perfusion (Pe=300) was compared to a diffusion-driven process (Pe=0). Simulated time was set to 90 min, which is the time (t_f) required for a viral particle to travel a distance s equal to 200 mm (the channel height) by Brownian motion, calculated from the Einstein's relation:

$$t_f = \frac{s^2}{2 \cdot D},$$

where D is the diffusion coefficient of the virus in the medium. Given the stochasticity of the model, one hundred computational simulations were performed and results were reported as mean with corresponding stochastic variability. Fig. 2.5a shows results derived from the simulation in which colored

dots represent cells. Red dots represent non-infected cells, whereas the other dots represent infected cells with the corresponding number of viruses as reported in the legend. A convection-driven infection with continuous perfusion of virus-containing medium leads to marked inlet/outlet effects in the number of infected cells and number of number of viruses (Fig. 2.5a up). On the other hand, a homogeneous infection can be observed in a diffusion-driven infection (Fig. 2.5a down).

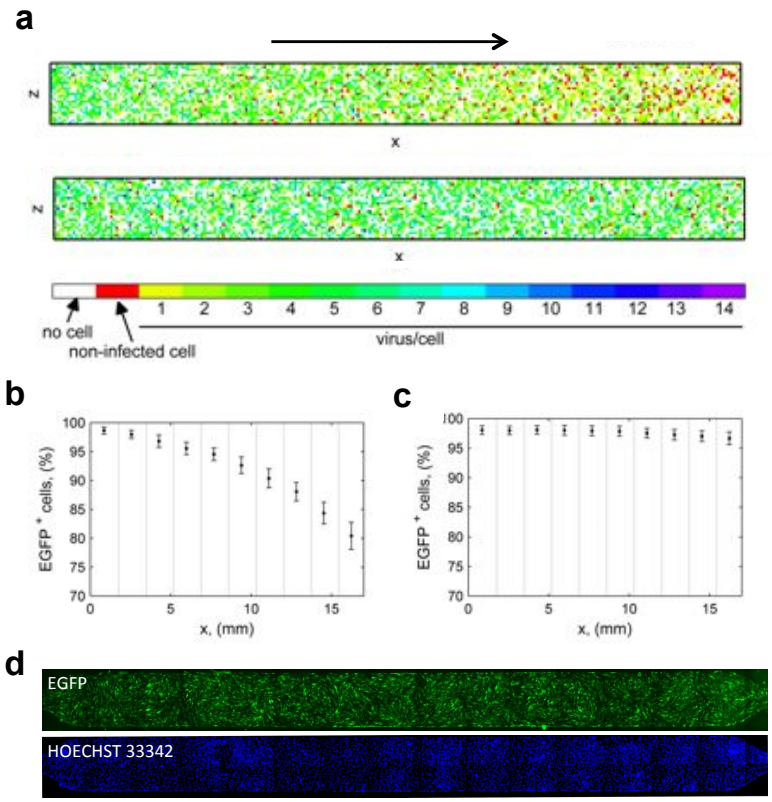

Figure 2.5 (**a**) Results of stochastic simulations with MOI 20 of continuous channel perfusion (Pe=300) for 90 min (up) and of discontinuous channel perfusion (Pe=0) for 90 min (down). Inlet/outlet heterogeneity in number of infected cells and number of viruses per cell can be observed in the first case (up), whereas no significant inlet/outlet differences in the second case are observed (down). Black arrow indicates flow direction. (**b**, **c**) Percentage of $EGFP^+$ cells in each of the 10 equal sectors of the channel indicated by the dotted lines showing differences in infection homogeneity in continuous (**b**) and discontinuous (**c**) virus-containing medium delivery. Error bars indicate mean ± standard deviation of 100 simulations. Cell concentration is 150 cell/mm^2. (**d**) Efficient cell infection in the microfluidic channel obtained with a discontinuous delivery of virus-containing medium as revealed by EGFP fluorescence and nuclei staining.

The length of the channel was also divided in 10 sectors and in each sector the percentage of $EGFP^+$ cells, i.e., of cells infected by at least one virus, was calculated. The results are shown in Fig. 2.5b-c, confirming previous results of spatial heterogeneity in viral infection.

Spatial heterogeneity is a relevant phenomenon introduced by perfusion that

affects the quality of the resulting cell population. Thus, a discontinuous flow protocol better preserves cell microenvironment, while ensuring a homogenous transfection along the microfluidic channel as experimentally demonstrated (Fig. 2.5d).

The effect of MOI on the percentage of $EGFP^+$ cells and the infecting-viruses distribution was also computationally investigated, by simulating the transduction process in a microfluidic channel for a cell density of 150 cell/mm^2 at four different MOIs: 1 (equal to a concentration of 750 PFU/mL), 5 (3750 PFU/mL), 10 (7500 PFU/mL) and 20 (15,000 PFU/mL). Fig. 2.6a shows the resulting probability and complementary cumulative distributions of the percentage of cells infected with increasing MOI values from 1 to 20, as calculated by the model. At MOI 1, almost all the cells infected have only one virus, but at higher MOIs, heterogeneity is visible in the cell population. As expected, the efficiency of the infection process increases at higher MOIs.

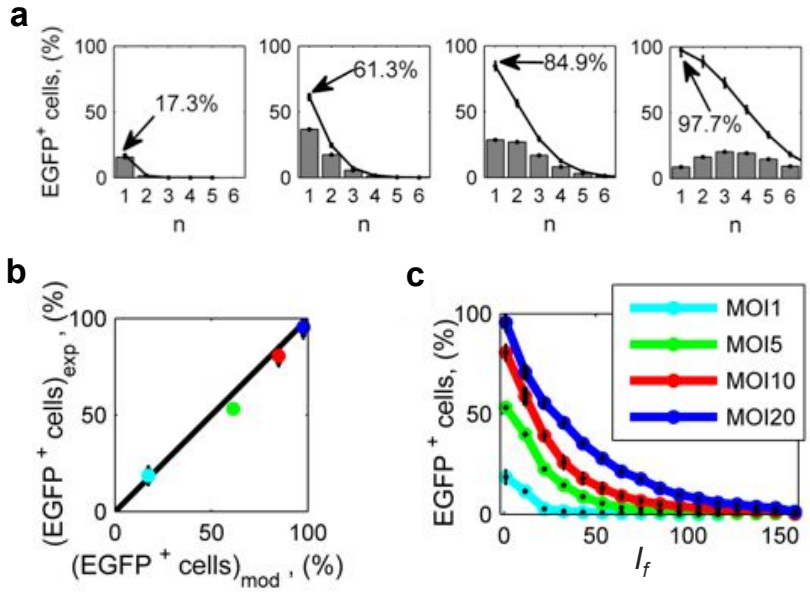

Figure 2.6 (**a**) Probability and complementary cumulative distributions of the percentage of cells infected with increasing MOI values from 1 (left) to 20 (right), as calculated by the stochastic model. (**b**) Comparison of theoretical number of infected cells, as predicted from the stochastic model, and experimental results obtained by measuring the number of fluorescent cells, for different MOIs. (**c**) Cumulative distribution, associated at the level of fluorescence intensity, I_f, of infected cells at different MOIs.

Experiments of viral transduction in the microfluidic platform were performed under the same conditions simulated above and cell population was characterized at 24h after the beginning of infection. This period of time was assumed sufficient for infected cells to express EGFP protein, as reported previously in de Martin et

al.[5]. Very good agreement between the percentages of $EGFP^+$ cells obtained from experimental data and predicted by the model (Fig. 2.6b) demonstrates the stochastic model fairly describes the overall infection process within the microfluidic platform.

The experimental heterogeneity of the cell population expressing EGFP was investigated at the single-cell level, through quantification of the intensity of fluorescence, I_f, of each cell by image analysis, as described in Appendix B. The results are shown in Fig. 2.6c, in terms of complementary cumulative distributions for different MOIs. Besides increasing the percentage of cells expressing EGFP, AdV transduction performed at higher MOIs enhances the amount of exogenous RNA and consequently the amount of EGFP produced by single cells. This could be related to the increase in the number of viruses infecting each cell, as explored computationally.

Although high efficiency of infection can be achieved, this results transient, thus long-term expression (several days) of transfected genetic material requires further investigations. In this perspective, different infection strategies can be followed, such as a single high-dose infection or low-dose repeated infections.

These two strategies were first explored computationally, through the stochastic model, by comparing the outcome of a single viral transduction at MOI 20 (MOI 20 × 1) with that of two infections at MOI 10 (MOI 10 × 2), and of four infections at MOI 5 (MOI 5 × 4). The total number of viruses entering the system was thus the same, but three different regular temporal sequences were used (Fig. 2.7a-c). Theoretically the same outcome is achievable with a single high-dose infection or with a low-dose multi-infection strategy, in terms of percentage of $EGFP^+$ cells and of the distribution of the number of viruses per cell as shown in Fig. 2.7a-c.

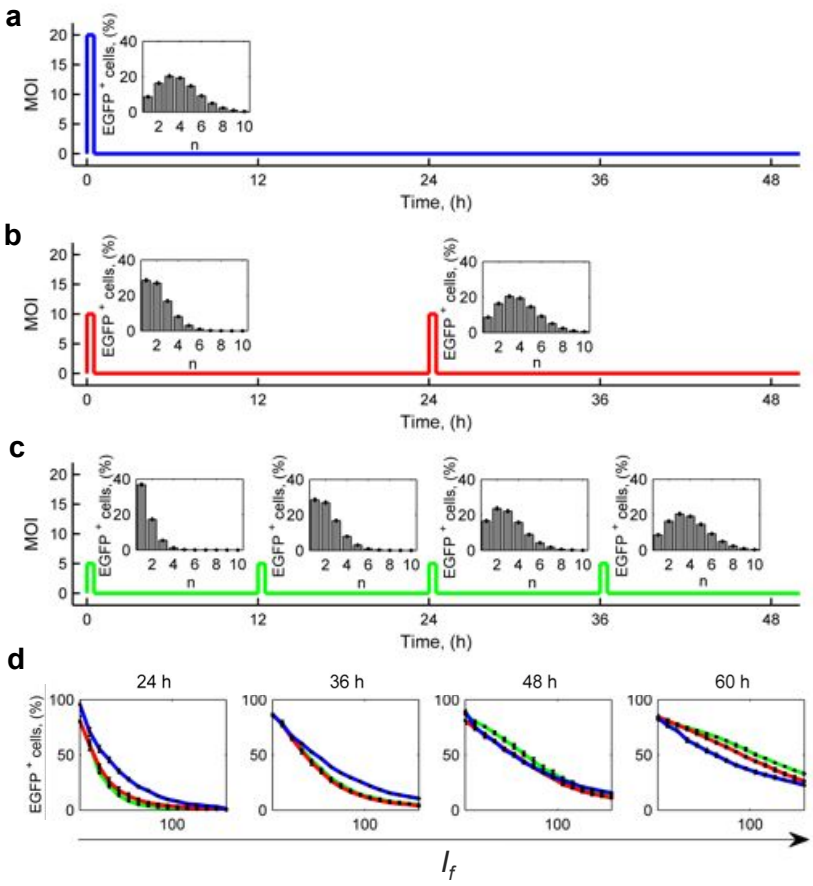

Figure 2.7 Single high dose infection vs. multiple low dose infections. (**a-c**) Distribution of EGFP-expressing cells, calculated through the stochastic model, for a single infection with MOI 20 (MOI 20 × 1) (**a**), two repeated infections with MOI 10 (MOI 10 × 2) (**b**) and four repeated infections with MOI 5 (MOI 5 × 4) (**c**). Cell concentration was 150 cell/mm^2. Error bars indicate mean ± standard deviation of 100 simulations at each condition. (**d**) Fluorescence intensity distribution of EGFP expressing cells experimentally analyzed at four different time-points (24h, 36h, 48h and 60h) for the three different infection strategies. After 60h from the beginning of the experiment multiple low dose infection (MOI 5 × 4) protocol gives a higher percentage of cells expressing more EGFP, compared to a single high dose infection (MOI 20 × 1).

The three simulated strategies of infection were experimentally reproduced and efficiency of infection, in terms of fluorescence distribution, was analyzed at different time-points: 24h, 36h, 48h and 60h. Despite an initial condition in which single high-dose infection results more efficient, as more cells express more fluorescence signal, at 60 h from beginning of the experiment, an higher percentage of cells result more fluorescent if using the multi-infection protocol (MOI 5 × 4), probably due to a loss of EGFP expression (or protein degradation) over time, occurred using the single high-dose infection (Fig. 2.7d).

Thus, low dose multi-infection could be an effective solution when long-term expression is required, ensuring a higher percentage of infected cells and avoiding potential issues related to viral dose toxicity.

2.3 Temporal control of oxygen concentration

It is well recognized that oxygen regulates nearly every cellular process, from cell metabolism, to differentiation and cell division. In the laboratory, cells are commonly cultured in air supplemented with 5% CO_2 to complement the sodium bicarbonate buffer in the growth medium, which balances the pH. Oxygen concentration is commonly regulated in conventional humidified chambers or incubators with a controlled oxygen partial pressure in the gas phase.

One of the major goals in biological studies is to recreate spatial and temporal pO_2 gradients, arising *in vivo* in both physiological and pathological conditions. In this perspective, technology developed at the microscale level is an effective solution to accurately control oxygen partial pressure at cellular-size level. This is feasible, thanks to the laminar flow regime and the time scale of diffusive mass transport phenomena that are closely related to the characteristic length of the system.

While spatial gradients of oxygen concentration are easily achievable by using parallel steady-state laminar flows at decreasing oxygen concentration in the same microfluidic device[6,7,8], the generation of fast and sudden oxygen depletion in the cell culture medium, for example to mimic oxygen concentration drop in blood vessels when an ischemic event occurs, requires specific technological improvements, compared to standard devices. The major issues that have to be considered concern:

i) an almost perfect insulation of the system from external environment;

ii) the fast oxygen removal from cellular solution without perturbing cell microenvironment.

In this perspective a system with separate compartments for liquid and gas phase was designed. Each of them has defined height, inlet and outlet flowrates and oxygen partial pressure, whereas a thin, non-porous and highly permeable membrane, made in PDMS, allows rapid oxygen exchange from the gas to the liquid layer, without any perturbation of the detection system. A schematic representation of the system is reported in Fig. 2.8a.

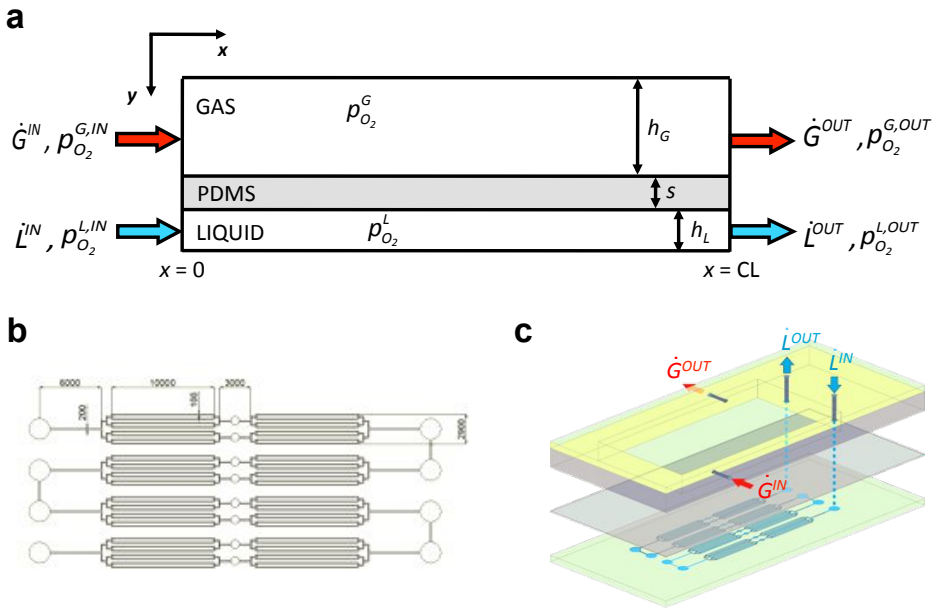

Figure 2.8 Microfluidic gas exchanger design. (**a**) Schematic representation of gas exchange system with different compartment for liquid and gas flow, with defined inlet and outlet flowrates (*L* and *G*) and oxygen partial pressure. Oxygen exchange occurs along x-coordinate through a thin, permeable PDMS membrane. (**b**) Top-view of the fluidic layer channel network (all dimension values are in μm). (**c**) 3D schematic view of the three layer-microfluidic gas exchanger.

The fluidic layer is formed by a network of microfluidic channels etched in a glass substrate, in order to achieve complete gas sealing. The imprinting of micro-channels in the glass slide was obtained by an acid solution-based wet-etching technique. Flow channels network is characterized by a series of gas exchanger unit, and each unit is formed by 8 parallel microchannels 100 mm wide (Fig. 2.8b). This modular design allows to add series of units, until obtaining the total length required for a given exchange efficiency.

The micrometric thickness of the gas permeable membrane ensures low oxygen diffusion resistance. The gas domain is a low-volume rectangular chamber that allows high gas flow rate and, consequently, almost uniform oxygen partial pressure within the gas chamber.

The oxygen concentration profile, and consequently the oxygen partial pressure, within the liquid phase domain of the microfluidic gas exchanger was described by a simplified analytical model and by computational solution of the species mass balance, as reported in Appendix A. The theoretical model was solved through computational analysis and used for proper gas exchanger design. Fig. 2.9a shows oxygen partial pressure profile along x-coordinate for different values of medium flowrate, *L*, (50, 100 and 200 μL min^{-1}), at constant channel height,

and different channel heights, h_L, (40, 70 and 100 μm), at constant flowrate for eight exchanger units, with total length CL equal to 8 cm.

In order to satisfy a specific target value of oxygen partial pressure L, h_L or the number of exchange units can be varied.

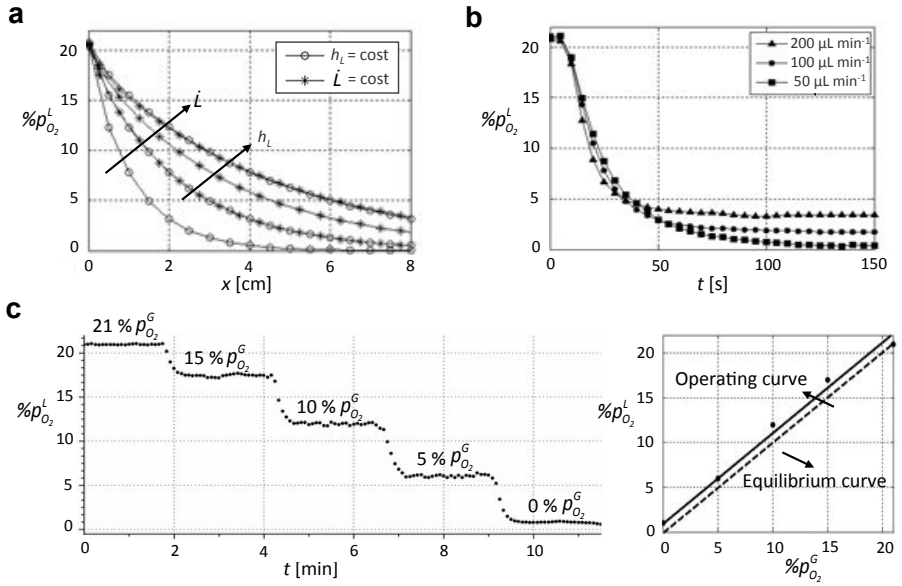

Figure 2.9 (**a**) Oxygen partial pressure profile as a function of x-coordinate, parametric in liquid flowrate, L, and channel height, h_L. (**b**) Oxygen partial pressure dynamic in the liquid phase during a step impulse of oxygen partial pressure in the gas phase (from 21 to 0%) analyzed at different medium flowrate with a ruthenium complex-based, Ru(ddp), fluorescent sensor. (**c**) $p^L_{O_2}$ profile for five different $p^G_{O_2}$ with $\dot{L}$=100 μl min^{-1} (left). Equilibrium and operating curves obtained by calibration (right).

The dynamics of oxygen depletion, following a step pulse from 21 to 0% of oxygen partial pressure in the gas phase, was also investigated for three different values of medium flowrate with h_L equal to and 8 exchange units (Fig. 2.9b). As predicted from the model, different stationary state values of oxygen partial pressures can be achieved. However, the dynamic of the process results in the order of seconds, meaning the system could be efficiently used for mimicking fast oxygen depletion in cell culture medium. This last aspect is of particular interest for investigating *in vitro* physio-pathologic effects occurring in cardiac tissue during ischemia, when a rapid drop of oxygen supply to cardiac cells occurs.

Thus, the developed device allows fast and accurate tuning of oxygen partial pressure in cell culture medium by simply tuning oxygen partial pressure in the gas compartment. Constant gas flow rate and oxygen composition were maintained in the gas chamber using air and nitrogen mass flow meters and regulating their flowrates ratio. A multiple step experiment was designed by

setting $p_{O_2}^G$ at 5 different values from 21% to 0% with 5% interval. The resulting $p_{O_2}^L$ step profile is shown in Fig. 2.9c (left). Corresponding values of $p_{O_2}^L$ and $p_{O_2}^G$ were correlated to obtain operating curve shown in Fig. 2.9c (right). Interestingly, the operating curve only slightly differs (about 2%) from the equilibrium curve, allowing almost anoxic conditions to be reproduced in the culture medium.

2.4 Control of mechanical stress

Mechanical stress plays a crucial role in the investigation of new physiological and pathological responses to cell culture microenvironment. It is recognized that active deformation promote cellular growth and survival, influence metabolic processes and gene expression, and governs tissue architecture in various cell types[9,10,11,12,13]. Several technological solutions have already been proposed for stretching cultured cells by using elastic membrane. Beside most common commercially-available cell-stretching device, developed by Flexcell Corporation and largely adopted in many works[9,10,14], a number of custom-made solutions have been proposed to perform mechanical stimulations on cell cultures in both uniaxial and biaxial directions. However, the accurate control in space and time of mechanical-induced deformations while observing the cellular behavior at single cell level is not straightforward. Moreover, the relative large scale of the existing technology hinders to investigate high temporal resolution cell behavior under fast cyclic mechanical stimulations and the intrinsic complexity of these systems prevents to simultaneously perform multi-parallel experiments analyzing the mechanical-associated single cell response in a high-throughput fashion.

2.4.1 Development of a microscale cell-stretching device

A cell-stretching device was properly designed in order to ensure: i) accurate control of mechanical stimulations at single-cell level, ii) high temporal resolution of cyclic mechanical stimulations, iii) optical accessibility for in line analysis, iv) statistical significance of treated samples, with internal un-stretched control.

Taking advantage of the microfluidic technology, an *ad hoc* cell-stretching device was designed. It is based on the deformation of a thin PDMS membrane, with 40μm thickness, through pressurization of a network of microfluidic channels. Microfluidic technology, that is recognized to provide highly reproducible and well-defined hydrodynamic conditions, was adopted in order to obtain accurate

control of pressure-driven mechanical deformation of elastic membrane underneath cell culture, in terms of amplitude, temporal profile and frequency of bidirectional deformation. Fig. 2.10a shows a schematic representation of how cells, cultured on the top of the PDMS membrane, are stretched when microfluidic channels are pressurized.

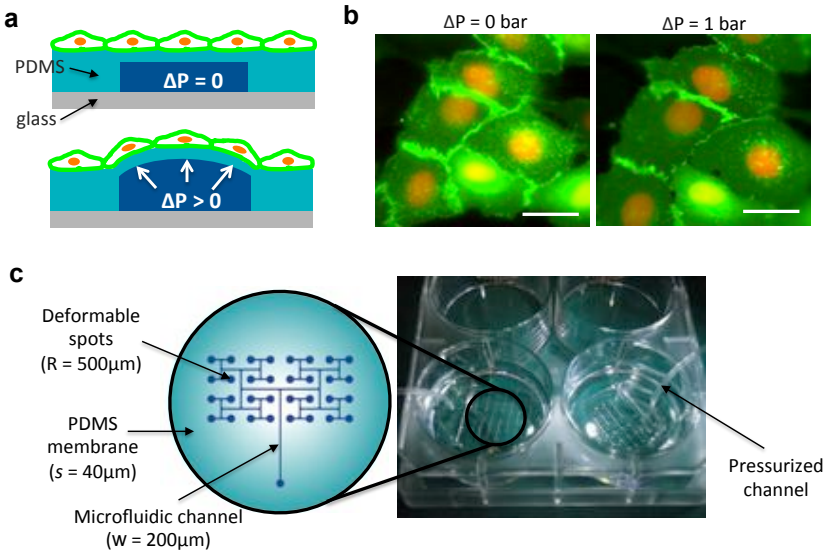

Figure 2.10 (**a**) Schematic representation of pressure-induced cell stretching through deformation of PDMS membrane with underneath microfluidic channels. (**b**) Deformation of a confluent monolayer of an endothelial cell line expressing EGFP. Nuclei are stained in red. Scale bar 20μm. (**c**) Top view of microfluidic cell-stretching device with 32 deformable circular spots (left). The device, provided of inlet tubing for gas-pressurization can be integrated into standard multi-well plates (right).

Cell deformation following pressure application is shown in Fig. 2.10b for a confluent monolayer of endothelial cells. Cell deformation in biaxial directions can be appreciated by endogenous expression of fluorescent protein EGFP, whereas cells nuclei are stained in red.

Microscale allows applying accurate cyclic mechanical deformation on several micro-regions inside the same culture chamber, both in radial and circumferential directions. Microfluidic compartment includes 32 deformable circular spots with radius 500 μm. All individual spots are connected through a microfluidic channel network with hydraulic symmetry, for each microfluidic path, as shown in Fig. 2.10c left, in order to apply identical pressure-induced membrane deformation to all spots. Moreover, thanks to this configuration, with both stretchable and un-deformable areas in the same device, an internal un-stimulated control can be used in every single experiment. Microfluidic cell-stretching device can be easily

integrated in standard multi-well plates (Fig. 2.10c right) or directly coupled with an optical microscope for in line analysis. This latter solution requires an additional PDMS layer to hold medium up during observation.

Biaxial mechanical deformation induced on cells was estimated by developing a Finite Element Model (FEM) of elastic membrane, assisting microfluidic channel configuration design (Appendix E). Computational modeling to fully characterize elastic membrane deformation under application of the internal pressure and to estimate the level of local strains supported the development of the device. These data were adopted in order to accurately calibrate the mechanical bi-directional deformation induced on the cells. Typical data from the FEM analysis are shown in Fig. 2.11a and 2.11b for a spot with radius of 500 μm and thickness 40 μm, showing complete deformation of the spot in both radial and circumferential direction respectively.

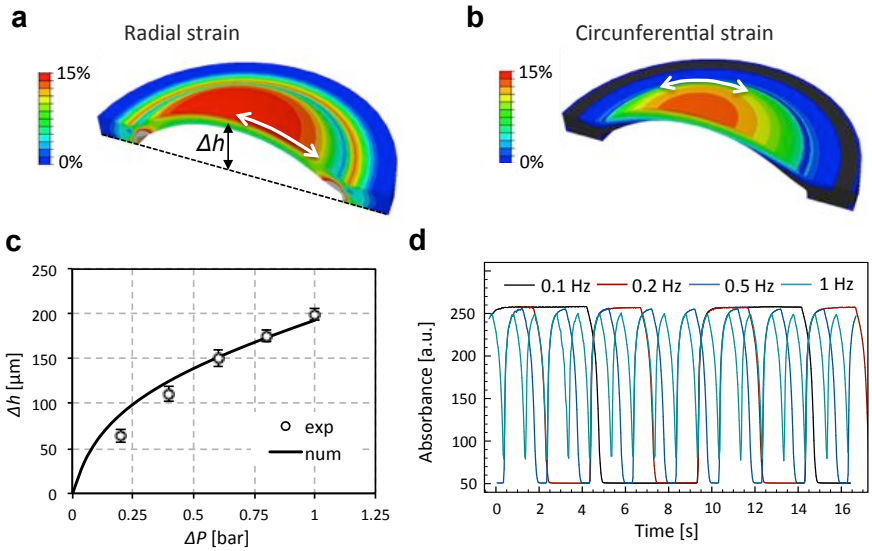

Figure 2.11 (**a-b**) Predicted distribution of radial (**a**) and circumferential (**b**) deformations of a single spot with *ΔP* equal to 1 bar. (**c**) Predicted profile and experimental values of the vertical displacement in the center of the spot with the applied pressure. (**d**) Temporal profile of the mechanical stimulus at different frequencies, obtained by filling microfluidic channels with a dye and recording the absorbance in the center of the membrane at different frequencies.

The derived model was experimentally validated by measuring vertical displacements of the membrane in the center of the spot, with different pressures. Fig. 2.11c shows the vertical displacement on the top of the PDMS membrane as a function of the applied pressure. Theoretical profile obtained by numerical solution results in good agreement with the experimental values.

Microscopic dimensions of microfluidic channels allow manipulation of few

microliters for system pressurization, thus providing fast dynamics of the stimulation and uniform spatial and temporal stimulus on cells. In order to assess the robustness of the system and the reproducibility of mechanical stimuli during cyclic deformations, microfluidic channels were filled with a dye and the absorbance of deformed areas during pressurization cycles, was detected at different frequency. These values of absorbance can be directly correlated to the vertical displacement of the membrane. Fig. 2.11d shows temporal profiles of absorbance acquired at different frequencies from 0.1 to 1 Hz and demonstrates the efficiency of the system in terms of stability of the mechanical deformation and fast dynamics.

2.5 References

1. Xia, Y. & Whitesides, G. M. Soft Lithography. *Angew. Chem. Int. Ed.* **37,** 550–575 (1998).
2. Whitesides, G. M., Ostuni, E., Takayama, S., Jiang, X. & Ingber, D. E. Soft Lithography in Biology and Biochemistry. *Annu. Rev. Biomed. Eng.* **3,** 335–373 (2001).
3. Kim, L., Toh, Y.-C., Voldman, J. & Yu, H. A practical guide to microfluidic perfusion culture of adherent mammalian cells. *Lab. Chip* **7,** 681–694 (2007).
4. Liu, Q. & Muruve, D. A. Molecular basis of the inflammatory response to adenovirus vectors. *Gene Ther.* **10,** 935–940 (2003).
5. De Martin, R., Raidl, M., Hofer, E. & Binder, B. R. Adenovirus-mediated expression of green fluorescent protein. *Gene Ther.* **4,** 493–495 (1997).
6. Polinkovsky, M., Gutierrez, E., Levchenko, A. & Groisman, A. Fine temporal control of the medium gas content and acidity and on-chip generation of series of oxygen concentrations for cell cultures. *Lab. Chip* **9,** 1073–1084 (2009).
7. Adler, M., Polinkovsky, M., Gutierrez, E. & Groisman, A. Generation of oxygen gradients with arbitrary shapes in a microfluidic device. *Lab. Chip* **10,** 388–391 (2010).
8. Lam, R. H. W., Kim, M.-C. & Thorsen, T. Culturing Aerobic and Anaerobic Bacteria and Mammalian Cells with a Microfluidic Differential Oxygenator. *Anal. Chem.* **81,** 5918–5924 (2009).

9. Salameh, A. *et al.* Cyclic Mechanical Stretch Induces Cardiomyocyte Orientation and Polarization of the Gap Junction Protein Connexin43. *Circ. Res.* **106,** 1592–1602 (2010).
10. Kumar, A. Cyclic mechanical strain inhibits skeletal myogenesis through activation of focal adhesion kinase, Rac-1 GTPase, and NF- B transcription factor. *FASEB J.* **18,** 1524–1535 (2004).
11. Kook, S.-H. *et al.* Cyclic mechanical stretch stimulates the proliferation of C2C12 myoblasts and inhibits their differentiation via prolonged activation of p38 MAPK. *Mol. Cells* **25,** 479–486 (2008).
12. Suresh Babu, S. *et al.* Mechanism of Stretch-Induced Activation of the Mechanotransducer Zyxin in Vascular Cells. *Sci. Signal.* **5,** ra91 (2012).
13. Hsu, H.-J., Lee, C.-F., Locke, A., Vanderzyl, S. Q. & Kaunas, R. Stretch-Induced Stress Fiber Remodeling and the Activations of JNK and ERK Depend on Mechanical Strain Rate, but Not FAK. *PLoS ONE* **5,** e12470 (2010).
14. Trepat, X. *et al.* Universal physical responses to stretch in the living cell. *Nature* **447,** 592–595 (2007).

Chapter 3

Multi-stage generation of functional hPSCs-derived cardiac and hepatic cells on a chip

HPSCs differentiation into functional tissue-specific cells requires a multi-stage process, in which exogenous/endogenous factors balance plays a central role. Frequency of medium delivery allows proper factor supply in each of these developmental steps, driving hPSCs into functional cardiac and hepatic cells.
Differentiated cells display mature phenotypes, meaning that differentiated cells derived in the microfluidic channels can be directly used for dynamic multi-parametric and large-scale drug screening or for developing micro-engineered human organ models.

3.1 HPSCs expansion and pluripotency maintenance in microfluidic platform

Exogenous and endogenous cell-secreted factors have been demonstrated to play a major role in regulating stem cells pluripotency and self renewal, determining cell fate[1,2]. This aspect could be greatly emphasized in a micro-scale environment, where, thanks to the high surface/volume ratio, accumulation and local concentration of autocrine-paracrine factors are greatly enhanced.
Intermittent medium delivery with proper frequency of medium change, *f*, has been shown to provide suitable conditions for healthy and homogeneous growth of pluripotent stem cells inside microfluidic channels (§2.2.2). Moreover, variable *f* could be used to modulate exogenous/endogenous factors supply, as low *f* promotes higher accumulation of endogenous and depletion of exogenous factors, whereas higher *f* allows sustained supply of endogenous factors to the cells and a more frequent wash-out of cell-secreted factors.
It is reasonable to hypothesize that these factors have a synergic positive effect *in vitro* in promoting transcriptional activity of pluripotency genes, as schematized in Fig. 3.1a. The model summarizes relevant phenomena to highlight the effect of dynamic changes in extrinsic factors modulated by *f*, on a hypothetic

transcriptional activity. Black arrows in Fig. 3.1a indicate chemical reactions involved in the process. In particular, reactions (1) and (2) describe the coupling of exogenous, *Ex*, and endogenous, *En*, factors to specific membrane receptors, which promotes the activation of transcriptional factor, *Tr*. In addition, *Tr* is activated at a basal level through reaction (3) and induces expression of pluripotency-associated genes through reaction (4). Gene transcripts, *Gt*, in turn, produce newly *En*, as indicated by reaction (5).

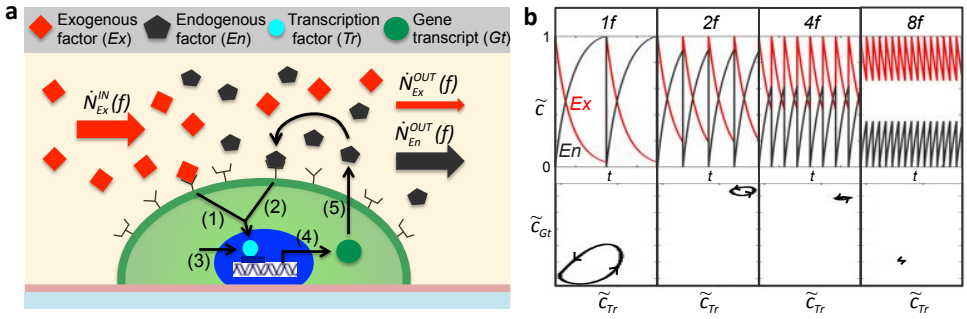

Figure 3.1 Pluripotency-associated signaling pathway model in microfluidic stem cell culture. (**a**) Exogenous (*Ex*) and endogenous (*En*) factors synergistically contribute to transcriptional activity of pluripotency genes transcripts (*Gt*), through activation of target transcription factors (*Tr*). (**b**) Model output. Temporal profiles of normalized *Ex* and *En* factors concentrations in the microfluidic channel at increasing frequencies (up). Gene transcript concentration profiles versus transcription factor concentrations during a single cycle of medium perfusion at the same increasing frequencies (down).

Mass balances of all species involved consist in a system of ordinary equations, which was computationally solved with MATLAB to obtain pseudo-stationary profiles of species concentrations, at different *f* (Fig. 3.1b and Appendix C). These computational investigations revealed that frequency of medium delivery strongly affects accumulation of exogenous and endogenous factors, thus regulating transcriptional activity of target genes. A frequency increase reduces the amplitude of temporal fluctuations of both exogenous and endogenous factors (Fig. 3.1b), thus maintaining sustained transcriptional activity of the associated target genes. However, higher frequencies of medium change produce decreased expression of gene transcript, due to continuous wash-out of endogenous secreted factors.

In order to experimentally validate theoretical hypothesis described above, human embryonic stem cells were cultured up to 5 days in microfluidic channels with different *f* and pluripotency genes expression was analyzed. The qRT-PCR analysis of pluripotency markers Oct-4 and Nanog showed the highest expression level by using f=2d^{-1} (Fig. 3.2a), comparable with standard static conditions in

Petri dish. Significant three-fold higher expression compared to lower (f=1d^{-1}) and higher frequencies (f=3d^{-1}, f=4d^{-1} and f=8d^{-1}) was observed. These results are consistent with the initial hypothesis that an appropriate optimal balance of exogenous molecules and endogenous cell-secreted factors has to be provided.

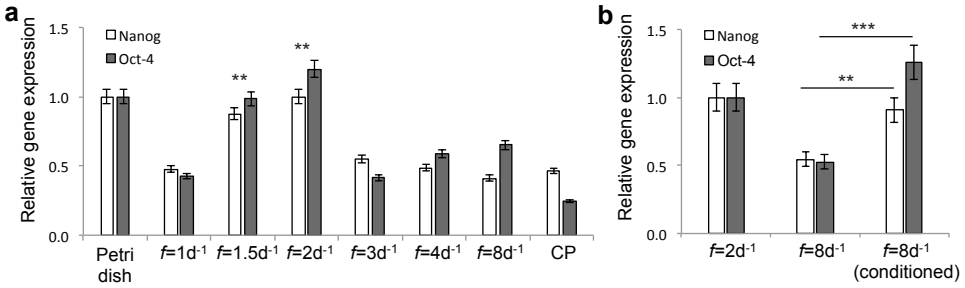

Figure 3.2 (**a**) Frequency-dependent pluripotency markers Nanog and Oct-4 expression after 5 days of culture, compared to standard static culture control and continuous perfusion (CP). (**b**) Significant recovering of Nanog and Oct4 expression in non-optimal frequency conditions, i.e. f=8d^{-1}, as in optimal condition (f=2d^{-1}). Data are normalized on GAPDH expression. Student's t-test p-value ***P≤0.001. Data are shown as mean ± s.d. (n=3).

In order to demonstrate f=2d^{-1} is effectively the optimal frequency, which allows accumulations of factors essential for pluripotency maintenance in microfluidics, conditioned medium containing these factors was used to culture the same stem cell line in pro-exogenous not-optimal conditions, i.e. f=8d^{-1}, and looking if the use of this conditioned medium can recover pluripotency markers expression. Fig. 3.2b shows that accumulated secreted factors can significantly restore markers expression as observed in optimal conditions.

3.2 Frequency-driven germ layer commitment

In order to investigate whether the frequency of medium perfusion could be used also for directing early germ layer commitment, according to extrinsic endogenous and exogenous factors concentration, hESCs were expanded in microfluidic channels and induced to spontaneously differentiate for 4 days at different frequencies. Expression levels of early germ layers markers were analyzed through qRT-PCR analysis of β-III tubulin, OTX2 (ectoderm), Brachyury T, GATA4, aSMA (mesoderm), AFP, EOMES and FOXA2 (endoderm). Under these conditions, the static culture showed ectoderm and mesoderm expression but not endoderm. On the other hand, frequency-dependent germ layer enrichment was observed in microfluidic culture (Fig. 3.3).

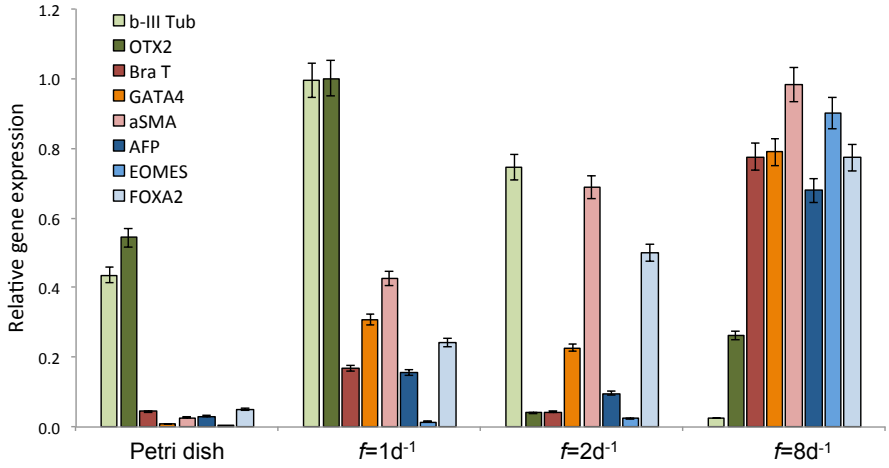

Figure 3.3 Spontaneous differentiation of hESC on-a-chip at different frequencies. The qRT-PCR analysis (gene expression normalized on glyceraldehyde 3-phosphate dehydrogenase) of Oct-4, β-III tubulin, brachyury T and alpha-fetoprotein in hESC spontaneous differentiation on chip, under different *f*. Data are shown as mean ± s.d. (*n*=3).

Ectoderm resulted highly expressed at lower frequencies (f=1d^{-1} and f=2d^{-1}) and it is completely down regulated at higher frequency (f=8d^{-1}), whereas mesoderm and endoderm expression are enhanced at higher frequency (f=8d^{-1}). Interestingly, pluripotency markers are down regulated as the frequency increases. These experimental observations are consistent with the hypothesis that ectoderm differentiation requires high accumulation of extrinsic endogenous factors to be induced[3,4], whereas strong endoderm enrichment is possible only with specific exogenous factors delivery. All together, these results suggest that periodic perfusion frequency is an additional player in directing early germ layer commitment.

To verify whether an efficient and selective induction of the three germ layers could be achieved, hESCs were induced to ectoderm, mesoderm and endoderm by specific differentiation protocols, containing germ layers-induction factors, within microfluidic platforms (Fig. 3.4a). Interestingly, a significantly higher expression of ectoderm marker β-III tubulin was obtained in microfluidic conditions, compared to conventional differentiation in Petri dish. It seems that microfluidic environment effectively allows to wash out the endogenous factors that inhibit endoderm differentiation, and efficiently delivers the exogenous pro-endoderm factors. Immunofluorescence analyses confirmed that highly selective commitment for all germ layers, with extremely low contamination from the

others, is achievable also at the protein level in each specific differentiation protocol (Appendix C).

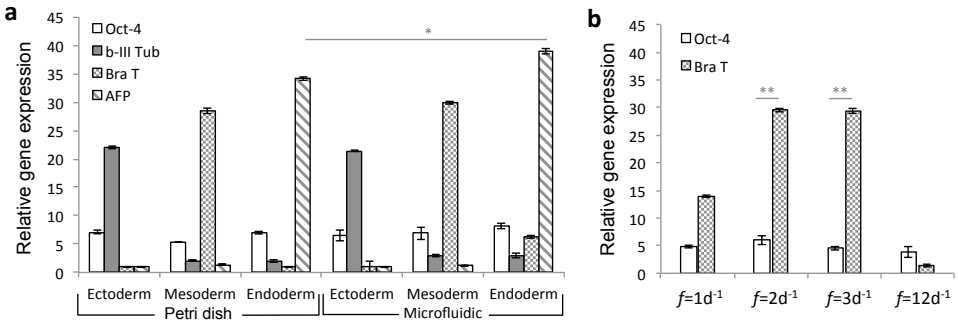

Figure 3.4 (**a**) Early germ layer induction with specific media. The qRT-PCR analysis of Oct-4, β-III tubulin, brachyury T and AFP, and comparison between standard static control and microfluidic differentiation. Data are shown as mean ± s.d. (n=3). (**b**) Mesoderm induction optimization. The qRT-PCR analysis of Oct-4 and Brachyury T expression in different frequencies of medium change for germ layer commitment optimization. brachyury T expression is comparable between f=3d^{-1} and f=2d^{-1}, while there is a significantly lower expression at high and low frequencies. Student's t-test p-values *P≤0.05 **P≤0.01. Data are shown as mean ± s.d. (n=3).

Perfusion frequency can also be adjusted for optimizing germ layer induction when specific differentiation protocols are used. As proof of concept, results in Fig. 3.4b shows how selective induction of mesoderm can be achieved by adjusting frequency of periodic perfusion. A significant 3 fold higher brachyury T expression was found at f=2d^{-1} and f=3d^{-1}, compared to f=1d^{-1} and almost null expression at f=12d^{-1}.

Collectively, these findings indicate that the frequency of periodic perfusion is an additional parameter, which can be adjusted, in order to enhance robustness and efficiency of early germ layer specification, even when specific protocols are adopted. In particular, it could carry advantages for endoderm differentiation, as it requires large quantities of exogenous molecules (e.g. ActivinA) and washing out of endogenous inhibiting factors. On the other hand, mesoderm differentiation seems to require a proper balance between exogenous and endogenous molecules that can be achieved by frequency optimization, although dependent on cell culture density and media composition.

From technological point of view, small-scale microfluidic volume leads to extremely reduced medium consumption (few microliter per day per channel) and rapid and accurate perturbation of medium composition that is an important prerequisite for multi-stage differentiation process.

3.3 Functional cardiac and hepatic cells derivation

Cardiac and hepatic cells, derived from mesoderm and endoderm germ layers, respectively, are extremely relevant for organs on a chip applications. Cell differentiation was achieved by combining *ad hoc* hPSCs differentiation stages, germ layer commitment and mature differentiation with proper frequencies of periodic perfusion and chemical regulation of soluble microenvironment. Detailed cardiac and hepatic cell differentiation protocols are reported in Appendix C.

3.3.1 Cardiac tissue derivation

Cardiac cells on a chip were derived through a frequency-dependent multi-stage differentiation protocol, consisting in mesoderm induction, through Wnt up-regulation, early cardiac commitment, through Wnt inhibition, and functional cardiac maturation, through the supply of pro-cardiac factors as shown in Fig. 4.5.

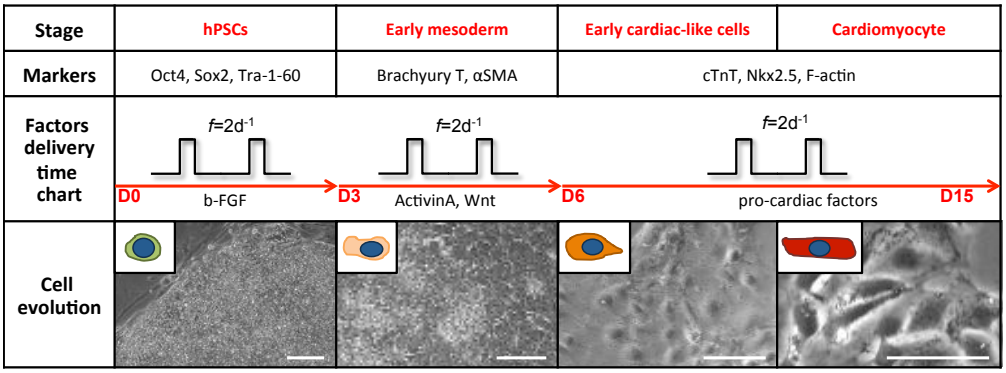

Figure 3.5 Frequency-dependent cardiac differentiation on a chip from hPSCs, with corresponding cell morphology changes. Scale bars 200 μm.

Beating cells were obtained in 10-15 days from both hESCs and hiPSCs. 60% of total cells resulted positive for cardiac troponin-T staining, showing defined cardiac sarcomeric organization. Moreover, these cells showed spontaneous calcium transients and excitation contraction coupling. Analyzing calcium handling of hPSC-cardiomyocytes in microchannels, cardiomyocytes functional response to 0.5 μM Verapamil with reduced calcium release after L-type channel inhibition was observed, and response to 10 mM caffeine with cytosolic calcium increase after ryanodine channel activation (Appendix C).

3.3.2 Hepatic tissue derivation

The same multi-stage methodology was applied to derive hepatocytes on a chip, consistently with previously endoderm-optimized conditions. Hepatic cells were

obtained from both hESCs and hiPSCs by early endoderm commitment, definitive endoderm specification and hepatocyte-like cell maturation steps, driven by specific periodic medium delivery as shown in Fig. 3.6.

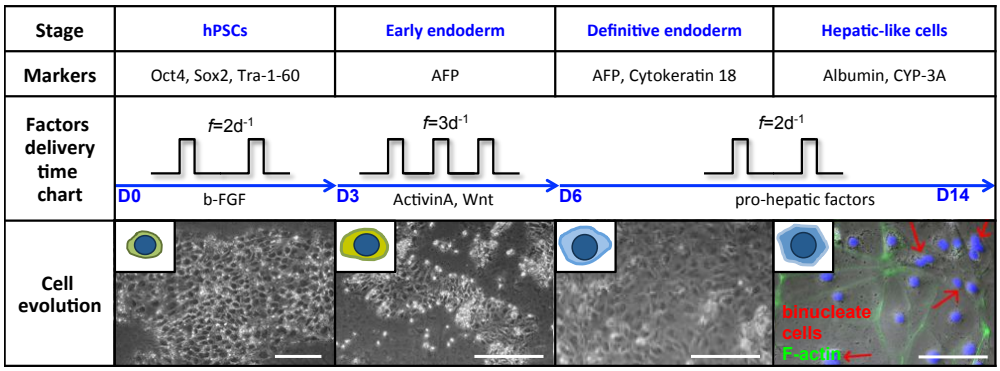

Figure 3.6 Frequency-dependent hepatic differentiation on a chip from hPSCs, with corresponding cell morphology changes. Red arrows indicate binucleate cells, typical of hepatic tissue, in the last stage. Scale bars 200 μm.

Characteristic polygonal-shaped hepatocyte-like cells were obtained, with presence of bi-nucleate cells at the late stage, showing high expression of the specific hepatic markers albumin and cytochrome P450-3A. Moreover, quantitative immunofluorescence analysis (count of number of positive cells) of late stage marker albumin and CYP-3A in hESCs-derived hepatocytes shows higher expression in microfluidic differentiated cells compared to differentiation control on Petri dish. The hepatic cells also show metabolic activity by high glycogen storage capacity (75% of total cells) and indocyanine green uptake and clearance, is extremely relevant for hepatic drug metabolism studies. As expected from prior results, compared to static conditions, we obtained a shortening of the time required for differentiation (from 16d to 14d) and 40% greater albumin secretion rate on the last day of maturation. All results of functional differentiation are reported in Appendix C.

The microfluidic environment together with optimized periodic perfusion frequency provides an effective methodology for generating hepatic-like tissues on a chip with remarkable functional differentiation also compared to conventional cell culture methods.

These results confirm that it is possible to generate functional cardiac cells on a chip and to directly perform dynamic biochemical stimulations taking advantage of the microfluidic environment, which allows robust, accurate, fast, and cost-effective spatial-temporal control of cell microenvironment[1].

3.4 References

1. Huh, D., Torisawa, Y., Hamilton, G. A., Kim, H. J. & Ingber, D. E. Microengineered physiological biomimicry: Organs-on-Chips. *Lab. Chip* **12,** 2156–2164 (2012).

2. Huh, D. *et al.* A Human Disease Model of Drug Toxicity–Induced Pulmonary Edema in a Lung-on-a-Chip Microdevice. *Sci. Transl. Med.* **4,** 159ra147–159ra147 (2012).

3. Przybyla, L. M. & Voldman, J. Attenuation of extrinsic signaling reveals the importance of matrix remodeling on maintenance of embryonic stem cell self-renewal. *Proc. Natl. Acad. Sci.* **109,** 835–840 (2012).

4. Giobbe, G. G. *et al.* Confined 3D microenvironment regulates early differentiation in human pluripotent stem cells. *Biotechnol. Bioeng.* **109,** 3119–3132 (2012).

Chapter 4

Development of disease on a chip assays

Mimicking physio-pathologic stimuli that cells experience *in vivo* allows achieving better insights into disease pathogenesis and for testing potential therapies.

In this perspective, two case studies were analyzed. The first one concerns the investigation of hypoxia-induced effects on calcium-handling machinery in cardiac tissue, whereas the second one is about the role of cyclic mechanical stretch on cellular membrane integrity in a Duchenne Muscular Dystrophy *in vitro* model. To this purpose, microfluidic oxygen exchanger and cell strecthing device describd in Chapter 2 were employed.

4.1 Calcium dynamics alteration in cardiomyocytes during acute hypoxia transient

Cardiac ischemia occurs when blood supply to part of the organ is suddenly reduced or completely interrupted for a discrete amount of time. Ischemic tissues undergo rapid changes in cellular environment, such as reduced nutrient supply, accumulation of metabolic wastes, drop in oxygen concentration and increase in carbon dioxide concentration. In a highly energy demanding tissue, like the myocardium, hypoxic conditions that are generated when oxygen demand exceeds oxygen supply are reached in very short time[1] and lead to irregular ion fluxes with generation of arrhythmias[2]. In particular, hypoxia-induced effects on calcium handling and L-type Ca^{2+} channels activity have been found to occur in these conditions.

The study of early hypoxia-induced effects on cardiac tissue *in vitro* needs a tightly controlled system able to suddenly (within few minutes) reduce oxygen partial pressure in the culture medium.

4.1.1 Experimental set-up

Investigation on calcium transients during hypoxia requires a fine-tuning of

oxygen partial pressure in the cell culture medium. To this purpose, a microfluidic cell culture system, with integrated cardiac cells, was coupled with the multilayer microfluidic gas-exchanger described in §2.3, in order to ensure a fast and accurate oxygen concentration control inside the culture chamber and provide a precise and repeatable hypoxic stimulus to the cell culture.

An enriched population of rat cardiomyocytes, constantly stimulated with electrical stimuli at 0.7 Hz and 20 V cm^{-1}, to have the same beating rate in all cells, was employed in order to test the sensitivity of the assay (Appendix A). Hypoxic stimuli on cells have been generated by setting only the oxygen partial pressure in the gas phase without perturbing flowing medium. Cellular calcium dynamics were analyzed directly on line by a fluorescence confocal microscope. An external system for control and data acquisition allowed precisely controlling gas phase partial pressures and flow rates, while an uniform medium flow rate was maintained during all the experiments (Fig. 4.1).

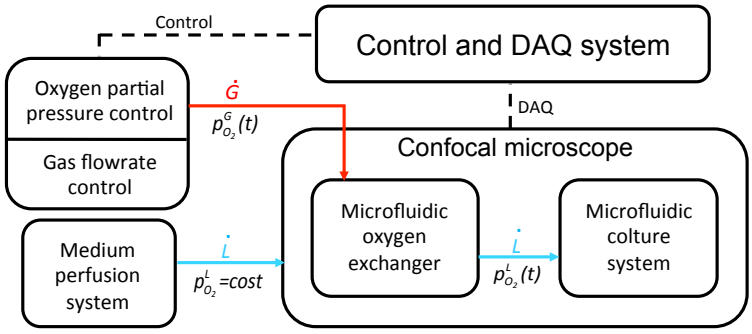

Figure 4.1 Schematic view of experimental set-up. Fast and accurate control of oxygen partial pressure inside a microfluidic cell culture chamber is performed by the multilayer microfluidic gas-exchanger. Hypoxic stimuli on a cardiomyocytes population are generated by setting gas oxygen partial pressure and cells' calcium dynamics are analyzed in line by a confocal microscopy. An external system for control and data acquisition ensures tight regulation of gas phase partial pressure and flow rate, whereas a stable medium flow rate is maintained during experiments.

The same system could be used with hPSC-derived cardiomyocytes directly degenerated inside the microfluidic chip as reported in Chapter 3.

4.1.2 Calcium dynamics analysis in hypoxia

Experimental set-up, as previously described, allows accurate oxygen partial pressure control, while avoiding any perturbations of liquid media. These technical improvements make possible to perform long-term confocal acquisitions of calcium transients on the same region of interest, using the same cell as its own control, continuously acquiring biological data prior and during the hypoxic

stimulation.

In order to rationally study the hypoxia-induced effects on calcium handling during excitation-contraction coupling it is important to investigate the duration of hypoxic stimulation that could exert a cell physiological response. In this perspective, Fig. 4.2a shows a sequence of calcium dynamics recorded in response to a fast drop of oxygen partial pressure in the medium, $p_{O_2}^L$, as a function of time.

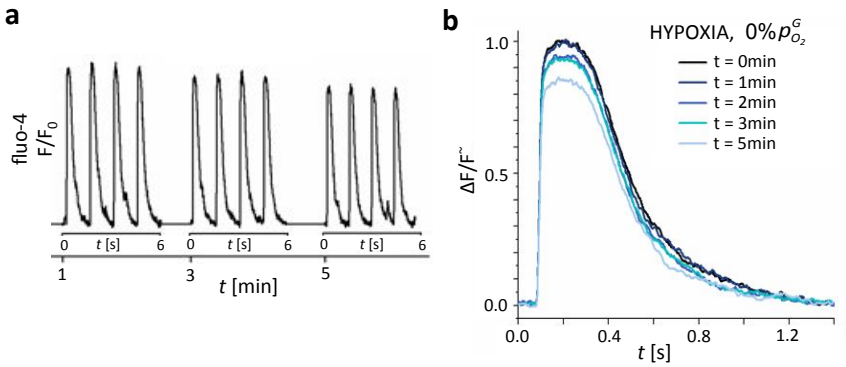

Figure 4.2 Hypoxia-induced effects on calcium transients. (**a**) Calcium transients sequence at different time points after hypoxic stimulus to the cell culture. (**b**) Comparison of single normalized calcium transients at different time points after hypoxic stimulus.

A comparison of normalized calcium transient peaks at different time points (Fig. 4.2b) shows a significant alteration of the fluorescence intensity peak maximum after 5 min from hypoxic stimulus. Therefor, all other experiments were performed considering this time frame as a minimal value to elicit a hypoxia-induced physiological response.

Another question to be addressed is the determination of the hypoxic level at which hypoxia-induced effects on calcium handling can be recorded. A multiple step experiment was designed by setting $p_{O_2}^G$ at 5 different values from 21% to 0% with 5% interval and the resulting $p_{O_2}^L$ step profile is shown in Fig. 4.3a.

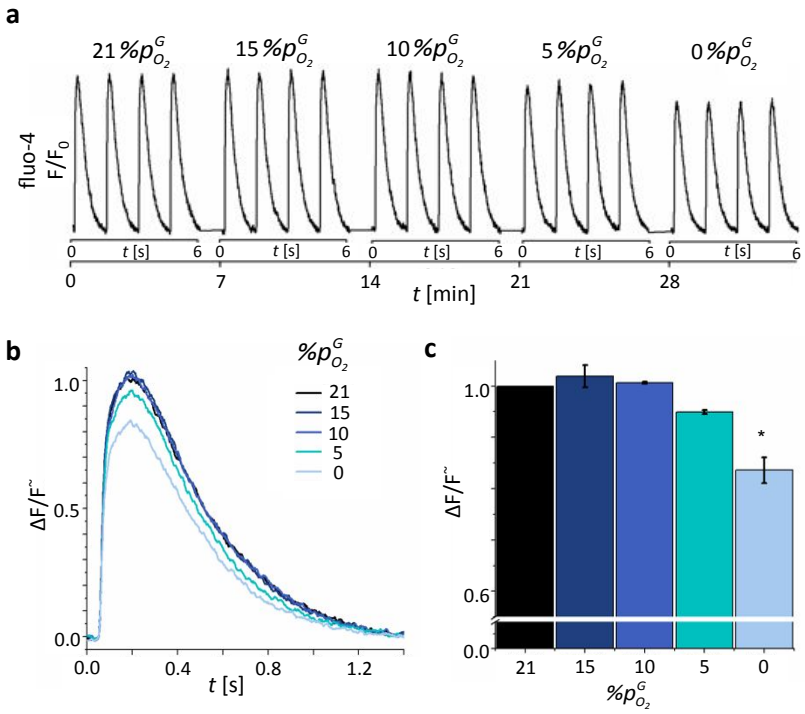

Figure 4.3 Oxygen level threshold. (A) $p^L_{O_2}$ profile for five different $p^G_{O_2}$ with $\dot{L}$=100 µl min^{-1}. Insert shows equilibrium and operating curve obtained by calibration. (B) Calcium transients sequence at different $p^L_{O_2}$ measured 7 minutes after $p^G_{O_2}$ set-point change. Blue arrows show correspondence between $p^G_{O_2}$ set-point and calcium transient sequence (Fig. 5A). (C) Comparison of single normalized calcium transients at different oxygen partial pressure. (D) Averaged values of normalized calcium transients peak height at different oxygen partial pressure. The histogram is based on 5 replicates of same conditions.

Fig. 4.3b shows the corresponding sequence of calcium transients acquired for 6 s at different $p^L_{O_2}$ levels measured 7 minutes after the $p^G_{O_2}$ set-point change. The fluorescence baseline maintained the same intensity for all the duration of the experiment and the effect of hypoxic stimulation emerged with a decrease of the maximum of the normalized calcium transient peak (Fig. 4.3b). The analyzed cells did not display calcium cycling alterations for $p^G_{O_2}$ > 5% (n=5). At 5% a poor significant difference (P<0.05, n=5) decrease was observed, whereas at $p^G_{O_2}$= 0% the alteration of calcium transient was observed with higher statistical relevance (P<0.01, n=5) (Fig. 4.3c). These data show that the observed effect reveals itself only in highly hypoxic nearly anoxic conditions, remaining latent at higher oxygen concentrations.

To test if hypoxia-induced Ca^{2+} fluxes changes are reversible and, concurrently, exclude artifact deriving form long term confocal acquisition such as dye photo-

bleaching, the cardiomyocyte culture was subjected to a fast drop of $p_{O_2}^L$ and maintained in hypoxic conditions for 10 min followed by 10 min of reperfusion with normoxic medium. Whole-cell calcium dynamics were acquired every 10 min and results are reported in Fig. 4.4a.

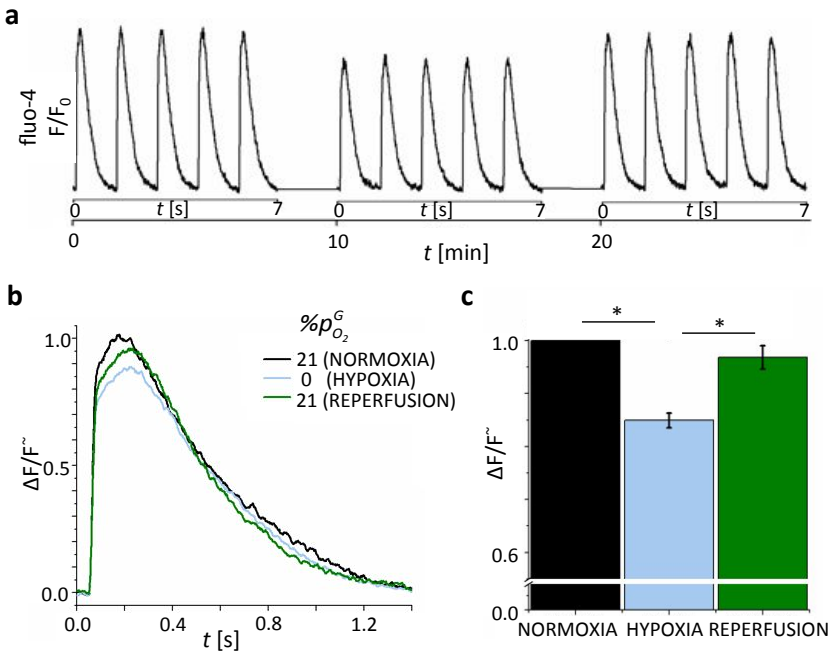

Figure 4.4 Reversible effect of hypoxia on calcium cycling. (**a**) Calcium transients sequence measured in normoxic, hypoxic ($p_{O_2}^G$ = 0%) and normoxic conditions. (**b**) Comparison of single normalized calcium transients in normoxic, hypoxic ($p_{O_2}^G$ = 0%) and normoxic condition. (**c**) Averaged values of normalized calcium transients peak height in normoxic, hypoxic ($p_{O_2}^G$ = 0%) and normoxic condition. The histogram is based on 5 replicates of same conditions.

In response to hypoxic stress a decrease of the maximum calcium transient peak was observed (Fig. 4.4b), with no alteration of the fluorescence baseline (n=8). After recovering normoxic conditions, cardiomyocytes displayed again the same fluorescence intensity, indicating a recovery of calcium cycling towards basal conditions. By analyzing the variation of fluo-4 fluorescence after 10 minutes of hypoxia and subsequent 10 minutes of reperfusion by means of percentage decrease against normoxic fluorescence intensity, a statistically relevant decrease (~15%, P<0.01) emerged (Fig. 4.4c). The recovery of normal calcium transients after re-establishment of normoxic conditions highlights the reversibility of the biological effect and excludes the responsibility of dye photo-bleaching from the observed decrease of fluorescence.

All together, these results show that there is a significant reversible alteration of

calcium homeostasis in excitation-contraction coupling during fast hypoxic stimuli. This experimental evidence underlines the ability of the cells to sense oxygen level and rapidly adapt to normoxic/hypoxic/normoxic transitions by regulating either directly or through secondary pathways the molecular machinery involved in cardiac Ca^{2+} homeostasis[3].

Similar calcium peak reductions were recorded using different concentrations of L-type voltage-gated calcium channels (VGCC) activity inhibitors (Nifedipine and Verapamil) in normoxic conditions (Appendix A). These findings confirm that a hypoxia-induced alteration of primary calcium entry through L-type VGCCs could turn in a reduced calcium concentration during excitation-contraction coupling and consequently, in an alteration of the physiological activity of cardiomyocytes, also suggesting that a cardioprotective mechanism during early phases of acute ischemia takes place through the reduction of calcium homeostasis in excitation-contraction coupling.

In this context, a fully reversible adaptive mechanism of cardiopreservation might take place during the early events of ischemic stress through fast alteration in ion channel function in response to changes in cellular oxygen. Rational understanding of how the cardiomyocyte adapts to acute ischemic stress and sustains its survival represents an important challenge because it might help in finding novel strategies to enhance cardiomyocytes survival in patients.

4.2 Role of cyclic mechanical stress in dystrophic myotubes membrane integrity

Duchenne Muscular Dystrophy (DMD) is an inherited genetic disease caused by mutations in the gene encoding for protein dystrophin, which plays a structural and regulatory role in many tissues, especially in skeletal and cardiac muscle, preserving cellular membrane integrity and homeostasis[4]. Mechanical stress seems to deeply affect the pathogenesis of muscle fibers, as resulted in many studies on mdx, a DMD mouse model. In this context, the effect of dystrophin lack in membrane integrity preservation, after prolonged mechanical stimulation, was investigated in a human *in vitro* model.

4.2.1 Mechanical stress-induced membrane damage

The integrity of membrane proteins complex, including dystrophin, is crucial for

the contracting myofiber to withstand the mechanical stress generated by sarcomeres and to prevent contraction-induced sarcolemma injuries[5]. Muscle fibers damage is exacerbated during normal muscle contractions and initiates a lethal cascade of events that can cause death of the myofiber[6] (necrosis) and fibrotic tissue formation[7].

Lack of dystrophin in mdx mouse, a DMD mouse model, has been shown to cause aberrant mechano-transduction in skeletal muscle fibers[8,9], and mechanical stress seems to deeply affect the disease pathogenesis by triggering intracellular calcium increase, which finally leads to fibers necrosis[10,11].

Conversely, there is broad evidence that muscle fibers from mdx mouse are weaker and more permeable to soluble factors and macromolecules when exposed to cycles of mechanical stimulations. Moreover, eccentric contractions allow soluble cytosolic proteins such as creatine kinase, to leak out of the plasma membrane, whereas extracellular proteins, such as albumin and fibronectin can be detected inside the muscle[12,13]. These experimental evidences on mdx mice prove that cyclic mechanical stimulation strongly affects the maturation of dystrophic muscle phenotype, suggesting a central role also in humans. However, a human *in vitro* study directed at recapitulating physiological mechanical stress-induced effects on dystrophic skeletal muscle has never been reported yet.

For this reason, a human DMD skeletal muscle *in vitro* model was developed through integration of human myotubes derived from healthy and diseased patients within cell stretching device described in §2.4, in order to investigate the role of cyclic mechanical stress in affecting membrane integrity.

Microfluidic cell-stretching devices were opportunely functionalized, in order to achieve long-term cell attachment during myoblasts differentiation. Human myoblasts derived from biopsies of healthy donors and DMD patients were seeded at high density and induced to differentiate into fused myotubes, through proper factors supply (Appendix E), the day after (Day 1) for 6 days.

At Day 6 both healthy and dystrophic myotubes express late myogenic marker myosin heavy chain, MHC, with defined sarcomere organization, which represents the functional unit for muscle contraction, whereas only healthy myotubes show dystrophin expression with clear membrane localization (Appendix E).

A membrane impermeant dye, FM 1-43, was used to analyze large molecules

membrane permeability induced by mechanical stresses in both healthy and diseased cells during physiologic deformation (10-15%). In order to verify the efficacy of the probe in the developed system, healthy myotubes were exposed to a mechanical overloaded (about 50% deformation) to induce membrane damage. When micro-ruptures in the plasma membrane occur the amphiphilic molecule FM 1-43, absorbed within plasma membrane, interact with the inner membrane layer entering into the cytosol and fluorescence can be observed as shown in Fig. 4.5.

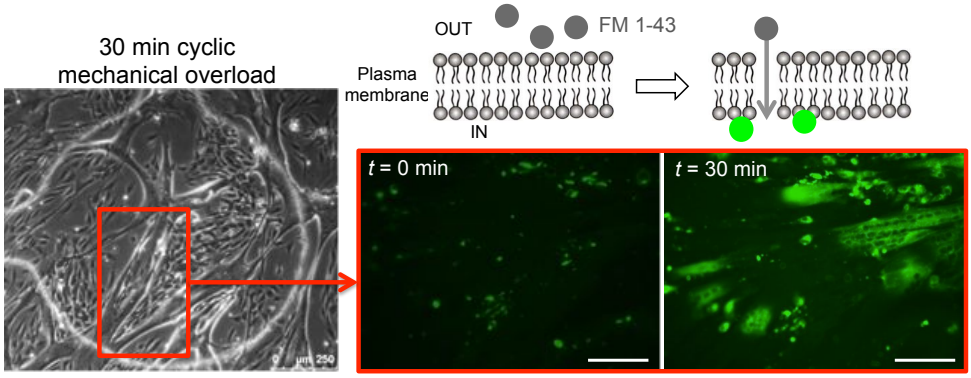

Figure 4.5 30 minutes of cyclic mechanical overload (1Hz) applied to healthy myotubes induce micro-ruptures in plasma membrane allowing up-take and fluorescence of dye FM 1-43 into cell cytosol.

The developed assay can be used to induce more physiologic stimulations (15%) on both healthy and dystrophic, in order to investigate the role of cyclic mechanical stretch in affecting membrane integrity of healthy and diseased cells.

4.2.2 Stretch-induced membrane permeability is higher in dystrophic myotubes

Human myotubes were loaded with 4 μM FM 1-43 dye and cyclically stretched with 15% physiological deformation for 45 or 90 min at 0.5 Hz. Immediately after stimulation, fluorescence intensity due to dye uptake was detected in stretched and un-stimulated myotubes in the same device. Fig. 4.6a shows representative pictures of dystrophic myotubes after 45 min stimulation, compared to control un-stretched conditions, with similar uptake of FM1-43 dye.

Taking advantage of having an internal un-stretched control, fluorescence intensity of stretched and control myotubes was analyzed in the same conditions and with the same fluorescence background. Fluorescence intensity in the cytosolic regions of myotubes was quantified as described in Appendix E and

results were represented as intensity mean distribution of region of interests, ROIs (*N*=100).

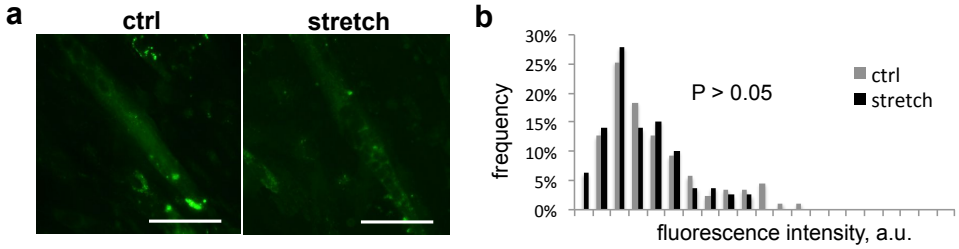

Figure 4.6 Stretch-induced membrane permeability analysis in dystrophic myotubes after 45min cyclic stimulation. (**a**) Representative pictures of FM 1-43 dye uptake in dystrophic myotubes after 45 min cyclic stretch (0.5 Hz, 15% deformation), compared to un-stimulated control myotubes. (**b**) Fluorescence intensity distribution of stretched myotubes is not statistically different from the un-stretched control.

Quantification of fluorescence intensity confirms a non-significant difference between the two distributions (Fig. 4.6b).

The same experiment was repeated for an higher temporal interval, i.e. 90 min and in this case cyclic deformation induces a partial increase of dye uptake in healthy myotubes, in comparison to un-stretched myotubes, whereas elevated and widespread up-take of FM 1-43 dye in cytosolic regions of stretched dystrophic myotubes was observed if compared with un-stretched control (Fig. 4.7a).

Fig. 4.7b shows a non-significant difference between control and stretched myotubes distributions (P-value=0.973) for the healthy control; on the other hand, stretched dystrophic myotubes resulted in a significant (P-value=0.029) stretch-induced dye uptake increase in respect to un-stimulated control, as revealed by comparing fluorescence intensity distributions (Fig. 4.7c).

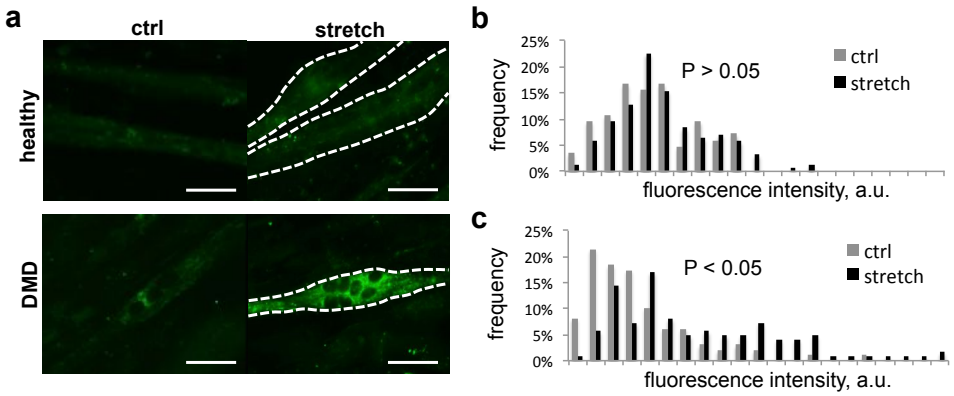

Figure 4.7 Stretch-induced membrane permeability analysis in dystrophic compared to healthy myotubes after 90 min cyclic stimulation. (**a**) Representative pictures of FM 1-43 dye uptake in healthy and dystrophic myotubes after 90 min cyclic stretch (0.5 Hz, 15% deformation), compared to un-stimulated control myotubes. (**b**) Fluorescence intensity distribution of stretched healthy myotubes is not statistically different from the un-stretched control. (**c**) Fluorescence intensity distribution of stretched DMD myotubes result statistically different from the un-stretched control.

These results demonstrate that lack of dystrophin strongly affects membrane permeability of human myotubes, when subjected to cycles of mechanical stretch that closely mimic physiological deformation of muscle fibers. These results also validates the hypothesis proposed by Allen et al., that increased permeability in dystrophic muscle fibers is likely due to the slow accumulation (about 1 hour) of intracellular calcium, which activates stretch-activated ion channels, rather than to the formation of membrane tears as a consequence of stimulation-induced membrane injury[12].

The developed assay could be used in order to test potential biological mechanisms triggering stress-induced membrane-damage, such as activation of components proteasome system (calpains), but it could also be used as platform for investigate new therapeutic targets or for drug screening investigations.

4.3 References

1. Diaz, R. J. & Wilson, G. J. Studying ischemic preconditioning in isolated cardiomyocyte models. *Cardiovasc. Res.* **70,** 286–296 (2006).

2. Saint, D. A. Persistent (current) in the face of adversity ... A new class of cardiac anti-ischaemic compounds on the horizon? *Br. J. Pharmacol.* **156,** 211–213 (2009).

3. Shimoda, L. A. & Polak, J. Hypoxia. 4. Hypoxia and ion channel function. *Am. J. Physiol. - Cell Physiol.* **300,** C951–C967 (2011).

4. Yeung, E. W. *et al.* Effects of stretch-activated channel blockers on [Ca2+]i and muscle damage in the mdx mouse. *J. Physiol.* **562,** 367–380 (2005).

5. Rahimov, F. & Kunkel, L. M. Cellular and molecular mechanisms underlying muscular dystrophy. *J. Cell Biol.* **201,** 499–510 (2013).

6. McNally, E. M. & Pytel, P. Muscle Diseases: The Muscular Dystrophies. *Annu. Rev. Pathol. Mech. Dis.* **2,** 87–109 (2007).

7. Blake, D. J., Weir, A., Newey, S. E. & Davies, K. E. Function and Genetics of Dystrophin and Dystrophin-Related Proteins in Muscle. *Physiol. Rev.* **82,** 291–329 (2002).

8. Khairallah, R. J. *et al.* Microtubules Underlie Dysfunction in Duchenne Muscular Dystrophy. *Sci. Signal.* **5,** ra56 (2012).

9. Kumar, A. Loss of dystrophin causes aberrant mechanotransduction in skeletal muscle fibers. *FASEB J.* **18,** 102–113 (2004).

10. Matsumura, C. Y., Taniguti, A. P. T., Pertille, A., Neto, H. S. & Marques, M. J. Stretch-activated calcium channel protein TRPC1 is correlated with the different degrees of the dystrophic phenotype in mdx mice. *Am. J. Physiol. - Cell Physiol.* **301,** C1344–C1350 (2011).

11. Mann, C. *et al.* Aberrant repair and fibrosis development in skeletal muscle. *Skelet. Muscle* **1,** 21 (2011).

12. Allen, D. G. & Whitehead, N. P. Duchenne muscular dystrophy – What causes the increased membrane permeability in skeletal muscle? *Int. J. Biochem. Cell Biol.* **43,** 290–294 (2011).

13. Zhang, B.-T. *et al.* Pathways of Ca2+ entry and cytoskeletal damage following eccentric contractions in mouse skeletal muscle. *J. Appl. Physiol.* **112,** 2077–2086 (2012).

Chapter 5

MicroRNAs as regulators of hPSCs differentiation

MicroRNAs are non-coding RNAs regulating gene expression at transcriptional level. They have the ability to simultaneously target groups of genes determining cell phenotype. They possess recognized roles in development and disease, suggesting they can be used to drive hPSCs differentiation toward specific developmental stages.

5.1 MicroRNAs biogenesis and targeting

MicroRNAs are small non-coding RNAs of 20-22 nucleotides, regulating gene expression post-transcriptionally. MiRNAs genes are transcribed by either RNA polymerase II or RNA polymerase III into primary miRNA transcripts (pri-miRNA), which are next cleaved in the nucleus by Drosha/DGCR8 (DiGeorge Critical Region 8) proteins complex[1]. Pri-miRNAs are further transferred from the nucleus through protein Exportin-5 and processed into cytosol. Mature miRNAs and Argonaute (Ago) proteins form the RNA-induced silencing complex (RISC), a ribonucleoprotein complex mediating post-transcriptional gene silencing, which pair to the messages of protein-coding genes to direct the post-transcriptional repression of these mRNAs[2,3].

This effect generally occurs through direct base-pairing of the mature miRNA to the 3'-UTR region of partially complementary messenger RNAs. Interaction of the miRNA with target mRNAs typically results in either destabilization or suppressed translation.

Like transcription factors, they have the ability to control expression of multiple genes in the same time, as they can match several targets RNAs regulating cell phenotype through their repression[4]. These microRNAs have recognized roles in several diseases, such as cancer and neurodegenerative disorders, reprogramming of somatic cells to hiPSCs and development.

Several works demonstrated human pluripotent stem cells express a unique pattern of

microRNAs, which seem to regulate hPSCs cell cycle and pluripotency maintenance[5]. MiRNAs are also essential for development, as knockout of the RNA-processing ribonuclease protein Dicer1and DGCR8 in mice has been shown to disrupt active miRNA biogenesis, which is lethal during embryogenesis[5]. This unique microRNAs pattern expression, characterizing pluripotent state, suggests they also regulate germ layer specification and differentiation. Indeed, the switch from pluripotent to lineage-specified cells is accompanied by the up-regulation of many tissue-specific miRNAs[4].

5.2 Role of microRNAs in hPSCs differentiation

The differentiation process from hPSCs to lineage specific cells is associated to a defined temporal pattern of microRNAs expressions, which guide stem cells in cell cycle exit, germ-layer commitment and tissue specification.

In this perspective, these microRNAs can be used to drive hPSCs differentiation towards specific germ-layers, thanks to their ability to simultaneously regulate expression of groups of genes. They could be particularly advantageous in those cases in which hPSCs require an high content of expensive and potentially harmful exogenous factors to be pushed towards specific lineages. This is the case of hepatic differentiation in which the first stage of endoderm commitment requires an elevated concentration of exogenous ActivinA and other factors harmful for cell survival, leading to low yield of differentiation cells calculated on the total of starting cells.

In this context, the following approach was adopted:

1) The main early endoderm markers and transcription factors where identified in the literature;
2) For each of them all corresponding microRNAs were predicted;
3) Common microRNA where analyzed;

Table 5.1 shows a list of genes known to be involved in early endoderm commitment of hPSCs[6,7,8]. For each of them targets microRNAs were predicted through the use of software Targetscan and all potential candidates, as predicted from the Software, were listed.

Table 5.1 Genes associated with endoderm development with the corresponding targeting microRNAs predicted by TargetScan software. 40% of these genes share a common microRNA cluster, miR-141/200a (in bold).

Endoderm genes	Targetscan-predicted associated microRNAs
CXCR4	miR-9/9ab
SOX17	**miR-141/200a**; miR-26ab/1297/4465; miR-194
MIXL1	-
CER1	miR-4766-3p
FOXA2	**miR-141/200a**
HNF1B	miR-217; miR-375; miR-24/24ab/24-3p; miR-25/32/92abc/363/363-3p/367; miR-200bc/429/548a; miR-194; miR-26ab/1297/4465
LHX1	miR-182; **miR-141/200a**; miR-30abcdef/30abe-5p/384-5p; miR-217; miR-26ab/1297/4465; miR-139-5p; miR-182; miR-194; miR-30abcdef/30abe-5p/384-5p; miR-144; miR-128/128ab; miR-138/138ab; miR-96/507/1271; miR-218/218a
EOMES	miR-182; miR-96/507/1271; miR-135ab/135a-5p; miR-25/32/92abc/363/363-3p/367; miR-96/507/1271; miR-182; miR-103a/107/107ab
GATA6	miR-124/124ab/506; miR-128/128ab; **miR-141/200a**; miR-375; miR-196abc; miR-10abc/10a-5p; miR-7/7ab; miR-181abcd/4262; miR-25/32/92abc/363/363-3p/367
LEFTY	miR-93/93a/105/106a/291a-3p/294/295/302abcde/372/373/428/519a/520be/520acd-3p/1378/1420ac
FOXH1	miR-18ab/4735-3p
PITX2	miR-140/140-5p/876-3p/1244; miR-21/590-5p; **miR-141/200a**
JMJD3	miR-138/138ab; miR-99ab/100; miR-216a; miR-135ab/135a-5p; miR-29abcd; miR-101/101ab; miR-148ab-3p/152; miR-17/17-5p/20ab/20b-5p/93/106ab/427/518a-3p/519d; miR-7/7ab; miR-139-5p; miR-30abcdef/30abe-5p/384-5p; miR-146ac/146b-5p; miR-144

Surprisingly about 40% of analyzed genes show a common target microRNAs cluster, miR-141/200a, which was found to be involved in epithelial to mesenchymal transition (EMT) process[9]. This result was used in order to test if repression of these two microRNAs, during endoderm differentiation of human pluripotent stem cells, can lead to increased expression of endoderm commitment markers, compared to a mock control.

Human embryonic stem cells were transfected with both miR-141 and miR-200a inhibitors through FugeneHD (Promega) to induce their repression and, 24h later, they were induced to differentiate into endoderm for 5 days, according to protocol reported in Appendix D. Efficiency of infection resulted in 67% of transfected cells

as analyzed by flow-cytometry analysis, using a fluorophore-labeled miRNA inhibitor control. Transfection was repeated after 3 days from the beginning of the differentiation protocol in order to maintain miRNAs repression. At day 5 cells were collected for total RNAs extraction and analyzed through qPCR analysis for both microRNAs and RNAs expression.

Fig. 5.1a shows expression of miR-302a, which is known to be expressed in embryonic stem cells, miR-141 and miR-200a in undifferentiated cells (D0), transfected cells at day 5 of differentiation (D5) and the same cells transfected with a mock control (D5 ctrl). D5-cells show a significant reduction of expression of both miR-141 and miR-200a, compared to the control, meaning that transfection of microRNAs inhibitors worked.

The same samples were further analyzed for RNAs expression of pluripotent gene Nanog, mesoderm marker Brachyury-T and four endoderm transcription factors: EOMES, GATA6, FOXA2 and Sox17, as shown in Fig. 5.1b. A significant reduction of expression of all the endoderm genes was observed and, interestingly, three of these four genes, i.e. GATA6, FOXA2 and Sox17, were predicted targets of the miR-141/200a cluster.

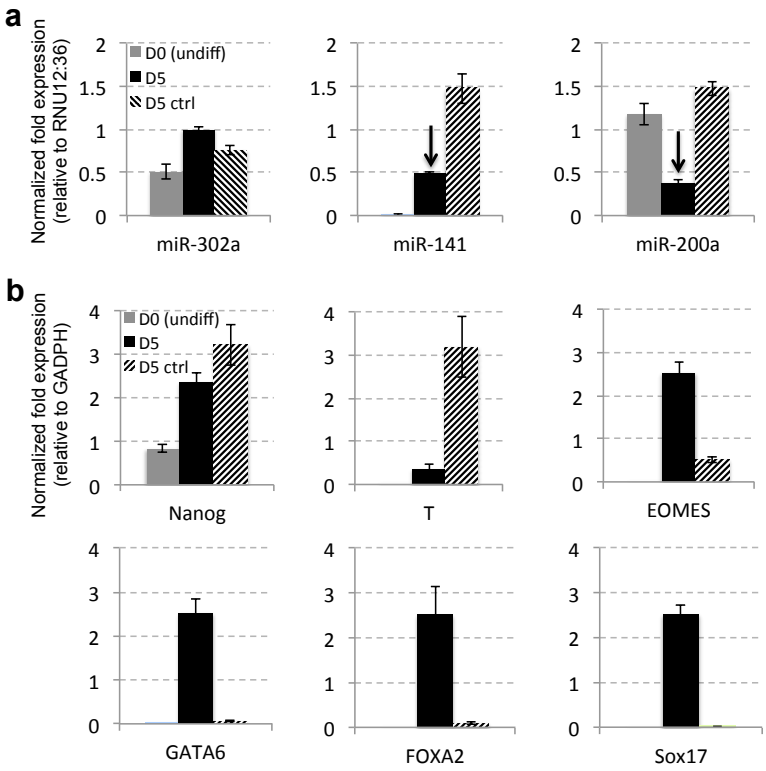

Figure 5.1 (**a**) QPCR analysis of embryonic stage miR-302a and miR-141/200a cluster in undifferentiated hESCs (D0), differentiated cell (D5), transfected with miR141/200a inhibitors and mock control (D5 ctrl). MiR-141/200a expression reduction in D5 cells proves efficient tranfection. (**b**) QPCR analysis of pluripotency marker Nanog, mesoderm marker Brachyury-T and four endoderm transcription factors: EOMES, GATA6, FOXA2 and Sox17in the same samples. A significant increase in endoderm markers expression was observed in transfected cells compared to the mock control and undifferentiated cells. (2 biological replicates and 3 technical replicates for each analysis were performed).

This result, which certainly requires validation at protein level through western blot analysis, validates the hypothesis that microRNAs can effectively be used to drive differentiation of pluripotent stem cells.

5.3 Future perspectives

These preliminary results open new perspectives for future investigations on potential role of microRNAs in programming hPSCs toward specific developmental stage or reprogramming adult somatic cells to other tissue-specific cells.

This last purpose requires an accurate temporal pattern of overexpression or repression of specific microRNAs to guide cells from one phenotype to another one. Microscale system described in Chapter 2 could be an efficient tool to regulate and

efficiently deliver genetic material to sustain long-term expression and this perspective contributes to the development of human tissues on a chip from pluripotent stem cells or directly from adult cells.

5.4 References

1. Winter, J., Jung, S., Keller, S., Gregory, R. I. & Diederichs, S. Many roads to maturity: microRNA biogenesis pathways and their regulation. *Nat. Cell Biol.* **11,** 228–234 (2009).

2. Bartel, D. P. MicroRNAs: genomics, biogenesis, mechanism, and function. *Cell* **116,** 281–297 (2004).

3. Grimson, A. *et al.* MicroRNA targeting specificity in mammals: determinants beyond seed pairing. *Mol. Cell* **27,** 91–105 (2007).

4. Ivey, K. N. & Srivastava, D. MicroRNAs as Regulators of Differentiation and Cell Fate Decisions. *Cell Stem Cell* **7,** 36–41 (2010).

5. Leonardo, T. R., Schultheisz, H. L., Loring, J. F. & Laurent, L. C. The functions of microRNAs in pluripotency and reprogramming. *Nat. Cell Biol.* **14,** 1114–1121 (2012).

6. D'Amour, K. A. *et al.* Efficient differentiation of human embryonic stem cells to definitive endoderm. *Nat. Biotechnol.* **23,** 1534–1541 (2005).

7. Drukker, M. *et al.* Isolation of primitive endoderm, mesoderm, vascular endothelial and trophoblast progenitors from human pluripotent stem cells. *Nat. Biotechnol.* **30,** 531–542 (2012).

8. Teo, A. K. K. *et al.* Pluripotency factors regulate definitive endoderm specification through eomesodermin. *Genes Dev.* **25,** 238–250 (2011).

9. Gregory, P. A. *et al.* The miR-200 family and miR-205 regulate epithelial to mesenchymal transition by targeting ZEB1 and SIP1. *Nat. Cell Biol.* **10,** 593–601 (2008).

Conclusions

The main goal of this work concerned the development of functional human tissues on a chip from pluripotent stem cells, to be used in developing new in vitro disease models or drug screening and toxicity assays, more predictive than poor predictive animal models, and overcoming issues related to primary cell sources recruitment.

Specifically, the focus was pointed on cardiac and hepatic tissues, which are recognized as the major targets of drug toxicity. Moreover, no human primary cells are easily available for these tissues, due to obvious limitations in ex vivo extraction.

Human pluripotent stem cells (hPSCs), comprising both embryonic and induced pluripotent stem cells, were successfully integrated within automatized microfluidic platforms, expanded and induced to differentiate into cardiomyocytes or hepatocytes through a multistage protocol, resembling embryonic development.

The different developmental stages required cell niche specification in terms of accurate balance between extrinsic and intrinsic cell signaling, through optimal in vitro delivery of exogenous factors and removal of endogenous cell-secreted factors.

In general, continuous medium perfusion resulted to generate soluble factors spatial gradients, lead to heterogeneous cells phenotype along the microfluidic channel. On the other hand, a discontinuous periodic medium delivery with stage-dependent frequency (number of cycles of medium change per day) was proved to represent an effective strategy for modulating delivery of growth factors and viral vectors in vitro.

Indeed, intermittent perfusion with defined frequency of medium delivery allowed optimal control of endogenous/exogenous factors balancing in cell microenvironment to sustain pluripotency and self-renewal or to selectively induce germ-layer commitment with higher specificity, than in standard static conditions in petri dish.

Cardiac and hepatic cells, derived respectively through mesoderm and endoderm induction, and functional maturation, displayed highly differentiated phenotypes and ability to respond to external stimuli.

These functionally differentiated cells on a chip can be directly used for dynamic multi-parametric and large-scale drug screening or for developing micro-engineered human organ models.

The recent generation of adult somatic cells from human induced pluripotent stem cells (hiPSCs) provided a new effective tool to obtain patient-specific stem cells and potentially screen genetic diversity among cells patients to identify rare responders, analyze drug toxicity, or perform 'clinical trials on a chip' using hiPSC-derived diseased cells.

In this new perspective, it would be of paramount importance to generate patient-specific functional-differentiated tissues on a chip and to develop technology for assisting in vitro assays for developing new therapeutic strategies or for screening among potential clinical cures. In particular, design of proper functional assays to test cellular responses to drugs or external stimuli, such as mechanical stress or hypoxia, in a physiologic or pathologic context allow investigations of specific disease targets and associated therapeutic treatments.

In this context, the role of acute hypoxia in calcium handling machinery of a cardiomyocytes population was investigated, mimicking early effects of ischemia characterized by a sudden and rapid depletion of oxygen content in cardiac microenvironment. Technological improvements, compared to already developed microscale devices for mimicking oxygen gradient, were performed, which led to the design of a microfluidic gas exchanger able to accurately reproduce fast temporal gradients of oxygen partial pressure in the culture medium.

Results showed a significant reversible alteration of calcium homeostasis in excitation-contraction coupling occurs during fast hypoxic stimuli. This suggests that a fully reversible adaptive mechanism of cardio-preservation might take place during the early events of ischemic stress through fast alteration in ion channel function, specifically L-type voltage-gated calcium channels, in response to changes in cellular oxygen content. Rational understanding of how the cardiomyocyte adapts to acute ischemic stress and sustains its survival represents an important challenge because it might help in finding novel strategies to enhance cardiomyocytes survival in patients.

Beside this, the role of cyclic mechanical stress, which plays a crucial role in the investigation of new physiological and pathological responses to cell culture microenvironment, was analyzed in a muscular dystrophy in vitro model.

Specifically, in Duchenne Muscular Dystrophy (DMD) is an inherited genetic disease caused by mutations in the gene encoding for protein dystrophin, which plays a

structural and regulatory role in many tissues preserving cellular membrane integrity and homeostasis, mechanical stress seems to deeply affect the pathogenesis of muscle fibers, as resulted in many studies on mdx, a DMD mouse model. The effect of dystrophin lack in membrane integrity preservation, after prolonged mechanical stimulation, was investigated in a human in vitro model through evaluation of the up-take of a fluorescent membrane impermeable compound.

Development of a microfluidic-based cell-stretching device allowed subjecting cells to defined mechanical deformations in biaxial direction with defined frequency and having an internal non-stimulated control. After prolonged cyclic deformations dystrophic myotubes derived from dystrophic patients biopsies displayed significant membrane permeability increase, compared myotubes from healthy patients, probably due to their altered phenotype.

The combination of tissues development on a chip and micro-technology assisting for functional assay on a chip opens new and substantial perespective in generating a human in vitro model that properly resemble the physio-pathological behaviour of a tissues or organs within humna body. As a near future perspective we envisage the use of diseased cells and donor-derived cells as healthy control to generate “Disease on a chip” models representative of human patho-physiology in vivo.

Appendix A

Reversible alteration of calcium dynamics in cardiomyocytes during acute hypoxia transient in microfluidic platform

Sebastian Martewicz[1,2,+], Federica Michielin[1,2,+], Elena Serena[1,2], Alessandro Zambon[1,2], Marco Mongillo[2,3], Nicola Elvassore[1,2].

1. Dipartimento di Principi e Impianti di Ingegneria Chimica, University of Padova, Via Marzolo 9, 35131 Padova, Italy.
2. Venetian Institute of Molecular Medicine, Padova, Italy.
3. Department of Biomedical Sciences, University of Padova, Via Colombo 3, 35131 Padova, Italy.
+ These authors equally contributed.

Integrative Biology
Volume 4(2):153-64
10.1039/c1ib00087j

A.1 Abstract

Heart diseases are the leading cause of mortality in western countries. Apart from congenital and anatomical alterations, ischemia is the most common agent causing myocardial damage. During ischemia, a sudden decrease in oxygen concentration alters cardiomyocyte function and compromises cell survival. The calcium handling machinery, which regulates the main functional features of a cardiomyocyte, is heavily compromised during acute hypoxic events. Alterations in calcium dynamics have been linked to both short- and long-term consequences of ischemia, ranging from arrhythmias to heart failure. In this perspective, we aimed at investigating the calcium dynamics in functional cardiomyocytes during the early phase of a hypoxic event. For this purpose, we developed a microfluidic

system specifically designed for controlling fast oxygen-concentration dynamics through a gas micro-exchanger allowing in line analysis of intracellular calcium concentration by confocal microscopy. Experimental results show that exposure of Fluo-4 loaded neonatal rat cardiomyocytes to hypoxic conditions induced changes in intracellular Ca^{2+} transients. Such behavior was reversible and was detected for hypoxic levels below 5% of oxygen partial pressure. The observed changes in Ca^{2+} dynamics were mimicked using specific L-type Ca^{2+} channel antagonist, suggesting that alterations in calcium channel function occur at low oxygen levels. Reversible alteration in ion channel function, that takes place in response to changes in cellular oxygen, might represent an adaptive mechanism of cardiopreservation during ischemia.

A.2 Insight, innovation, integration

Recreating in vitro a low oxygen environment is fundamental for a better understanding of the cellular consequences of hypoxia and to screen novel therapeutic strategies targeting common ischemic diseases, e.g. coronary heart disease. Here, we present a microfluidic platform specifically developed to expose cultured cardiomyocytes to acute hypoxic stimuli, allowing robust and high quality live confocal imaging.

Thanks to this novel technology, we were able to observe rapid and reversible changes in the electrically-induced cardiomyocyte calcium transients following the acute decrease of oxygen partial pressure in the cell environment. Similar changes in calcium dynamics were observed upon pharmacological inhibition of L-type Ca^{2+} channels, suggesting a possible target of hypoxia in cardiac cells.

A.3 Introduction

Cardiovascular diseases are the leading cause of mortality and morbidity in the Western countries. Heart diseases due to coronary dysfunction alone were responsible for nearly 22% of all deaths in Europe in 2008.[1] Cardiac ischemia occurs when blood supply to part of the organ is suddenly reduced or completely interrupted for a discrete amount of time. Ischemic tissues undergo rapid changes in cellular environment such as reduced nutrient supply, accumulation of metabolic wastes, drop in oxygen concentration and increase in carbon dioxide concentration. In a highly energy demanding tissue, like the myocardium, hypoxic

conditions that are generated when oxygen demand exceeds oxygen supply are reached in very short time.[2]

The time scale of the changes in oxygen concentration has a great importance for cell physiology, viability and adaptation to stress conditions. In particular, the cellular response to hypoxia depends on its onset kinetics and duration: (i) rapid acute hypoxia (seconds or minutes) leads to alterations of the preexisting protein pool through post-translational modifications and protein interactions; (ii) sustained chronic hypoxia (hours or days) results in whole proteome changes through activation of different gene expression patterns.[3]

In order to recreate *in vitro* ischemia pathological models, accurate gas concentration dynamics are one of the most difficult parameters to control; for instance, in hypoxia studies, gas leakage through liquid-air interface or gas permeable materials is extremely difficult to detect and may lead to low experimental reproducibility. Studies on chronic hypoxia (lasting hours or days) can be easily performed by culturing the cells in airtight chambers in which the oxygen concentration control is exerted by tuning the gaseous partial pressure inside the chamber. In this steady state experiments, the cell response at desired time points is commonly independent from the oxygen dynamics at the initial experiment set up.[4] On the other hand, observing cellular responses to fast hypoxic transients, simulating the early phase of acute ischemic events, is essential in understanding how cell biology and physiology are affected by sudden changes in oxygen concentrations. However, investigating the immediate effects of a rapid drop in oxygen partial pressure requires tight control on the cellular environment, a condition hard to achieve with standard culture methods. As such, current technological limitations have hindered cellular experiments on hypoxia.

In this perspective, we aimed to develop a novel tool for *in vitro* investigation of the acute cellular response of cultured cardiomyocytes to fast changes in the environmental conditions, including components of the culture medium, drugs and oxygen concentration. In this work, we used such approach to investigate the effect of acute hypoxic events on Ca^{2+} homeostasis, through in line confocal image acquisition.

Cardiomyocyte function relays upon proper ion handling during contraction cycles, involving both ion channels regulating membrane potential and intracellular calcium release. Hypoxia has been proven to modify the activity of

most of the molecular components concerned in these features, resulting in unbalanced ion fluxes and generation of arrhythmias.[5] Rat ventricular cardiomyocytes in low p_{O2} conditions displayed an increase of the late Na^+ current ($I_{Na\text{-}L}$) while the fast Na^+ (I_{Na}) current appeared reduced.[6,7] Effects on potassium channels were also described in guinea-pig cardiomyocytes as a decrease in the slow component of the delayed rectifier K^+ channel (I_{Ks}) current, without affection of the rapid component (I_{Kr}).[8] Ca^{2+} handling, essential in both action potential generation and contraction triggering, seems to be influenced by hypoxia as well. In particular, the activity of the L-type Ca^{2+} channel is altered with a decrease of basal current ($I_{Ca\text{-}L}$) and unchanged current–voltage (I-V) relationship.[9,10] Sensitivity of the channel to β-adrenergic stimulation appears to be increased resulting in a pro-arrhythmic substrate during ischemic events.[11] The precise mechanism through which hypoxia modifies the function of the L-type Ca^{2+} channel is still unclear. Both direct modifications in the C-terminal region of the channel[12,13] and indirect modulation of its function through mechanisms involving mitochondrial ROS formation[14] or protein kinases A and C[15] have been proposed.

All these studies clearly show that rapid changes in oxygen concentration affect ion handling in cardiac myocytes, but so far no hypoxia-induced effects on calcium handling during excitation-contraction coupling were reported, although many components of this machinery appear to be altered in ischemia-mimetic conditions.[16,17]

In this work, we aimed at analyzing calcium dynamics in Fluo-4-loaded functional rat cardiomyocytes in response to brief and sudden transients of hypoxia. In particular, we focused on the early response to hypoxia induction and re-oxygenation, by monitoring electrically stimulated Ca^{2+} changes.

For this reason, we designed and developed a device enabling confocal microscopy analysis while finely tuning the oxygen concentration in the culture medium and maintaining proximal cell environment isolated from atmospheric conditions. In addition, the device allows exposure of the cells to fast transient changes in the environment without perturbing the data acquisition process. Particular care has been placed to avoid, manipulation of the liquid phase that could generate pressure waves in the cell culture chamber and cause loss of focal plane leading to artifactual changes in fluorescence signals.

As mentioned above, conventional humidified chambers or incubators with a controlled p_{O2} in the gas phase show equilibration time of the order of hours,[19] due to the great volumes involved and the low oxygen diffusion coefficient in the culture medium (2.1×10^{-5} cm^2 s^{-1}).[18] Such characteristic time can only be slightly decreased using particular expedients like gas-permeable membrane-based dishes[20] or by forcing gas exchange through bubbling of gas mixtures in chemostats or flasks.

In this perspective, technology developed at the microscale level can be an effective practical solution for obtaining a system able to accurately control oxygen partial pressure for two main reasons:

(i) at microscale liquid flow regime is typically laminar, allowing to accurately control the delivery of nutrients, soluble species and gas in the culture medium;[21-23]

(ii) the time scale of diffusive mass transport phenomena are related to the characteristic length of the system and scaling down the system highly accelerates the gas exchange dynamics.

For this reason, many microfluidic bioreactors were developed to provide solely moderate to long-term control of the cellular environment, including dissolved gas concentrations.[24-27] Some miniaturized devices include gas-microexchangers that generate spatial gradients of oxygen partial pressure by on-chip gas mixing and allow to study the influence of the oxygen concentration on the cell growth.[28-30]

However, only few microfluidic devices for rapid generation of hypoxic conditions in cell culture were designed, due to the difficulty in obtaining fast oxygen concentration transients from a saturated level to a very low partial pressure, without perturbing the cell culture environment and the data acquisition system. For instance, Oppergard *et al.* have developed a microfabricated insert that nests into a standard multiwell plate and serves as a passive microfluidic gas network with a permeable membrane aimed to modulate oxygen delivery to adherent cell with an equilibration time on the order of few minutes,[31] however no in-line analysis can be made with such device. Other groups have developed an *ad hoc* system to rapidly set the oxygen partial pressure in the cell culture and study particular cellular responses under hypoxic conditions.[32,33]

The complexity of the devices previously described induces to find out a structurally simpler microfluidic platform able to perform and control fast oxygen

concentration dynamics and that could be coupled with any other miniaturized bioreactor or culture chamber. Unlike other works, we are aimed to engineer a new oxygen micro-exchanger to carry out on line analysis on the cell culture, for example using confocal microscopy, during an oxygen shift in the culture medium, and acquire particular cellular responses without any perturbation of the detection system.

A.4 Experimental methods

A.4.1 Experimental set up

Our investigation on calcium transient requires a fine tuning of oxygen partial pressure inside a microfluidic cell culture chamber by a multilayer microfluidic gas-exchanger. The device has to ensure a fast and accurate oxygen concentration control inside the culture chamber in order to provide a precise and repeatable hypoxic stimulus to the cell culture. Hypoxic stimuli on a cardiomyocyte population are generated by setting only the oxygen partial pressure in the gas phase without perturbing flowing medium. Cellular calcium dynamics were analyzed directly on line by a fluorescence confocal microscope. An external system for control and data acquisition allowed to precisely set gas phase partial pressures and flow rates, while an uniform medium flow rate was maintained during all the experiments (Fig.1).

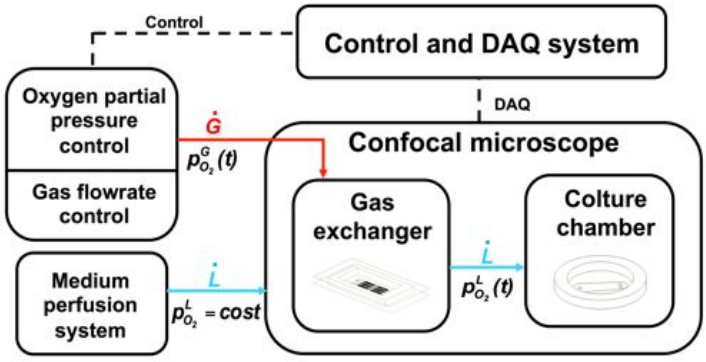

Figure 1. **Schematic view of experimental set up**. Fast and accurate control of oxygen partial pressure inside a microfluidic cell culture chamber is performed by a multilayer microfluidic gas-exchanger. Hypoxic stimuli on a cardiomyocytes population are generated by setting gas oxygen partial pressure and cells' calcium dynamics are analyzed in line by a confocal microscopy. An external system for control and data acquisition ensures fine tuning of gas phase partial pressure and flow rate, whereas a stable medium flow rate is maintained during experiments.

A.4.2 Microfluidic gas exchanger fabrication

Fig. 2A shows a schematic view of the multilayer microfluidic gas exchanger. The oxygen exchange process between the gas and liquid compartments takes place through a thin, non-porous, permeable membrane. Microfluidic gas exchanger consists in a three-layer structure: a fluidic layer containing cell culture medium, a gas chamber for gas flow with defined oxygen partial pressure and an oxygen permeable membrane. The fluidic layer is formed by a network of microfluidic channels in an oxygen non-permeable glass substrate to achieve complete gas sealing. The micrometric thickness of the gas permeable membrane ensures low oxygen diffusion resistance. The gas domain is a milliliter rectangular chamber that allows high gas flow rate and, consequently, almost uniform oxygen partial pressure within the gas chamber.

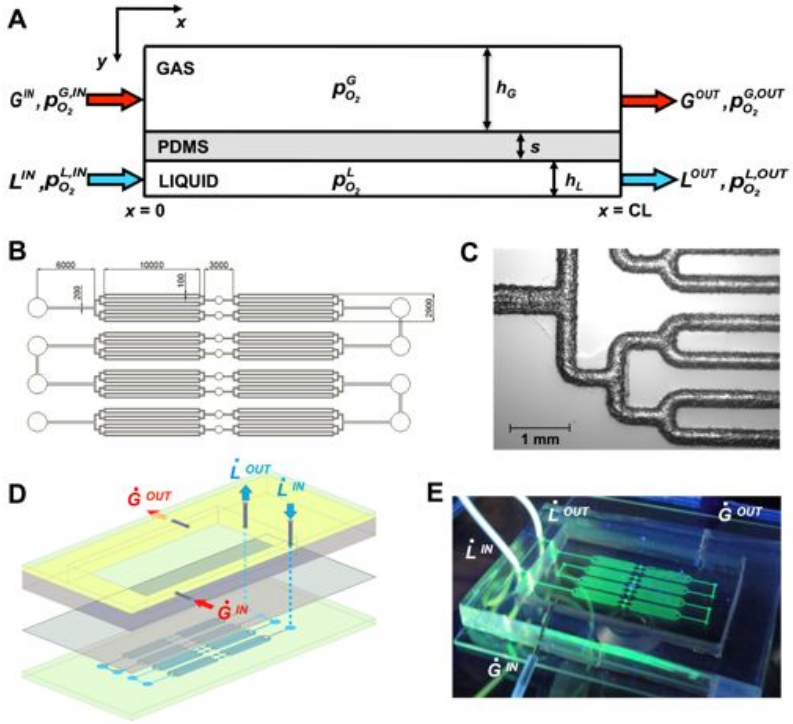

Figure 2. **Microfluidic gas exchanger**. (A) Schematic representation of the three-layered microfluidic system; inlet/outlet flow rates and oxygen partial pressure are shown for both gas, G, and liquid, L, phase. (B) Top view of the fluidic layer channel network (all dimensional values are in µm). (C) Image of glass-etched microfluidic channels network obtained by wet-etching technique and observed under inverted optical microscope. (D) Schematic view of the three different layer of the gas exchanger. Red and blue arrows show gas and liquid phase inlet and outlet inside the platform. (E) Image of the gas-exchanger with inlet/outlet connections for liquid and gas phase perfusion. The microfluidic channels are perfused with 1 mM fluorescein solution.

In the fluidic layer, the flow channels network is characterized by a series of gas exchanger unit and each unit is formed by 8 parallel microchannels 100 µm wide (Fig. 2B). This modular design allows to add series of units, up to obtain the total

length required for a given exchange efficiency. The imprinting of microchannels in the glass slide was achieved by wet-etching technique. A borosilicate glass slide 50 × 75 mm was cleaned using MICRO90 Cleaning Solution (Sigma-Aldrich, USA), placed in an oven for 1 h at 403 K, cooled at 303 K and silanized with hexamethyldisilazane, HDMS, (Sigma-Aldrich, USA) for 3 minutes at 403 K. The glass slide was spin-coated with 5 g of SPR220-7.0 positive photoresist (Rohm&Haas, Dow, USA), to obtain an homogeneous film with a thickness of 15 μm and subsequently photolithografically patterned using standard procedures.[34] The glass slide was immersed in an aqueous 40% fluoridric acid solution (HF, Sigma-Aldrich, USA) at 298 K and only exposed areas were etched. After patterning, the slide was washed with distilled water, deep into an aqueous 98% sulfuric acid solution (H_2SO_4, Sigma-Aldrich, USA) to remove etching-reaction byproducts and rinsed with distilled water. The protective photoresist layer was removed with 1-methyl-2-pyrrolidone (Sigma-Aldrich, USA) and the patterned glass slide was cleaned in piranha solution (H_2SO_4:H_2O_2, 3:1). Fig. 2C shows an image of the etched microchannels on glass under an inverted microscope (Leica, Germany).

Channels section shape and depth were analyzed with a profilometer (Alpha Step IQ surface profiler, KLA Tencor, USA). Rounded cross-section shape was observed, while channels depth resulted etching-time dependent; depths of 40, 70 and 100 μm were obtained with an immersion time in HF solution of 2.5, 5 and 7.5 min, respectively.

A thin polydimethylsiloxane, PDMS, permeable membrane with defined and homogenous thickness was obtained by spinning the unpolimerized solution on a silicon wafer. A premixed 10:1 ratio of PDMS prepolymer and curing agent (Sylgard 184 kit, Dow Corning, USA) was spin-coated on a previously silanized 5 in Si wafer at 1400 rpm for 1 min to obtain a thickness of 40 ± 5 μm and cured on a hotplate at 353 K for 1 h.

The gas layer consists in a 5 cm^3 PDMS chamber in which gas phase flows at defined flow rate and p_{O2}. Residence time is only of few seconds to maintain an uniform oxygen partial pressure during steady-state experiments.

PDMS layers were punched with a 22G stainless steel needle (Small Parts Inc, USA) to obtain gas and liquid inlet/outlet holes. A 50 × 75 mm glass cover slide, gas chamber, PDMS membrane and fluidic layer were assembled and sealed by

plasma bonding (Plasma Cleaner, Harrick Plasma, USA). All fluidic connections to the microfluidic device were made using PTFE microtubing (Cole Parmer, USA). Fig. 2D shows a schematic view of the assembled layers. The red arrows indicate gas inlet/outlet, whereas blue lines show the liquid track inside the platform.

Different liquid flow rates through the fluidic microchannels were obtained by a syringe pump (Harvard Pump, Harvard Apparatus, USA). A constant gas flow rate and oxygen composition were maintained in the gas chamber using air and nitrogen mass flow meters (Bronkhorst, The Netherlands), controlled through software FlowDDE32.

A.4.3 Oxygen measurement

A 100 μM solution of tris(4,7-diphenyl-1,10-phenanthroline)-ruthenium(II)-dichloride, Ru(ddp), (Sigma-Aldrich, USA) in a 30% ethanol in PBS 1X (Invitrogen, USA) solution was used to measure oxygen partial pressure inside the microfluidic channels. Fluorescence of Ru(ddp) was detected by an inverted fluorescence microscope LeicaDMI6000B equipped with a mercury short-arc reflector lamp (Leica, Germany) excited at BP 450-490 nm and acquired at LP 590 (Fig. 2E).

Oxygen partial pressure was also continuously monitored with a fiber optic oxygen sensor (OceanOptics, USA) at the microchannel outlet. Fluorescence intensity is linearly correlated to the oxygen partial pressure in the sample. Both sensors are based on fluorescence quenching that increases with the oxygen partial pressure. The degree of quenching can be correlated to the oxygen partial pressure of the sample by Stern-Volmer equation:

$$\frac{I_0}{I} = 1 + kp_{O_2} \tag{1}$$

where I_0 is the fluorescence intensity at zero partial pressure of oxygen, I is the fluorescence intensity at a particular p_{O_2} and k is the Stern-Volmer constant which depends on the chemical composition of the sensor and on the temperature. Calibration of the sensor at 298 K was achieved using five liquid standards, obtained by bubbling a gas mixture with a partial pressure of 0%, 5%, 10%, 15% and 21%. Complete oxygen removal was achieved with 8 hours of humidified

argon bubbling (Rivoira, Italy). Stern-Volmer constant value was obtained by correlating experimental data.

A.4.4 Microfluidic cell culture chamber

Microfluidic cell culture chamber was made by standard soft-litography technique.[34] Briefly, design shown in Fig. 3A was produced by CAD program and patterned in a silicon substrate using negative photoresist SU8-2100 (Microchem, Germany). After silanization with HDMS under vacuum for 1 h, 10:1 ratio of PDMS prepolymer and curing agent was casted and cured for 2 h at 343 K in an oven. Through a 27 mm punch, PDMS mold was extracted. In order to ensure an electrical stimulation to the cell culture, a platinum wire was inserted in the PDMS mold and wired to an electrical stimulator. The glass slide hosting the cell culture was located in a standard microscopy aluminum holder (20 mm diameter hole), covered by the PDMS mold and pressure sealed by a teflon cover (Fig. 3B).

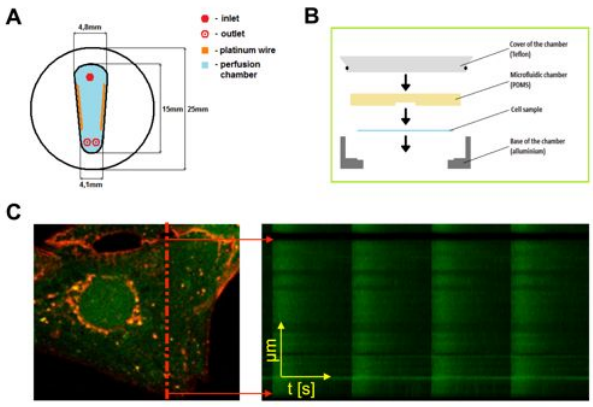

Figure 3. **Cell culture chamber and calcium dynamic acquisition.** (A) Microfluidic cell culture chamber top view. The chamber is characterized by 1 inlet and 2 outlets and by 2 platinum wires placed in the lateral walls to electrically stimulate cells. (B) Assembly of the microfluidic chamber within microscope holder to perform on line detection. (C) Confocal image and calcium dynamic of a cardiomyocyte under electrical stimulation. Line scan (yellow line) is placed between nucleus and sarcolemma of the cell and calcium transient are continuously detected as a function of time.

The perfusion culture chamber was connected to the microfluidic exchanger through silica tubings in order to avoid external oxygen infiltrations. All the experiments were performed with a 100 µl min^{-1} flow rate using syringe pumps (Harvard Pump, Harvard Apparatus, USA) allowing fast exchange of medium without any apparent change in cellular calcium dynamics.

A.4.5 Cardiomyocytes isolation and culture

Neonatal rat cardiomyocytes were obtained from Sprague-Dawley pups 1-3 days old. The cells were plated on 20 μg/ml laminin-coated (BD Bioscience, USA) glass coverslips in Day1 medium: 25 mM Hepes Dulbecco's Modified Eagle's Medium (Gibco, USA), 17% Medium M199 (Gibco, USA) 10% Horse Serum (Gibco, USA), 5% Newborn Calf Serum (Gibco, USA), 2 mM L-Glutammine (Gibco, USA), Penicillin-Streptomycin (EuroClone, Italy). After 24 hours, the Day1 medium was replaced with Day2 medium: Day1 medium with 5% Horse Serum and 0.5% Newborn Calf Serum. Experiments were performed 4 days after plating. The animals were housed and operated at the Animal Colony of the Venetian Institute of Molecular Institute. All experiments with animals were approved by Padova University's Institutional Animal Care Committee (Comitato Etico di Ateneo per la Sperimentazione Animale).

A.4.6 Calcium dynamic acquisition and analysis

Confocal Calcium measurements were performed as reported in Fig. 3C. Cardiomyocytes were loaded in serum-free D-MEM (Gibco, USA) supplemented with 3 μM fluorescent calcium dye fluo-4 AM (Invitrogen, USA) for 20 minutes at 310 K in presence of 2 μM Pluronic F-127 (Invitrogen, USA) and 20 μM sulfinpyrazone (Sigma-Aldrich, USA), then incubated for additional 10 minutes at 310 K in Fluo-4-free D-MEM to allow complete de-esterification of the dye, and added with 0.2 μM di-8-ANEPPS (Invitrogen, USA). After loading, the coverslips were transferred to the microfluidic chamber and perfused with recording solution: NaCl 125 mM, KCl 5 mM, Na_3PO_4 1 mM, $MgSO_4$ 1 mM, Hepes 20 mM, $CaCl_2$ 2 mM, Glucose 5.5 mM, to pH 7.4 with NaOH. Line scan was acquired with Leica TCS SP5 confocal microscope equipped with a 63×, 1.4 NA oil immersion objective, with 488 nm Ar laser line as excitation source, 700 Hz acquisition frequency. To reduce dye photo-bleaching and photo-toxic effects on the analyzed cells, the laser power was set at minimum possible. During all the experiments, the culture was constantly filed-stimulated with electrical pulses at 0.7 Hz, 20 V cm^{-1}, to overcome spontaneous beating activity allowing acquisition at the same beating rate in all cells. Nifedipine and Verapamil (Sigma-Aldrich, USA) were dissolved in DMSO (Sigma-Aldrich, USA) or deionized H_2O, respectively, at a 10 mM starting concentration and diluted to the desired

concentration in recording solution immediately prior to the experiments. All data analysis were performed with ImageJ and Origin7 software.

Data are presented as means of percentage decrease normalized on the reference conditions ± standard error of mean (SEM). The effects of different oxygen concentrations on calcium transients were compared by a one way ANOVA followed by Bonferroni's mean comparison. We considered $P < 0.01$ to be statistically significant.

A.4.7 Mathematical modeling

The oxygen concentration profile, and consequently the oxygen partial pressure, within the liquid phase domain of the microfluidic gas exchanger was described by simplified analytical model and by computational solution of the species mass balance. The simplified model was validated with computational analysis and used for a proper gas exchanger design.

Mass transfer was assumed to be governed by convective transport in the gas phase, diffusive resistance in the permeable membrane and convective-diffuse regime in the liquid phase. The concentration in the gas phase was assumed constant along spatial coordinates because, according to the high gas flow rate, the permanence time in the gas chamber is much smaller than the characteristic time of the membrane oxygen exchange process.

On the other hand, the oxygen concentration in the liquid phase changes from the inlet ($x = 0$) to the outlet ($x = CL$) of the microfluidic gas exchanger. For this reason, in order to describe oxygen concentration profile along y-coordinate (height of the microfluidic channel), both hydrodynamic and mass transport models should be solved simultaneously. Due to the low Reynolds numbers (1÷10) an analytical solution of fully developed hydrodynamic profile between flat planes was assumed.[35] Considering that Péclet number (convection/diffusion ratio) is much greater than 1 for all experimental conditions tested in this work, we assumed that diffusive flux is relevant only in the y-direction, whereas convective flux occurs in the x-direction. Moreover, we define h_L as the equivalent channel height, which is obtained as the area of the cross-section divided by the width of the channel.

Under these assumptions and considering all mass transfer resistances localized at the interfaces, the steady-state mass balance equation in the liquid domain takes the following form:

$$\begin{cases} \dfrac{u}{H}\dfrac{\partial p_{O_2}^{L}(x)}{\partial x} + N_{O_2,y}(x, y = h_L) = 0 \\ p_{O_2}^{L}(x = 0) = p_{O_2}^{L,IN} \end{cases} \tag{2}$$

where $p_{O_2}^{L}$ is the oxygen partial pressure of the liquid phase, u is the axial velocity, H is the Henry's constant of oxygen solubility in water at experimental temperature condition, $N_{O_2,y}(x, y = h_L)$ is the total oxygen flux at liquid-membrane interface along x-coordinate and $p_{O_2}^{L,IN}$ is the boundary condition at channel inlet. The total oxygen flux at liquid-membrane interface, $N_{O_2,y}(x, y = h_L)$, can be expressed as the product of the overall mass transfer resistance and the total driving force:

$$N_{O_2,y}(x, y = h_L) = < K_G > (p_{O_2}^{L}(x) - p_{O_2}^{G})a \tag{3}$$

$p_{O_2}^{G}$ is the constant oxygen partial pressure in gas phase, a is specific surface, which corresponds to the inverse of the equivalent channel height h_L, whereas $< K_G >$ is the averaged overall mass transfer coefficient. The analytical expression of $< K_G >$ is derived by equating oxygen fluxes for the three different domains and its general form can be expressed as follows:

$$\frac{1}{< K_G >} = \frac{1}{k_G} + \frac{s}{p} + \frac{H}{k_L}. \tag{4}$$

k_G and k_L are the mass transfer coefficients in the gas and liquid phase respectively, p the oxygen permeability in PDMS and s the membrane thickness.

Integration of equation (2) from the inlet to the outlet of the channel leads to the following relation:

$$\frac{p_{O_2}^{L,OUT} - p_{O_2}^{G}}{p_{O_2}^{L,IN} - p_{O_2}^{G}} = \exp\left(-\frac{< K_G > HL}{h_L u}\right) \tag{5}$$

Equation (5) relates the oxygen partial pressure in the microchannel to the length and geometry of the channel, operative conditions and mass transfer properties. This relation is used to calculate the minimal channel length necessary to ensure a defined oxygen concentration at the outlet of the system.

The solution of equation (5) requires a proper estimation of the mean overall mass transfer coefficient by equation (4). Due to the high oxygen diffusivity in the gas phase compared to those in the liquid and solid phase, the first resistance term in equation (4) results negligible.

The mass transfer coefficient in the liquid phase, k_L, can be evaluated from empirical correlations for laminar flow which relate together dimensionless groups (Péclet, Reynolds and Sherwood numbers). In the developing diffusive concentration profile and for boundary layers which are extremely thin relative to the channel width, the following relation has been proposed:[36]

$$\begin{cases} \dfrac{k_L h_L}{D} = 1.233\left(\dfrac{xD}{uh_L^2}\right)^{-1/3}, \dfrac{xD}{uh_L^2} \le c_1 \\ \dfrac{k_L h_L}{D} = c_2, \dfrac{xD}{uh_L^2} > c_1 \end{cases} \tag{6}$$

where D is the oxygen diffusion coefficient in the liquid phase. c_1 and c_2 are constant values that can be evaluated by computationally solving oxygen mass balance equations for the system shows in Fig. 2A.

The numerical solution of the convective-diffusion equation for the fluidic domain and the diffusive equation for the solid domain were obtained with the support of the software COMSOL Multiphysics 3.4 at different operative conditions. Boundary and initial conditions were set as follows: the top of the membrane domain is taken to be at a constant concentration in equilibrium with the adjacent gas phase, whereas oxygen concentration at the bottom surface is equilibrated with that in the fluidic domain. In the inlet section of the fluidic domain it was set a constant concentration, whereas at the outlet section it was considered only a convective flux. The remaining walls were assumed to be impermeable to oxygen. All values for the parameters used for the simulations are listed in Table 1.

Table 1. **Summary of physical properties.**

Property	**U.M.**	**Value**	**Ref.**
D, oxygen diffusion in PBS	$m^2\ s^{-1}$	2.1×10^{-9}	37
p, oxygen permeability in PDMS	$(10^{-10}\ cm^3(STP) \times cm/cm^2 \times s \times cmHg)$	800	38
O_2 solubility in PBS at 1 atm and 298K	$mol\ m^{-3}$	1.045	39

A.5 Results and discussion

A.5.1 Microfluidic platform validation

Fig. 4A shows the oxygen concentration distribution in the microfluidic channel obtained by computational simulation of oxygen mass balance equations. Boundary conditions were set as follows: inlet oxygen partial pressure, $p_{O_2}^{L,IN}$, was set to 21%, whereas oxygen partial pressure in the gas phase, $p_{O_2}^{G}$, is assumed to be constant at 0%. Oxygen flux through the PDMS membrane is directed from the liquid phase to the gas compartment according to the oxygen partial pressure gradient. Oxygen flux at the membrane interface decreases along the *x*-coordinate due to the progressive reduction of the gradient for 1 mm channel length as shown in Fig. 4B.

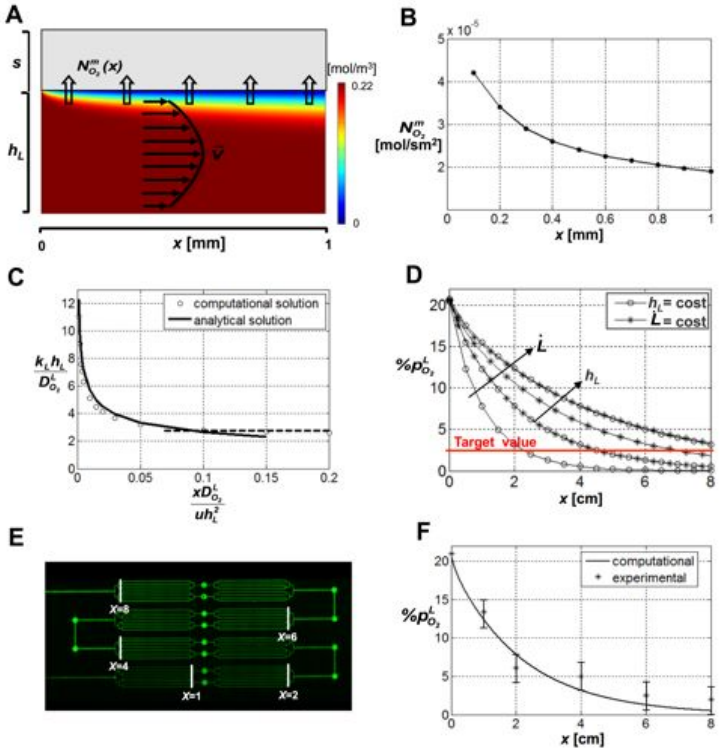

Figure 4. **Mass transport model development and validation**. (A) 2D representation of oxygen concentration obtained by computational solution of mass balance equations in the microfluidic channel longitudinal cross-section. Empty arrows show oxygen flux directed from liquid phase to the gas one, in which oxygen partial pressure is assumed to be 0%. Full arrows show *y*-direction velocity profile. (B) Profile of the oxygen flux normal to the PDMS membrane interface along *x*-coordinate. (C) Comparison of computational and analytical solution in term of adimensional numbers according to Eq. 6. (D) Oxygen partial pressure profile obtained from analytical solution given by Eq. 5 as a function of *x*-coordinate, parametric in liquid flow rate, $\dot{L}$, and channel height, h_L. Red line shows design target value of 2%. (E) Fluorescence imaging of fluidic layer filled with Ru(ddp) solution, using $\dot{L}$=100 µl/min and h_L=40 µm. White mark shows the region of interest for fluorescence quantification reported in Fig. 4F (values of *x*-coordinate are in cm). (F) Comparison of $p^L_{O_2}$ experimental profile inside the fluidic layer and the analytical solution obtained by Eq. 5.

In order to properly design the gas exchanger, the application of computational simulation to a larger portion or overall microfluidic channel could be time consuming and computational intensive. For this reason a simplified analytical theory to fairly describe mass transport inside the microfluidic device was derived. The mass balance analytical expression (Eq. 5) can describe oxygen profile inside the channel as a function of all operative parameters that affect mass transfer process and of the mean overall mass transfer coefficient ($<K_G>$) and, in particular, liquid mass transfer coefficient (k_L). In this work, we adopt the model proposed by Vollmer and coworkers [36] to our system using computational results to estimate model parameters. We found out that c_1 and c_2 constant values of Eq 6 are 0.10 and 2.62 respectively. Fig. 4C shows a comparison between computational simulation and modified analytical model (Eq. 6) in terms of adimensional numbers. This analytical model allows to fairly estimate the liquid mass transfer coefficient for several experimental conditions, in particular for different liquid flow rates $(\dot{L})$ and channel heights (h_L).

On the other hand, the minimal channel length for achieving a target $p_{O_2}^L$ reduction using specific liquid flow rate and channel height can be easily estimated by Eq. 5. Fig. 4D shows $p_{O_2}^L$ profiles as a function of *x*-coordinate, obtained by varying both $\dot{L}$ and h_L.

In order to experimentally validate the developed theory we mapped fluorescence intensity of the oxygen sensitive dye in the overall fluidic layer of the oxygen exchanger (Fig. 4E). Fig. 4E shows a fluorescence intensity increase along *x*-coordinate from the inlet to the outlet according to $p_{O_2}^L$. Fig. 4F shows a comparison of experimental $p_{O_2}^L$ measured at different *x*-coordinate values (reported in Fig. 4E) and analytical solution obtained from Eq. 4. Very good agreement between profiles within the experimental uncertainty has been observed. Finally, using the simplified analytical theory, we designed a gas exchanger that is able to perform a $p_{O_2}^L$ reduction of 95% with a steady state flow rate of 100 µl min^{-1}. The gas exchanger configuration consists in 8 exchanger units in series formed by 8 parallel channels with 80 mm total length, 40 µm height and 100 µm width.

A.5.2 Calcium dynamics in hypoxia

The microfluidic cell culture chamber and gas exchanger must preserve cardiomyocytes physiological characteristics while providing fast transient biochemical stimulation. The cell culture chamber was properly designed to obtain a uniform laminar flow avoiding unpaired velocity profile, back flow and stagnant dead volumes. This ideal condition was experimentally verified by observing the dynamic of a pulse of fluorescein in the cell culture chamber at different flow rates (data not shown). In addition, before each experiment, the culture was maintained in perfusion for 1 hour in normoxic solution while recording calcium dynamics. The cardiomyocytes displayed normal calcium dynamics during electrical stimulation. In order to test the time course of substance delivery to the microfluidic chamber, we injected a 50 µl bolus of 10 mM caffeine solution in the perfusion line. The caffeine stimulated Ca^{2+} release from sarcoplasmic reticulum (SR) had a rapid onset and resulted in the change in fluorescence intensity. Such effect lasted 45 s, after which the calcium transients amplitude returned to normal indicating complete caffeine wash out (Fig. 5A). This time is consistent with the estimated permanence time of caffeine within the microfluidic chamber, as evaluated through fluorescence dye experiments.

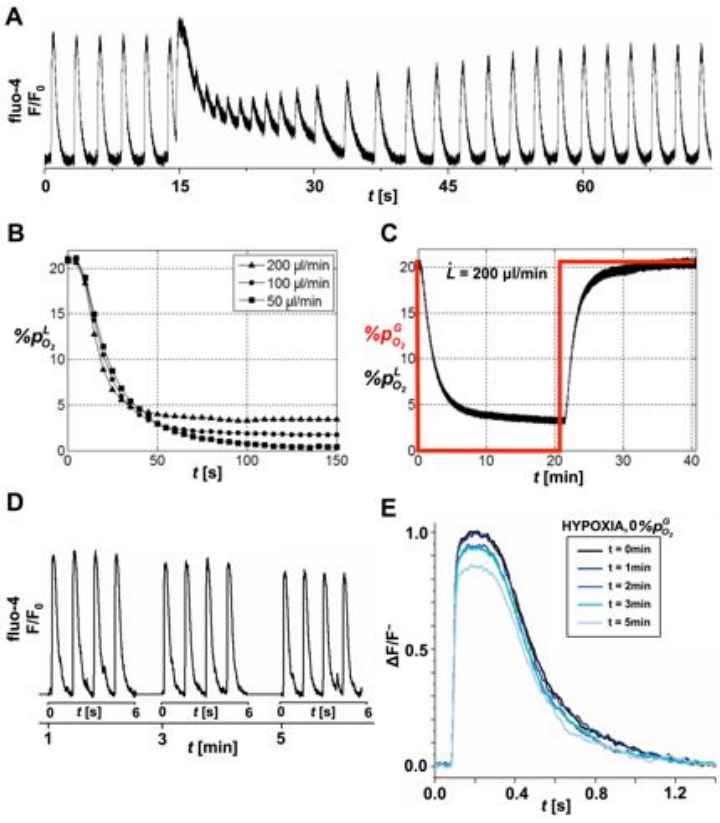

Figure 5. **Effect of hypoxia on calcium transients**. (A) Calcium dynamic in a cardiomyocyte under electrical stimulation revealed through fluo-4 in the microfluidic culture chamber during perfusion of 50 µl of 10 mM caffeine solution; cardiomyocyte displays normal Ca^{2+} transients and response to caffeine with full recovery after wash out. (B,C) Liquid phase oxygen dynamic during step impulse of the oxygen partial pressure in the gas phase monitored by Ru(ddp) with three different flowrates (B) and by optic fiber sensor with $\dot{L}$ = 200 µl min^{-1} (C) at exchanger outlet. (D) Calcium transients sequence at different time points after hypoxic stimulus to the cell culture. (E) Comparison of single normalized calcium transients at different time points after hypoxic stimulus.

In order to analyze the early effect of hypoxic events on cardiac physiology it is fundamental to fully characterize the oxygen partial pressure dynamics after set point variations. For this reasons, oxygen partial pressure at the outlet of the gas exchanger were measured by continuously detecting intensity fluorescence of oxygen sensitive dye during a $p_{O_2}^G$ set point change from 21% to 0% at three different flow rates: 50, 100 and 200 µl min^{-1} (Fig. 5B). The $p_{O_2}^L$ half decay value of 10 s for all different flow rates ensures fast oxygen dynamics. Different hypoxic steady state levels ($p_{O_2}^L$ < 5%) can be achieved by varying medium flow rate (Fig. 5B). In order to exclude gas leakage between the gas exchanger and the culture chamber, oxygen partial pressure values, $p_{O_2}^L$, were continuously monitored at cell culture chamber inlet by fiber optic probe. Fig. 5C shows $p_{O_2}^L$ steady state values (black line) reached after two $p_{O_2}^G$ set point variations (red line): 21% to 0% and 0% to 21%. Consistent measurements reported in Fig. 5B-C confirms an efficient gas insulation.

All together, these results show that the microfluidic experimental set up (as reported in Fig. 1) is able to accurately control oxygen partial pressure on cell culture in terms of steady state levels and rapid set point variations. It is worth to underline that oxygen partial pressure control is achieved without any perturbations on liquid media, allowing long term confocal acquisitions on same region of interest. These technical improvements make possible to perform experimental investigations using the same cell as its own control, continuously acquiring biological data prior and during the hypoxic stimulation.

In order to rationally study the hypoxia-induced effects on calcium handling during excitation-contraction coupling it is important to investigate the duration of hypoxic stimulation that could exert a cell physiological response.

In this context, Fig. 5D shows a sequence of calcium dynamics in response to fast $p_{O_2}^L$ drop as a function of time. A comparison of normalized calcium transient peaks at different time points (Fig. 5E) shows a significant alteration of the fluorescence intensity peak maximum after 5 min from hypoxic stimulus. All other experiments were performed considering this time frame as a minimal value to elicit a hypoxia-induced physiological response.

We then sought to determine the hypoxic level at which hypoxia-induced effects on calcium handling during excitation-contraction coupling can be recorded. A multiple step experiment was designed by setting $p_{O_2}^G$ at 5 different values from 21% to 0% with 5% interval and the resulting $p_{O_2}^L$ step profile is shown in Fig. 6A. Corresponding values of $p_{O_2}^L$ and $p_{O_2}^G$ were correlated to obtain operating curve shown in Fig. 6A insert. Interestingly, the operating curve differs slightly from the equilibrium curve within the accuracy used in the gas exchanger design ($p_{O_2}^L$ = 2% as target value (Fig. 4D), corresponding to 95% reduction from normoxic conditions).

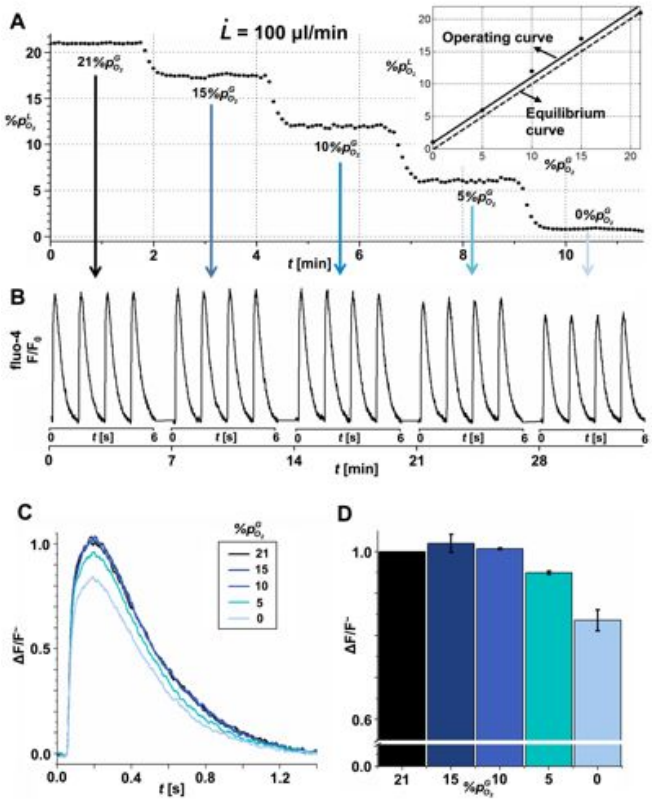

Figure 6. **Oxygen level threshold.** (A) $p_{O_2}^L$ profile for five different $p_{O_2}^G$ with $\dot{L}$=100 µl min^{-1}. Insert shows equilibrium and operating curve obtained by calibration. (B) Calcium transients

sequence at different $p_{O_2}^L$ measured 7 minutes after $p_{O_2}^G$ set-point change. Blue arrows show correspondence between $p_{O_2}^G$ set-point and calcium transient sequence (Fig. 5A). (C) Comparison of single normalized calcium transients at different oxygen partial pressure. (D) Averaged values of normalized calcium transients peak height at different oxygen partial pressure. The histogram is based on 5 replicates of same conditions.

Fig. 6B shows the corresponding sequence of calcium transients acquired for 6 s at different $p_{O_2}^L$ levels measured 7 minutes after the $p_{O_2}^G$ set-point change. Blue arrows show correspondence between $p_{O_2}^G$ set-point values and calcium transients. The baseline fluorescence maintained the same intensity for all the duration of the experiment and the effect of hypoxic stimulation emerged with a decrease of the maximum of the normalized calcium transient peak (Fig. 6C). The analyzed cells did not display calcium cycling alterations for $p_{O_2}^G$ > 5% (n=5). At 5% a poor significant difference ($P<0.05$, n=5) decrease was observed, whereas at $p_{O_2}^G$ = 0% the alteration of calcium transient was observed with high statistical relevance ($P<0.01$, n=5) (Fig. 6D). These data show that the observed effect reveals itself only in highly hypoxic nearly anoxic conditions, remaining latent at higher oxygen concentrations.

To test the reversibility of the hypoxia induced Ca^{2+} changes and, concurrently, exclude artifact deriving form long term confocal acquisition such as dye photo-bleaching, the cardiomyocyte culture was subjected to a fast drop of $p_{O_2}^L$ and maintained in hypoxic conditions for 10 min followed by 10 min of reperfusion with normoxic medium (Fig. 7A).

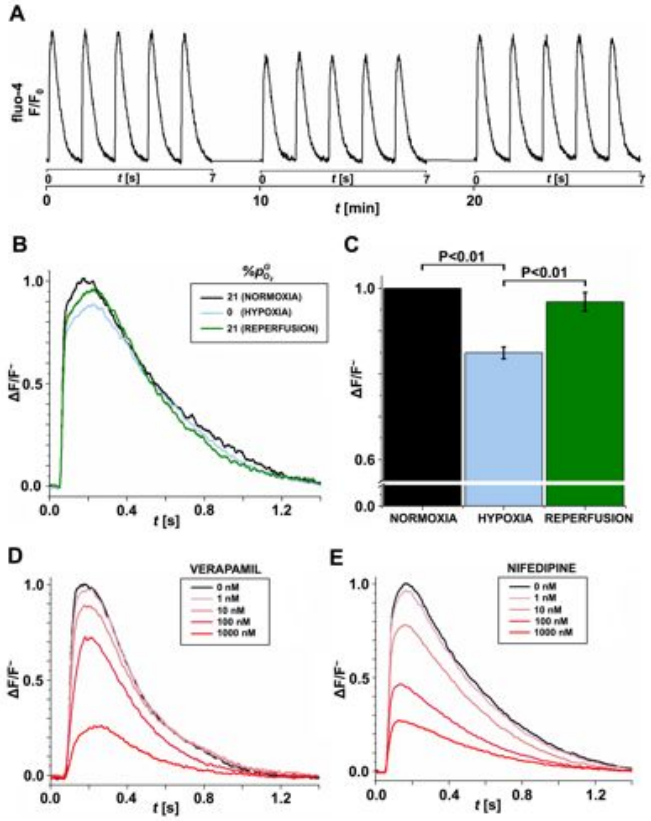

Figure 7. **Reversible effect of hypoxia on calcium cycling.** (A) Calcium transients sequence measured in normoxic, hypoxic ($p_{O_2}^G$ = 0%) and normoxic conditions. (B) Comparison of single normalized calcium transients in normoxic, hypoxic ($p_{O_2}^G$ = 0%) and normoxic condition. (C) Averaged values of normalized calcium transients peak height in normoxic, hypoxic ($p_{O_2}^G$ = 0%) and normoxic condition. The histogram is based on 5 replicates of same conditions. (D,E) Normalized calcium transients for different concentrations of L-type Ca^{2+} channel antagonist Verapamil (D) and Nifedipine (E).

Whole-cell calcium dynamics were acquired every 10 min. In response to hypoxic stress we observed a decrease of the maximum calcium transient peak (Fig. 7B) with no alteration of the baseline fluorescence (n=8). After recovering the normoxic conditions, the cardiomyocytes displayed again the same fluorescence intensity, indicating a recovery of calcium cycling towards basal conditions. By analyzing the variation of fluo-4 fluorescence after 10 minutes of hypoxia and subsequent 10 minutes of reperfusion by means of percentage decrease against normoxic fluorescence intensity, a statistically relevant decrease (~15%, P<0.01) emerged (Fig. 7C). The recovery of normal calcium transients after the return to normoxic conditions highlights the reversibility of the biological effect and excludes the responsibility of dye photo-bleaching from the observed decrease of fluorescence.

All together, these results show that there is a significant reversible alteration of calcium homeostasis in excitation-contraction coupling during fast hypoxic stimuli. This experimental evidence underlines the ability of the cell to sense oxygen level and rapidly adapt to normoxic/hypoxic/normoxic transitions by regulating either directly or through secondary pathways the molecular machinery involved in cardiac Ca^{2+} homeostasis.[3] In addition to direct channel sensing or specifically target protein modification (such as phosphorylation and cysteine reduction), hypoxia may also alter the regulation of these channels via indirect bulk mechanisms, such as changes in cell redox state by action of ROS.[3] However, all these hypoxia-induced phenomena affect membrane depolarization and concurrently alter of L-type voltage-gated calcium channels (VGCC) function, which provide the main entry pathway for extracellular Ca^{2+} into cardiomyocytes and are a major component of excitation-contraction coupling machinery. L–type VGCCs trigger the calcium-induced calcium release (CICR) process through extracellular calcium influx; calcium entry through VGCCs, which are topologically associated to calcium-release channels (ryanodine receptors) in the sarcoplasmic reticulum (SR) membrane, cause further calcium SR release within cytosol compartment. These secondary calcium dynamics can be easily measured as reported in this study.

In this context, the alterations in excitation-contraction coupling under hypoxia could be related to impaired CICR for hypoxia-dependent desensitization of L-type VGCCs.

In order to explore this hypothesis, experimental investigation of calcium transients upon inhibition of the L-type Ca^{2+} channel with two antagonists was performed. Fig. 7D and 7E show normalized calcium transient at different concentrations of channel blocker ranging from 1 nm to 1000 nM in normoxic conditions. Similar calcium peak reductions recorded for hypoxia below 5% $p_{O_2}^{L}$ were observed with 100nM of Verapamil and 10 nM of Nifedipine Fig. 7D and Fig. 7E, respectively.

These findings confirm that a hypoxia-induced alteration of primary calcium entry through L-type VGCCs could turn in a reduced calcium concentration during excitation-contraction coupling and consequently, in an alteration of the physiological activity of cardiomyocytes.

Our results suggest that a cardioprotective mechanism during early phases of

acute ischemia takes place through the reduction of calcium homeostasis in excitation-contraction coupling.

A reversible adaptation of myocardium after short ischemic stress (5 min and 15 min ischemia/reperfusion) *in vivo* was first observed by Heyndrickx and co-workers.[40] They demonstrated that a fully reversible dysfunction of the ischemic heart is prolonged after hypoxic stress, named "myocardial stunning". The molecular basis behind this physiological behavior is still unclear. Myocardial stunning results from different adaptive mechanisms such as down-regulation of myocardial metabolism, and leads to activation of long-term cardioprotective responses including activation of cell survival pathways resulting in changes in gene and protein expression.[41]

In this context, we first show that a fully reversible adaptive mechanisms of cardiopreservation might take place during the early events of ischemic stress through fast alteration in ion channel function in response to changes in cellular oxygen.

A.6 Conclusions

A microfluidic gas exchanger was designed to accurately and very quickly regulate $p_{O_2}^L$ without perturbing medium flux and consequently on line acquisition. By developing an *ad hoc* mass transfer theory, supported by computational simulations, we were able to predict $p_{O_2}^L$ inside cell culture chamber as a function of operative parameters (liquid flow rate). Experimental validation of $p_{O_2}^L$ profile inside the gas-exchanger microchannels confirmed that both constructive method and analytical model were valid.

With the support of the developed technological system we observed a significant calcium handling alteration in a neonatal rat cardiomyocyte population after an exposure to 5 min of hypoxic conditions. Thanks to accuracy in tuning oxygen level in our system we found a threshold value of 5% $p_{O_2}^L$, above which no significant calcium transients peak decreases were observed.

The recovery of normal calcium transients after the return to normoxic conditions highlights the reversibility of the biological effect and excludes the responsibility of sample damaging phenomena like dye photo-bleaching from the observed decrease of fluorescence.

We also explored the hypothesis that calcium-handling alteration in hypoxia could be affected by the desensitization of voltage gated calcium channels. In order to support our hypothesis we compared calcium transients peak obtained during a hypoxic stimulus and those obtained under effect of L-type calcium antagonist, Verapamil and Nifedipine.

Rational understanding of how the cardiomyocyte adapts to acute ischemic stress and sustains its survival represents an important challenge because it might help in finding novel strategies to enhance cardiomyocytes survival in patients.

A.7 References

1. S. Allender, C. Foster, L. Hutchinson and C. Arambepola, J. Urban Health, 2008, 85, 938–951.
2. R. J. Diaz and G. J. Wilson, Cardiovasc. Res., 2006, 70, 286–296.
3. L. A. Shimoda and J. Polak, Am. J. Physiol.: Cell Physiol., 2010, 300, C951–C967.
4. A. L. Russ, K. M. Haberstroh and A. E. Rundell, Exp. Mol. Pathol., 2007, 83, 143–159.
5. D. A. Saint, Br. J. Pharmacol., 2009, 153, 1133–1142.
6. Y. K. Ju, D. A. Saint and P. W. Gage, J. Physiol., 1996, 497, 337–347.
7. W. P. Wang, J. H. Ma, P. H. Zhang and A. T. Luo, Pfluegers Arch., 2007, 454, 461–475.
8. L. C. Hool, J. Physiol., 2004, 554, 743–754.
9. I. M. Fearon, A. C. V. Palmer, A. J. Balmforth, S. G. Ball, G. Mikala, A. Schwartz and C. Peers, J. Physiol. (London), 1997, 500, 551–556.
10. L. C. Hool, Circ. Res., 2000, 87, 1164–1171.
11. N. Gaur, Y. Rudy and L. Hool, Circ. Res., 2009, 105, 1196–1203.
12. I. M. Fearon, G. Varadi, S. Koch, I. Isaacsohn, S. G. Ball and C. Peers, Circ. Res., 2000, 87, 537–539.
13. S. Movafagh and M. Morad, Ann. N. Y. Acad. Sci., 2010, 1188, 153–158.
14. L. C. Hool, C. A. Di Maria, H. M. Viola and P. G. Arthur, Cardiovasc. Res., 2005, 67, 624–635.
15. T. J. Kamp and J. W. Hell, Circ. Res., 2000, 87, 1095–1102.
16. P. Kaplan, E. Babusikova, J. Lehotsky and D. Dobrota, Mol. Cell. Biochem., 2003, 248, 41-47.
17. L. Guerra, E. Cerbai, S. Gessi, P. A. Borea and A. Mugelli, Br. J. Pharmacol., 1996, 118, 1278–1284.
18. J. W. Allen and S. N. Bhatia, Biotechnol. Bioeng., 2002, 82, 253–262.
19. C. B. Allen, B. K. Schneider and C. W. White, Am. J. Physiol.: Lung Cell. Mol. Physiol., 2001, 281, L1021–L1027.
20. D. E. Powers, J. R. Millman, S. Bonner-Weir, M. J. Rappel and C. K. Colton, Biotechnol. Prog., 2010, 26, 805–818.
21. L. Kim, Y. Toh, J. Voldman and H. Yu, Lab Chip, 2007, 7, 681–694.
22. D. J. Beebe, G. A. Mensing and G. M. Walker, Annu. Rev. Biomed. Eng., 2002, 4, 261–286.
23. D. N. Breslauer, P. J. Lee and L. P. Lee, Mol. BioSyst., 2006, 2, 97–112.
24. Z. Y. Zhang, P. Boccazzi, H. G. Choi, G. Perozziello, A. J. Sinskey and K. F. Jensen, Lab Chip, 2006, 6, 906–913.
25. A. Groisman, C. Lobo, H. J. Cho, J. K. Campbell, Y. S. Dufour, A. M. Stevens and A. Levchenko, Nat. Methods, 2005, 2, 685–689.
26. E. Leclerc, Y. Sakay and T. Fujii, Biotechnol. Prog., 2004, 20, 750–755.
27. R. Gomez-Sjoberg, A. A. Leyrat, D. M. Pirone, C. S. Chen and S. R. Quake, Anal. Chem., 2007, 79, 8557–8563.
28. M. Polinkovsky, E. Gutierrez, A. Levchenko and A. Groisman, Lab Chip, 2009, 9, 1073–1084.
29. M. Adler, M. Polinkovsky, E. Gutierrez and A. Groisman, Lab Chip, 2010, 10, 388–391.
30. R. H. W. Lam, M. C. Kim and T. Thorsen, Anal. Chem., 2009, 81, 5918–5924.
31. S. C. Oppegard, K. H. Nam, J. R. Carr, S. C. Skaalure and T. Eddington, PLoS One, 2009, 4, e6891.

32. P. Abbyad, P. L. Tharaux, J. L. Martin, C. N. Baroud and A. Alexandrou, Lab Chip, 2010, 10, 2505–2512.
33. J. E. Baumgardner and C. M. Otto, Respir. Physiol. Neurobiol., 2003, 136, 131–139.
34. E. Figallo, C. Cannizzaro, S. Gerecht, J. A. Burdick, R. Langer, N. Elvassore and G. Vunjak-Novakovic, Lab Chip, 2007, 7, 710–719.
35. R. B. Bird, W. E. Stewart and E. N. Lightfoot, Transport Phenomena, 2nd edn, John Wiley & Sons, 2001.
36. A. P. Vollmer, R. F. Probstein, R. Gilbert and T. Thorsen, Lab Chip, 2005, 5, 1059–1066.
37. H. Shiku, T. Saito, C. C. Wu, T. Yasukawa, M. Yokoo, H. Abe, T. Matsue and H. Yamada, Chem. Lett., 2006, 234–235.
38. T. C. Merkel, V. I. Bondar, K. Nagai, B. D. Freeman and I. Pinnau, J. Polym. Sci., Part B: Polym. Phys., 1999, 38, 415–434.
39. S. A. M. van Stroe-Biezen, A. P. M. Janssen and L. J. J. Janssen, Anal. Chim. Acta, 1993, 280, 217–222.
40. G. R. Heyndrickx, R. W. Millard, R. J. McRitchie, P. R. Maroko and S. F. Vatner, J. Clin. Invest., 1975, 56, 978–985.
41. C. Depre and S. F. Vatner, Heart Failure Rev., 2007, 12, 307–317.

Appendix B

Stochastic model-assisted development of efficient low-dose viral transduction in microfluidics

Camilla Luni[1,2,*], Federica Michielin[1,2,*], Luisa Barzon[3], Vincenza Calabrò[4], Nicola Elvassore[1,2].

1. Department of Industrial Engineering (DII), University of Padova, Via Marzolo 9, 35131 Padova, Italy.
2. Venetian Institute of Molecular Medicine, Via Orus 2, 35129 Padova, Italy.
3. Department of Molecular Medicine, University of Padova, Via Gabelli 63, 35121 Padova, Italy.
4. Department of Engineering Modeling, University of Calabria, Via P. Bucci, 87036 Arcavacata di Rende (CS), Italy.
* These authors equally contributed.

Biophysical Journal
Volume 104(4):934-42
10.1016/j.bpj.2012.12.049

B.1 Abstract

Adenoviruses are commonly used *in vitro* as gene transfer vectors in multiple applications. Nevertheless, issues such as low infection efficiency and toxicity effects on host cells have not been resolved yet. This work aims at developing a new versatile tool to enhance the expression of transduced genes while working at low viral doses in sequential manner.

We developed a microfluidic platform with automatically controlled sequential perfusion stages, which includes 10 independent channels. In addition, we built a stochastic mathematical model, accounting for the discrete nature of cells and viruses, to predict not only the percentage of infected cells, but also the associated infecting-virus distribution in the cell population.

Microfluidic system and mathematical model were coupled to define an efficient experimental strategy. We used human foreskin fibroblasts, infected by replication-incompetent adenoviruses carrying EGFP gene, as the testing system. Cell characterization was performed through fluorescence microscopy, followed by image analysis. We explored the effect of different aspects: perfusion, multiplicity of infection, and temporal patterns of infection.

We demonstrated feasibility of performing efficient viral transduction at low doses, by repeated pulses of cell-virus contact. This procedure also enhanced the exogenous gene expression in the sequential microfluidic infection system compared to a single infection at a higher, non-toxic, viral dose.

B.2 Introduction

The precise control of *in vitro* viral transduction is highly desirable in several applications, like the optimization of gene therapies (1-3), RNA interference experiments (4), induced pluripotent stem (iPS) cell production (5), or for promoting stem cell differentiation (6). Non-replicating adenoviral vectors (AdVs) are increasingly used for such purposes, because they introduce transgenes into cells without uncontrollable random integrations in host DNA and minimizing other perturbations of cell homeostasis (7). In addition, they are easy to manufacture and have the ability to infect also quiescent cells (8). On the other hand, transduction by AdVs suffers from low efficiency (9), and using high viral doses to achieve sufficient transduction induces cytotoxicity, as previously demonstrated not only *in vivo* (7, 10), but also *in vitro* (7, 11-14), using different types of primary cells and cell lines. Cytotoxicity is dose-dependent, and *in vitro* studies do not show significant effects on the cells at low multiplicities of infection (MOIs) (11, 12). MOI is defined as the number of viral particles per cell. Chuck and Palsson used convective flow conditions to enhance virus-cell contact and increase the probability of virus entrance into the cells (15). Furthermore, microfluidics can improve the control over virus-mediated gene delivery even at very low MOIs. In fact microfluidic devices overcome some of the limitations of conventional bench-top systems, taking advantage not only of their high surface-to-volume ratio but also of laminar flow in the microfluidic channels (16). Microfluidics has already been used in applications involving viral particles, especially in the field of biosensors, for example for infectious virus detection

(17, 18). However, some devices were also developed for novel interesting applications: to measure virus infectivity and antiviral drug efficacy (19), for efficiently studying virus inactivation (20), and for virus-blood cell separation (21). Furthermore, a microfluidic bioreactor for virus production (22), and a device for protein production generating virus concentration gradients (23) were designed.

The highly-defined environment in a microfluidic system, coupled with the possibility of easily automating its control, makes simple to explore a huge range of experimental conditions, also for viral transduction. However, a precise understanding of the physical and biological phenomena involved is needed for a rational experimental design. Multiple mathematical models describing viral infection have been developed on different scales. Efforts to quantitatively describe viral dynamics *in vivo* have been reviewed by Perelson (24). More detailed computational models, based on *in vitro* viral infection data, include works describing virus transport to the cell surface (25, 26), virus-cell interaction (25, 27, 28), and intracellular viral trafficking (29, 30). Tayi et al developed a very exhaustive deterministic mathematical model including the steps from virus transport in the extra-cellular medium to viral transgene expression (31). Although computationally more requiring, a stochastic approach in modeling virus transduction dynamics is more appropriate, as both viruses and cells are discrete particles. Seisenberger et al experimentally showed that viruses move within the culture medium by Brownian motion and, once they get to a cell surface, they have a certain probability of penetration through the membrane (26). Some of the models mentioned above partly adopted a probabilistic approach, but including only the discrete nature of viruses and not of cells (25, 27-29). Thus, they could not calculate how viruses distribute within the cell population without further assumptions, such as the approximation of a Poisson distribution for the fraction of cells infected by a given number of viruses (31).

In this work, we developed a useful methodology for the accurate control of time-dependent gene delivery by AdVs, by integrating experimental and theoretical analyses. We realized a microfluidic platform to perform up to ten parallel independent experiments in a single miniaturized chip, with accurate control of perfusion stages. Given this setup, multiple operating conditions, in terms of mass transport parameters and temporal profiles of virus delivery, could be easily

tested. Enhanced green fluorescent protein (EGFP) was used as a reporter of cell infection for online detection of the temporal evolution of the experiment. In parallel, we developed a stochastic simulation algorithm to theoretically study the viral transduction process. The model accounts for the discrete nature of both cells and viruses in a three-dimensional space. The computational simulations show not only the percentage of infected cells, but also the distribution of viral particles in the cell population. With these tools, we studied the feasibility of performing efficient AdV transduction experiments at low viral dose, by performing multiple sequential pulses of viral transduction.

B.3 Materials and methods

B.3.1 Cell culture

Human foreskin fibroblasts (HFF) were expanded in gelatin-coated 75-mL flasks with high-glucose Dulbecco's Modified Eagle's Medium (DMEM 41965, Invitrogen, USA), supplemented with 10% fetal bovine serum (Invitrogen) and 1% penicillin/streptomycin (Invitrogen). At 90% confluency cells were trypsinized with trypsin-EDTA 0.25% (Invitrogen), centrifugated at 1200 rpm for 5 minutes and re-suspended in growth medium for seeding.

B.3.2 Adenoviral Vectors

Replication-incompetent adenoviral vectors (AdVs) based on the Ad5 genome and lacking the E1 and E3 regions were constructed by homologous recombination in *E. coli* using AdEasy vector system (Qbiogene, Carlsbad, CA). In these vectors, human cytomegalovirus promoter was used to drive expression of EGFP. Transgenic adenoviral vectors were propagated in E1-complementing HEK 293 cells, purified by cesium chloride density centrifugation, and titrated by $TCID_{50}$ cpe endpoint assay according to the AdEasy production protocol. Viral vector stocks were stored at $2 \cdot 10^8$ pfu/mL concentration in 10% glycerol at -80°C until use.

B.3.3 Microfluidic device

The microfluidic platform contains 10 independent channels for cell culture, each connected to a built-in medium reservoir of ~70 μL, and to a syringe pump system

for fluid handling. A schematic representation of the microfluidic system is shown in Fig. 1A, and its dimensions are reported in Fig. 1B.

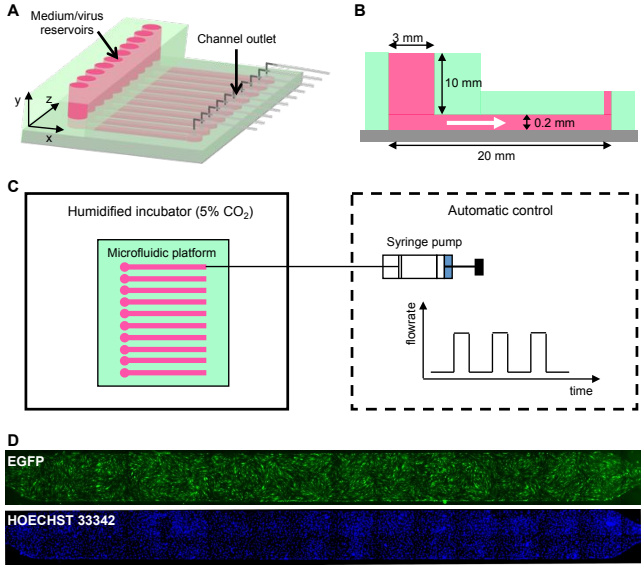

Figure 1 Microfluidic experimental setup. (**A**) 3-D graphical representation of the microfluidic platform composed of 10 parallel independent channels. (**B**) Lateral section of one channel indicating its geometrical dimensions. White arrow indicates flow direction. (**C**) Overview of the whole system: the microfluidic platform (top view on the left) is placed in a biological incubator during experiments, and medium perfusion (from left to right) in every channel is provided by a set of syringe pumps, whose temporal pattern of flow rate is automatically controlled. (**D**) Images of the whole microfluidic channel taken with a fluorescence microscope to detect $EGFP^+$ cells and cell nuclei.

The microfluidic chip was fabricated by common soft-lithographic techniques (32). The master was photolitographically patterned by using SU8-2100 negative photoresist (Microchem, USA) to obtain a final thickness of 200 μm, according to manufacturer's indications. A PDMS mold was obtained by casting a premixed 10:1 ratio prepolimer and curing agent solution (Sylgard 184 kit, Dow Corning, USA) on the silicon wafer. After curing at 70°C for 2 h, the PDMS mold was cut, peeled off and punched with a 21G stainless steel needle (Small Part Inc, USA) to obtain inlet/outlet holes. The PDMS mold was assembled and sealed to a 50×75 mm cleaned glass slide by plasma bonding. 10 independent medium reservoirs, one for each channel, were obtained by sealing an additional PDMS block to the top of the device by plasma bonding. The assembled device was cleaned with isopropanol (Sigma-Aldrich, USA) and sterilized in autoclave. A syringe pump with a 10-syringe rack (Harvard Pump, Harvard Apparatus, USA) was used to control the medium flow rate from the reservoirs into the microfluidic channels. 0.5 ID Tygon tubings (Cole Parmer, USA) and 21G stainless-steel needles with

polypropylene luer (Microtest, Taiwan) were used to connect the microfluidic chip to the syringes. The entire experimental setup is shown in Fig. 1C.

B.3.4 Viral transduction experiments

Before cell seeding, the microfluidic channels were coated with gelatin 0.6% and incubated at 37°C and 5% CO_2 atmosphere for 24 h. The cell suspension was injected into each channel and the microfluidic chip was incubated overnight at 37°C and 5% CO_2 atmosphere without perfusion. We used a proper cell seeding concentration in order to achieve confluent cell culture (corresponding to a final cell density of 150 cell/mm^2) at 24 h after seeding. Then, discontinuous medium refill was achieved by automatically controlling the multichannel syringe pump through Labview 8.2 (National Instruments Corp., USA), without further manual intervention. The pump was programmed to run every 3 h for 4 min with a flow rate of 3 μL/min for medium change.

24 h after cell seeding, AdV transduction was performed. The viral stock solution was thawed and diluted with culture medium to the final concentration. Medium perfusion into the micro-channels was performed with different dynamics through the automated syringe pump that aspirates medium from the channels. Each experimental condition was tested in at least two microfluidic channels in parallel. Parallel control experiments were performed in micro-channels supplied with AdV-free medium during viral transduction.

The conventional bench-top system used as a reference is a 24-well tissue culture plate (Becton Dickinson, USA). Cells were seeded and cultured for 24 h in 1-mL medium. Then, medium was replaced with 200-μL AdV-containing medium at different concentrations. After incubation for $t_f = 90$ min at 37°C and 5% CO_2, medium was changed again with 1-mL virus-free medium that was kept until the end of the experiment. Each experimental condition was tested in at least three wells in parallel. Three wells were used as controls in every experiment and were supplied with medium without AdVs during viral transduction.

B.3.5 Cell characterization

Cell count and EGFP expression were detected *in situ* by fluorescence microscopy (Leica DMI 6000-B, Leica Microsystems, Italy). Cell nuclei were stained by incubating live cells with 2 μg/mL Hoechst 33342 dye (Invitrogen) in culture

medium for 30 min. Bright field and fluorescence images were taken at 10X magnification, with exposure, gain and intensity parameters equal to the respective control in each culture system. Every channel was entirely captured for the microfluidic system (Fig. 1D), and three randomly chosen positions in every well were acquired for the multi-well plate.

The cell density and the percentage of $EGFP^+$ cells were quantified by image analysis, using MATLAB (The MathWorks, Natick, MA), as previously described (16). We performed this image analysis using different values for the threshold of fluorescence intensity, f, that discriminates between EGFP positive and negative cells. In this way we could quantify, besides the number of $EGFP^+$ cells, also the number of cells expressing EGFP at different levels.

B.3.6 Stochastic simulation algorithm

The mathematical model developed includes the extra-cellular virus transport in the culture medium (by diffusion and convection) and the entrance of viruses into the cells. Convective transport, present only in the microfluidic channels during filling and emptying, occurs in the x-direction (Fig. 2A) with a parabolic velocity profile, $v_x(y)$.

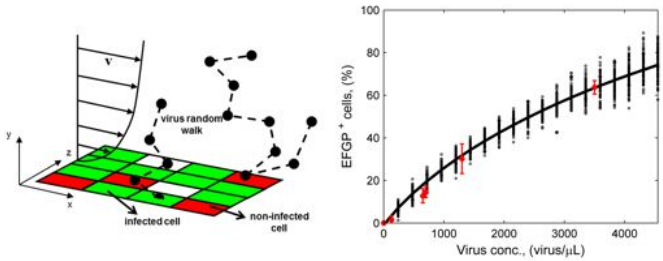

Figure 2 Stochastic model processes and parameter fitting. (**A**) Graphical representation of the phenomena included in the stochastic model: medium convection with parabolic velocity profile, virus brownian motion in 3-D space, virus entering a cell with a certain probability when it gets on its surface. Plane xz represents the bottom surface of the channel where cells are randomly distributed within a regular square grid. (**B**) Results of model parameter fitting. Experimentally, transduction was performed in a 24-well plate using 200 μL of virus-containing medium for 90 min. Cell concentration was 130 cell/mm^2. The percentage of cells expressing EGFP 24 h after AdV transduction is shown as a function of virus concentration by red error bars, which represent mean ± standard deviation values obtained in independent experiments, each performed in double or triple. Simulations by the stochastic model reproduce the experimental conditions. In the model, $EGFP^+$ cells are given by cells infected by at least one virus. The model outcome is shown as black dots, each obtained from one simulation at the given virus concentration. 100 simulations were performed at each condition. Black solid line indicates simulation mean results.

The geometry simulated includes the whole culture channel for the microfluidic system. While for the conventional multi-well plate a representative sub-volume

of the well (1.73-mm^2 bottom area), having the same height as the medium during viral transduction ($H = 1$ mm), was simulated.

Choosing a time step Δt for the simulation, the position (x_i, y_i, z_i) of the i-th virus at time $t + \Delta t$, given that at time t, was computed according to the Euler scheme of discretization for the Smoluchowski stochastic differential equation, as follows:

$$\begin{cases} x_i(t+\Delta t) = x_i(t) + v_x(y)\cdot\Delta t + \sqrt{2\cdot D\cdot\Delta t}\cdot\xi_{x,i} \\ y_i(t+\Delta t) = y_i(t) + \sqrt{2\cdot D\cdot\Delta t}\cdot\xi_{y,i} \\ z_i(t+\Delta t) = z_i(t) + \sqrt{2\cdot D\cdot\Delta t}\cdot\xi_{z,i} \end{cases} \quad (1)$$

where D is the diffusion coefficient of the virus in medium, and $\xi_{x,i}$, $\xi_{y,i}$, and $\xi_{z,i}$ are normally distributed random variables with zero mean and unit variance. The model was solved in MATLAB.

In both systems, cells were randomly distributed at the bottom within a regular square grid (Fig. 2A), to have the same density as in the experiments. The grid size was equal to $d_{cell} = 65.7$ μm, in order to have squares of the same cell surface area as that experimentally measured (4300±560 μm^2). We neglected cell division because contact inhibition prevails at the cell seeding density used, as we verified during the experiments (Supporting Material).

In the simulated sub-domain of the multi-well plate, at time $t = 0$ viruses were randomly placed within the three-dimensional medium volume to match the experimental concentration. Instead, in simulating the microfluidic system, virus concentration was null at time $t = 0$, and then viruses progressively entered with the flowing medium, at the appropriate concentration, distributed randomly on the inlet section surface.

Virus entrance into the cells was described in the model as a partially adsorbing boundary condition at $y = 0$, because not all cell-virus contacts are successful for introducing the virus into the cell (26). Formally, the probability that the i-th virus enters a cell in the time span Δt is given by $P_1\sqrt{\Delta t}$, if the virus has $y_i(t+\Delta t) \le 0$, where P_1 is a model parameter; or $P_1\sqrt{\Delta t}\cdot\exp\left[-y_i(t)\cdot y_i(t+\Delta t)/(D\cdot\Delta t)\right]$, otherwise. More details on this boundary condition are provided in the Supporting Material and in (33). The other boundary conditions were set as reflection, a part for the open boundaries at medium inlet

and outlet of the channel. We assumed that cells infected by at least one virus, then express EGFP.

B.3.7 Model parameter values

The model parameter values are summarized in Table I. The parameters related to system geometries and operative variables were fixed to match the experimental conditions. The value of the diffusion coefficient (D) was taken from the literature (34).

Table I. Parameter values of the model.

Parameter	Value
Cell equivalent size $\left(d_{cell}\right)$	$65.7 \mu m$
Culture volume height $\left(H\right)$	$1000 \mu m$ (multi-well) $200 \mu m$ (microfluidics)
Culture volume length $\left(L\right)$	$1314 \mu m$ (multi-well) $17 \cdot 10^3 \mu m$ (microfluidics)
Culture volume width $\left(W\right)$	$1314 \mu m$ (multi-well) $1500 \mu m$ (microfluidics)
Virus diffusion coefficient $\left(D\right)$	$3.67 \mu m^2 / s$
AdV-cell interaction constant $\left(P_1\right)$	$0.0079\ s^{-0.5}$
Cell seeding density $\left(\rho_{cell}\right)$	$130-150\ cell / mm^2$
AdV transduction duration $\left(t_f\right)$	$90\ min$
Simulated time step $\left(\Delta t\right)$	$0.16\ s$

Parameter P_1 was derived by fitting the experimental data obtained in the multi-well plate under static conditions. Specifically, we minimized the following cost function, φ:

$$\varphi = \sum_i \frac{\left(x_i^{mod} - x_i^{exp}\right)^2}{\left(\sigma_i^{exp}\right)^2}, \tag{2}$$

where superscripts mod and exp refer to model and experimental values, respectively; and x_i and σ_i are the mean and standard deviation of the percentage of EGFP$^+$ cells, obtained at the i-th virus concentration. Parameter fitting results are shown in Fig. 2B, in terms of both mean and standard deviation due to experimental uncertainty and model stochasticity.

B.4 Results and discussion

B.4.1 Spatial heterogeneity in microfluidics

To perform transduction experiments in a microfluidic channel, virus-containing medium needs to be perfused over the cells. As medium flows from inlet to outlet, it gets depleted of the viruses that enter the cells in between; hence, cells located in the downstream part of the channel are exposed to a lower MOI than those near the inlet. We computationally investigated how relevant is spatial heterogeneity in a perfused channel.

First, we simulated a channel perfused with a constant flow rate of 0.1 μL/min (Peclet number equal to 300). The medium entering the system had a virus concentration corresponding to an instantaneous MOI of 20 in the system, given a cell density of 130 cell/mm^2. We defined the MOI as instantaneous because it represents the number of viruses per cell within the channel at a given time. On the other hand, a global MOI can be defined by considering the total number of viruses entering the system during the whole time span of infection. The time of perfusion was set to 90 minutes, because it is the time (t_f) required for a viral particle to travel a distance $s = 200\,\mu\text{m}$ (the channel height) by Brownian motion, calculated from the Einstein's relation:

$$t_f = \frac{s^2}{2 \cdot D} \tag{3}$$

where D is the diffusion coefficient of the virus in medium. 100 stochastic simulations were performed. We verified that the whole channel was perfused by calculating that, at the flow rate simulated, 90 min correspond to 1.7 residence times.

The length of the channel was divided in ten sectors and in each sector the percentage of EGFP$^+$ cells, i.e. of cells infected by at least one virus, was calculated. The results are shown in Fig. 3A (top) and C. The percentage of positive cells in the last sector, near the outlet, is about 20% less than that in the first sector, at the inlet. Thus, spatial heterogeneity can be a relevant phenomenon introduced by perfusion that affects the quality of the resulting cell population. We also studied this aspect at different MOIs in the Supporting Material. Although at high MOI all the cells are infected, we verified that heterogeneity is still present in terms of virus distribution within the cell population, producing a gradient of infection level along the channel (Fig. 3A (bottom)).

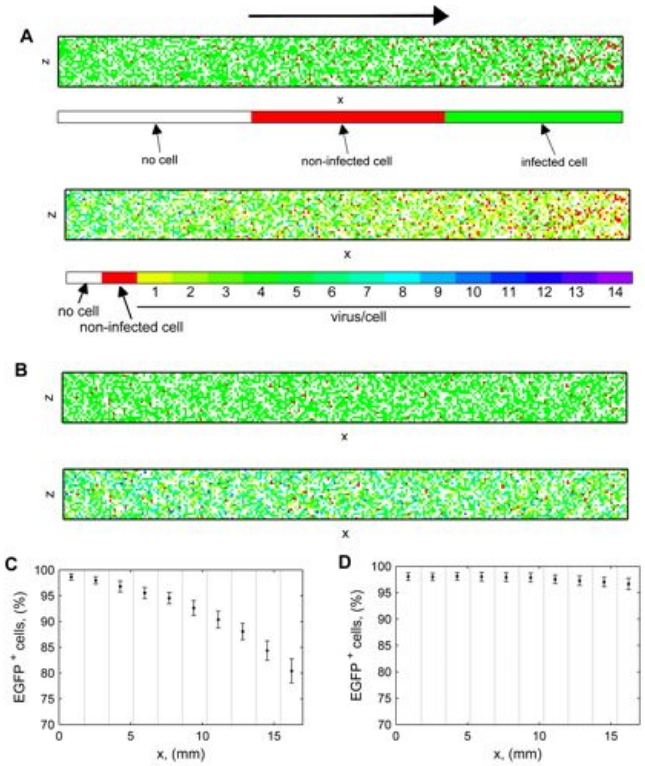

Figure 3 Computational study of spatial heterogeneity in the microfluidic system. (**A**, **C**) Results of stochastic simulations of continuous channel perfusion with a flow rate of 0.1 µL/min for 90 min. (**B**, **D**) Results of simulations of discontinuous perfusion: 2 min of inflow at 6 µL/min, 90 min without perfusion, and 2 min of outflow at 6 µL/min. (**A**, **B**) Bottom of a microfluidic channel: the $EGFP^+$ cells (top) and the number of virus/cell (bottom) are shown, color meaning is explained in color bars in (**A**). The black arrow indicates flow direction. (**C**, **D**) Percentage of $EGFP^+$ cells in each of the 10 equal sectors of the channel indicated by the dotted lines. Error bars indicate mean ± standard deviation of 100 simulations. (**A**-**D**) Cell concentration is 130 cell/mm^2, instantaneous MOI is 20.

To avoid this issue, we developed a different strategy for providing virus-containing medium to the cells, based on discontinuous perfusion. Keeping the same system geometry, cell density, and virus concentration as in the previous case, we simulated a perfusion of 2 min at a flow rate of 6 µL/min, 90 min without perfusion, and then 2 min of outflow. We verified that the shear stress occurring at 6 µL/min, approximately 6.8 mPa, is well below the threshold of cell damage (35), and can be effectively used during biological experiments. As shown in Fig. 3B and D, by performing the infection under these discontinuous conditions, spatial heterogeneity is within the stochastic noise of the system. $EGFP^+$ cells are homogeneously distributed along the channel, because the 2 min of inflow and outflow negligibly affect the overall outcome. The whole channel is filled in less than a minute at this flow rate and virus adsorption does not occur fast enough to produce a gradient in the infection level along the channel. On the

contrary, in the previous case, channel filling took about 50 min, a time of the same order of magnitude of the characteristic time of adsorption. Other conditions of flow were simulated confirming this hypothesis, whose results are presented in the Supporting Material. Furthermore, it is worth to underline that perfusion conditions may also affect the overall cell quality by changing the accumulation of endogenous factors in cell microenvironment, as recently reported (36). A discontinuous flow protocol better preserves cell microenvironment while ensuring a homogenous transfection along the microfluidic channel.

The homogeneity of transfection was confirmed also by experimental observations in our microfluidic system, as shown in the Supporting Material. All the results presented in the next sections, both computational and experimental, are obtained applying a discontinuous flow.

B.4.2 Effect of MOI after Single Viral Infection

We computationally investigated the effect of MOI on the percentage of $EGFP^+$ cells and the infecting-viruses distribution. We simulated the transduction process in a microfluidic channel for a cell density of 150 cell/mm^2 at four different MOIs: 20 (equal to a concentration of 15000 pfu/μL), 10 (7500 pfu/μL), 5 (3750 pfu/μL), and 1 (750 pfu/μL). Fig. 4 shows the resulting probability and complementary cumulative distributions of the percentage of cells infected with different numbers of viruses, as calculated by the model. Despite the spatial homogeneity performing AdV transduction in microfluidics under discontinuous flow (Fig. 3), the discrete nature of cells and viruses and how they are randomly distributed on the bottom surface and in the medium volume, respectively, can still generate a heterogeneous cell population as for the number of viruses infecting each cell. At MOI 1 almost all the cells infected have only 1 virus, but at higher MOIs heterogeneity is visible in the cell population (Fig. 4). Furthermore, the effective mean number of viruses per cell is much lower than the theoretical one, given by the MOI, confirming previous work (37). For example, at MOI 20 the mean number of viruses per cell is only between 3 and 4 (Fig. 4D). Fig. 4 shows also the percentage of cells infected by at least one virus, i.e. of $EGFP^+$ cells, according to the hypotheses described in Materials and Methods section. As expected, the efficiency of the infection process increases at higher MOIs.

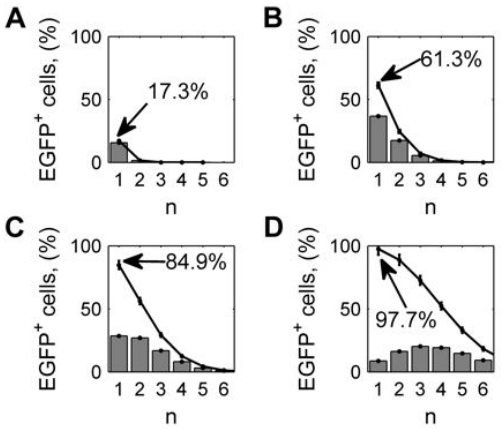

Figure 4 Computational study of viral transduction at different MOIs. Results of 100 stochastic simulations at MOI 1 (**A**), 5 (**B**), 10 (**C**), and 20 (**D**), in a microfluidic channel under discontinuous flow conditions, at a cell concentration of 150 cell/mm^2. Bar plots represent the percentage of EGFP$^+$ cells infected by n viruses. Black lines show the corresponding complementary cumulative distribution. In each plot the percentage of EGFP$^+$ cells (i.e. cells infected by at least 1 virus) is also indicated. Error bars indicate mean ± standard deviation of the 100 simulations.

Experimentally, given the very great surface-to-volume ratio of microfluidic systems, we first verified that there were not substantial AdV losses due to binding on the surfaces of the channels. The results are reported in the Supporting Material. Then, we performed experiments of viral transduction in the microfluidic platform under the same conditions simulated above and characterized the cell population at 24 h after the beginning of infection. We assumed that this period of time is sufficient for infected cells to express EGFP protein, as reported previously (38). The very good agreement between the percentages of EGFP$^+$ cells obtained from experimental data and predicted by the model (Fig. 5A), shows the stochastic model fairly describes the overall infection process within the microfluidic platform. This result is particularly relevant considering that all extra and intra-cellular biological phenomena of viral infection (excluding those related to extra-cellular viral particle mass transport) are lumped in an overall limiting step, whose parameter was obtained by experimental data collected under static conditions in a multi-well plate.

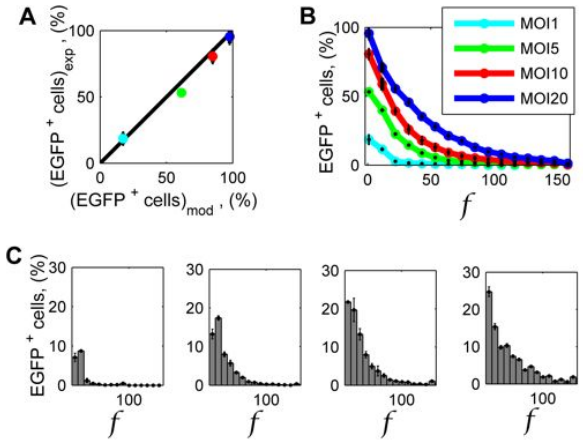

Figure 5 Experimental study of viral transduction in the microfluidic platform at different MOIs. (**A**) Comparison of experimental (subscript *exp*) and simulated (subscript *mod*) percentage of $EGFP^+$ cells. Marker colors are defined by legend in (B). (**B**) Complementary cumulative distribution of the percentage of $EGFP^+$ cells showing a fluorescence intensity > f (see *Cell Characterization* section). (**C**) Probability distribution of the percentage of $EGFP^+$ cells showing a fluorescence intensity f at MOI 1, 5, 10, and 20 (from left to right). (**A-C**) The percentage of cells expressing EGFP was detected 24 h after AdV transduction. Cell concentration was 150 cell/mm^2. Error bars represent mean ± standard deviation values obtained in independent experiments, each performed in double or triple.

We investigated the experimental heterogeneity of the cell population as for the EGFP produced at the single-cell level. We quantified the intensity of fluorescence, f, of each cell by image analysis, as described in Materials and Methods section. The results are shown in Fig. 5B and C, in terms of complementary cumulative distribution and of probability distribution, respectively. Besides increasing the percentage of cells expressing EGFP, AdV transduction performed at higher MOIs enhances the amount of exogenous RNA and consequently the amount of EGFP produced by single cells. This could be related to the increase in the number of viruses infecting each cell, as explored computationally (Fig. 4). However, multiple other processes overlap (such as, virus intracellular transport, cell cycle, regulation of transcription and translation), and a straight correlation between the two variables, number of virus per cell and intensity of cell fluorescence, is not possible.

B.4.3 Multiple Pulses of Viral Transduction

Thanks to the developed technology, the same efficiency of infection of cell culture could be obtained by infecting cells several times at low MOI, thus preventing any cytotoxic effect due to external viral particles. For this reason, we explored the possibility of performing multiple sequential pulses of infection at

low viral doses in order to increase protein expression over time and also avoiding the cell toxicity of high MOIs. We compared the outcome of a single viral transduction at MOI 20 (still low enough not to be toxic) with that of two infections at MOI 10, and of 4 infections at MOI 5. The total number of viruses entering the system was thus the same, but three different regular temporal sequences were used (Fig. 6). We simulated these three scenarios with the stochastic model, and found that theoretically the same outcome is achievable with a multi-pulse strategy, in terms of percentage of $EGFP^+$ cells and of the distribution of the number of viruses per cell (Fig. 6).

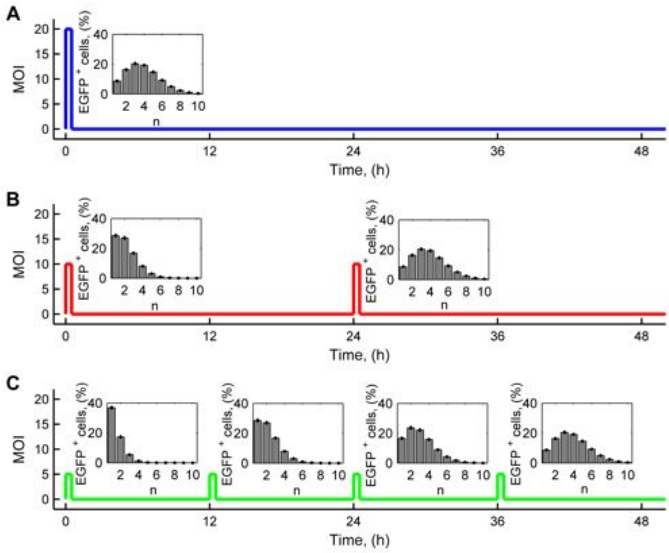

Figure 6 Multiple viral transductions strategy and computational results. Repeated 90-min AdV infections with MOI 20 (**A**), 10 (**B**), and 5 (**C**), at the time points indicated. Insets show model predictions of the percentage of $EGFP^+$ cells infected by n viruses at the end of each pulse of infection. Cell concentration was 150 cell/mm^2. Error bars indicate mean ± standard deviation of 100 simulations at each condition.

Taking advantage of the precise automation of flow rate control in the microfluidic platform, we performed the experiment corresponding to the theoretical simulations described above. We infected the cells at time 0 and the other time points given in the three protocols, using a discontinuous flow strategy, i.e. 2 min of virus-containing medium flow (or virus-free medium in the channels not to be infected), 90 min of infection under static conditions, and 2 min of virus-free medium flow. We monitored the level of cell EGFP expression 24 h after each infection, i.e. at the following time points: 24, 36, 48, and 60 h after the first infection. The results are presented in Fig. 7, in terms of probability and complementary cumulative distributions. Fig. 7D shows a comparable EGFP gene expression with the three protocols after 48 h, while at 60 h channels treated with

multi-pulse viral transduction at lower MOIs show a higher percentage of cells being more fluorescent (Fig. 7D).

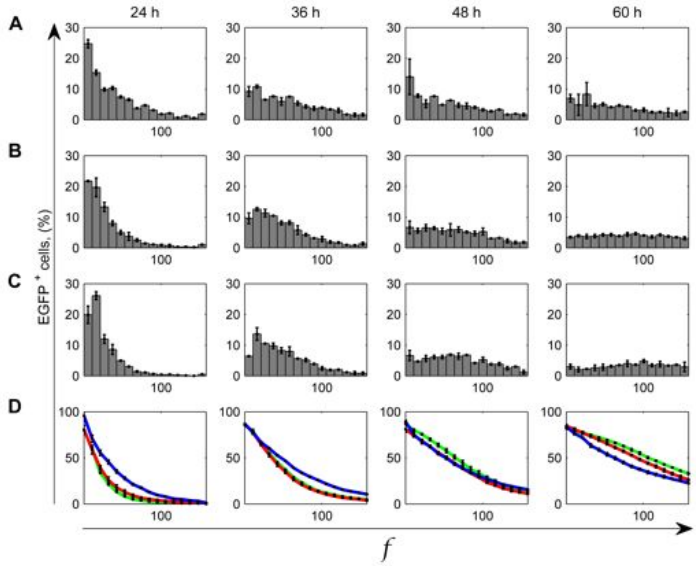

Figure 7 Results from experiments of multiple viral transductions within the microfluidic platform. AdV transduction timing followed the strategy shown in Figure 6: one infection at MOI 20 (**A** and blue line in **D**), two infections at MOI 10 (**B** and red line in **D**), and 4 at MOI 5 (**C** and green line in **D**). $EGFP^+$ cell fluorescence intensity, *f*, was measured at 24, 36, 48, and 60 h after the first infection. Cell concentration was 150 cell/mm^2. Error bars indicate mean ± standard deviation of experiments repeated twice. (**A-C**) Probability distribution of the percentage of $EGFP^+$ cells showing a fluorescence intensity *f*, and (**D**) associated complementary cumulative distribution.

In this experiment, the maximum MOI used was 20. As previously verified, this is below the threshold of cytotoxicity, identified approximately at MOI 50 (11, 12). These conditions, coupled with a constant cell density due to contact inhibition, are useful to detect the effect of a sequential infection strategy at net of cell division and death phenomena, which are also not included in the stochastic model. Overall, a comparison between the percentage of $EGFP^+$ cells (Fig. 7D) shows the feasibility of performing sequential viral transduction experiments without loss of efficiency, and highlights the importance of the multi-pulse infection strategy in cases when cytotoxicity is a concern. We performed sequential transduction experiments also at very high MOIs, as reported in the Supporting Material, and the results strongly support the reduction in cytotoxicity achievable.

Furthermore, the higher EGFP expression achieved after repeated infections at MOI 5 than after a single one at MOI 20, confirms the complexity of gene expression regulation, which is not linearly dependent on the amount of exogenous DNA inserted. Thus, the sequential infection strategy may be a useful

means also to study complex dynamics of gene expression in a highly controlled system.

B.5 Conclusions

Viral vectors are increasingly used to insert exogenous genetic material in cells. Low efficiency of infection at low MOIs and cytotoxicity at high MOIs are two critical limitations affecting the process. In this work, we showed the feasibility of performing sequential infections at low viral dose with high efficiency, taking advantage of microfluidic technology to provide a highly-defined temporal control over the cell culture environment.

We coupled the experiments with a theoretical analysis through a stochastic model to follow the dynamics of virus entrance into the cells under continuous and discontinuous flow conditions. In particular, being discrete in its description of viruses and cells, the model can recapitulate also the heterogeneity in the cell population without further assumptions.

Under the simplifying hypotheses of the model, one infection at high viral dose and multiple at low doses, using the same overall amount of viruses, should give the same outcome in terms of distribution of viruses in the infected cell population. However, we also found experimentally that, compared to a single infection at high MOI, performing multiple low-dose infections affects the gene expression profile of the resulting cell population. Thus, the strategy developed to perform time-controlled multi-pulse infections, besides reducing viral toxicity, could be a powerful tool to investigate the dynamic complexity of the expression of exogenous genes using a highly controlled system.

Supporting material is available at:

http://www.biophysj.org/biophysj/supplemental/S0006-3495(13)00038-6

B.6 References

1. Wu, Z. J., A. Asokan, and R. J. Samulski. 2006. Adeno-associated virus serotypes: Vector toolkit for human gene therapy. Mol Ther 14:316-327.
2. Carty, M., and A. G. Bowie. 2010. Recent insights into the role of Toll-like receptors in viral infection. Clin Exp Immunol 161:397-406.
3. Ames, R. S., and Q. Lu. 2009. Viral-mediated gene delivery for cell-based assays in drug discovery. Expert Opin Drug Discov 4:243-256.
4. Arts, G. J., E. Langemeijer, R. Tissingh, L. B. Ma, H. Pavliska, K. Dokic, R. Dooijes, E. Misic, R. Clasen, F. Michiels, J. van der Schueren, M. Lambrecht, S. Herman, R. Brys,

K. Thys, M. Hoffmann, P. Tomme, and H. van Es. 2003. Adenoviral vectors expressing siRNAs for discovery and validation of gene function. Genome Res 13:2325-2332.

5. Takahashi, K., K. Tanabe, M. Ohnuki, M. Narita, T. Ichisaka, K. Tomoda, and S. Yamanaka. 2007. Induction of pluripotent stem cells from adult human fibroblasts by defined factors. Cell 131:861-872.
6. Takayama, K., M. Inamura, K. Kawabata, K. Katayama, M. Higuchi, K. Tashiro, A. Nonaka, F. Sakurai, T. Hayakawa, M. K. Furue, and H. Mizuguchi. 2012. Efficient Generation of Functional Hepatocytes From Human Embryonic Stem Cells and Induced Pluripotent Stem Cells by HNF4 alpha Transduction. Mol Ther 20:127-137.
7. Liu, Q., and D. A. Muruve. 2003. Molecular basis of the inflammatory response to adenovirus vectors. Gene Ther 10:935-940.
8. Ghosh, S. S., P. Gopinath, and A. Ramesh. 2006. Adenoviral vectors: a promising tool for gene therapy. Appl Biochem Biotechnol 133:9-29.
9. Stadtfeld, M., M. Nagaya, J. Utikal, G. Weir, and K. Hochedlinger. 2008. Induced Pluripotent Stem Cells Generated Without Viral Integration. Science 322:945-949.
10. Bangari, D. S., and S. K. Mittal. 2006. Current strategies and future directions for eluding adenoviral vector immunity. Curr Gene Ther 6:215-226.
11. Brand, K., R. Klocke, A. Possling, D. Paul, and M. Strauss. 1999. Induction of apoptosis and G2/M arrest by infection with replication-deficient adenovirus at high multiplicity of infection. Gene Ther 6:1054-1063.
12. Matkovic, U., M. Pacenti, M. Trevisan, G. Palu, and L. Barzon. 2009. Investigation on Human Adrenocortical Cell Response to Adenovirus and Adenoviral Vector Infection. J Cell Physiol 220:45-57.
13. Hartman, Z. C., E. P. Black, and A. Amalfitano. 2007. Adenoviral infection induces a multi-faceted innate cellular immune response that is mediated by the toll-like receptor pathway in A549 cells. Virology 358:357-372.
14. Mueller, J., C. Thirion, and M. W. Pfaffl. 2011. Electric cell-substrate impedance sensing (ECIS) based real-time measurement of titer dependent cytotoxicity induced by adenoviral vectors in an IPI-2I cell culture model. Biosens Bioelectron 26:2000-2005.
15. Chuck, A. S., and B. O. Palsson. 1996. Consistent and high rates of gene transfer can be obtained using flow-through transduction over a wide range of retroviral titers. Hum Gene Ther 7:743-750.
16. Cimetta, E., M. Franzoso, M. Trevisan, E. Serena, A. Zambon, S. Giulitti, L. Barzon, and N. Elvassore. 2012. Microfluidic-driven viral infection on cell cultures: Theoretical and experimental study. Biomicrofluidics 6:024127.
17. Cheng, X., G. Chen, and W. R. Rodriguez. 2009. Micro- and nanotechnology for viral detection. Anal Bioanal Chem 393:487-501.
18. Kremser, L., D. Blaas, and E. Kenndler. 2009. Virus analysis using electromigration techniques. Electrophoresis 30:133-140.
19. Zhu, Y., J. W. Warrick, K. Haubert, D. J. Beebe, and J. Yin. 2009. Infection on a chip: a microscale platform for simple and sensitive cell-based virus assays. Biomed Microdevices 11:565-570.
20. Bailey, M. R., D. Chen, W. R. Emery, P. K. Lambooy, J. Nolting, M. T. Quertinmont, and P. A. Shamlou. 2008. Evaluation of microfluidics reactor technology on the kinetics of virus inactivation. Biotechnol Bioeng 99:1384-1391.
21. Zhao, C., and X. Cheng. 2011. Microfluidic separation of viruses from blood cells based on intrinsic transport processes. Biomicrofluidics 5:032004.
22. Vu, H. N., Y. Li, M. Casali, D. Irimia, Z. Megeed, and M. L. Yarmush. 2008. A microfluidic bioreactor for increased active retrovirus output. Lab Chip 8:75-80.
23. Walker, G. M., M. S. Ozers, and D. J. Beebe. 2004. Cell infection within a microfluidic device using virus gradients. Sens Actuators B Chem 98:347-355.
24. Perelson, A. S. 2002. Modelling viral and immune system dynamics. Nat Rev Immunol 2:28-36.
25. Anekal, S. G., Y. Zhu, M. D. Graham, and J. Yin. 2009. Dynamics of virus spread in the presence of fluid flow. Integr Biol 1:664-671.
26. Seisenberger, G., M. U. Ried, T. Endress, H. Buning, M. Hallek, and C. Brauchle. 2001. Real-time single-molecule imaging of the infection pathway of an adeno-associated virus. Science 294:1929-1932.
27. Gibbons, M. M., T. Chou, and M. R. D'Orsogna. 2010. Diffusion-Dependent Mechanisms of Receptor Engagement and Viral Entry. J Phys Chem B 114:15403-15412.
28. Nowak, S. A., and T. Chou. 2009. Mechanisms of Receptor/Coreceptor-Mediated Entry of Enveloped Viruses. Biophys J 96:2624-2636.

29. Lagache, T., E. Dauty, and D. Holcman. 2009. Quantitative analysis of virus and plasmid trafficking in cells. Phys Rev E 79:011921.
30. Sidorenko, Y., and U. Reichl. 2004. Structured model of influenza virus replication in MDCK cells. Biotechnol Bioeng 88:1-14.
31. Tayi, V. S., B. D. Bowen, and J. M. Piret. 2009. Mathematical Model of the Rate-Limiting Steps for Retrovirus-Mediated Gene Transfer Into Mammalian Cells. Biotechnol Bioeng 105:195-209.
32. Gomez-Sjoberg, R., A. A. Leyrat, D. M. Pirone, C. S. Chen, and S. R. Quake. 2007. Versatile, fully automated, microfluidic cell culture system. Anal Chem 79:8557-8563.
33. Erban, R., and S. J. Chapman. 2007. Reactive boundary conditions for stochastic simulations of reaction-diffusion processes. Phys Biol 4:16-28.
34. Oliver, C. J., K. F. Shortridge, and G. Belyavin. 1976. Diffusion coefficient and molecular weight of type 5 adenovirus by photon-correlation spectroscopy. Biochim Biophys Acta 437:589-598.
35. Hua, J. M., L. E. Erickson, T. Y. Yiin, and L. A. Glasgow. 1993. A review of the effects of shear and interfacial phenomena on cell viability. Crit Rev Biotechnol 13:305-328.
36. Moledina, F., G. Clarke, A. Oskooei, K. Onishi, A. Guenther, and P. W. Zandstra. 2012. Predictive microfluidic control of regulatory ligand trajectories in individual pluripotent cells. P. Natl. Acad. Sci. USA. 109:3264-3269.
37. Andreadis, S., T. Lavery, H. E. Davis, J. M. le Doux, M. L. Yarmush, and J. R. Morgan. 2000. Toward a more accurate quantitation of the activity of recombinant retroviruses: Alternatives to titer and multiplicity of infection. J Virol 74:1258-1266.
38. deMartin, R., M. Raidl, E. Hofer, and B. R. Binder. 1997. Adenovirus-mediated expression of green fluorescent protein. Gene Ther 4:493-495.
39. Dinh, A. T., T. Theofanous, and S. Mitragotri. 2005. A model for intracellular trafficking of adenoviral vectors. Biophys J 89:1574-1588.

Appendix C

A mechanical checkpoint controls multicellular growth through YAP/TAZ regulation by actin capping/severing factors

Mariaceleste Aragona[1], Tito Pancera[1], Andrea Manfrin[1], Stefano Giulitti[2], Federica Michielin[2], Nicola Elvassore[2] and Sirio Dupont[1], Stefano Piccolo[1].

1. Department of Molecular Medicine, University of Padua School of Medicine, viale Colombo 3, 35131 Padua, Italy.
2. Department of Industrial Engineering (DII), University of Padua, via Marzolo 9, 35131 Padua, Italy.

Cell
Volume 154(5):1047-1059
10.1016/j.cell.2013.07.042

C.1 Summary

Key cellular decisions, such as proliferation or growth arrest, typically occur at spatially-defined locations within tissues. Loss of this spatial control is a hallmark of many diseases, including cancer. Yet, how these patterns are established is incompletely understood. Here we report that physical and architectural features of a multicellular sheet inform cells about their proliferative capacity through mechanical regulation of YAP and TAZ, known mediators of Hippo signaling and organ growth. YAP/TAZ activity is confined to cells exposed to mechanical stresses, such as stretching, location at edges/curvatures contouring an epithelial sheet, or stiffness of the surrounding extracellular matrix. We identify the F-actin capping/severing proteins Cofilin, CapZ and Gelsolin as essential gatekeepers that limit YAP/TAZ activity in cells experiencing low mechanical stresses, including contact inhibition of proliferation. We propose that mechanical forces are

overarching regulators of YAP/TAZ in multicellular contexts, setting responsiveness to Hippo, WNT and GPCR signaling.

C.2 Introduction

Spatially restricted patterns of cell proliferation shape embryonic development and maintain adult epithelial tissues. How these local growth patterns are established remains unclear. In the past decades, major emphasis has been placed on graded distribution of soluble growth factors or their restricted activity in "niches". This view, however, does not fully explain how the microenvironment can robustly template cell behavior in time and space, with micrometer accuracy (Discher et al., 2009; Huang and Ingber, 1999). Moreover, soluble factors alone can hardly account for some remarkable examples of ordered proliferation, differentiation and self-organization of entire organs emerging in vitro from naïve cells cultured in media saturated of mitogens and growth factors (Sasai, 2013). This suggests that tissues are somehow endowed with the capacity to inform individual cells on their proliferative competence, likely including the responsiveness to soluble cues. Although the molecular nature of these informational systems is uncertain, an intriguing model is that the architectural form of the tissue - its shape and three-dimensional geometry - serves as template to initiate and self-sustain asymmetric patterns of cell proliferation (Nelson and Bissell, 2006; Nelson et al., 2005). Key elements of such architectural signal are cell shape, cell geometry and deformation generated by the pulling forces of the extracellular matrix (ECM) and of neighboring cells, and the associated changes in cytoskeletal organization and tension (Berrier and Yamada, 2007; Miranti and Brugge, 2002; Schwartz, 2010; Vogel and Sheetz, 2006). In this model, a specific tissue conformation would translate into a pattern of mechanical forces potentially targeting individual cells with exquisite detail. Supporting this "biomechanical" perspective, the physical properties of the microenvironment are increasingly recognized as potent and pervasive regulators of cell behavior, such as proliferation and differentiation (Halder et al., 2012). A critical step forward in understanding these processes has been the discovery that mechanical signals are transduced by two related transcriptional coactivators, YAP and TAZ (Dupont et al., 2011). These are powerful regulators of cell proliferation and survival, playing critical roles in organ growth (Pan, 2010; Zeng and Hong, 2008). A number of

human cancers hijack these properties to foster their own growth, including induction of cancer stem cells and metastatic colonization (Cordenonsi et al., 2011; Harvey et al., 2013). YAP and TAZ shuttle between the cytoplasm and the nucleus, where they interact with TEAD transcription factors to regulate transcription. Classically, the Hippo cascade has been regarded as the major regulatory input upstream of YAP/TAZ (Pan, 2010). Very recently, WNT and GPCR signaling pathways have also been recognized as important regulators of YAP/TAZ (Azzolin et al., 2012; Yu et al., 2012). Thinking along the connections between tissue architecture, cell mechanics and YAP/TAZ biology, we asked: is the mechanical regulation of YAP and TAZ translating spatial force distribution into patterned growth within multicellular layers? If so, how is positional information transmitted to YAP/TAZ? Are the different inputs feeding on YAP/TAZ (e.g. mechanical stimulation, Hippo, WNT or GPCR signaling) parallel or interdependent regulations? Here we started to shed light on these issues by discovering that cell proliferation in an epithelial monolayer is profoundly influenced by a mechanical and cytoskeletal checkpoint that regulates YAP and TAZ. This tissue-level checkpoint is enforced by the F-actin capping and severing proteins CapZ, Cofilin and Gelsolin. These factors inhibit YAP and TAZ in cells that, within a monolayer, are located at sites of low mechanical stress. Conversely, YAP/TAZ-mediated proliferative competence occurs in cells that exhibit higher contractility in response to stretching forces, depending on the shape of the epithelial sheet or on the rigidity of the surrounding ECM. We propose that mechanical stresses are overarching regulators of YAP/TAZ in multicellular contexts, also setting cell responsiveness to Hippo, WNT and GPCR signaling.

C.3 Results

C.3.1 Mechanical regulation of cell proliferation through YAP/TAZ

A classic paradigm on the control of proliferation in multicellular aggregates is contact inhibition of proliferation (CIP), a process by which cultured cells stop dividing when they become confluent occupying the entire space allotted to them. This behavior recapitulates the proliferative arrest of most epithelia typically leading to cell differentiation or death. Interestingly, loss of CIP is considered a hallmark of cancer (McClatchey and Yap, 2012; Zeng and Hong, 2008). In CIP, a

unifying theme is the regulation of YAP and TAZ, that tend to remain nuclear in cells growing at low density and relocate in the cytoplasm in confluent cultures (Zhao et al., 2007). CIP is associated with phosphorylation of YAP and TAZ, indicating the activation of the Hippo pathway kinases (Zhao et al., 2007). However, the regulation of YAP/TAZ by contact inhibition appears more complex. For example, recent data show that, at least in MEFs or keratinocytes, the mammalian Hippo homologue MST1/2 and LATS1/2 are dispensable for CIP (Schlegelmilch et al., 2011; Zhou et al., 2009). Here we decided to explore a different scenario, in which CIP incorporates a mechanical regulation of YAP and TAZ. To test this, we compared immortalized human mammary epithelial cells (MEC) plated at different densities (3000, 15000, 75000 cells/cm^2) (Figure 1A). At the lowest plating density (hereafter called "sparse"), cells exhibited no or minimal contact between neighboring cells. At the intermediate plating density ("confluent"), cells were confluent with all-around cell-cell contacts, while, at the highest density ("dense"), space constraints caused cells to form a densely packed monolayer. Using anti-E-Cadherin immunofluorescence to identify cell borders, we quantified that the projected cell area dropped more than ten folds with increasing density, from 1400 μm^2 in sparse cells, to 700 μm^2 in confluent cells and down to 130 μm^2 in dense cells (Figure 1A). As measured by BrdU incorporation, confluent cultures displayed about a 30% reduction of S-phase entry when compared to sparse cultures (Figure 1B). This degree of proliferative inhibition is in agreement with the expected contribution of cell-cell contact and E-Cadherin engagement to CIP (Kim et al., 2011), and was paralleled by a partial YAP/TAZ cytoplasmic relocalization (Figure 1C). That said, both nuclear YAP/TAZ levels and proliferation remained clearly evident in confluent cultures (Figures 1B and 1C), with YAP/TAZ activity being causal for S-phase entry (Figure 1B). This suggests that cell-cell contact per se is not sufficient to induce either post-confluence inhibition of proliferation, or robust YAP/TAZ inactivation. This is in contrast to the cells seeded at high density (dense), which are overtly growth arrested and exhibit largely cytoplasmic, transcriptionally inactive YAP/TAZ (Figures 1B, 1C, S1A). CIP is reversible, as inducing a "wound" in the monolayer by scraping away a stripe of cells caused the cells lying within a few cell diameters from the edge of the wound to stretch without losing cell-cell contacts, re-localize YAP/TAZ to the nuclei and proliferate

(Figure S1B and data not shown). Similar results were observed by using immortalized human HaCaT keratinocytes (Figures S1C-F and data not shown). YAP/TAZ inactivation in the course of CIP has been associated with activation of cell-cell adhesion machinery and activation of the Hippo pathway (Zhao et al., 2007). We thus asked if the distinct degrees of YAP/TAZ inactivation observed in confluent and dense cultures, were dependent on catenins and LATS. Consistently with previous reports (Kim et al., 2011; Schlegelmilch et al., 2011), knockdown of α-catenin, p120-catenin or LATS1/2 rescued YAP/TAZ transcriptional activity in confluent cultures, as measured by the expression of YAP/TAZ target genes CTGF, CYR61 and ANKRD1 (Figures S1G-I and data not shown). Surprisingly, however, the same depletions had marginal effects on YAP/TAZ signaling in dense cultures (Figures S1G-I). The above results suggest that, beside cell-cell contacts, the main determinant for YAP/TAZ inhibition and post-confluent growth arrest is actually to attain a small cell size - intended as adhesion to a small ECM substrate area (Figure 1A). Indeed, cells attaching to a small area are known to experience low mechanical stresses, as they display decreased integrin-mediated focal adhesions, reduced actin stress fibers, and blunted cell contractility (Berrier and Yamada, 2007; Schwartz, 2010; Vogel and Sheetz, 2006). Importantly, these mechanical cues have recently been shown to be essential for YAP/TAZ nuclear localization and activity (Dupont et al., 2011; Wada et al., 2011). In this perspective, CIP would represent the response to a mechanical constraint: as cell crowding progressively boxes individual cells into smaller areas, these would be subjected to the same YAP/TAZ-regulating mechanotransduction pathways that affect isolated cells plated on small ECM islands. In line with this view, MEC plated as single cells on micropatterned fibronectin islands of defined areas displayed strong inhibition of YAP/TAZ nuclear levels and BrdU incorporation when individual cell-size dropped below 300 μm^2 (Figures 1D and 1E), independently of cell-cell contacts. Similarly, decreasing mechanical cues by culturing cells on soft substrates (i.e., fibronectin-coated acrylamide hydrogels) also caused cell rounding, YAP/TAZ nuclear exclusion and proliferative inhibition (Figures 1F, 1G and S1J).

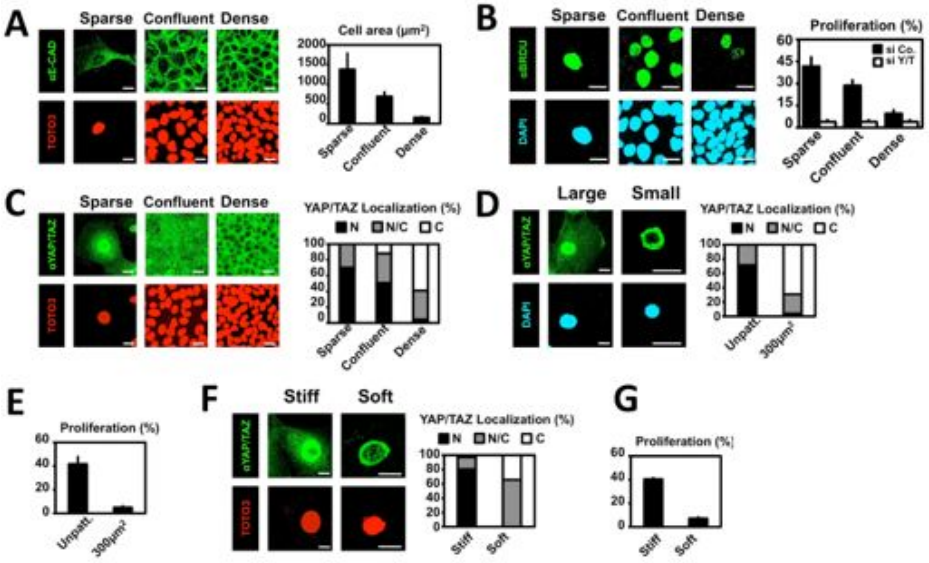

Figure 1: High Cell Density, Small Cell Geometry, and Soft ECM All Lead to Restriction of Cell Area, YAP/TAZ Relocalization, and Growth Arrest (A) Cells plated at different densities display increasingly smaller cell-substrate adhesion areas. MECs were seeded to obtain sparse cells and confluent or dense monolayers. After 2 days, cells were fixed for immunofluorescence with anti-E-cadherin antibody (anti-E-CAD) to visualize formation of cell-cell contacts by confocal microscopy. TOTO3 is a nuclear counterstain. Scale bar, 20 mm. (Right) Average cell area in the three seeding conditions. Similar results were obtained with HaCaT keratinocytes (Figure S1C). (B) MECs were plated as in (A); after 2 days, cells were incubated for 1 hr with a pulse of BrdU to label cells undergoing DNA duplication. Cells were fixed and processed for anti-BrdU immuno-fluorescence (aBRDU). (Right) Quantitation of proliferation measured as the percentage of BrdU-positive cells. Similar results were obtained with HaCaT keratinocytes (Figure S1D). Note minimal residual proliferation in dense cells, even after YAP/TAZ depletion, suggesting that cell proliferation in culture may not be totally dependent on YAP/TAZ. (C) MECs were plated as in (A) and stained for immunofluorescence with anti-YAP/TAZ antibody (aYAP/TAZ). TOTO3 is a nuclear counterstain. Scale bar, 20 μm. (Right) Proportion of cells dis- playing preferential nuclear YAP/TAZ localization (N, black), even distribution of YAP/TAZ in nucleus and cytoplasm (N/C, gray), or cytoplasmic YAP/ TAZ (C, white). Similar results were obtained with HaCaT keratinocytes (Figure S1E) and with an in- dependent anti-YAP antibody (not shown). (D and E). Restricting cell-substrate adhesion area to levels comparable to those of dense cells is sufficient to cause YAP/TAZ nuclear exclusion and inhibition of proliferation. MECs were seeded as individual cells plated on fibronectin-coated glass (large) or on square microprinted fibronectin islands of 300 mm^2 (small). In (D), cells were fixed after 1 day for immunofluorescence with anti-YAP/ TAZ antibody (aYAP/TAZ). DAPI is a nuclear counterstain. Scale bar, 20 μm. (Right) YAP/TAZ nucleo/cytoplasmic localization was scored as in (C). In (E), cells were processed for BrdU incorporation as in (B). (F and G) Effects of a soft ECM substrate on epithelial proliferation. Confocal immunofluorescence images of YAP/TAZ of MECs plated on fibronectin-coated stiff (plastic) and soft (acrylamide hydrogels of 0.7 kPa) substrates. TOTO3 is a nuclear counterstain. Scale bar, 20 mm. On the right: YAP/TAZ nucleo/cytoplasmic localization was scored as in (C). In (G) cells were processed for BrdU incorporation as in (B). Similar results were obtained using acrylamide hydrogels of 40 kPa or plastics (Dupont et al., 2011 and data not shown). Data are mean and SD. Experiments were per- formed at least three times with three biological replicates each time. Quantitations were carried out by scoring at least 2,000 cells for each sample. Pictures show representative results. See also Table S1 for siRNA sequences and Figure S1.

The remarkable phenotypic similarities between cells cultured in small, soft or dense conditions clearly suggest that these apparently different modalities to regulate YAP/TAZ may actually all correspond to the control of YAP/TAZ by mechanical cues. To address more directly the notion that in a multicellular layer

the control of YAP/TAZ activity and cell proliferation occurs through mechanical cues, we developed a microdevice that reproduces some of the mechanical challenges experienced by tissues, such as stretching (Figure 2A and S2A-C). This microdevice was built by fabricating into polydimethylsiloxane silicone (PDMS) a microfluidic network of hollow channels connecting larger "chambers" filled with saline solution. The surface of PDMS was coated with ECM (fibronectin) to allow cell attachment. MECs were seeded on this surface at high cell density causing cells to exclude YAP/TAZ from nuclei and undergo CIP. Next, we slowly applied computer-controlled pressure to the system, imposing cells to radially stretch as the PDMS membrane overlaying each chamber inflated (Figure 2A). This applied strain increased the cell adhesive surface to 150%, as quantified from measurements of the cell-projected area (Figure 2B). This was associated to a remodeling of the F-actin cytoskeleton with appearance of phalloidin-positive actin bundles in stretched cells (Figure S2D). Remarkably, stretched cells rapidly reactivated YAP/TAZ, as monitored by nuclear localization, and re-entered S-phase (Figure 2C and 2D). Based on these experiments we conclude that mechanical forces acting on specific areas of an epithelial sheet reflect into changes of shape and mechanics of the individual cells, and act as spatially localized determinants of cell proliferation through YAP/TAZ regulation.

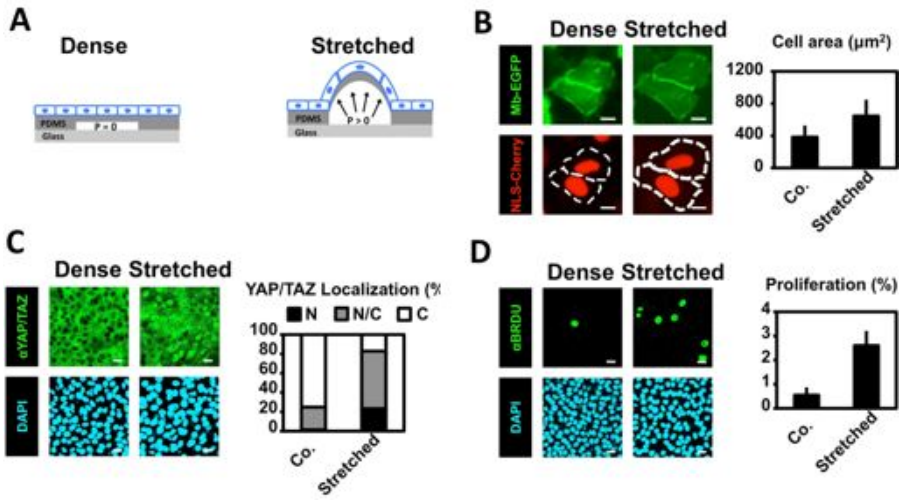

Figure 2: Stretching of an Epithelial Monolayer Overcomes YAP/TAZ Inhibition and Growth Arrest in Contact-Inhibited Cells (A) A monolayer stretching device. Cells were seeded on the upper surface of a PDMS substrate to obtain a dense monolayer (see also Figure S2A). Underneath the PDMS is a chamber filled of fluid (white space between the PDMS and glass). At atmospheric pressure (dense, p = 0), the cell monolayer remains flat; when pressure is applied to the fluid

inside the chamber (stretched, p = 0), the increase of the chamber volume causes a corresponding increase of the surface to which the monolayer is attached. (B) MECs stably expressing membrane-bound EGFP (Mb-EGFP) and nuclear-localized mCherry (NLS-Cherry) were seeded at dense conditions as in Figure 1A on top of the stretching device. After 2 days, cells were imaged under the epifluorescent microscope before (Co.) and immediately after stretching. Pressure was then maintained constant during observation. Projected cell area was measured in the two conditions (dashed lines in the lower pictures indicate the cell boundaries before and after stretching). The graph shows the average quantitation of cell area. The ramping of pressure increase was set in order to avoid destruction of cell-cell contacts (as monitored with Mb-EGFP; data not shown). Scale bar, 20 mm. (C) MECs were plated on the stretching device as in (B). After 2 days, cells were subjected to 6 hr of static stretching, fixed with the device still under pressure, and then processed for immunofluorescence with anti-YAP/TAZ antibody (aYAP/TAZ). DAPI is a nuclear counterstain. Scale bar, 20 mm. (Right) Proportion of cells displaying preferential nuclear YAP/TAZ localization (N, black), even distribution of YAP/TAZ between the nucleus and the cytoplasm (N/C, gray), or prevalently cytoplasmic YAP/TAZ (C, white). Similar results were obtained after 3 hr of stretching (not shown). (D) MECs were plated on the stretching device as described in (B). After 2 days, cells were subjected to 6 hr of static stretching in the presence of BrdU to label cells undergoing DNA duplication. Scale bar, 20 mm. (Right) Quantitation of proliferation measured as the percentage of BrdU-positive cells. Throughout the panels, data are mean and SD. Experiments were performed at least three times with at least three biological replicates each time. Quantitations were carried out by scoring at least 2,000 cells for each sample. Pictures show representative results. See also Figure S2.

C.3.2 F-actin-capping and -severing proteins are YAP/TAZ inhibitors

We next sought to identify molecular players involved in YAP/TAZ regulation by mechanical cues. F-actin regulatory proteins appeared as ideal candidates: treatments that disrupt F-actin or cytoskeletal contractility oppose YAP/TAZ function (Dupont et al., 2011; Wada et al., 2011; Zhao et al., 2012); then, it is recognized that cells respond to external mechanical cues by adjusting the tension and overall organization of their actin cytoskeleton by engaging a plethora of actin-binding proteins (Berrier and Yamada, 2007). Finally, cells plated on small ECM islands, on soft ECM or in a dense monolayer are characterized by similar F-actin organization, as they retain cortical F-actin, but all display reduced or absent F-actin bundles (Figure S2D and data not shown). We thus reasoned that knockdown of endogenous negative regulators of F-actin should restore cytoskeletal structures required for YAP/TAZ activity in inhibitory mechanical conditions. We selected a total of 62 genes identified as F-actin inhibitors in a genome-wide screen (Rohn et al., 2011). In order to specifically identify genes relevant for YAP/TAZ regulation by mechanical cues, we screened them using an unambiguous mechanotransduction assay, that is, the rescue of YAP/TAZ-dependent transcription on soft ECM substrates. MECs were transfected with two pairs of siRNAs for each F-actin inhibitor and seeded on soft hydrogels (approximating an elastic modulus of 0.7 kPa). Cells were harvested after 48 hours and analysed by qPCR for CTGF mRNA expression as read-out of

YAP/TAZ activity (Figure 3A). Although most siRNAs were ineffective, few siRNAs reactivated CTGF expression to levels comparable to, or higher than, those of cells growing on a stiff matrix (Figure 3B). These candidates were then validated by using individual siRNAs and testing their effectiveness at activating multiple YAP/TAZ endogenous targets (CTGF, ANKRD1, CYR61); among the candidates, Cofilin1/2, Capzb and Gelsolin, well-established organizers of F-actin distribution and dynamics (Pollard and Cooper, 2009), stood out as potent YAP/TAZ inhibitors (Figure 3C and S3A and data not shown). Cofilin and Gelsolin (also known as Actin Depolymerizing Factors) increase the turnover of F-actin by severing microfilaments; after severing, Gelsolin remains attached to the newly formed barbed end, preventing filament annealing and polymerization. CapZ (also known as β-actinin or Capping Protein) shares with Gelsolin such actin-capping function (Pollard and Cooper, 2009). Most of what we know about Cofilin, Gelsolin and CapZ in mammalian cells is based on cell migration studies, particularly in the context of dynamic cell protrusions, or from in vitro studies (Pollard and Cooper, 2009), while little data is available on their role in other relevant biological processes. In sparse MECs, depletion of Cofilin, CapZ and Gelsolin caused a general increase in F-actin staining, with particularly thickened stress-fibers, and increased peripheral protrusions resembling filopodia and lamellipodia (Figure 3D and S3B). Supporting the notion that F-actin capping and severing proteins do work through F-actin modification to regulate YAP/TAZ, we found that CapZ depletion could not increase YAP/TAZ activity in cells treated with LatrunculinA, an F-actin inhibitory drug (Figure S3C). To further dissect which subset of the F-actin networks is relevant for YAP/TAZ activity we treated cells with chemical inhibitors of formins (SMIFH2) or ARP2/3 (CK666; CK869; see Supplemental Information for details): these compounds preferentially inhibit formation of F-actin bundles (formin-dependent), or of F-actin branched networks that sustain lamellipodia formation (ARP-dependent). qPCR for CTGF indicated that YAP/TAZ activity mostly depends on F-actin bundles (Figure 3E). Taken together, the results link mechanical regulation of YAP/TAZ activity to F-actin capping/severing proteins and formation of stress fibers. We next used F-actin capping/severing proteins as tools to further query the nature of YAP/TAZ inhibition by cell density. Depletion of Cofilin, CapZ or Gelsolin rescued formation of stress fibers as well as YAP/TAZ nuclear localization, TAZ protein

stability and YAP/TAZ-dependent gene expression in dense cells (Figures 4A-C, S4A and S4B). These findings support the notion that control of YAP/TAZ by high cell density entails a mechanical and cytoskeletal regulation.

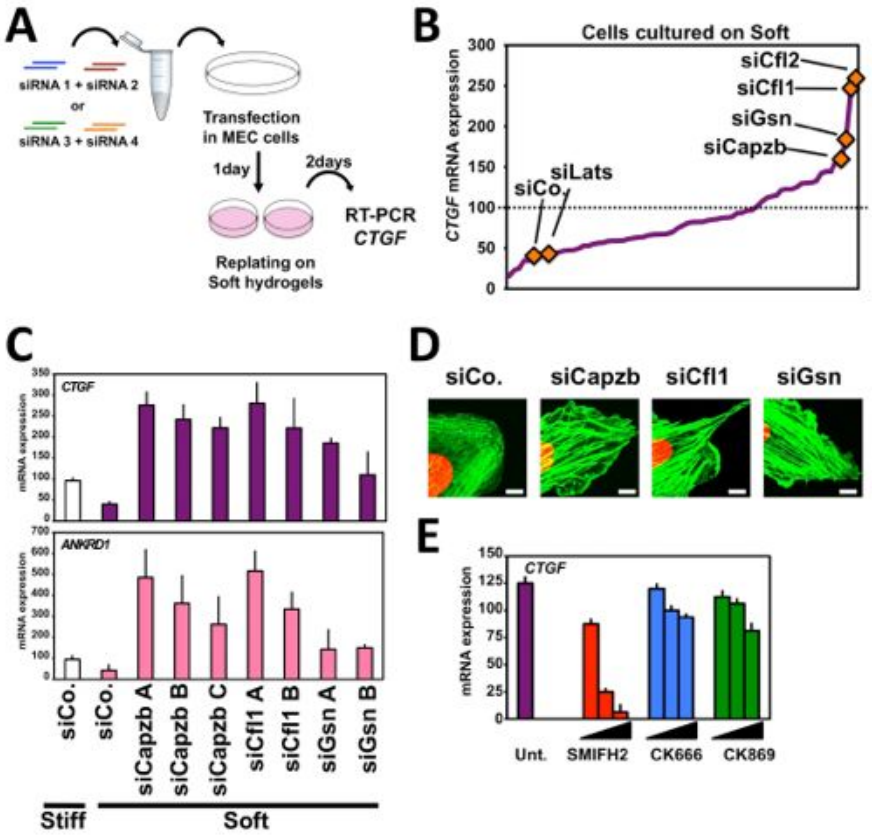

Figure 3: CapZ, Cofilin, and Gelsolin Inhibit YAP/TAZ Activity (A and B) siRNA screen for negative regulators of the F-actin cytoskeleton impinging on YAP/TAZ activity. (A) Schematic overview of the screening procedure. MECs were transfected with two independent couples of siRNAs against each gene (siRNA 1+2 or siRNA 3+4). The day after transfection, cells were replated as single cells on a soft ECM hydrogel (0.7 kPa) and harvested after 2 more days for qPCR analysis. (B) Results of the screening, where each point of the purple line corresponds to a single siRNA/gene. The orange diamonds indicate the effects of controls and of selected siRNAs that were further validated (see text). Cfl, Cofilin; Gsn, Gelsolin. The dotted line represents CTGF levels in cells transfected with siControl (siCo.) but plated on a stiff ECM substrate. Here and throughout the figures, CTGF levels are relative to GAPDH expression. (C) Loss of capping and severing proteins rescues YAP/TAZ inhibition on soft ECM. CTGF (purple) and ANKRD1 (violet) expression in MECs are independent readouts of YAP/TAZ transcriptional activity. Cells were transfected with single siRNA against each gene (A, B, or C). Stiff (white column) is a stiff ECM substrate; soft (colored columns) is a 0.7 kPa ECM hydrogel. See Figure S3A for knockdown efficiencies on endogenous proteins. (D) Loss of Capzb, Cfl1, and Gsn induces formation of thicker actin bundles. Close-up confocal immunofluorescence of MECs transfected with the indicated siRNA and stained for F-actin with phalloidin (green) and nuclei (TOTO3, red). Scale bar, 20 μm. See Figure S3B for increased filopodia and lamellipodia after Capzb, Cfl1, and Gsn knockdown. Consistent results were obtained with independent siRNAs (not shown). (E) Regulation of F-actin dynamic and assembly by formin proteins is required for YAP/TAZ activity. MECs were plated on a stiff ECM substrate and treated for 24 hr with increasing doses of the inhibitor of formin-homology 2 domains SMIFH2 (used at 5, 15, 30 μM) or of the Arp2/3 inhibitors CK666 (5, 10, 50 mM) and CK869 (5, 10, 50 μM). Data are mean and SD. Experiments were performed three times with at least three biological replicates each time. See also Figure S3 and Tables S1 and S2.

C.3.3 Role of YAP/TAZ and F-actin inhibitors in mechanical patterning of cell proliferation

Next, we wondered whether YAP/TAZ reactivation by depletion of F-actin capping and severing proteins is also paralleled by a rescue of CIP. To address this question, we employed microfabrication methods to stamp fibronectin-coated substrates of defined shape and area. This set-up allows studying how patterns of mechanical forces generate patterned growth within a monolayer: cells located at the borders of the island experience higher mechanical stress than cells located in the center (Nelson et al., 2005). MECs were uniformly seeded at high density on circular islands and, after 48 hours, cell proliferation rate was assayed by BrdU incorporation (Figure S4C). As shown in Figure 4D, the number of cells in S-phase greatly decreased in the center of the island but persisted at the border, matching the distribution of physical forces (Nelson et al., 2005). Knockdown of YAP and TAZ revealed that proliferation at the border was YAP/TAZ dependent (Figure 4D). This growth pattern - as previously noticed (Nelson et al., 2005) - was driven by tensional forces, since inhibition of non-muscle myosin II with blebbistatin, or of myosin light chain kinase with ML-7, greatly reduced proliferation at the culture borders, phenocopying attenuation of YAP/TAZ (Figure 4D). Strikingly, depletion of CapZ and Cofilin clearly prevented CIP in center cells. Importantly, this occurred without increasing the growth of cells at the border, thus partially leveling the growth differentials within the epithelial sheet (Figure 4D). The restoration of proliferation by depletion of capping and severing proteins was dependent on YAP and TAZ (Figure 4D). We obtained similar results by seeding cells on square-shaped islands, where YAP/TAZ-dependent proliferation was concentrated at corners and edges (Figures S4D, S4E and data not shown). The above results suggest that the form of an epithelial monolayer generates patterns of tensional forces that translate into differentials of YAP/TAZ activity, whose establishment requires F-actin inhibitors. Yet, in vivo, distinct tissues not only exhibit specific shapes, but also their ECM composition varies greatly, due to the content, crosslinking and topology of collagen fibers (Butcher et al., 2009).

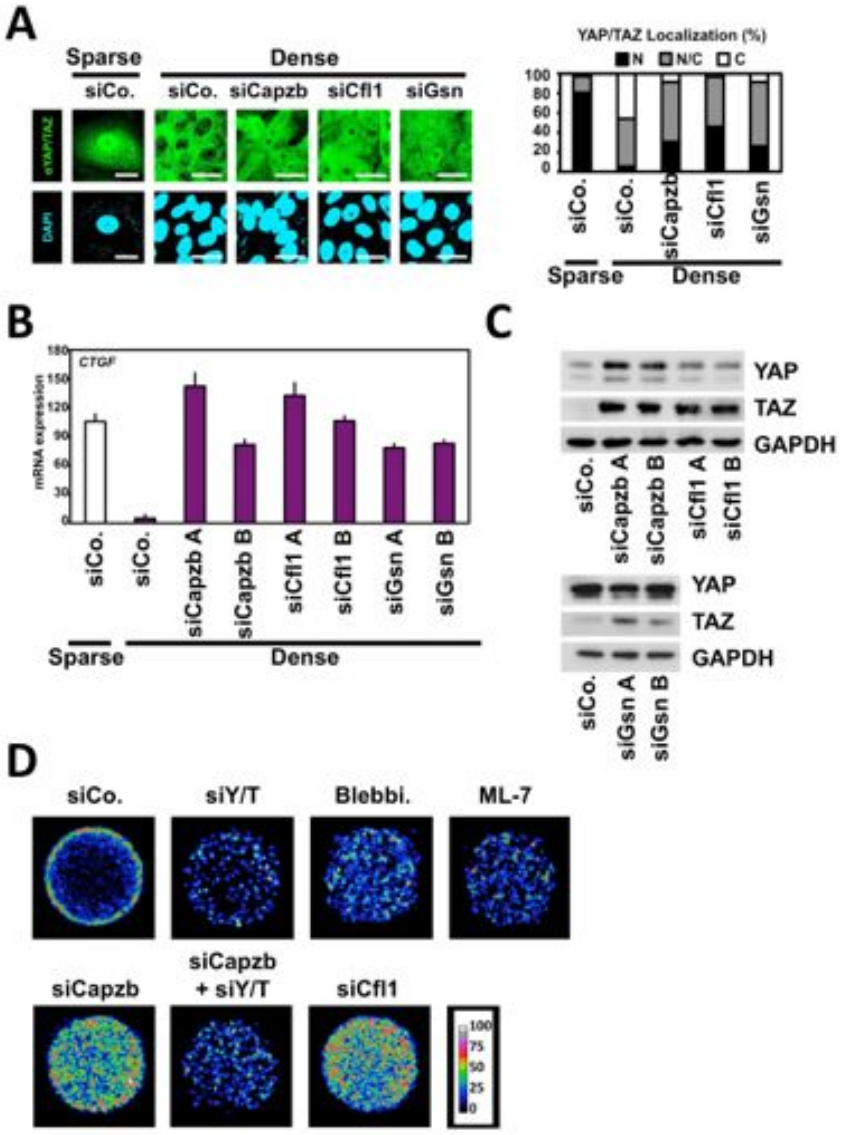

Figure 4: Knockdown of F-Actin-Capping and -Severing Factors Rescues Contact Inhibition of Proliferation (A) Loss of Capzb, Cfl1, or Gsn rescues YAP/TAZ nuclear localization in dense monolayers. MECs were transfected with the indicated siRNA and were seeded to obtain sparse cells or a dense mono- layer. After 2 days, cells were fixed for immunofluorescence with anti-YAP/TAZ antibody (aYAP/ TAZ). DAPI is a nuclear counterstain. Scale bar, 20 μm. (Right) Proportion of cells displaying preferential nuclear YAP/TAZ localization (N, black); even distribution of YAP/TAZ between the nucleus and the cytoplasm (N/C, gray); or cytoplasmic YAP/ TAZ (C, white). Consistent results were obtained with independent siRNAs (not shown). (B) CTGF expression in MECs transfected and seeded as in (A). Loss of Capzb, Cfl1, and Gsn rescues YAP/TAZ transcriptional activity in dense monolayers. (C) Western blotting for TAZ and YAP in MECs transfected and seeded as in (A). GAPDH is a loading control. (D) Panels show colorimetric stacked images of BrdU incorporation, used to visualize spatial variations of proliferation in cell monolayers of defined shape and dimensions. MECs were plated as monolayers on large microprinted fibronectin islands (diameter, 350 μm) and processed as described in the text and as in the Figure S4C legend. The color scale indicates the extent of cell proliferation in a given position of the monolayers. The proliferation rate decreases to nearly undetectable levels at the center of the circle due to CIP (black/blue color), whereas cells continue proliferating along the border of the cellular sheet (green/ red color). Cultures were treated with blebbistatin (Blebbi, 50 μM) or myosin light-chain kinase inhibitor (ML-7, 10 μM) overnight before the BrdU pulse. For experiments with siRNAs, cells were first transfected with the indicated siRNA and were re- plated after 1 day. Similar results were obtained on islands of square shape (Figures S4D and S4E). Data are mean and SD. Experiments were per- formed at least twice

with biological replicates each time. Quantitations were carried out by scoring at least 2,000 cells for each sample. Pictures show representative results. See also Figure S4 and Table S1.

To mimic such integration, we investigated the roles of YAP/TAZ, and F-actin capping and severing proteins, on the behavior of MECs growing in three dimensions (3D). For this, we used reconstituted ECM containing a mix of basement membrane (BM; Matrigel) and collagenI (COL), whose concentration can be changed to obtain soft and stiff BM/COL gels (COL 1.2 mg/ml or 3 mg/ml, respectively) (Paszek et al., 2005) (see Figure S5A for validation of these gel compositions as mechano-regulators of YAP/TAZ). After 8 days in culture, MECs growing embedded in soft BM/COL gels formed growth-arrested acini (Figure 5A). When collagen concentration was increased, we observed the formation of larger spheroids, actively growing tubules and organoid-like structures (Figure 5A). By immunofluorescence, YAP/TAZ were predominantly evenly distributed in cells cultured in soft ECMs, but were clearly nuclear in cells embedded in the stiffer ECM (Figure 5B). Transcriptional activation of YAP/TAZ by increased ECM stiffness in 3D cultures was confirmed by induction of endogenous markers, such as CTGF, CYR61 and ANKRD1 mRNAs (Figure S5B). siRNA-mediated knockdown of YAP and TAZ caused severe reduction of the overall number and size of the 3D colonies, that in no case expanded beyond small aggregates, regardless of substrate rigidity (data not shown). We next sustained endogenous YAP/TAZ activity in cells embedded in the soft ECM through siRNA-mediated knockdown of Cofilin or Gelsolin. Strikingly, this induced the formation of bigger acini and caused the appearance of elongated or branched structures (Figure 5C) and was paralleled by YAP/TAZ-dependent induction of CTGF and CYR61 mRNAs (Figure 5D). Using phospho-histone-3 as proliferation marker, acini transfected with control-siRNA were mainly growth arrested, while Cofilin or Gelsolin-depleted spheroids retained proliferative activity (Figure 5E). We conclude that YAP/TAZ regulation by F-actin capping and severing proteins plays a critical role in regulating the growth of epithelial cells in a 3D reconstituted ECM.

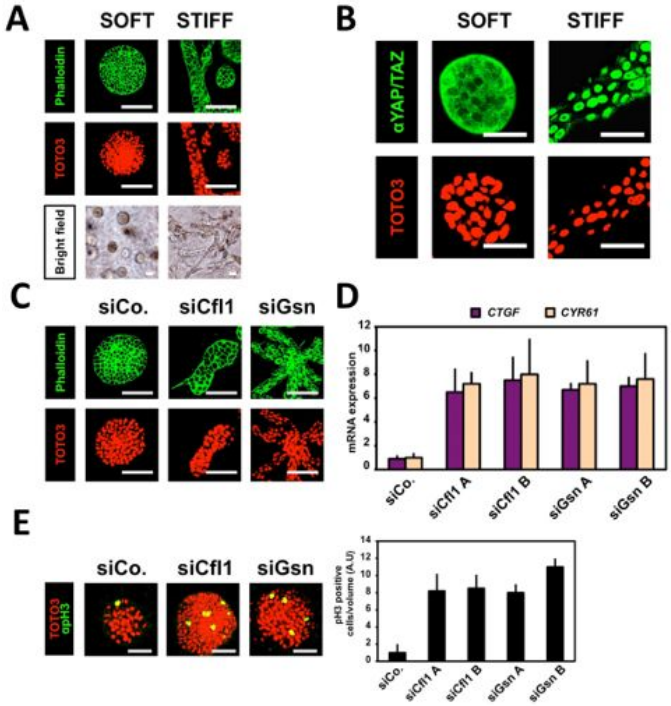

Figure 5: 3D Matrix Stiffness Regulates Growth and Morphogenesis of Mammary Epithelial Cells through YAP/TAZ (A) Mammary epithelial cells (MECs) were embedded as a single cell in a matrix formed of a different mixture of Matrigel and CollagenI (see Experimental Procedures). Soft matrix contained 1.2 mg/ml CollagenI, whereas stiff matrix contained 3 mg/ml CollagenI (Paszek et al., 2005). After 8 days, cells were fixed and stained for phalloidin to help visualize the morphology of multicellular structures. TOTO3 is a nuclear counterstain. Scale bar, 100 μm. Bottom panels show bright fields at lower magnification. (B) 3D matrix density regulates YAP/TAZ localization, as assayed by confocal immunofluorescence with anti-YAP/TAZ antibody (aYAP/TAZ). MECs were plated as in (A) and were fixed after 6 days. TOTO3 is a nuclear counterstain. Scale bar, 100 μm. (C) Loss of Cfl1 and Gsn promotes the formation of tubule-like structures in soft 3D matrix. MECs were transfected with the indicated siRNAs and then embedded in soft matrix as in (A). After 8 days, acini were fixed and stained for phalloidin. TOTO3 is a nuclear counterstain. Scale bar, 100 μm. (D) Loss of Cfl1 and Gsn increases YAP/TAZ transcriptional activity in soft 3D matrix. MECs were treated as in (C) and were harvested for qPCR of the YAP/TAZ target genes CTGF and CYR61. (E) Loss of Cfl1 and Gsn promotes proliferation of cells embedded in 3D soft matrix. MECs were treated as in (C) and were stained with anti-pH3 antibody to mark mitotic cells. pH3 signal is shown merged with the TOTO3 nuclear counterstaining. Scale bar, 100 μm. (Right) Quantitation of cell mitosis normalized to the volume of the multicellular structures, as calculated from 3D z stacks reconstructions. Data are mean and SD obtained from at least 20 structures per condition. Data are mean and SD. Experiments were performed at least twice with biological replicates each time. Pictures show representative results. See also Figure S5 and Table S1.

C.3.4 Cytoskeletal regulation of YAP/TAZ dominates over Hippo signaling

We next sought to investigate the intersections between the control of YAP/TAZ activity by cytoskeletal cues and the classical Hippo cascade, centered on the activity of two kinases, MST1/2 (Hippo in Drosophila) and LATS1/2, the latter directly phosphorylating YAP/TAZ and causing their inhibition (Pan, 2010). CIP has been associated to increased YAP/TAZ phosphorylation mediated by LATS1/2 (Zhao et al., 2007); similar phosphorylation occurs in cells rounded

after placing them in suspension, or upon disruption of the F-actin cytoskeleton (Kim et al., 2013; Wada et al., 2011; Zhao et al., 2012). Fully confirming these associations, we also found increased YAP/TAZ phosphorylation in cells treated with LatrunculinA, an F-actin inhibitory drug (Figure 6A). YAP/TAZ phosphorylation, however, may not automatically surrogate for biological function, and no previous studies supported this biochemical observation with functional evidence (Halder et al., 2012). To investigate the functional role of LATS, we used independent pairs of validated siRNAs targeting both LATS1 and LATS2. We first controlled the efficacy of LATS-depletion by reconstituting NF2 expression, a bona fide upstream regulator of the Hippo cascade, in the NF2-null breast cancer cell line MDA-MB-231 (Dupont et al., 2011). NF2 re-expression caused a dramatic inhibition of TEAD luciferase reporter and LATS1/2 inactivation completely abolished this effect, confirming the efficacy of our siRNAs (Figure 6B). Similarly, NF2 re-expression was completely ineffective in cells expressing only a LATS-insensitive, phosphorylation mutant form of YAP or TAZ (Figure S6A and data not shown). Next, we wondered if LATS1/2 were downstream of mechanical cues. If this were the case, as in the above NF2 paradigm, loss-of-LATS1/2, or loss-of-YAP/TAZ phosphorylation, should also rescue YAP/TAZ activity in cells on soft ECM or dense cultures. In stark contrast to this hypothesis, the results for mechanical regulation were different: depletion of LATS1/2 could not rescue YAP/TAZ inhibition by a soft environment (Figures 6C), indicating that F-actin and mechanical regulation affect YAP/TAZ activity independently from their phosphorylation by LATS. In line, cells expressing only LATS-insensitive YAP or TAZ mutants (5SA-YAP, 4SA-TAZ) did not escape mechanical inhibition when cultured on soft hydrogels (Figure S6B and S6C). Using CapZ inactivation as paradigm of cytoskeletal remodeling, we also found that cells expressing 4SA-TAZ were still responding to depletion of CapZ (Figure S6D). Finally, knockdown of CapZ left the YAP/TAZ phosphorylation levels completely unchanged, as shown by Phos-TAG analysis (Figure 6D); collectively, the results strongly suggest that YAP/TAZ control by the F-actin cytoskeleton and Hippo signaling represent formally distinct regulations. An unexpected discovery came when we simultaneously inactivated CapZ together with LATS1/2 in MECs cultured in soft or dense conditions. The results actually showed that LATS1/2 are effective inhibitors of YAP/TAZ only in the context of a mechanically competent

F-actin cytoskeleton. Several results support this conclusion: (i) combined depletion of CapZ and LATS1/2 cooperated to fully induce nuclear localization of YAP and TAZ in cells seeded on soft hydrogels and dense conditions (Figure 6E and 6F); (ii) LATS1/2 depletion in either soft or dense MEC cultures was inconsequential per se but potently synergized with CapZ depletion to maximize YAP/TAZ transcriptional activity (Figure 6G and 6H); (iii) in large square (or round) fibronectin-coated islands, LATS1/2 depletion alone could not rescue CIP (Figure 6I, S6E, S6F), and left proliferation of cells at the border still sensitive to inhibitors of cytoskeletal tension (Figure S6E). However, combined depletion of CapZ and LATS1/2 fully rescued the blockade of S-phase entry in cells located at the center of the epithelial sheets triggering unabated proliferation evenly throughout the island (Figure 6I and S6F). We next tested how loss of YAP/TAZ regulation by the Hippo kinases impacted on MECs growing in 3D within a soft or stiff ECM. To this end, we compared MECs stably expressing near to endogenous levels of wild-type TAZ, and LATS phosphorylation-insensitive 4SA-TAZ. As shown in Figure 6J, wild-type TAZ expressing cells behaved similarly to their parental counterparts. 4SA-TAZ expressing cells displayed increased protrusive activity in soft ECM, yet retained a spheroid structure. Notably, in the more rigid ECM, 4SA-TAZ expressing cells did not form tubular structures and invaded the matrix as single cells. As TAZ overexpression has been shown to induce Epithelial-to-Mesenchymal Transition in cells cultured on plastic in 2D (Lei et al., 2008), this 3D phenotype likely reflects fully unleashed TAZ activity. Finally, we asked if the permissive effect of the cytoskeleton is specific for the Hippo pathway or also applies to other regulatory inputs. To this end, we used two inducers of YAP/TAZ, WNT and GPCR signaling (Azzolin et al., 2012; Yu et al., 2012), and monitored their efficacy in soft vs. stiff extracellular conditions. As shown in Figure 6K, knockdown of APC (mimicking WNT signaling by inactivation of the APC/Axin/GSK3 TAZ destruction complex (Azzolin et al., 2012)) caused robust upregulation of YAP/TAZ-dependent transcription in cells cultured on stiff substrates, but had minimal effect in cells seeded on a soft matrix. Similarly, addition of TRAP6, a positive inducer of YAP/TAZ activity through GPCR-signaling, could operate only in cells cultured on stiff, but not on soft matrices (Figure 6L). Remarkably, depletion of capping and severing proteins re-empowered YAP/TAZ activation by WNT and GPCR

signaling (Figures 6K, 6L and data not shown). Collectively, the results suggest that mechanical and physical properties of the environment control not just Hippo signaling but also YAP/TAZ responsiveness to signaling cascades initiated by soluble growth factors.

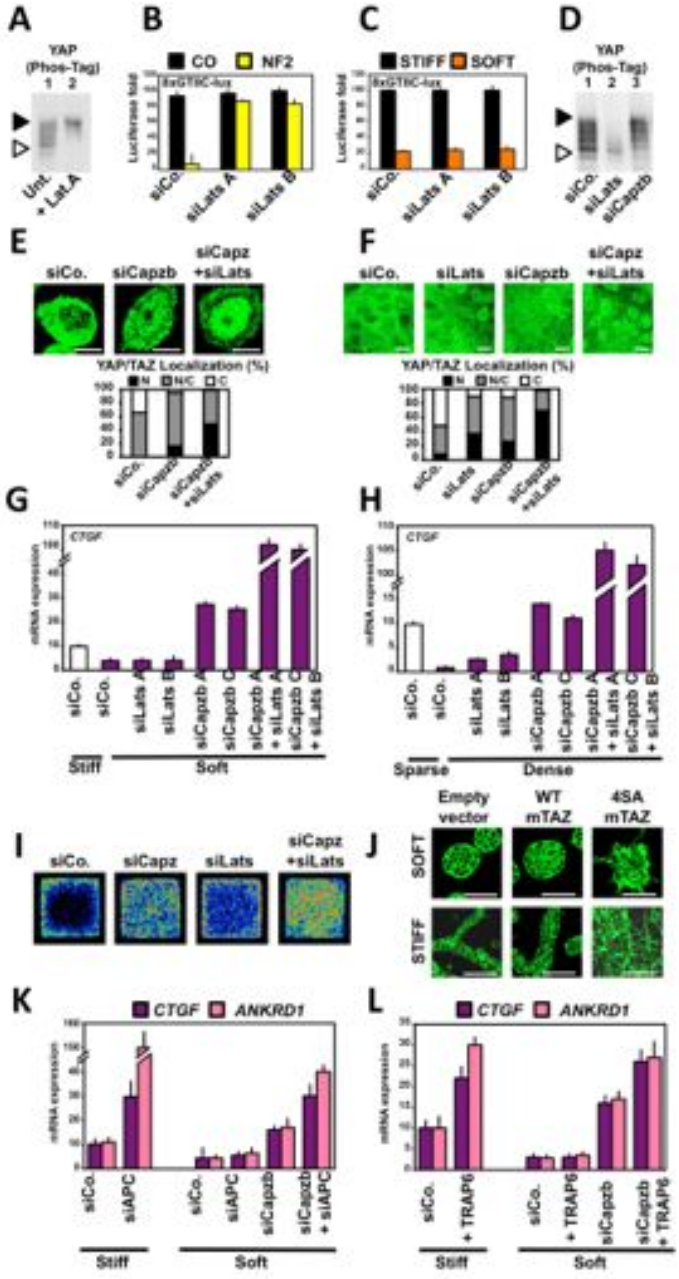

Figure 6: Cytoskeletal Mechanics Is a Dominant Input for YAP/TAZ Activity. (A) Disruption of the F-actin cytoskeleton induces YAP phosphorylation. Phos-TAG SDS-PAGE analysis of MECs plated as confluent monolayer and treated with LatrunculinA (Lat.A, 100 µM) for 3 hr. Black and white arrowheads indicate hyperphosphorylated or nonphosphorylated YAP, respectively. Identity of YAP isoforms was defined based on extracts from cells transfected with YAP siRNA and on l-phosphatase treatment (not shown). (B) LATS1/2 knockdown completely rescues YAP/ TAZ inhibition by NF2/Merlin. Luciferase reporter assay (8XGTIIC) in MDA-MB-231 transfected with the indicated siRNA and without (Co.) or with NF2 expression plasmid. See Figure S6A for similar results obtained with LATS-insensitive 5SA-YAP mutant. Similar results were obtained in

HeLa cells (not shown). (C) LATS1/2 knockdown does not rescue YAP/ TAZ inhibition by soft ECM. Luciferase reporter assay (8XGTIIC) in MDA-MB-231 cells transfected with the indicated siRNA and replated on stiff or soft ECM substrates. See Figure S6B for similar results obtained with LATS-insensitive 5SA-YAP mutant. Similar results were obtained in HeLa cells (not shown). Of note, inhibition of LATS by constitutive-activation of PI3K or AKT (Fan et al., 2013), known for being downstream of integrin signaling, could not rescue YAP/TAZ inhibition by soft ECM; and inhibition of PI3K, AKT, and mTOR by small-molecule inhibitors had no effect on a stiff ECM (data not shown). (D) Capzb knockdown does not result in a decrease of YAP phosphorylation. Phos-TAG SDS-PAGE analysis of MECs transfected with the indicated siRNAs and plated as confluent mono- layers. Black and white arrowheads indicate hyperphosphorylated or nonphosphorylated YAP, respectively. (E) MECs were transfected with the indicated siRNAs and were plated on soft ECM substrates. After 2 days, cells were fixed for immunofluorescence with anti-YAP/TAZ antibody. Scale bar, 10 μm. (Below the pictures) Proportion of cells displaying preferential nuclear YAP/TAZ localization (N, black), even distribution of YAP/TAZ between the nucleus and the cytoplasm (N/C, gray), or prevalently cytoplasmic YAP/TAZ (C, white). Transfection of LATS1/2 siRNA alone had no significant effects on YAP localization (not shown). Consistent results were obtained with independent siRNAs (not shown). (F) MECs were transfected with the indicated siRNAs and were seeded to obtain a dense monolayer. After 2 days, cells were fixed for immunofluorescence with anti-YAP/TAZ antibody. Scale bar, 20 μm. (Below the pictures) Proportion of cells displaying preferential nuclear YAP/TAZ localization (N, black), even distribution of YAP/ TAZ between the nucleus and the cytoplasm (N/C, gray), or prevalently cytoplasmic YAP/TAZ (C, white). (G) MECs were transfected with the indicated siRNAs and were plated on stiff (white column) or soft (colored columns) ECM substrates. After 2 days, cells were harvested for qPCR analysis. LATS knockdown has no effects on a soft ECM but potently enhances CTGF transcription upon combined depletion of Capzb. Similar results were obtained with ANKRD1 and CYR61. (H) MECs were transfected with the indicated siRNAs and plated as sparse cells (white column) or dense monolayers (colored columns). After 2 days, cells were harvested for qPCR analysis. Similar results were obtained with ANKRD1 and CYR61. (I) Combined depletion of LATS1/2 and Capzb completely rescues contact inhibition of proliferation. Panels show colorimetric stacked images of BrdU incor- poration in MECs transfected with the indicated siRNAs and seeded on top of microprinted square fibronectin islands (side, 500 μm). The synergistic effect of LATS and Capzb depletion is indicated by the stark increase of red-stained areas (indicating higher proliferation) compared to the other conditions. Similar results were obtained with circular microprinted fibronectin islands (see Figure S6F). (J) MECs were transfected with YAP/TAZ siRNA (to avoid interference from endogenous proteins) and reconstituted with siRNA-insensitive mouse TAZ (mTAZ). TAZ add-back was carried out with both WT and LATS-insensitive 4SA mTAZ. Cells expressing empty vector and transfected with control siRNA serve as controls. Cells were embedded as a single cell in a matrix formed of a different mixture of Matrigel and CollagenI to obtain softer and stiffer gels (see legend to Figure 5A and Experimental Procedures). After 6 days, cells were fixed and stained for phalloidin to help visualize the morphology of multicellular structures. Scale bar, 100 μm. (K and L) WNT and GPRC signaling efficiently promote YAP/TAZ-dependent transcription on soft substrates only after Capzb depletion. (K) MECs were transfected with control siRNA (siCo.), APC siRNA (siAPC) to activate WNT signaling, or with Capzb siRNA (siCapzb). Cells were plated on stiff or soft ECM substrates and were harvested after 2 days for qPCR of YAP/TAZ target genes (CTGF and ANKRD1). (L) MECs were transfected with the indicated siRNAs and were plated on stiff or soft ECM substrates. After 1 day, cells were serum starved overnight and were subsequently left untreated or treated with 2 μM TRAP6 for 3 hr. Data are mean and SD. Experiments were performed at least twice with biological replicates each time. Quantitations were carried out by scoring at least 2,000 cells for each sample. Pictures show representative results. See also Figure S6 and Table S1.

C.4 Discussion

How cell shape and tissue form connect with tissue function, growth and patterning is one of the most fascinating and least understood aspects of biology. Here we provide evidence that tissue shape and three-dimensional ECM compliance pattern the proliferative competence of an epithelial sheet. These

inputs localize YAP/TAZ activity at sites of high mechanical stresses, and inhibit it where mechanical forces are minimal. Thus, YAP and TAZ regulation serves as link between tissue architecture and a key cellular function, that is, proliferation. YAP/TAZ inhibition entails a remodeling of the F-actin cytoskeleton mediated by F-actin capping and severing proteins, for which we reveal an essential role as proliferative checkpoints in mammalian epithelial sheets through YAP/TAZ regulation. The presently described connections appear to hold a number of implications for the biology of epithelial cells. For organ size control, tissue regeneration and homeostasis cells must be constantly informed of the size and shape of the whole organ (Dischер et al., 2009; Huang and Ingber, 1999; Nelson and Bissell, 2006). This suggests that cells are able to perceive what happens many cell diameters away and respond to it with great spatial accuracy. Mechanical forces are ideally suited to serve as messenger of this global control, as it has been recently shown that forces display long-range and broad scale effects (Halder et al., 2012; Guo et al., 2012). Using monolayers of defined shape and size, here we show that patterns of mechanical stresses locally control YAP/TAZ activity. At sites of low mechanical forces, that is, in contact-inhibited center cells, YAP/TAZ are inhibited by F-actin capping and severing proteins, as loss-of-CapZ or Cofilin potently rescues YAP/TAZ nuclear localization, transcriptional activity and proliferation. In contrast, cells at edges and corners of the same multicellular sheets display YAP/TAZ dependent proliferation induced by cytoskeletal contractility and, here, loss-of-CapZ or Cofilin has marginal effects.

Inactivation of capping and severing proteins is accompanied by reappearance of F-actin stress fibers. Conversely, YAP/TAZ inactivation is phenocopied by inhibiting formin and myosin, which by themselves are essential for stress fibers formation and cellular contractility. These data collectively suggest that mechanical forces promote YAP/TAZ activity at least in part by inhibiting capping and severing proteins. However, this does not exclude a different scenario, one in which YAP/TAZ are regulated independently by mechanical forces and capping/severing proteins; the latters may operate to unbalance the distribution of microfilaments to different, perhaps competing, F-actin pools (e.g. cortical F-actin, stress fibers and nuclear actin) endowed with different YAP/TAZ activating capacities. In other words, while this study unambiguously identifies

endogenous F-actin capping and severing proteins as YAP/TAZ inhibitors, a more detailed picture of their function will necessarily require the unraveling of the precise mechanisms by which F-actin affects YAP/TAZ-dependent transcription as well as a more comprehensive understanding of cellular rigidity sensing. Classical experiments using transformed mammary epithelial cells grown as spheroids in three-dimensional ECM of distinct rigidities and compositions unequivocally showed that the physical properties of the matrix could lead to tumor cells "reversion" to a near normal phenotype, overriding oncogenic aberrations (Nelson and Bissell, 2006). Conversely, ECM stiffening, and ensuing cytoskeletal tension, cooperate with oncogenes, and may even initiate aberrant proliferation (Butcher et al., 2009). Yet, how the microenvironment intercepts the malignant phenotype at the level of gene-expression is a major question in cancer biology. Here we show that transformed mammary epithelial cells grown in low-collagen 3D environments display low levels of YAP/TAZ activity, while collagen-rich matrices induce YAP/TAZ nuclear localization, YAP/TAZ target genes and YAP/TAZ dependent proliferation. These observations are consistent with the positive correlations between collagen content and tissue stiffness (as determined by mammographic density) with breast cancer risk and metastasis (Butcher et al., 2009). Here we show that F-actin capping and severing proteins are instrumental for the effects of a soft ECM, as their depletion induces YAP/TAZ activation and proliferation, phenocopying the attributes of a more rigid ECM environment. This work also provides a unifying principle for how contact inhibition of proliferation is realized. We propose a two-step model of this classic phenomenon (McClatchey and Yap, 2012). As cells engage in cell-cell adhesion - starting from a situation of unrestricted adhesive areas with fully nuclear YAP/TAZ - the E-cadherin/catenins system triggers LATS activation and YAP/TAZ phosphorylation, as previously reported (Kim et al., 2011; Zeng and Hong, 2008), but this is insufficient for overt growth arrest. Then, as proliferation continues, cell crowding causes reduction of cell size and low mechanical stress, now leading to a more effective contact inhibition. We show that the regulation of YAP/TAZ by cell mechanics is not only distinct from Hippo pathway-induced YAP/TAZ phosphorylation and inhibition, but in fact dominates over it. Remarkably, LATS1/2 inactivation is per se inconsequential in cells experiencing a low mechanical stress. Moreover, depletion of F-actin capping/severing proteins

sustains YAP/TAZ activity without affecting their phosphorylation. In fact, LATS-mediated inhibition of YAP/TAZ requires a mechanically competent cytoskeleton, as the effect of LATS knockdown becomes manifest only in the absence of F-actin capping/severing proteins. Our finding that LATS and F-actin organization act independently to regulate YAP/TAZ is also supported by genetic evidence in Drosophila (Fernández et al., 2011; Sansores-Garcia et al., 2011). In fly wing development, inactivation of the CapZ homologue induces organ overgrowth similarly to Hippo mutations, and the extent of this phenotype can be either counteracted or amplified, respectively by overexpression or inactivation of LATS, altogether making unlikely an epistatic relationship between the two inputs. Our data further suggest that the scale of activation of YAP/TAZ may be particularly broad, depending on the relative intensity and duration of cytoskeletal and Hippo controls. There is ample genetic evidence for the Hippo pathway as an intrinsic regulator of organ size; for example, inactivation of the upstream Hippo kinase MST1/2, or of its cofactor Salvador/WW45, causes remarkable tissue overgrowth in several organs, including liver, intestine and skin (Ramos and Camargo, 2012). According to our findings, the effect of a Hippo pathway mutation should not indiscriminately affect all cells, but preferentially expand the cell populations experiencing a mechanical stress. The existence of a second control layer for YAP/TAZ activity overseeing the effects of an Hippo mutation is supported by in vivo observations: in the liver, YAP/TAZ hyperactivation by Hippo deficiencies generates a functional and histologically well-organized organ (Ramos and Camargo, 2012; Zhou et al., 2009), a finding incompatible with global and uncontrolled cell proliferation. Similarly, in the α-catenin knockout mouse model, YAP activation remains spatially restricted to the basal layer of the skin, where YAP protein is normally confined (Schlegelmilch et al., 2011), suggesting that cell attachment to the appropriate ECM is instrumental to locally sustain normal as well as aberrant YAP activation. Finally, the idea that the cytoskeleton is a key input for YAP/TAZ in vivo is supported by recent genetic evidence: kidney development requires YAP activation by the CDC42 Rho-GTPase, well known promoter of F-actin polymerization (Reginensi et al., 2013).
Besides the Hippo pathway, mechanical cues also dominate the cellular response to soluble cues positively affecting YAP and TAZ activity. We show that YAP/TAZ activation by WNT or GPCR signaling requires a mechanically

stressed cytoskeleton, or, in cells experiencing a soft ECM, inactivation of F-actin capping and severing proteins. In the same line of thought, the fact that YAP/TAZ are stabilized and act in stem and progenitor cells, typically lodged in specific tissue-niches (Ramos and Camargo, 2012), is an enticing argument that the status of the ECM, the cell's cytoskeletal organization and tension may impart a "physical" competence for stemness and differentiation.

C.5 Experimental procedures

C.5.1 Plasmids

siRNA-insensitive FLAG-hYAP1 WT and 5SA were generated by PCR and subcloned in pcDNA3. pXJ40-HA-Merlin/NF2 S518A is Addgene# 19701. 8xGTIIC-lux (Dupont et al., 2011) is Addgene# 34615.

C.5.2 Cell cultures and Transfections

MCF10A and MII cells were used with equal results, except for experiments shown in Figure 3 and 5 where we used only MII cells. Micropatterned glass slides were from Cytoo. Fibronectin-coated hydrogels were as previously described (Dupont et al., 2011). The monolayer stretching-device was fabricated by using standard soft-lithography techniques. For 3D assays, cells were embedded into mixes of Growth Factor Reduced Matrigel (BD Biosciences) and CollagenI (TREVIGEN CULTUREX 3D Culture Matrix Rat CollagenI). For assays on large square and circular fibronectin-coated islands, 1.000.000 cells were plated in a 35mm dish containing a single Cytoo glass slide. siRNA transfections were done with Lipofectamine RNAi-MAX (Life technologies). Sequences of siRNA are provided in Table S1 and S2. DNA transfections were done with TransitLT1 (Mirus Bio). siRNA and DNA transfection were performed on sparse cells plated on tissue culture plastics before replating on the various ECM substrates and islands. For Retroviral infections see (Azzolin et al., 2012).

C.5.3 Antibodies and Bioassays

Antibodies: anti-YAP/TAZ (sc101199), anti-CAPZB (sc81804), anti-COFILIN1 (Epitomics 6663-1), anti-GELSOLIN (sc57509), anti-GAPDH (Millipore mAb374), anti-LATS1 (CST) and anti-LATS2 (Abcam), anti-E-Cadherin (BD

Biosciences). For microscopy, luciferase, proliferation and real-time PCR assays see Extended Experimental Procedures.

Supplemental Information includes Extended Experimental Procedures, six figures, and two tables and can be found with this article online at http://dx.doi.org/10.1016/j.cell.2013.07.042

C.6 References

[1] Discher, D.E., Mooney, D.J., and Zandstra, P.W. (2009). Growth factors, matrices, and forces combine and control stem cells. Science 324 , 1673– 1677.
[2] Huang, S., and Ingber, D.E. (1999). The structural and mechanical complexity of cell-growth control. Nat. Cell Biol. 1 , E131–E138.
[3] Sasai, Y. (2013). Cytosystems dynamics in self-organization of tissue architec- ture. Nature 493 , 318–326.
[4] Nelson, C.M., Jean, R.P., Tan, J.L., Liu, W.F., Sniadecki, N.J., Spector, A.A., and Chen, C.S. (2005). Emergent patterns of growth controlled by multicellular form and mechanics. Proc. Natl. Acad. Sci. USA 102 , 11594–11599.
[5] Nelson, C.M., and Bissell, M.J. (2006). Of extracellular matrix, scaffolds, and signaling: tissue architecture regulates development, homeostasis, and cancer. Annu. Rev. Cell Dev. Biol. 22 , 287–309.
[6] Berrier, A.L., and Yamada, K.M. (2007). Cell-matrix adhesion. J. Cell. Physiol. 213 , 565–573.
[7] Miranti, C.K., and Brugge, J.S. (2002). Sensing the environment: a historical perspective on integrin signal transduction. Nat. Cell Biol. 4 , E83–E90.
[8] Schwartz, M.A. (2010). Integrins and extracellular matrix in mechanotransduc- tion. Cold Spring Harb. Perspect. Biol. 2 , a005066.
[9] Vogel, V., and Sheetz, M. (2006). Local force and geometry sensing regulate cell functions. Nat. Rev. Mol. Cell Biol. 7 , 265–275.
[10] Halder, G., Dupont, S., and Piccolo, S. (2012). Transduction of mechanical and cytoskeletal cues by YAP and TAZ. Nat. Rev. Mol. Cell Biol. 13 , 591–600.
[11] Dupont, S., Morsut, L., Aragona, M., Enzo, E., Giulitti, S., Cordenonsi, M., Zan- conato, F., Le Digabel, J., Forcato, M., Bicciato, S., et al. (2011). Role of YAP/ TAZ in mechanotransduction. Nature 474 , 179–183.
[12] Pan, D. (2010). The hippo signaling pathway in development and cancer. Dev. Cell 19 , 491–505.
[13] Zeng, Q., and Hong, W. (2008). The emerging role of the hippo pathway in cell contact inhibition, organ size control, and cancer development in mammals. Cancer Cell 13 , 188–192.
[14] Cordenonsi, M., Zanconato, F., Azzolin, L., Forcato, M., Rosato, A., Frasson, C., Inui, M., Montagner, M., Parenti, A.R., Poletti, A., et al. (2011). The Hippo transducer TAZ confers cancer stem cell-related traits on breast cancer cells. Cell 147 , 759–772.
[15] Harvey, K.F., Zhang, X., and Thomas, D.M. (2013). The Hippo pathway and human cancer. Nat. Rev. Cancer 13 , 246–257.
[16] Azzolin, L., Zanconato, F., Bresolin, S., Forcato, M., Basso, G., Bicciato, S., Cordenonsi, M., and Piccolo, S. (2012). Role of TAZ as mediator of Wnt signaling. Cell 151 , 1443–1456.
[17] Yu, F.-X., Zhao, B., Panupinthu, N., Jewell, J.L., Lian, I., Wang, L.H., Zhao, J., Yuan, H., Tumaneng, K., Li, H., et al. (2012). Regulation of the Hippo-YAP pathway by G-protein-coupled receptor signaling. Cell 150 , 780–791.
[18] McClatchey, A.I., and Yap, A.S. (2012). Contact inhibition (of proliferation) redux. Curr. Opin. Cell Biol. 24 , 685–694.Zeng, Q., and Hong, W. (2008). The emerging role of the hippo pathway in cell contact inhibition, organ size control, and cancer development in mammals. Cancer Cell 13 , 188–192.
[19] Zhao, B., Li, L., Wang, L., Wang, C.-Y., Yu, J., and Guan, K.-L. (2012). Cell detachment activates the Hippo pathway via cytoskeleton reorganization to induce anoikis. Genes Dev. 26 , 54–68.

[20] Schlegelmilch, K., Mohseni, M., Kirak, O., Pruszak, J., Rodriguez, J.R., Zhou, D., Kreger, B.T., Vasioukhin, V., Avruch, J., Brummelkamp, T.R., and Camargo, F.D. (2011). Yap1 acts downstream of a -catenin to control epidermal proliferation. Cell 144 , 782–795.
[21] Kim, N.-G., Koh, E., Chen, X., and Gumbiner, B.M. (2011). E-cadherin medi- ates contact inhibition of proliferation through Hippo signaling-pathway com- ponents. Proc. Natl. Acad. Sci. USA 108 , 11930–11935.
[22] Berrier, A.L., and Yamada, K.M. (2007). Cell-matrix adhesion. J. Cell. Physiol. 213 , 565–573.
[23] Wada, K.-I., Itoga, K., Okano, T., Yonemura, S., and Sasaki, H. (2011). Hippo pathway regulation by cell morphology and stress fibers. Development 138, 3907–3914.
[24] Rohn, J.L., Sims, D., Liu, T., Fedorova, M., Schock, F., Dopie, J., Vartiainen, M.K., Kiger, A.A., Perrimon, N., and Baum, B. (2011). Comparative RNAi screening identifies a conserved core metazoan actinome by phenotype. J. Cell Biol. 194 , 789–805.
[25] Pollard, T.D., and Cooper, J.A. (2009). Actin, a central player in cell shape and movement. Science 326 , 1208–1212.
[26] Nelson, C.M., Jean, R.P., Tan, J.L., Liu, W.F., Sniadecki, N.J., Spector, A.A., and Chen, C.S. (2005). Emergent patterns of growth controlled by multicellular form and mechanics. Proc. Natl. Acad. Sci. USA 102 , 11594–11599.
[27] Butcher, D.T., Alliston, T., and Weaver, V.M. (2009). A tense situation: forcing tumour progression. Nat. Rev. Cancer 9 , 108–122.
[28] Paszek, M.J., Zahir, N., Johnson, K.R., Lakins, J.N., Rozenberg, G.I., Gefen, A., Reinhart-King, C.A., Margulies, S.S., Dembo, M., Boettiger, D., et al. (2005). Tensional homeostasis and the malignant phenotype. Cancer Cell 8 , 241–254.
[29] Kim, M., Kim, M., Lee, S., Kuninaka, S., Saya, H., Lee, H., Lee, S., and Lim, D.-S. (2013). cAMP/PKA signalling reinforces the LATS-YAP pathway to fully suppress YAP in response to actin cytoskeletal changes. EMBO J. 32 , 1543–1555.
[30] Lei, Q.-Y., Zhang, H., Zhao, B., Zha, Z.-Y., Bai, F., Pei, X.-H., Zhao, S., Xiong, Y., and Guan, K.-L. (2008). TAZ promotes cell proliferation and epithelial- mesenchymal transition and is inhibited by the hippo pathway. Mol. Cell. Biol. 28 , 2426–2436
[31] Guo, C.-L., Ouyang, M., Yu, J.-Y., Maslov, J., Price, A., and Shen, C.-Y. (2012). Long-range mechanical force enables self-assembly of epithelial tubular pat- terns. Proc. Natl. Acad. Sci. USA 109 , 5576–5582.
[32] Zeng, Q., and Hong, W. (2008). The emerging role of the hippo pathway in cell contact inhibition, organ size control, and cancer development in mammals. Cancer Cell 13 , 188–192.
[33] Fernandez, B.G., Gaspar, P., Bras-Pereira, C., Jezowska, B., Rebelo, S.R., and Janody, F. (2011). Actin-Capping Protein and the Hippo pathway regulate F-actin and tissue growth in Drosophila. Development 138 , 2337–2346.
[34] Sansores-Garcia, L., Bossuyt, W., Wada, K.-I., Yonemura, S., Tao, C., Sasaki, H., and Halder, G. (2011). Modulating F-actin organization induces organ growth by affecting the Hippo pathway. EMBO J. 30 , 2325–2335.
[35] Ramos, A., and Camargo, F.D. (2012). The Hippo signaling pathway and stem cell biology. Trends Cell Biol. 22 , 339–346.
[36] Paszek, M.J., Zahir, N., Johnson, K.R., Lakins, J.N., Rozenberg, G.I., Gefen, A., Reinhart-King, C.A., Margulies, S.S., Dembo, M., Boettiger, D., et al. (2005). Tensional homeostasis and the malignant phenotype. Cancer Cell 8 , 241–254.

Appendix D

Integrated multi-stage tissue on a chip generation from human pluripotent stem cells

Giovanni G. Giobbe[1,2,3,+], Federica Michielin[1,2,+], Sebastian Martewicz[1,2], Stefano Giulitti[1,2], Camilla Luni[1,2], Annarosa Floreani[3], Nicola Elvassore[1,2].

1. Department of Industrial Engineering (DII), University of Padua, via Marzolo 9, 35131 Padua, Italy.
2. Venetian Institute of Molecular Medicine (VIMM), Via Orus 2, 35129 Padova, Italy.
3. Department of Surgery, Oncology and Gastroenterology (DiSCOG), University of Padova, Via Giustiniani 2, 35124 Padova, Italy.
[+] equally contribution

Nature Methods
(under revision)

D.1 Abstract

Micro-engineering human tissues and "organs-on-chips" remains an open challenge from both scientific and technological points of view. Here, we describe a robust and efficient microfluidic-based approach for the differentiation of human pluripotent stem cells into functional cells. Specific frequency of periodic medium perfusion enhances the selectiveness of early germ layer differentiation and cell commitment through extrinsic microfluidic signal perturbations. Human cardiomyocytes and hepatocytes generated on chip from human pluripotent stem cells through multi-stage approach show functional differentiation, which opens a new perspective for multi-parametric and large scale human organ-based screening assays.

D.2 Results

The development of human organs-on-chips, in which the microscale engineering

technologies are combined with cultured human cells to recapitulate whole living organ microenvironment, offers a unique opportunity to study human physiology and pathophysiology in an organ-specific context[1,2,3]. This technological perspective could provide an effective solution to the limitations of conventional cell culture models that fail to recapitulate complex, organ-level disease processes in humans and it could overcome the use of costly and time-consuming animal testing, which often shows poor predictive power of human physiology. Moreover, the scientific community, the major pharmaceutical companies and the government agencies are recognizing the paramount importance of developing new technologies, which allow to perform cost effective and multi-parametric assay for *ad hoc* studies in development, disease and pathogenesis, or for screening specific therapeutic strategies.

Recently, successful examples of organs-on-chips development have been provided[4,5,6,7], however, they were obtained from primary animal cells and, in few cases, from primary human cells. The possibility of developing direct organogenesis-on-chip from human pluripotent stem cells (hPSCs) could overcome the limited availability of human primary cells, such as human hepatocytes or cardiomyocytes. Human embryonic stem cells (hESCs) and induced pluripotent stem cells (hiPSCs) grown in culture have the potential to give rise to any fetal and adult cell type, but they also show intrinsic and unexpected levels of emergent self-organization for generating highly ordered structures and tissues[8,9,10], thus opening a wide perspective for multi-organ generation on a chip.

Organogenesis and tissue generation are complex developmental processes starting from germ layer specification and phenotypic differentiation to tissue morphogenesis. Biomimetic scale down of this multi-stage developmental process could take advantage of the intrinsic properties of micro-technologies and microfluidics that allow accurate control of cell culture microenvironment, of temporal evolution of chemical gradients and of mechanical features, which support specific tissue differentiation[11,12,13]. Few studies reported on mouse embryonic stem cell cultures using microfluidic systems and highlight the importance of accurate soluble microenvironment regulation to maintain pluripotency and self-renewal[14,15,16]. We reported for the first time on hESCs culture on a chip[17] and few other works dealt with hESCs modulating flow

perfusion, mainly for maintaining pluripotency[18,19]. Integrated functional hPSC differentiation on a chip, which certainly requires step-by-step control of hPSCs programming for resembling early stages of organogenesis, has not yet been developed.

Here, we explored whether we can control stem cell expansion, selective germ layer commitment and derive functional tissue-specific cells on a chip from both hESCs and hiPSCs through a multi-stage microfluidic-based technology. The different developmental stages required cell niche specification in terms of accurate balance between extrinsic and intrinsic cell signaling, through optimal in vitro delivery of exogenous factors and removal of endogenous cell-secreted factors. Continuous microfluidic flow perfusion has been recently shown to generate soluble factor spatial gradients along the microfluidic channel that lead to heterogeneous cell phenotype. Here, we showed that a discontinuous periodic medium delivery with stage-dependent frequency (number of cycles of medium change per day) is an effective strategy for modulating stem cell niche specification *in vitro*.

Identification of the essential role of extrinsic autocrine-paracrine factors in pluripotency and self-renewal and germ layer commitment[20], suggests a synergic mechanism of specific exogenous and endogenous factors in promoting transcriptional activity of pluripotency genes (Fig. 1a). The computational investigations on extrinsic signaling model (Supplementary Methods for model details) revealed that frequency of periodic medium delivery strongly affects accumulation of exogenous and endogenous factors, thus regulating transcriptional activity of target genes. A frequency increase reduces the amplitude of temporal fluctuations of both exogenous and endogenous factors (Fig. 1b), thus maintaining sustained transcriptional activity of the associated target genes. However, higher frequencies of medium change produce decreased expression of gene transcript, due to continuous endogenous secreted factors wash-out. This simple schematic modeling reveals high correlation between frequency of medium change and extrinsic signaling regulation.

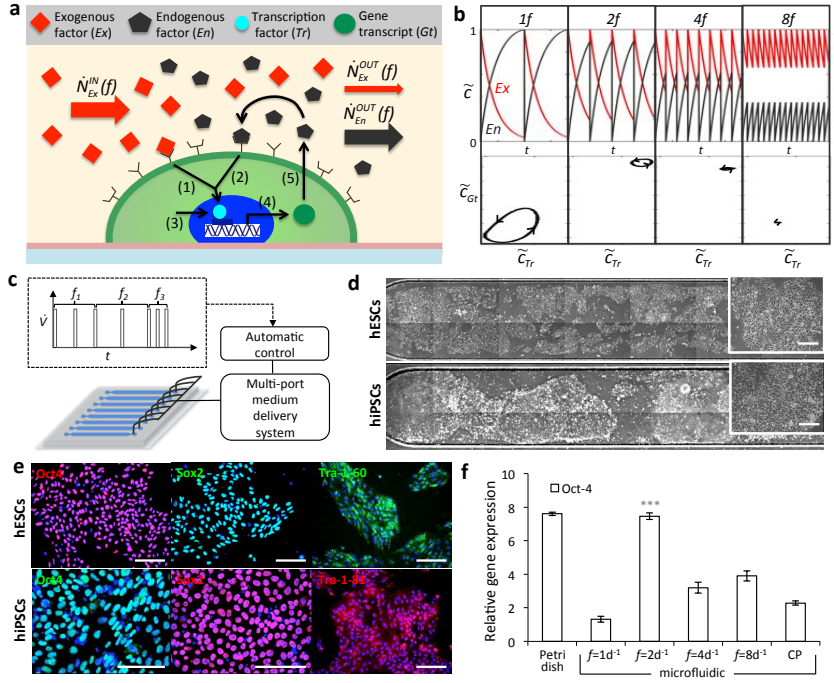

Figure 1 Pluripotent stem cell culture on-a-chip. (**a**) Pluripotency signaling model in microfluidic stem cell culture. Both exogenous (*Ex*) and endogenous (*En*) factors contribute to transcriptional activity of pluripotency genes through activation of target transcription factors (*Tr*). (**b**) Signaling model output. Temporal profiles of normalized *Ex* and *En* factor concentrations in the microfluidic channel at increasing frequencies (up). Gene transcript (*Gt*) concentration profile plotted versus corresponding Transcription factor (*Tr*) variation during a single medium perfusion at increasing frequencies. (**c**) Experimental set-up. Periodic medium delivery in microfluidic channels (200 μm high, 1.5 mm width, 1.8 mm length and 6 μL volume) is controlled through a multi-port delivery system. Different frequencies sequences are automatically programmed through Labview software. (**d**) Microfluidic hPSCs culture. Half channel views showing hESCs and hiPSCs expanded for 6 days in microfluidic conditions with f=2d^{-1}. Insets show typical morphology of stem cells colonies. Scale bar 50 μm. (**e**) Immunofluorescence analysis of pluripotency markers Oct-4, Sox2, Tra-1-60 and Tra-1-81 for hESCs and hiPSCs after 6 days in microfluidic channels. (**f**) Frequency-dependent Oct4 expression. QRT-PCR analysis of pluripotency marker Oct-4 expression of hESCs at different frequencies, f, compared to standard static culture control and continuous perfusion (CP). Student's t-test p-value ***P≤0.001. Data are shown as mean ± s.d. (n=3).

First, we investigated the best condition for both hESC line hES2 and hiPSC line ADHF#1 expansion in microfluidic channels to maintain high stemness and homogeneous morphology among colonies at different regions along the channels. HPSCs were injected into multiple microfluidic platforms, each containing 8 independent channels and connected to a multi-port syringe pump (Fig. 1c), were cultured with different frequencies up to 6 days (Fig. 1d). Immunofluorescence staining revealed that both hESCs and hiPSCs homogeneously express pluripotency markers such as Oct-4, Sox2, Tra-1-60 and Tra-1-81 (Fig. 1e). We

optimized the hESC microfluidic culture to maintain high pluripotency in the channels, comparable to standard static conditions. The qRT-PCR analysis of pluripotency marker Oct-4 after 6 days of culture, showed an optimal frequency of f=2d^{-1} (Fig. 1f). Significant three-fold higher expression compared to lower (f=1d^{-1}) and higher frequencies (f=4d^{-1} and f=8d^{-1}) was observed. These results are consistent with the initial hypothesis that an appropriate balance of exogenous molecules and endogenous cell-secreted factors has to be provided. The presented data show a crucial effect of medium change frequency on hPSCs pluripotency maintenance and homogeneity in microfluidics, to allow proper factor supply, while avoiding up-downstream effects throughout the channels (Supplementary Fig. S1).

We next investigated whether the frequency of periodic perfusion could be used for directing early germ layer commitment according to extrinsic endogenous and exogenous factors concentration (as schematized in Fig. 2a). HES2 cells were expanded for 3 days and differentiated for 4 days at different frequencies in spontaneous differentiating conditions (Supplementary Methods). Expression levels of early germ layers markers were analyzed through qRT-PCR analysis of β-III tubulin (ectoderm), brachyury T (mesoderm) and alpha-fetoprotein (endoderm). Under these conditions, the static culture showed ectoderm and mesoderm expression but not endoderm. On the other hand, frequency-dependent germ layer enrichment was observed in microfluidic culture (Fig. 2a). Ectoderm resulted highly expressed at lower frequencies (f=1d^{-1} and f=2d^{-1}) and it is completely down regulated at higher frequency (f=8d^{-1}) whereas mesoderm and endoderm expression are enhanced at higher frequency (f=8d^{-1}). Interestingly, pluripotency markers are down regulated as the frequency increases. Gene expression is associated with cell morphology changes (Fig. 2a). These experimental observations are consistent with the hypothesis that ectoderm differentiation requires high accumulation of extrinsic endogenous factors[14,20], whereas strong endoderm enrichment is only possible with specific exogenous factor delivery. All together, these results suggest that periodic perfusion frequency is an additional player in directing early germ layer commitment.

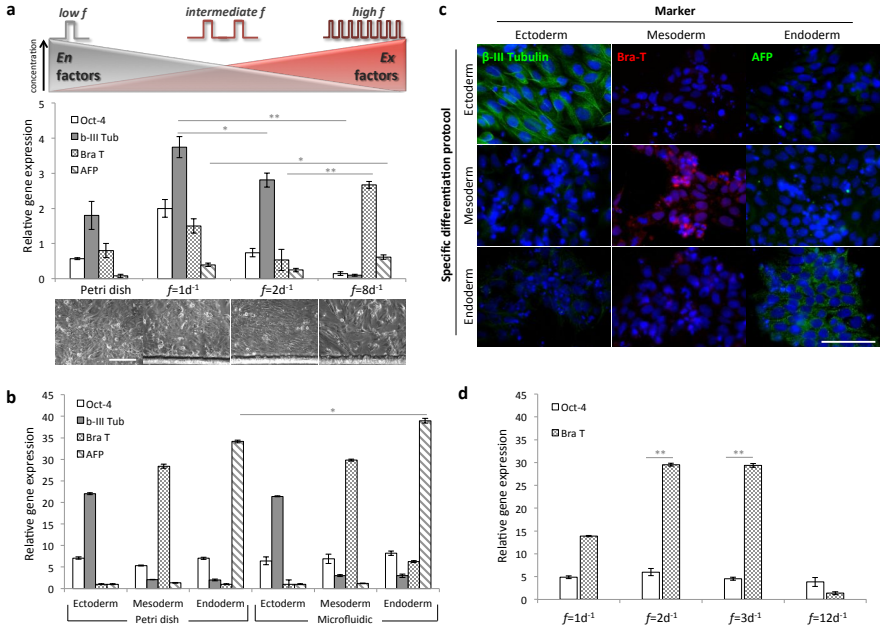

Figure 2 | Early germ layer induction of hESC on-a-chip. (**a**) Frequency-dependent differentiation. Schematic of frequency, *f*, relation to *En* and *Ex* factors balance (up). The qRT-PCR analysis (gene expression normalized on glyceraldehyde 3-phosphate dehydrogenase) of Oct-4, β-III tubulin, brachyury T and alpha-fetoprotein in hESC spontaneous differentiation on chip, under different *f*. Cell morphology in phase contrast for each differentiation condition. Scale bar 50 μm. Data are shown as mean ± s.d. (*n*=3). (**b**) Early germ layer induction with specific media. The qRT-PCR analysis of Oct-4, β-III tubulin, brachyury T and AFP, and comparison between standard static control and microfluidic differentiation. Data are shown as mean ± s.d. (*n*=3). (**c**) Specific differentiation marker expression. Differentiation protocols applied on hESC line cultured on matrigel-coated channels. Immunofluorescence analysis of each differentiation protocol, with high expression of β-III tubulin in ectoderm, brachyury T in mesoderm and AFP in endoderm. Scale bar 50 μm. (**d**) Mesoderm optimization. The qRT-PCR analysis of Oct-4 and brachyury T expression in different frequencies of medium change for germ layer commitment optimization. brachyury T expression is comparable between f=3d^{-1} and f=2d^{-1}, while there is a significantly lower expression at high and low frequencies. Student's *t*-test *p*-values *P≤0.05 **P≤0.01. Data are shown as mean ± s.d. (*n*=3).

To verify whether an efficient and selective induction of the three germ layers could be achieved, hES2 cells were induced to ectoderm, mesoderm and endoderm by specific differentiation media and with *ad hoc* frequency (Fig. 2b). Particularly, according to previous results, f=1d^{-1} was used for ectoderm specification whereas f=2d^{-1} and f=3d^{-1} for mesoderm and endoderm, respectively. Selective germ layer commitment was successfully obtained as reported by qRT-PCR analysis, which showed high expression of specific germ layer genes for each differentiation protocol. All other non-specific germ layer genes are strongly down regulated. Interestingly, endoderm is significantly higher expressed in

microfluidic condition, compared to conventional differentiation in Petri dish. It seems that microfluidic environment effectively washed out the endogenous factors that inhibit endoderm differentiation, and efficiently delivered the exogenous pro-endoderm factors. Immunofluorescence analyses (Fig. 2c) confirmed that highly selective commitment for all germ layers, with extremely low contamination from the others, is achievable also at the protein level in each specific differentiation protocol.

Next, we examined if perfusion frequency can be further adjusted for optimizing germ layer microfluidic induction when specific differentiation protocols are used. As proof of concept, results in Fig. 2d showed how selective induction of mesoderm was achieved by adjusting frequency of periodic perfusion. In particular, we found a 3 fold higher brachyury T expression at f=2d^{-1} and 3d^{-1}, compared to f=1d^{-1} and almost null expression at f=12d^{-1}.

Collectively, our findings indicate that the frequency of periodic perfusion is an additional parameter to enhance robustness and efficiency of early germ layer specification, even when specific protocols are adopted. In particular, we found major advantages for endoderm differentiation, because it requires large quantities of exogenous molecules (e.g. activin A) and washing out of endogenous inhibiting factors. On the other hand, mesoderm differentiation seems to require a proper balance between exogenous and endogenous molecules that can be achieved by frequency optimization, although dependent on cell culture density and media composition. Ectoderm commitment is mainly driven by endogenous stimulations and microfluidic differentiation can reproduce the results obtained with conventional cell culture methods. From technological point of view, small-scale microfluidic volume leads to extremely reduced medium consumption (few microliter per day per channel) and rapid and accurate perturbation of medium composition that is an important prerequisite for multi-stage differentiation process.

Therefore, we then demonstrated whether functional tissue-specific cell generation on chip could be achieved. We focused on cardiac and hepatic cells that are derived from mesoderm and endoderm germ layers, respectively, and are extremely relevant for organ-on-a-chip applications. Cell differentiation was achieved by combining *ad hoc* hPSCs differentiation stages, germ layer specification and mature differentiation with proper frequencies of periodic

perfusion and chemical regulation of soluble microenvironment. Cardiac and hepatic cell differentiation protocols are described in Supplementary Methods.

We first showed how cardiac cells on chip were derived after 15 days of frequency-dependent multi-stage differentiation protocol (Fig. 3a), consisting on mesoderm induction (by Wnt induction), early cardiac commitment (by Wnt inhibition) and functional cardiac maturation (by pro-cardiac factors supply). Typically 5 to 10 thousands cells per channel were obtained. We robustly achieved spontaneous contractile activity from both hES2 and ADHF#1-derived cardiomyocytes, 60% of cardiac troponin-T positive cells showing defined cardiac sarcomeric organization (Fig. 3b). HPSC-derived cardiomyocytes show spontaneous calcium transients and excitation contraction coupling (Fig. 3c). In the line scan magnification in Fig. 3c both calcium transients and spark-like spontaneous activity are presented. Analyzing calcium handling of hPSC-cardiomyocytes in microchannels, we observed cardiomyocyte functional response to 0.5 μM Verapamil with reduced calcium release after L-type channel inhibition, and response to 10 mM caffeine with cytosolic calcium increase after ryanodine channel activation (Fig. 3d). We successfully showed that it is possible to generate functional cardiac cells on chip and to directly perform dynamic biochemical stimulations taking advantage of the microfluidic environment, which allows robust, accurate, fast, and cost-effective spatio-temporal control of cell microenvironment[11].

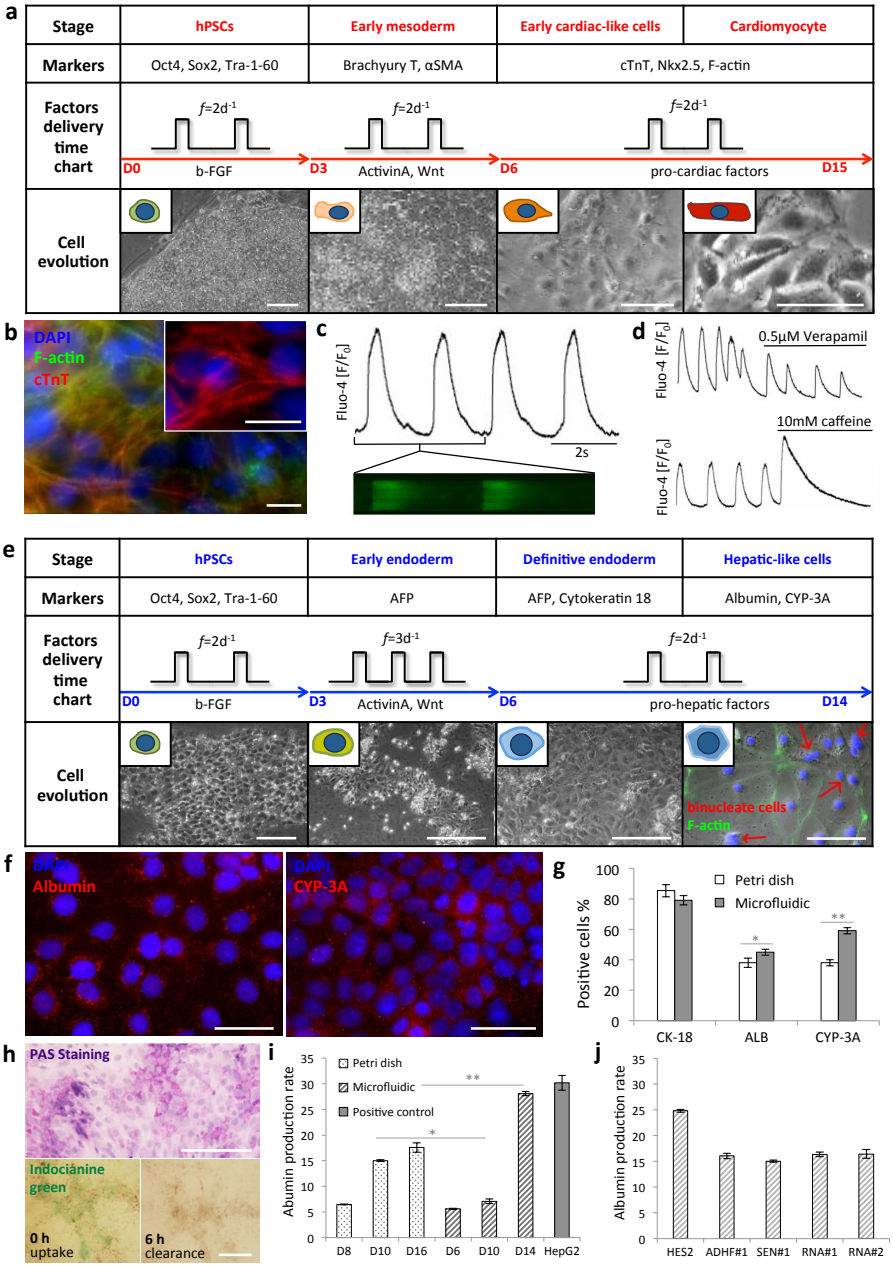

Figure 3 | Cardiac and hepatic functional differentiation on-a-chip from both hESCs and hiPSCs. (**a**) Microfluidic cardiomyocyte differentiation protocol and morphology changes from pluripotent state to differentiated cell type. Scale bars 200 μm. (**b**) Immunofluorescence analysis of hES-derived CM showing F-actin and cardiac troponin-t organization. Scale bars 20 μm (**c**) Microfluidic calcium dynamics. Spontaneous calcium transients in hPSC-cardiomyocytes recorded with Fluo-4 indicator. (**d**) Functional cardiomyocytes response to 0.5 μM verapamil with reduction in calcium release, and to 10 mM caffeine with increase in cytosolic calcium. (**e**) Hepatic differentiation protocol and cell morphology change up to hepatocyte-like cells. Red arrows indicate binucleate cells in late stages. Scale bars 200 μm. (**f**) Immunofluorescence analysis of hepatocyte-like markers albumin and cytochrome P450 3A from hESCs. Scale bars 30 μm. (**g**) Quantification of immunofluorescence markers. Microfluidic hepatic cells show significant higher expression of albumin and CYP-3A compared to static control. Data are shown as mean ± s.d. (n=10). (**h**) PAS staining of hepatic cells derived on chip; nuclei are stained in blue, pink-violet colored cells show glycogen storage. Indocyanine green staining of live hepatic cells; colorant is

absorbed and metabolized in 6 h by functional hepatocyte-like cells. Scale bars 100 μm. (**i**) ELISA albumin secretion quantification. Microfluidic-derived hepatocyte-like cells secrete 40% more albumin compared to static control at the last day of differentiation (albumin production rate is expressed as ng/mL/day/2x10^5 cells). Student's *t*-test *p*-values *P≤0.05 **P≤0.01. Data are shown as mean ± s.d. (*n*=3). (**j**) Comparison of Albumin production at Day 14 for different hiPSC lines differentiated in hepatocytes-like cells. Levels of albumin production comparable to hES2 hESC line derived hepatocytes were obtained for hiPSCs lines ADHF#1, derived with retroviruses, SEN#1, derived with Sendai viruses and RNA#1-2, derived with mRNA technology. Albumin production rate is expressed as ng/mL/day/2x10^5 cells.

We next applied our methodology to derive hepatocytes on chip, consistently with the previously endoderm-optimized conditions, which showed higher efficiency in endoderm differentiation than conventional cell culture. Hepatic cells were robustly obtained from hES2 and ADHF#1 cells by early endoderm commitment, definitive endoderm specification and hepatocyte-like cell maturation steps, driven by specific periodic medium delivery (Fig. 3e). Characteristic polygonal-shaped hepatocyte-like cells were obtained, with presence of bi-nucleate cells at the late stage, showing high expression of the specific hepatic markers albumin and cytochrome P450-3A (Fig. 3e-f and Supplementary Fig. S3a-b). Quantification of immunofluorescence of late stage albumin and CYP-3A in hES2 cells shows higher expression in microfluidic differentiated cells compared to differentiation control on Petri dish (Fig. 3g and Supplementary Fig. S3c-d). Similar results were obtained by applying our method to other hiPSCs lines derived with non-integrating methods: SEN#1, derived with non-integrating Sendai viruses and RNA#1 and RNA#2, derived with mRNA technology (Supplementary methods and Supplementary Fig. S4). The hepatic cells show functional activity by high glycogen storage capacity (75% of total cells) and indocyanine green uptake and clearance (Fig. 3h), which is extremely relevant for hepatic drug metabolism studies. As expected from prior results, compared to static conditions, we obtained a shortening of the time required for differentiation (from 16d to 14d) and 40% greater albumin secretion rate on the last day of maturation (Fig. 3i). An albumin production rate comparable with hESCs derived hepatocytes was obtained with the four different hiPSCs lines (ADHF#1, SEN#1, RNA#1 and RNA#2), confirming the robustness of the method (Fig. 3j). The microfluidic environment together with optimized periodic perfusion frequency provides an effective methodology for generating hepatic-like tissues on a chip

with remarkable functional differentiation also compared to conventional cell culture methods.

In conclusion, we derived functional tissue-specific cells on a chip through a robust multi-stage microfluidic technology, which allows accurate spatio-temporal control of cell soluble microenvironment through regulation of periodic-perfusion frequencies. Moreover, functionally differentiated cells derived in the microfluidic channels can be directly used for dynamic multi-parametric and large-scale drug screening or for developing micro-engineered human organ models. This technology opens a new perspective in generating organs-on-chips from hPSCs overcoming the issues related to the limited availability of human primary cell sources. This last aspect will require strong scientific and technological efforts for further mimicking the organogenesis *in vitro*.

D.3 References

1. Huh, D., Torisawa, Y., Hamilton, G. A., Kim, H. J. & Ingber, D. E. *Lab. Chip* **12,** 2156–2164 (2012).
2. Huh, D. *et al. Sci. Transl. Med.* **4,** 159ra147–159ra147 (2012).
3. Ghaemmaghami, A. M., Hancock, M. J., Harrington, H., Kaji, H. & Khademhosseini, A. *Drug Discov. Today* **17,** 173–181 (2012).
4. Huh, D. *et al. Science* **328,** 1662–1668 (2010).
5. Lee, S.-A. *et al. Lab. Chip* (2013). doi:10.1039/C3LC50197C
6. Jang, K.-J. *et al. Integr. Biol. Quant. Biosci. Nano Macro* (2013). doi:10.1039/c3ib40049b
7. Grosberg, A., Alford, P. W., McCain, M. L. & Parker, K. K. *Lab. Chip* **11,** 4165–4173 (2011).
8. Sasai, Y. *Nature* **493,** 318–326 (2013).
9. Eiraku, M. *et al. Nature* **472,** 51–56 (2011).
10. Eiraku, M. *et al. Cell Stem Cell* **3,** 519–532 (2008).
11. Discher, D. E., Mooney, D. J. & Zandstra, P. W. *Science* **324,** 1673–1677 (2009).
12. Dupont, S. *et al. Nature* **474,** 179–183 (2011).
13. Wan, C., Chung, S. & Kamm, R. D. *Ann. Biomed. Eng.* **39,** 1840–1847 (2011).
14. Przybyla, L. M. & Voldman, J. *Proc. Natl. Acad. Sci.* **109,** 835–840 (2012).
15. Przybyla, L. & Voldman, J. *Annu. Rev. Anal. Chem. Palo Alto Calif* **5,** 293–315 (2012).
16. Moledina, F. *et al. Proc. Natl. Acad. Sci.* **109,** 3264–3269 (2012).
17. Figallo, E. *et al. Lab. Chip* **7,** 710–719 (2007).
18. Korin, N., Bransky, A., Dinnar, U. & Levenberg, S. 64160N–64160N (2006). doi:10.1117/12.695558
19. Villa-Diaz, L. G. *et al. Lab. Chip* **9,** 1749 (2009).
20. Giobbe, G. G. *et al. Biotechnol. Bioeng.* **109,** 3119–3132 (2012).

D.4 Supplementary methods

D.4.1 Computational Model

Mathematical model of signaling pathway describing gene transcriptional activity promoted by synergic positive effect of extrinsic exogenous and endogenous factors is shown in Fig. 1a. The model takes into account only relevant phenomena to highlight the effect of dynamic changes in extrinsic factors modulated by medium delivery frequency, *f*, on a hypothetic transcriptional activity. Black arrows in Fig. 1a indicate chemical reactions involved in the pathway. In particular, reactions (1) and (2) describe the coupling of exogenous, *Ex*, and endogenous, *En*, factors to specific membrane receptors, which promotes the activation of transcriptional factor, *Tr*. In addition, *Tr* is activated at a basal level through reaction (3) and induces expression of pluripotency-associated genes through reaction (4). Gene transcripts, *Gt*, in turn, produce newly *En*, as indicated by reaction (5). The model consists of four ordinary differential equations describing dynamic mass balance equation for the involved species *Ex*, *En*, *Tr* and *Gt*:

$$\begin{cases} \dfrac{d\tilde{c}_{Ex}}{dt} = \dot{N}_{Ex}^{IN} - \dot{N}_{Ex}^{OUT} - V_1 \\ \dfrac{d\tilde{c}_{En}}{dt} = -\dot{N}_{En}^{OUT} - V_2 + V_5 \\ \dfrac{d\tilde{c}_{Tf}}{dt} = V_1 V_2 + V_3 \\ \dfrac{d\tilde{c}_{Gt}}{dt} = V_4 - V_5 \end{cases} \tag{1}$$

c are concentrations of species involved in the pathway (*Ex*, *En*, *Tr* and *Gt)*; ~ symbol indicates adimensional concentration normalized for the initial concentration value c^0. *N* is the molar flux, given from the product between the medium flow rate and the concentration of each species, at the inlet and outlet of the microfluidic channel. Exogenous inlet flux is constant, as exogenous factors are continuously supplied with medium, whereas outlet fluxes are time-dependent. All chemical reaction rates are assumed first order kinetics as follows:

$$V_1 = k_1 \tilde{c}_{Ex}$$

$$V_2 = k_2 \tilde{c}_{En}$$

$$V_3 = k_3 \tag{2}$$

$V_4 = k_4 \tilde{c}_{Tf}$

$V_5 = k_5 \tilde{c}_{Gt}$,

where k_i are constant of reaction with arbitrary value and dimension [t^{-1}].

As an intermittent flow perfusion for medium delivery will be used, system of equations (1) can be solved throughout an interval time equivalent to the reciprocal of the frequency, $1/f$, and for a defined number of cycles, N_{tot}. Consequently, null inlet and outlet fluxes and opportune initial periodic conditions were set. Time for medium change in the microfluidic channel was assumed negligible and periodic concentration values of *Ex* and *En* were set equal to 1 and 0 respectively after every time period ($1/f$). The system was solved for different values of f with periodic initial conditions written as follows:

$$\begin{cases} \dfrac{d\tilde{c}_{Ex}}{dt} = -k_1 \tilde{c}_{Ex} & \tilde{c}_{Ex}(t = \dfrac{i}{f}) = 1 \\ \dfrac{d\tilde{c}_{En}}{dt} = -k_2 \tilde{c}_{En} + k_5 \tilde{c}_{Gt} & \tilde{c}_{En}(t = \dfrac{i}{f}) = 0 \\ \dfrac{d\tilde{c}_{Tf}}{dt} = k_1 k_2 \tilde{c}_{Ex} \tilde{c}_{En} + k_3 & \tilde{c}_{Tf}(t = 0) = 0.1 \\ \dfrac{d\tilde{c}_{Gt}}{dt} = k_4 \tilde{c}_{Tf} - k_5 \tilde{c}_{Gt} & \tilde{c}_{Gt}(t = 0) = 0.1 \\ & i = 0,1,...,N \end{cases} \quad (3)$$

System of ordinary equations (3) was computationally solved with MATLAB, by using *ode15s function*. Constant rates k_1, k_2, k_4 and k_5 were arbitrarily set equal to 1, whereas k_3 was taken equal to 0.1. N_{tot} was chosen in order to achieve a pseudo-stationary of all species concentrations.

D.4.2 Microfluidic device micro-fabrication and protein functionalization

The microfluidic chip was fabricated by standard soft-lithographic techniques[1]. The master was photo-lithographically patterned by using SU8-2100 negative photoresist (MicroChem, Newton, MA) to obtain a final thickness of 200 micron, according to manufacturer's indications. A premixed 10:1 ratio of polydimethylsiloxane, PDMS, pre-polymer and curing agent solution (Sylgard 184 kit; Dow Corning, Midland, MI) was casted on the silicon wafer and cured at 70 C° for 2 h. The PDMS mold was cut, peeled off, and punched with a 21G

stainless steel needle (Small Part Inc., Logansport, IN) to obtain inlet/outlet holes. The PDMS mold was assembled and sealed to a 50×75 mm cleaned glass slide by plasma bonding. Eight independent medium reservoirs (3mm diameter and 4mm height for about 30microL volume), one for each channel, were obtained by sealing an additional PDMS block to the top of the device by plasma bonding. The assembled device was cleaned with isopropanol (Sigma-Aldrich, St. Louis, MO) and sterilized in an autoclave.

Microfluidic channels were filled with Matrigel Reduced Factor, MRF (BD) diluted in IMDM (Invitrogen) to a final concentration of 20% and incubated overnight at 4°C. Coating solution was aspirated and microfluidic device was incubated at 37°C and 5% CO_2 atmosphere for 1 h.

D.4.3 Sendai viruses-mediated hiPSCs generation

Human fibroblasts derived from skin-biopsy were plated and cultured in a 24-well plate and cultured to 70% confluence in fibroblast medium (DMEM supplemented with 10% FBS). CytoTune iPS Sendai Reprogramming Kit (Invitrogen) based on replication incompetent Sendai virus was used to deliver the four transcription factors Oct4, Sox2, Klf4 and c-Myc and induce reprogramming to iPSc, according to manufacturer instructions. After 24h transduction, cells were fed every other day for 7 days. Transduced cells were then transferred onto inactivated MEF feeder cells at a density of 1 x 10^4 cells on a 6-well plate and expanded as reported below.

D.4.4 mRNA-mediated hiPSCs generation

Human iPS reprogramming using modified mRNA (mmRNA) was performed following the protocol of Warren et al[2]. Briefly, inactivated human newborn foreskin fibroblast feeders (NuFF-RQ, AMS Biotechnology) were seeded in 6-well tissue culture plates, coated with gelatin 0.2%, at a density of 260 cell/mm^2, and cultured in DMEM supplemented with 10% fetal bovine serum, FBS (Invitrogen). Cells were always incubated at 37°C and 5% CO_2. After 24 h, human foreskin BJ fibroblasts (Miltenyi Biotec) were seeded at 10 cell/mm^2 and cultured in Eagle's minimal essential medium (EMEM, Invitrogen) with 10% FBS. After another 24 h, medium was replaced with Pluriton reprogramming medium (Miltenyi Biotec) supplemented with B18R interferon inhibitor (Prodotti Gianni) at a final concentration of 200 ng/mL, and transfections using mmRNA

(Miltenyi Biotec) were started and repeated for 18 days, 4 hours prior to daily medium changes. The transfection mix was prepared pooling two solutions: the first obtained diluting 5X 100 ng/μL mmRNA of Oct4, Sox2, Klf4, c-Myc, Nanog, Lin28, and nuclear GFP in OptiMEM (Invitrogen), and the second diluting 10X lipofectamine RNAiMAX (Invitrogen) in Opti-MEM. After mixing, the final solution was incubated for 15 min and then added to the culture medium. At day 6 after the first transfection, Pluriton reprogramming medium was replaced with B18R-supplemented NuFF-conditioned Pluriton medium, which was produced culturing in parallel NuFF cells in T75 flasks with Pluriton medium supplemented with bFGF (Peprotech) at 4 ng/mL. Two days after the last transfection, iPS colonies were picked and passaged to MEF-coated 12-well plates and expanded as reported below.

D.4.5 Human pluripotent stem cell expansion and microfluidic culture

HiPSCs (cell line ADHF#1, obtained from Center for iPS Cell Research and Application, iCeMS, Kyoto University; cell line SEN#1, generated with Sendai viruses; cell lines RNA#1 and RNA#2, generated with mRNA technology) and hESCs (cell line HES2, from National Stem Cell Bank, Madison, WI) were cultured in gelatin-coated multiwells with mitomycin C-treated mouse embryonic fibroblasts (MEF; Chemicon) co-culture, in expansion medium DMEM F-12 (Invitrogen), 20% KO serum (Invitrogen), 10% MEF conditioned medium (not used for hiPSCs), 20 ng/mL basic fibroblast growth factor for hESCs, 10 ng/mL for hiPSCs (b-FGF; Invitrogen), 0.1 mM β-mercaptoethanol (Invitrogen), 1% non-essential amino acid (Invitrogen) and 1% Pen/Strep (Invitrogen). HPSCs were passaged to new feeder using CTK solution (trypsin 0.25% - collagenase IV - Ca^{2+}) for hiPSCs and trypsin 0.25% for hESCs (Invitrogen). For MEFs depletion and cell expansion and differentiation, cells were passaged on matrigel-coated microchannels.

The hPSC suspension was injected into each channel and the microfluidic chip was incubated overnight at 37°C and 5% CO_2 atmosphere without perfusion, to allow cell adhesion to substrate. We used proper cell seeding concentration to achieve 70% confluence cell culture at 24 h after seeding.

A 9-port pump (Cavro® XR Rocket pump, TECAN, San Jose, CA) was used to independently deliver the medium from the reservoirs into each microfluidic channels. 0.5 ID Tygon tubings (Cole-Parmer, Vernon Hills, IL) and 21G stainless-steel needles with a polypropylene luer (Microtest, Taipei, Taiwan) were used to connect the microfluidic chip to the pump. Discontinuous medium delivery with defined temporal frequencies was achieved by automatically controlling the multi-channel syringe pump through LabView 8.2 (National Instruments, Austin, TX). For pluripotency maintenance, hPSCs were cultured with a 2-cycles/day expansion medium change. A minimum of 3 independent microfluidic channles were used for each experimental conditions.

D.4.6 HPSCs early germ layer microfluidic differentiation

For spontaneous differentiation, no exogenous factors and cytokines were used, and the basal medium is composed of KnockOut DMEM, FBS 20%, NEAA 1%, L-glutamine 0,5% and P/S 1% (all from Invitrogen). Ectoderm differentiation was induced with DMEM F-12 and Neurobasal medium (both from Invitrogen), 1:1 ratio, supplemented with B27 1% (Invitrogen), N2 1% (Invitrogen) and β-met 0.1 mM[3,4]. Mesoderm differentiation was induced with StemPro-34 (Invitrogen) supplemented with 2 mM L-glutamine (Invitrogen), transferrin 200 ng/mL, 0.5 mM ascorbic acid (Sigma), activin A 0.3 ng/mL (R&D), BMP-4 3 ng/mL (R&D)[5]. Endoderm differentiation was induced with RPMI1640 containing 1X B27 (both from Invitrogen), 1mM sodium butyrate (Sigma), 100 ng/ml activinA (Peprotech) and 50 ng/mL Wnt3a (R&D)[6] for the first 2 days. The second endoderm medium was KO DMEM with KO serum 20%, L-glutamine 1 mM, NEAA 1%, DMSO 1%, β-met 0.1 mM, P/S 1% for other 2 days. HPSCs specification was induced for 4 days in all three germ layers. A minimum of 3 independent microfluidic channles were used for each experimental conditions.

D.4.7 Microfluidic cell maturation

For cardiac differentiation cells were treated with activin A at 0.3 ng/mL (R&D) in RPMI/B27-insulin. After 24 h, the medium was changed to RPMI/B27-insulin supplemented with 5 ng/mL BMP4 (R&D) for another 4 days. At day 5, the

medium was changed to RPMI/B27-insulin. At day 7 the cells were transferred to RPMI/B27[7].

For hepatic differentiation cells were treated with 100 ng/ml activin A and 0.5mM NaB for 3 days in RPMI/B27. Medium was changed to KO-DMEM, 20%SR (both from Invitrogen), 1 mML-glutamine, 1% NEAA, 0.1 mMβ-met, 1% DMSO (Sigma) for 6 days. Hepatic-like cells were maturated with L15 medium (Sigma) supplemented with 8.3% FBS, 8.3% tryptose phosphate broth, 10 μM hydrocortisone 21-hemisuccinate, 1 μM insulin (all from Sigma) and 2 mML-glutamine containing 10 ng/ml hepatocyte growth factor and 20 ng/ml oncostatin M (both from R&D) for 6 days[8]. For adult specification and maturation, cells were cultured with f=2d^{-1} maturation medium change.

The functional differentation of cardiac and hepatic cells were performed in 30 and 50 independent microfluidic experiments, respectively.

D.4.8 Functional tests

For cardiac functional tests, cardiomyocytes were analyzed at confocal microscopy (Leica SP5) for calcium transient, and caffeine and verapamil treatments[9].

For hepatic functional tests, hepatocyte-like cells were stained with PAS staining (Sigma) according to manufacturer's instructions, for glycogen storage revelation. Indocyanine green test (ICG from Sigma) was performed on living tissue on chip by incubating living tissue for 15 min with dye solution. Green cells retaining ICG were photographed. After 6 hours, same fields were photographed in order to see complete clearance of ICG by functional hepatocyte-like cells. Albumin production and excretion was assessed by collection spent medium (10 μL from each micro-channel) and performing enzyme linked immunosorbent assay ELISA (Immunology Consultants Laboratory, Inc.) following manufacturer's instructions. Expression levels were detected by using plate reader Ininite F2000 PRO (Tecan).

D.4.9 Immunofluorescence and qRT-PCR

Immunofluorescence analyses were performed on paraformaldehyde 4% fixed cells for 15 min. Blocking and permeabilization was performed with heat

inactivated serum 5%, TritonX-100 (Sigma) 0.1% for 1h. Cells were stained using primary antibodies in blocking buffer 1 h room T, or overnight 4°C, depending on the antibody. Immunostaining was done with secondary antibodies Alexa Fluor 488, 594 (Invitrogen) and Hoechst nuclear staining incubation for 1 h at 37°C. Videos, bright fields and immunofluorescence images and merges were taken on Leica DMI 6000 B.

The qRT-PCR was performed with TaqMan gene expression assay probes (Invitrogen) according to manufactures instructions using GAPDH (glyceraldehyde 3-phosphate dehydrogenase), POU5F1 (oct4), TUBB3 (beta-III tubulin), AFP (alpha-fetoprotein), T (brachyury) probe sets (all from TaqMan Invitrogen). Reaction was done on ABI Prism 7000 machine and results were analyzed with ABI Prism 7000 SDS software. GAPDH expression was used to normalize values of gene expression, and data are shown as fold change relative to the value of the sample control.

D.4.10 Supplementary citations

1. Luni, C., Michielin, F., Barzon, L., Calabrò, V. & Elvassore, N. *Biophys. J.* **104,** 934–942 (2013).
2. Warren, L. *et al. Cell Stem Cell* **7,** 618–630 (2010).
3. Camnasio, S. *et al. Neurobiol. Dis.* **46,** 41–51 (2012).
4. Chambers, S. M. *et al. Nat. Biotechnol.* **27,** 275–280 (2009).
5. Kouskoff, V., Lacaud, G., Schwantz, S., Fehling, H. J. & Keller, G. *Proc. Natl. Acad. Sci. U. S. A.* **102,** 13170–13175 (2005).
6. Hay, D. C. *et al. Proc. Natl. Acad. Sci. U. S. A.* **105,** 12301–12306 (2008).
7. Lian, X. *et al. Proc. Natl. Acad. Sci.* **109,** E1848–E1857 (2012).
8. Hay, D. C. *et al. Stem Cells Dayt. Ohio* **26,** 894–902 (2008).
9. Martewicz, S. *et al. Integr. Biol. Quant. Biosci. Nano Macro* **4,** 153–164 (2012).

D.5 Supplementary figures

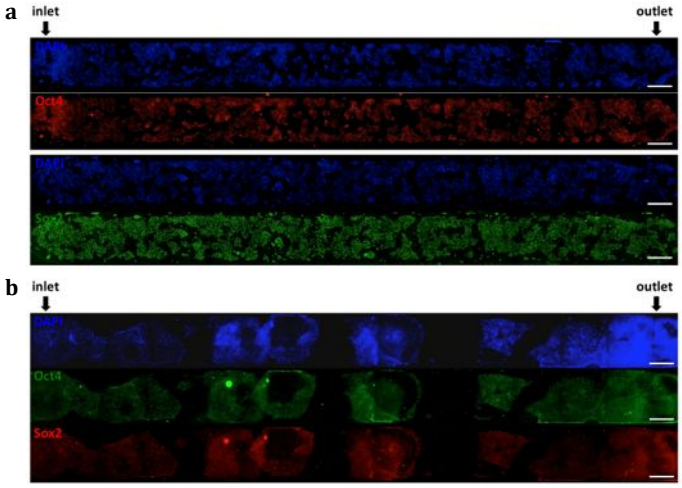

Supplementary Figure 1 Pluripotency marker expression in human pluripotent stem cells cultured in microchannels with f=2d^{-1}. (**a**) "HES2" hES cell line showing Oct-4 and Sox2 expression. (**b**) "ADHF#1" hiPS cell line showing Oct-4 and Sox2 expression. High homogeneity in expression is shown along the microchannels with no upstream and downstream effects. Scale bar 500μm.

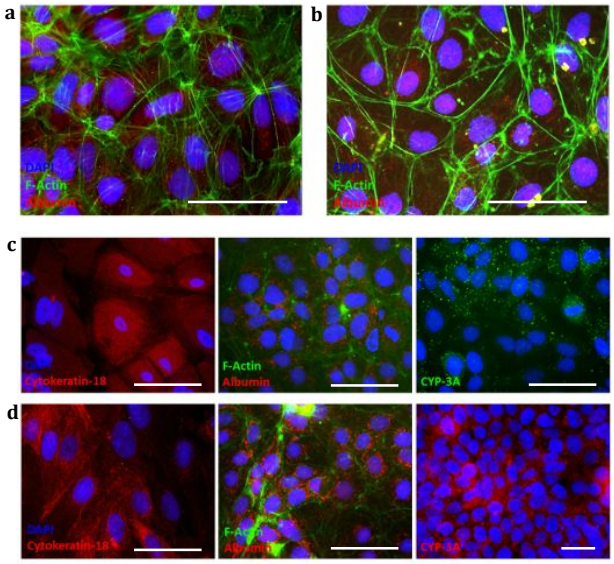

Supplementary Figure 3 (**a-b**) HES and hiPSC-derived hepatocyte-like cells. Cells from both cell lines show comparable differentiation into polygonal hepatocyte-like cells with similar albumin secretion. (**c-d**) Comparison between standard static (**c**) and microfluidic (**d**) hepatic differentiation of hPSC. Cells show similar expression of CK-18 hepatic endoderm marker. Microfluidic hepatocyte-like cells show higher expression of albumin and Cyp-3A compared to standard static differentiated cells. Scale bar 50μm.

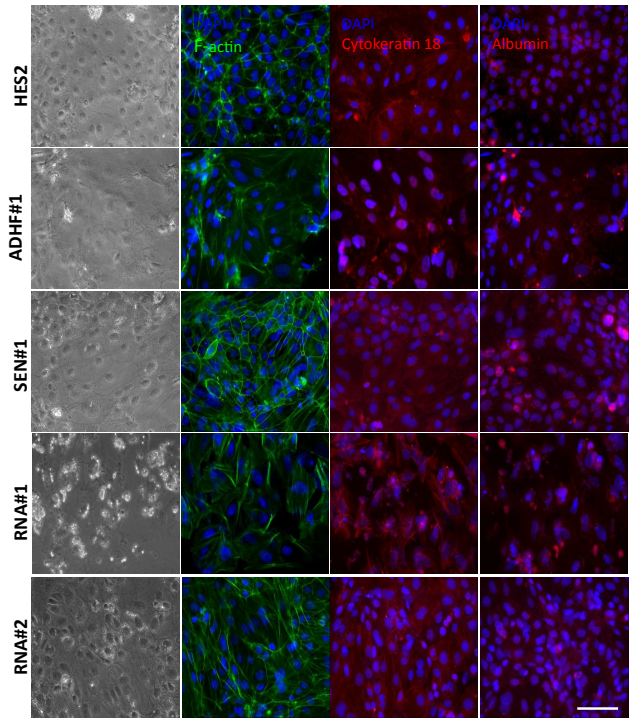

Supplementary Figure 4 Different hPSCs lines differentiated into hepatocyte-like cells: human embryonic stem cell line hES2; human induced pluripotent stem cell line ADHF#1 derived with retroviruses; SEN#1 derived with Sendai virus; RNA#1 and RNA#2 derived with mRNA tchnology. Panel shows cells in bright field and F-actin for cell morphology and polygonal-epithelial shape structure. Hepatocyte-like cells derived from each line have been marked for Cytokeratin 18, showing late hepatic endoderm epithelium, and Albumin, marking hepatocyte-like cells producing human albumin. Scale bar 50μm.

Appendix E

Cyclic mechanical microscale-stimulation affects cellular membrane integrity in a human muscle dystrophy *in vitro* model

Federica Michielin [1,2], Elena Serena[1,2], Piero Pavan[1], Nicola Elvassore[1,2].

1. Dipartimento di Principi e Impianti di Ingegneria Chimica, University of Padova, Via Marzolo 9, 35131 Padova, Italy.
2. Venetian Institute of Molecular Medicine, Via Orus 2, 35129 Padova, Italy.

To be submitted

E.1 Abstract

Cyclic mechanical stimulation has been found to deeply affect cell behavior in terms of cytoskeleton remodeling, signaling pathways alteration and differential gene expression in several diseases. In Duchenne Muscular Dystrophy (DMD), the lack of protein dystrophin, which plays a structural and regulatory role in preserving membrane integrity and homeostasis, mechanical stress seems to deeply affect the pathogenesis of muscle fibers, as resulted in many studies on mdx, a DMD mouse model.

In this study we aimed at investigate if the lack of dystrophin results in impairment of membrane integrity after prolonged mechanical stimulation in a human *in vitro* model. We developed an *ad hoc* microfluidic-based cell-stretching device in order to apply defined external stimuli, in terms of both frequency and intensity, to a primary myoblasts and myotubes cell culture. Computational modeling supported the design of the device and was adopted in order to estimate the mechanical state induced on the cells.

In order to validate the efficacy of our system, we subjected C2C12 myoblasts to both static and cyclic (1Hz) mechanical stretch for 2h, showing a frequency-

dependent cytoskeletal actin filaments remodeling along the direction of minimum strain.

Thanks to the developed technology we were able to investigate the role of cyclic stretch in affecting membrane permeability of both healthy and dystrophic myotubes through a membrane impermeable dye, showing that DMD myotubes have a higher stretch-induced membrane permeability compared to healthy myotubes, both subjected to 90 min cyclic deformation of 20%. Interestingly, the same effect was not observed after only 45 min of the same cyclic deformation. We also investigated the implication of increased stretch-dependent membrane permeability in the activation of the calcium dependent protease, calpain-2, which results aberrantly expressed in dystrophic myotubes, compared to the healthy ones.

In conclusion, we provide a new micro-technologic approach to effectively investigate early pathologic expressions of dystrophic muscle tissue, in a human DMD *in vitro* model, by mimicking mechanical stimuli to which muscle fibers are exposed *in vivo*. Moreover, the developed device could also be used as platform for investigating new therapeutic targets or for drug screening assays.

E.2 Introduction

Mechanical stress plays a crucial role in the investigation of new physiological and pathological responses to cell culture microenvironment. It is recognized that active deformation promotes cellular growth and survival, influence metabolic processes and gene expression, and governs tissue architecture in various cell types[1,2,3,4,5]. Muscle cells are highly responsive to mechanical forces; indeed, expression of skeletal muscle specific genes and skeletal muscle functional maturation, including sarcomeric structural organization and contractile apparatus development, can be modulated by applying an external mechanical stress[2,6]. Myofiber is the functional unit of skeletal muscle *in vivo*, in which a regular array of contractile units (sarcomeres), comprised of thin actin filaments and thick myosin filaments and additional structural and regulatory proteins, allow response to mechanical stress[7]. The peripheral myofibrils are connected to the sarcolemma along the Z-disks via interactions with sub-sarcolemmal protein complexes called costameres. These structures transmit contractile forces from sarcomeres of one myofiber to another, which prevents sarcolemma ruptures by synchronizing

contraction of myofibers within the muscle[7]. The integrity of this protein complex is crucial for the contracting myofiber to withstand the mechanical stress generated by sarcomeres and to prevent its fragile sarcolemma from contraction-induced injuries[7]. Failure to attach properly results in sarcolemmal disruption, which is the predominant underlying cause of several forms of muscular dystrophies. Among them, Duchenne Muscular Dystrophy is caused by mutation in the gene encoding for protein dystrophin, which is a large protein and central membrane complex component[8], compromising the mechanical stability of the muscle fiber and/or its sarcolemma. Muscle fibers damage is exacerbated during normal muscle contractions and initiates a lethal cascade of events that can cause death of the myofiber[8] (necrosis) and fibrotic tissue formation[9].

At cellular level, cytoskeletal protein dystrophin plays a crucial role in the structural maintenance of myofibers membrane integrity, as well as in the regulation of membrane homeostasis[10]. Lack of dystrophin in mdx mouse, a DMD mouse model, has been shown to cause aberrant mechano-transduction in skeletal muscle fibers[11,12], and mechanical stress seems to deeply affect the disease pathogenesis by triggering intracellular calcium increase, which finally leads to fiber necrosis[13,14].

Many studies recognize an increased stretch-sensible channels activity in mdx muscles, compared to the healthy ones[10,13,15,16,17]. This abnormal activity causes an accumulation of intracellular calcium, $[Ca^{2+}]_i$, which makes the membrane more permeable either through activation of phospholipase A2 or by excessive production of ROS, leading to lipid peroxidation, and enhances membrane permeability. Allen et al. reviewed that a variety of stretch-activated and store-activated channels have all been shown to function abnormally in dystrophic muscle, although the mechanism by which the absence of dystrophin triggers abnormal channel activity remains unclear[18].

Conversely, there is broad evidence that muscle fibers from mdx mouse are weaker and more permeable to soluble factors and macromolecules when exposed to cycles of mechanical stimulations. Moreover, eccentric contractions allow soluble cytosolic proteins such as creatine kinase, to leak out of the plasma membrane, whereas extracellular proteins, such as albumin and fibronectin can be detected inside the muscle[18,19]. Experimentally the increased membrane permeability has been repeatedly confirmed by studies in which markers normally

membrane-impermeable, such as albumin and Evans Blue dye, can be detected inside muscle fibers[18,20], whereas membrane damage was reduced by stretch-activated channel blockers which would have prevented the rise in intracellular calcium $[Ca^{2+}]_i$[21]. These experimental evidences on mdx mice prove that cyclic mechanical stimulation strongly affects the maturation of dystrophic muscle phenotype, suggesting a central role also in humans. A human *in vitro* study directed at recapitulating physiological mechanical stress induced effects on dystrophic skeletal muscle has never been reported yet.

For this reason we aim at developing a human DMD skeletal muscle *in vitro* model in order to investigate the role of cyclic mechanical stress in affecting membrane integrity. Mimicking stress-induced membrane damage *in vitro* requires the development of appropriate technological solutions, which allow tight control of stimulation distinguishing between physiologic and non-physiologic deformation and dynamics. A number of technological solutions have been proposed for stretching cultured cells using elastic membranes. Beside most common commercially-available cell-stretching device (Flexcell Corporation) largely adopted in many works[1,2,22], a number of custom-made solutions have been proposed to perform mechanical stimulations on cell cultures in uniaxial and biaxial directions. For instance, Grossi et al. used a magnetic beads-based assay to mechanically stimulate C2C12 myoblast under the effect of a magnetic field[23], whereas, Akbari et al. developed two sets of high-throughput single cell stretcher devices based on dielectric elastomer micro-actuators to stretch groups of individual cells with various strain levels in a single experiment[24]. However, the accurate control in space and time of mechanical-induced deformations while observing the cellular behavior at single cell through optical confocal microscopy, are not straightforward. Moreover, the relative large scale of the existing technology hinders to investigate high temporal resolution cell behavior under fast cyclic mechanical stimulations. Sophisticated technological solutions, such as by coupling Myotack sealant and micro-tweezers[25,26], were proposed for performing single cell mechanical stimulation. However, the intrinsic complexity of these systems make difficult to simultaneously perform multi-parallel experiments analyzing the mechano-associated single cell response in high-throughput fashion.

For this reason, we designed an *ad hoc* cell-stretching device, based on the microfluidic technology, in order to apply accurate cyclic mechanical deformation

on several micro-regions inside the same culture chamber, both in radial and circumferential directions. Miniaturization of the system allows a frequency up to 1 Hz with 32 independent observations and internal, not-stimulated controls. Computational modeling to fully characterize elastic membrane deformation under application of the internal pressure and to estimate the level of local strains supported the development of the device. These data were adopted in order to accurately calibrate the mechanical bi-directional deformation induced on the cells.

Thanks to the developed device we were able to investigate the effect of cyclic physiologic stretch on early pathological events in dystrophic myotubes using a human DMD *in vitro* model. We investigate the role of cyclic stretch in affecting membrane permeability of both healthy and dystrophic myotubes through the use of a membrane impermeable dye, showing an increase of membrane permeability in dystrophic myotubes, compared to the healthy control.

E.3 Experimental methods

E.3.1 Cell culture

Human myoblasts from both healthy and diseased patients were provided by ‘‘Telethon BioBank’’ (Telethon Research Service, Istituto Nazionale Neurologico ‘‘Carlo Besta’’, Milano, Italy). Myoblasts were expanded in 0.1% gelatin coated Petri dish with proliferative medium: 60% High-Glucose Dulbecco’s Modified Eagle’s Medium, DMEM, with Glutamax (Invitrogen, New York, NY), 20% M199Medium (Sigma-Aldrich, St. Louis, MO), 20% FBS (Invitrogen), 10 ng/ml EGF (PeproTech, Rocky Hill, NJ), 2 ng/ml β-FGF (PeproTech), 10 ng/ml insulin (insulin from bovine pancreas, Sigma-Aldrich), Penicillin-Streptomycin-Glutamine (Invitrogen). Before reaching the confluence, cells were trypsinized with 0.25% Tripsina-EDTA (Invitrogen) and replated either in a new dish or onto stretching devices. Myoblasts were induced to form myotubes in differentiating medium: 98% High-Glucose DMEM, 2% horse serum (Invitrogen), 30 ng/mL insulin, penicillin, streptomycin and glutamine.

E.3.2 Cell-stretching device fabrication and management

Stretching-devices were fabricated by using standard soft-lithography technique. High resolution-printed photo-mask was photo-lithografically patterned on a silicon wafer by spin-coating SU8-2050 negative photoresist (Microchem, Newton, MA) at 4000 rpm for 30 s to achieve a homogeneous pattern with thickness 50μm. Silicon wafer was treated with hexamethyldisilazane, HDMS, (Sigma-Aldrich) for 1h under vacuum. A premixed solution of polydimethylsiloxane, PDMS, pre-polymer and curing agent 10:1 ratio (Dow Corning, Midland, MI) was spun on the silicon wafer at 600 rpm for 1 min and cured at 80°C for 1h. Annular-shaped PDMS blocks were cut and assembled to the elastic membrane to confine cell culture medium. The assembled blocks were cut and peeled off, punched to obtain gas inlet holes and sealed to a glass slide by plasma bonding (Harrick Plasma, Ithaca, NY).

21G stainless steel needles (Small Parts Inc., Logansport, IN) and Tygon micro-tubings (Cole-parmer, Vernon Hills, IL) were used for fluidic connections. Membrane deformation was achieved by gas-pressurization of microfluidic channels; air pressure was accurately controlled through a 0.05bar resolution pressure regulator (RP1000-8G-02, CKD Corporation, Japan). Stretch frequency was set through an external home-made apparatus equipped with 8 independent automatic electro-valves (M3MAO, CKD Corporation, Japan) controlled by a digital DAQ system, NI USB-6008, (National Instruments, Austin, TX), managed with NI-DAQmx driver and Labview software (National Instruments).

E.3.3 Structural modeling

Finite Element models of different spots were developed in order to estimate the mechanical state induced on the cells. Stress-strain behavior of PDMS was evaluated by specific tensile mechanical tests (Planar Biaxial TestBench® Test System, Bose ElectroForce®, Eden Prairie, MI), pointing out its non-linearity. An incompressible isotropic hyperelastic constitutive model was adopted to describe the mechanical response of PDMS.

E.3.4 Substrates functionalization and cell seeding

PDMS substrates were coated with 2 μg/cm^2 bovine fibronectin solution (Sigma-Aldrich). Myoblasts were seeded at 50000 cells/cm^2 density and incubated at 37°C and 5% CO_2 to allow cells attachment on the stretching devices. After 24 h proliferating medium was replaced by differentiation medium, in order to induce myoblasts fusion. The medium was no longer changed for 6 days.

E.3.5 Stretching experiments and analysis

Cells cultured on microfluidic devices were washed twice with PBS and loaded with buffer solution: 125 mM NaCl, 5 mM KCl, 1 mM Na_3PO_4, 1 mM $MgSO_4$, 20 mM Hepes, 2 mM $CaCl_2$, 5.5 mM Glucose and NaOH to achieve pH 7.4. For membrane integrity assays, cells were also supplemented with 4 μM impermeant membrane dye FM 1-43 (Invitrogen).

Cell culture were stretched at defined frequency for 90 or 45 min and washed twice with PBS or fixed for immunostaining. Images were captured with an optical microscope (Leica Microsystems, Wetzlar, Germany) at 40x magnification. In order to quantify dye uptake in stretched and control myotubes, fluorescence intensity was analyzed on single myotube cytosolic regions, through LAS AF Lite software (Leica Microsystems). Data are presented as fluorescence intensity means distribution. Statistical significance was analyzed through "Two-sample Kolmogorov-Smirnov test" (MATLAB function kstest2) by considering a P-value<0.05 as statistically relevant. We considered $P<0.05$ to be statistically significant.

E.3.6 Immunostaining

Cells were fixed with 4% paraformaldehyde (Sigma-Aldrich) for 7 min at room temperature, permeabilized with 0.5% Triton X-100 (Sigma-Aldrich) and blocked in 10% scomplemented FBS in PBS for 45 min at room temperature. Cells were incubated with primary antibodies against desmin, rabbit polyclonal (Sigma-Aldrich), myosin heavy chain II, mouse mono-clonal, (Sigma-Aldrich), dystrophin, mouse monoclonal, (Nova Castra, Buffalo Grove, IL, USA) and calpain2 (rabbit polyclonal, Genetex, Irvine, CA) for 1h at room temperature. Cells were washed and incubated with Alexa488 and Alexa495 fluorescence-conjugated secondary antibody (Invitrogen) against mouse or rabbit, depending on primary antibody for 45 min at 37°C. Finally, nuclei were counterstained with

DAPI (Sigma-Aldrich). Samples were mounted with Fluoshield (Sigma-Aldrich) and analyzed through a fluorescence microscope.

E.3.7 RT-PCR analysis

Total RNA from cell coltures was extracted with TRIzol reagent (Invitrogen) and treated with a Turbo DNAfree kit (Applied Biosystems) to remove genomic DNA contamination. First-strand complementary DNA (cDNA) synthesis was performed using using an oligo-(dT)20 primer and the cDNA Reverse Transcription Kit (Applied Biosystems). PCR was performed with cDNA using AmpliTaq Gold (Applied Biosystems). Amplifications were performed with an annealing temperature of 55 or 58 °C for 30–35 cycles, then amplified fragments were resolved by electrophoresis on a 2% agarose gel, followed by staining with ethidium bromide.

E.4 Results and discussion

E.4.1 Stretching device design and fabrication

Cell-stretching device was properly designed in order to ensure: i) accurate control of mechanical stimulations at single-cell level, ii) high temporal resolution of cyclic mechanical stimulations, iii) optical accessibility for in line analysis, iv) statistical significance of treated samples, with internal un-stretched control.

Microfluidic technology, that is recognized to provide highly reproducible and well-defined hydrodynamic conditions, was adopted in order to obtain accurate control of pressure-driven mechanical deformation of elastic membrane underneath cell culture, in terms of amplitude, temporal profile and frequency of bidirectional deformation. Cell stretching device was developed as described in §2.2 through standard soft-lithography technique. A thin PDMS membrane with underlying patterned micrometric channels was provided of gas inlet and sealed to a glass slide. Microfluidic channels pressurization induces mechanical deformation of PDMS membrane and, consequently, of cells cultured above it, as schematically represented in Fig.1A.

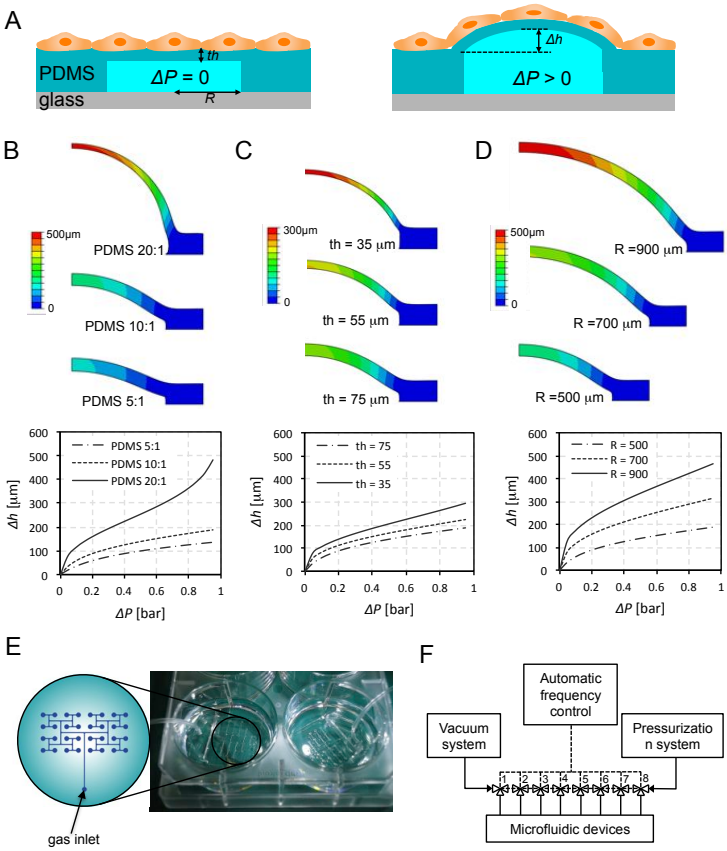

Figure 1 Microfluidic cell stretching device. (A) Microfluidic channel pressurization induces PDMS membrane deformation and, consequently, mechanical stimulation of cells cultured over it. (B) Schematic of the microfluidic network composed by 32 different elastic spots with diameter 1mm (left) and integration of the microfluidic cell stretch designing device in a standard 6-well multiwell plate (right). (B) Experimental set up: consisting in vacuum and pressurization (C) Predicted distribution of radial and circumferential deformations of a single spot at 0.8 bar. (D) Predicted profile and experimental values of the vertical displacement in the center of the spot with the applied pressure. (E) Temporal profile of the mechanical stimulus at different frequencies, obtained by filling microfluidic channels with a dye and recording the absorbance in the center of the membrane at different frequencies.

Biaxial mechanical deformation induced on cells was estimated by developing a Finite Element Model (FEM) of elastic membrane (§E.3.3), assisting microfluidic channel configuration design. Typical *in vivo* muscle fibers deformations range from 10 to 15% under physiological conditions. In order to reproduce similar elongations on myoblasts-derived myotubes *in vitro*, we computationally investigated how design parameters related to material composition and spot geometry affect membrane deformation with definite pressure.

Specifically, vertical displacement in the spot center was predicted for different values of PDMS composition, i.e. different prepolymer:curing agent ratios (5:1, 10:1, 20:1), membrane thickness (35, 55, 75μm) and spot radius (500, 700, 900μm) and defined pressure intensity, as reported in Fig. 1B-C-D, where colored

maps refer to membrane vertical displacement from the bottom of the spot at defined pressure. Graph in Fig. 1B shows vertical displacement in correspondence to the center of circular spots as a function of applied pressure for three different PDMS compositions. Extremely deformable membranes can be achieved by increasing prepolymer:curent agent ratio, although technical issues due to handling very fragile PDMS layers need to be considered. Similarly, lower membrane thicknesses allow higher vertical displacements, although technical issues due to handling very fragile PDMS layers have to be taken into account. Spot geometry can also affect vertical displacement at constant pressure and increasing radius dimension gives higher vertical displacement. Considering both manufacturing constraints and target deformation, a membrane with the following features was employed:

- PDMS with 10:1 prepolymer:curing agent ratio;
- Membrane thickness equal to 55μm;
- Spot radius equal to 500μm.

Microfluidic compartment includes 32 independent deformable circular spots with 1mm diameter. All individual spots are connected through a microfluidic channel network with hydraulic symmetry (constant pressure drop for each microfluidic path) as shown in Fig. 1E, in order to apply identical pressure-induced membrane deformation to all spots. Moreover, thanks to this configuration, with both stretchable and un-deformable areas in the same device, an internal un-stimulated control can be used in every single experiment. Microfluidic cell-stretching device can be easily integrated in standard multi-well plates (Fig. 1E) or directly coupled with an optical microscope for in line analysis. This latter solution requires an additional PDMS layer to hold medium up during observation.

The experimental set up adopted for stretching experiments is schematically represented in Fig. 1F. Pressurized air-line and a vacuum apparatus are connected to a set of micro-valves, which are alternatively open to pressure or vacuum. An external electronic device automatically regulates micro-valves switch through labview software, controlling mechanical stretch frequency in microfluidic devices.

Typical data from the FEM analysis are shown in Fig. 2A and 2B for a pressure of 1bar, showing complete deformation of the spot in both radial and circumferential direction respectively.

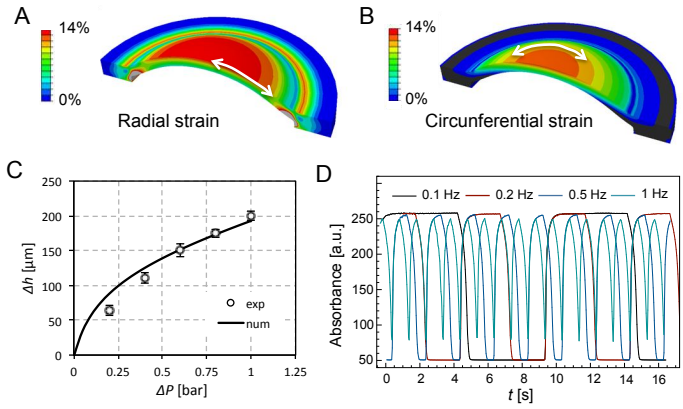

Figure 2 (A-B) Predicted distribution of radial (A) and circumferential (B) deformations of a single spot with ΔP equal to 1 bar. (C) Predicted profile and experimental values of the vertical displacement in the center of the spot with the applied pressure. (D) Temporal profile of the mechanical stimulus at different frequencies, obtained by filling microfluidic channels with a dye and recording the absorbance in the center of the membrane at different frequencies.

The derived model was experimentally validated by measuring vertical displacements of the membrane in the center of the spot, with different pressures. Fig. 2C shows the vertical displacement on the top of the PDMS membrane as a function of the applied pressure. Theoretical profile obtained by numerical solution results in good agreement with the experimental values.

E.4.2 Stretching device validation

Microscopic dimensions of microfluidic channels allow manipulation of few microliters for system pressurization, thus providing fast dynamics of the stimulation and uniform spatial and temporal stimulus on cells. In order to assess the robustness of our system and the reproducibility of mechanical stimuli during cyclic deformations, we filled microfluidic channels with a dye and detected the absorbance of deformed areas during pressurization cycles, at different frequency. These values of absorbance can be directly correlated to the vertical displacement of the membrane. Fig. 1E shows temporal profiles of absorbance acquired at different frequencies from 0.1 to 1 Hz and demonstrates the efficiency of the system in terms of stability of the mechanical deformation and fast dynamics.

In order to verify whether we can induce a biological response on a cell culture, we subjected a C2C12 myoblasts population to both static and cyclic (1Hz) mechanical stretch for 2h. Immunofluorescence analysis of cyclically stretched cells reported a remodeling of cytoskeletal actin filaments, confirmed by stress fibers alignment along the direction of minimum strain, i.e. the circumferential

direction, as shown in Fig. 3. The same result was not observed by applying a static deformation (Fig. 3).

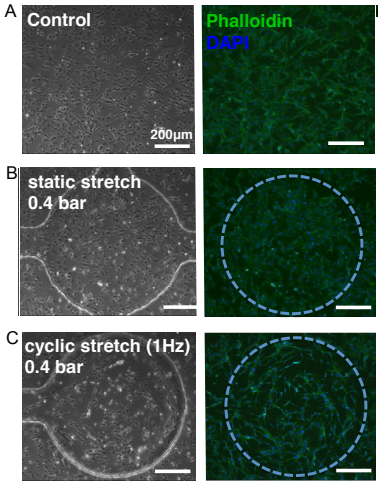

Figure 3 Stretch frequency-dependent cytoskeletal remodeling in C2C12 myoblasts. Bright field and phalloidin staining pictures of C2C12 myoblasts not stretched (A), statically stretched for 2h (0 Hz, 20% deformation) (B) and cyclically stretched for 2h (1 Hz, 15% deformation) (C).

These experimental observations provide evidence of a frequency-dependent cell cytoskeletal remodeling in response to mechanical stimulations.

E.5.3 Cyclic mechanical stretch affects dystrophic myotubes membrane integrity

We next investigated whether lacking of dystrophin protein, which is recognized to preserve membrane structure and homeostasis, in human skeletal muscle is associated with cyclic mechanical stress. In particular, we investigated whether cyclic mechanical stimulation affects membrane integrity in a human DMD *in vitro* model by subjecting human healthy and DMD patient-derived myotubes to a series of 15% physiological deformations at 0.5Hz.

For this purpose, microfluidic cell-stretching devices were opportunely functionalized as described in §2.3, in order to achieve long-term cell attachment during myoblasts differentiation. Human myoblasts derived from biopsies of healthy donors and DMD patients were seeded at high density and induced to differentiate into fused myotubes the day after (Day 1) for 6 days. We first verified dystrophin expression along with myotubes differentiation in both healthy and dystrophic cells. RT-PCR analysis reveals that the short ubiquitous dystrophin isoform Dp71 results expressed already at myoblasts stage from both healthy and diseased cells, whereas amplification of transcripts of the muscle-specific

dystrophin can be appreciated only in healthy myotubes with increasing expression during differential stages. The corresponding primer (Ex45DMD) was properly designed in order to recognize the exon region of the dystrophin, which was found to be mutated in patient biopsies.

Expression of the late myogenic marker myosin heavy chain, MHC in both healthy and diseased cells at Day 6 indicates myotubes are functionally mature.

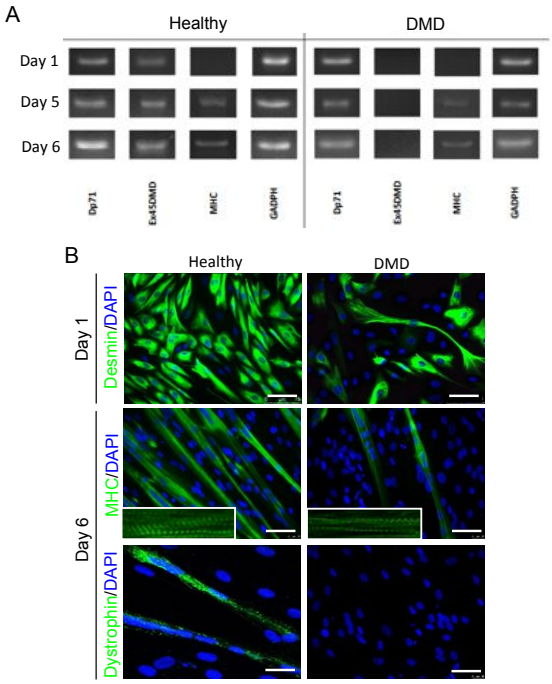

Figure 4 (A) RT-PCR analysis of ubiquitous dystrophin isoform Dp71, dystrophin transcript corresponding to the mutated region found in dystrophic patients, late myogenic marker myosin heavy chain, MHC, and housekeeping gene GAPDH reveal only healthy myotubes express transcripts for protein dystrophin, whereas both cells express MHC. (B) Immunofluorescence analysis of myoblasts at Day 1 of differentiation for myogenic marker desmin. At Day 6 both healthy and DMD myotubes express MHC with clear sarcomeric organization, whereas only healthy cells show dystrophin expression with membrane localization.

We also verified skeletal muscle mature phenotype of healthy and dystrophic myotubes on PDMS substrates at protein levels. Myoblasts positive for the skeletal muscle marker desmin at Day 1 formed multinucleated myotubes positive for the late myogenic-stage marker myosin heavy chain, with well-organized sarcomeric striations and defined dystrophin expression at membrane level. Negative staining of DMD myotubes against Dystrophin antibody confirmed diseased phenotype (Fig. S2).

Large molecules membrane permeability induced by mechanical stress was investigated in both healthy and diseased cells through FM 1-43 membrane

impermeable dye; human myotubes were loaded with 4 μM dye and cyclically stretched for 90 min at 0.5 Hz. Immediately after stimulation, fluorescence intensity due to dye uptake was detected in stretched and un-stimulated myotubes in the same device, as described in §E.3.5.

Cyclic deformation induces a partial increase of dye uptake in healthy myotubes, in comparison to un-stretched myotubes, whereas elevated and widespread uptake of FM 1-43 dye in cytosolic regions of stretched dystrophic myotubes was observed if compared with un-stretched control (Fig. 5A). Taking advantage of having an internal un-stretched control we could analyze fluorescence intensity of stretched and control myotubes in the same conditions and with the same fluorescence background. Fluorescence intensity in the cytosolic regions of myotubes was quantified as described in §E.3.5 and results were represented as intensity means distribution of region of interests, ROIs (*N*=100), as shown in Fig. 3B-C. Fig. 3B shows a not significant difference between control and stretched myotubes distributions (P-value=0.973); on the other hand, stretched dystrophic myotubes resulted in a significant (P-value=0.029) stretch-induced dye uptake increase in respect to un-stimulated control, as revealed by comparing fluorescence intensity distributions (Fig. 3C). These results demonstrate that lack of dystrophin strongly affects membrane permeability of human myotubes, when subjected to cycles of mechanical stretch that closely mimic physiological deformation of muscle fibers.

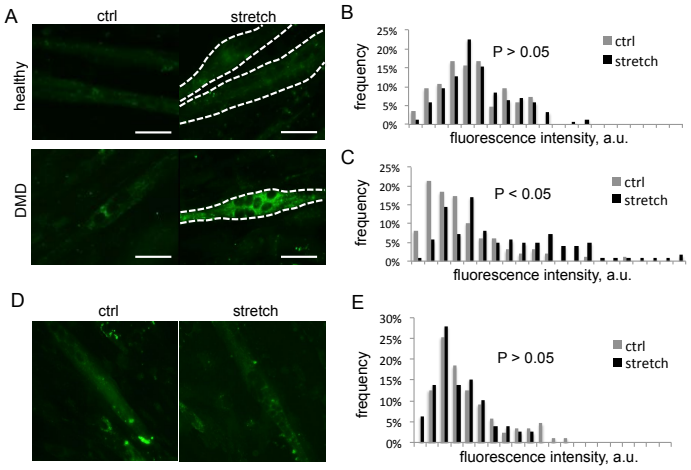

Figure 5 (A-C) 90 min stretch-induced membrane permeability analysis in dystrophic compared to healthy myotubes. (A) Representative pictures of FM 1-43 dye uptake in healthy and dystrophic myotubes after 90 min cyclic stretch (0.5 Hz, 15% deformation), compared to un-stimulated control myotubes. (B) Fluorescence intensity distribution of stretched healthy myotubes is not statistically different from the un-stretched control. (C) Fluorescence intensity distribution of stretched DMD myotubes result statistically different from the un-stretched control. (D-E) 45 min

stretch-induced membrane permeability analysis in dystrophic myotubes. (D) Representative pictures of FM 1-43 dye uptake in dystrophic myotubes after 45 min cyclic stretch (0.5 Hz, 15% deformation), compared to un-stimulated control myotubes. (E) Fluorescence intensity distribution of stretched myotubes is not statistically different from the un-stretched control.

We further investigated whether stretch-induced membrane permeability increase in dystrophic myotubes is already significant after a shorter period of cyclic stretch of 45 min. DMD myotubes were again loaded with FM 1-43 dye and stretched at 0.5Hz with 15% deformation for 45 min. Fig. 5D shows representative pictures of stretched and control myotubes with similar uptake of FM1-43 dye; quantification of fluorescence intensity confirms a not significant difference of the two distributions (Fig. 5E), meaning that permeability increase appears in a later temporal interval. This result also validates the hypothesis proposed by Allen et al., that increased permeability in dystrophic muscle fibers is likely due to the slow accumulation of intracellular calcium, which activates stretch-activated ion channels, rather than to the formation of membrane tears as a consequence of stimulation-induced membrane injury[18].

Indeed, many studies recognize an increased stretch-activated channels activity in DMD muscle fibers, which triggers abnormal cytosolic concentrations of intracellular calcium. Increased levels of intracellular calcium are also recognized to contribute to muscle degeneration through the aberrant activation of calcium dependent proteases, calpain-1 and calpain-2, rendering muscle fibers more permeable and eventually susceptible to fibrosis[27]. The implication of calpains in these disorders has identified them as important potential therapeutic targets and has raised interest in the use of specific calpain inhibitors as a potent treatment[28,29]. Observation of a four-fold increase in muscle calpain-2 mRNA levels in muscle fibers from DMD patients, compared to control, confirms enhanced expression of the calpain-2 gene in dystrophic condition, explaining the enhanced activity of the enzyme, and highlights its importance in DMD pathogenesis[30]. We therefore verified the role of cyclic stretch in affecting calpain-2 expression in dystrophic myotubes compared to the healthy ones by immunofluorescence analysis. Fig. 6 shows representative immuno-staining pictures of healthy and DMD myotubes stretched for 90 min at 0.5Hz and 15% deformation. Stretched healthy myotubes show an increased cytosolic signal if compared to the un-stretched controls, which in turn show a confined nuclear expression (Fig. 6A). This is probably due to a transient increase, during

mechanical stimulation, in intracellular calcium, which activates calcium-dependent proteases, like clapain-2. Interestingly both control and stretched DMD myotubes show a widespread calpain-2 cytosolic expression (Fig. 6B).

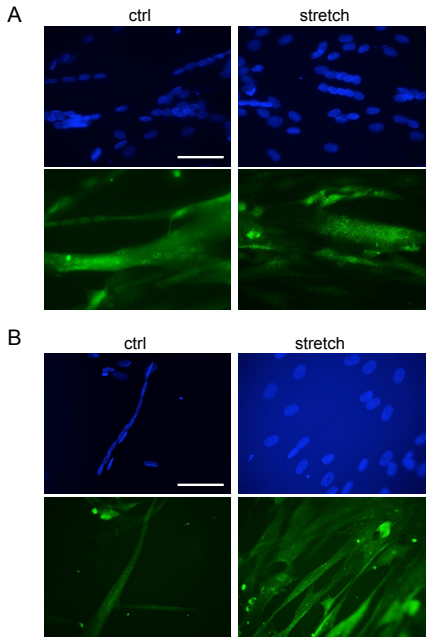

Figure 6 Calpain-2 immunofluorescence analysis of stretched healthy and DMD myotubes. (A) Comparison between control and stretched healthy myotubes. (B) Comparison between control and stretched DMD myotube.

We speculated that DMD myotubes derived from dystrophic patients have an elevated $[Ca^{2+}]_i$ per se and that cyclic mechanical stretch exacerbates the diseased phenotype leading to stretch-induced increased membrane permeability.

E.6 Conclusions

In conclusion, we investigated the role of cyclic mechanical stretch in a human DMD in vitro model, by developing an ad hoc microfluidic-based cell-stretching device in order to accurately mimic physiologic deformation to which muscle fibers are exposed in vivo. We first demonstrated that the developed device could be used to obtain a biological response on a cell culture, by showing a frequency-dependent cytoskeletal remodeling of F-actin filament after a cyclic mechanical stimulation. We then focused on the role of cyclic stretch in affecting membrane permeability increase of dystrophic myotubes compared to the healthy ones. Stretch-induced membrane permeability results to increase in a temporal window from 45 to 90 min, probably due to a slow accumulation of intracellular calcium, which results already altered in non-stretched dystrophic myotubes as

demonstrated by immunofluorescence analysis of calcium-dependent protease calpain-2.

The developed device could also be used as platform for investigate new therapeutic targets or for drug screening assays.

E.7 References

1. A. Salameh, A. Wustmann, S. Karl, K. Blanke, D. Apel, D. Rojas-Gomez, H. Franke, F. W. Mohr, J. Janousek, and S. Dhein, *Circulation Research*, 2010, **106**, 1592–1602.
2. A. Kumar, *The FASEB Journal*, 2004, **18**, 1524–1535.
3. S.-H. Kook, H.-J. Lee, W.-T. Chung, I.-H. Hwang, S.-A. Lee, B.-S. Kim, and J.-C. Lee, *Mol. Cells*, 2008, **25**, 479–486.
4. S. Suresh Babu, A. Wojtowicz, M. Freichel, L. Birnbaumer, M. Hecker, and M. Cattaruzza, *Sci. Signal.*, 2012, **5**, ra91.
5. H.-J. Hsu, C.-F. Lee, A. Locke, S. Q. Vanderzyl, and R. Kaunas, *PLoS ONE*, 2010, **5**, e12470.
6. P. G. De Deyne, *American Journal of Physiology-Cell Physiology*, 2000, **279**, C1801–C1811.
7. F. Rahimov and L. M. Kunkel, *J Cell Biol*, 2013, **201**, 499–510.
8. E. M. McNally and P. Pytel, *Annual Review of Pathology: Mechanisms of Disease*, 2007, **2**, 87–109.
9. D. J. Blake, A. Weir, S. E. Newey, and K. E. Davies, *Physiol Rev*, 2002, **82**, 291–329.
10. E. W. Yeung, N. P. Whitehead, T. M. Suchyna, P. A. Gottlieb, F. Sachs, and D. G. Allen, *J Physiol*, 2005, **562**, 367–380.
11. R. J. Khairallah, G. Shi, F. Sbrana, B. L. Prosser, C. Borroto, M. J. Mazaitis, E. P. Hoffman, A. Mahurkar, F. Sachs, Y. Sun, Y.-W. Chen, R. Raiteri, W. J. Lederer, S. G. Dorsey, and C. W. Ward, *Sci. Signal.*, 2012, **5**, ra56.
12. A. Kumar, *The FASEB Journal*, 2004, **18**, 102–113.
13. C. Y. Matsumura, A. P. T. Taniguti, A. Pertille, H. S. Neto, and M. J. Marques, *Am J Physiol Cell Physiol*, 2011, **301**, C1344–C1350.
14. C. Mann, E. Perdiguero, Y. Kharraz, S. Aguilar, P. Pessina, A. Serrano, and P. Muñoz-Cánoves, *Skeletal Muscle*, 2011, **1**, 21.
15. T. M. Suchyna and F. Sachs, *The Journal of Physiology*, 2007, **581**, 369–387.
16. D. G. Allen and N. P. Whitehead, *The International Journal of Biochemistry & Cell Biology*, 2011, **43**, 290–294.
17. Allen DG, Gervasio OL, Yeung EW, and Whitehead NP, *Canadian journal of physiology and pharmacology*, 2010, **88**, 83–91.
18. D. G. Allen and N. P. Whitehead, *The International Journal of Biochemistry & Cell Biology*, 2011, **43**, 290–294.
19. B.-T. Zhang, N. P. Whitehead, O. L. Gervasio, T. F. Reardon, M. Vale, D. Fatkin, A. Dietrich, E. W. Yeung, and D. G. Allen, *J Appl Physiol*, 2012, **112**, 2077–2086.
20. P. W. Hamer, J. M. McGeachie, M. J. Davies, and M. D. Grounds, *Journal of Anatomy*, 2002, **200**, 69–79.
21. E. W. Yeung and D. G. Allen, *Clinical and experimental pharmacology and physiology*, 2004, **31**, 551–556.
22. X. Trepat, L. Deng, S. S. An, D. Navajas, D. J. Tschumperlin, W. T. Gerthoffer, J. P. Butler, and J. J. Fredberg, *Nature*, 2007, **447**, 592–595.
23. A. Grossi, A. H. Karlsson, and M. A. Lawson, *Cell Biology International*, 2008, **32**, 615–622.
24. S. Akbari and H. R. Shea, *J. Micromech. Microeng.*, 2012, **22**, 045020.
25. R. J. Khairallah, G. Shi, F. Sbrana, B. L. Prosser, C. Borroto, M. J. Mazaitis, E. P. Hoffman, A. Mahurkar, F. Sachs, Y. Sun, Y.-W. Chen, R. Raiteri, W. J. Lederer, S. G. Dorsey, and C. W. Ward, *Sci. Signal.*, 2012, **5**, ra56.
26. B. L. Prosser, R. J. Khairallah, A. P. Ziman, C. W. Ward, and W. J. Lederer, *Journal of Molecular and Cellular Cardiology*, 2013, **58**, 172–181.
27. B.-T. Zhang, S. S. Yeung, D. G. Allen, L. Qin, and E. W. Yeung, *Journal of Applied Physiology*, 2008, **105**, 352–357.

28. M. Bartoli, N. Bourg, D. Stockholm, F. Raynaud, A. Delevacque, Y. Han, P. Borel, K. Seddik, N. Armande, and I. Richard, *J. Biol. Chem.*, 2006, **281**, 39672–39680.
29. N. P. Whitehead, M. Streamer, L. I. Lusambili, F. Sachs, and D. G. Allen, *Neuromuscular Disorders*, 2006, **16**, 845–854.
30. T. Hussain, H. Mangath, C. Sundaram, and M. Anandaraj, *Journal of Genetics*, 2000, **79**, 77–80.